EMULSION-BASED DELIVERY OF ALKALINITY FOR SUBSURFACE pH CONTROL

A dissertation submitted by

Katherine A. Muller

In partial fulfillment of the requirements

for the degree of

Doctor of Philosophy

in

Civil and Environmental Engineering

TUFTS UNIVERSITY

AUGUST, 2016

Advisor: Dr. C. Andrew Ramsburg

ABSTRACT

Emulsions are widely utilized to encapsulate, deliver, and release active ingredients and are routinely used in environmental applications. Alkalinity-releasing particles can be encapsulated within emulsions to provide long term pH control as alkalinity slowly releases from the oil droplets retained in the subsurface. Through a combination of laboratory experiments and mathematical modeling, this work addresses: (i) emulsion transport and retention in porous media; (ii) alkalinity release from particles encapsulated in emulsion oil droplets; and (iii) the ability of emulsions to provide passive, yet sustained, pH treatment. Concentrated emulsion transport and deposition behavior was predicted from particle transport models adapted and parameterized using data from transport of dilute emulsion. Dispersivity was found to increase with decreasing water saturation (i.e., from mass retention) in emulsion systems, but also more broadly in partially saturated air-water and NAPL-water systems as a whole. Encapsulation of alkalinity-releasing particles within the emulsion oil droplets was able to control the rate of alkalinity release through the increased resistance to mass transfer via the oil-water interface (orders of magnitude reduction in rates of release). Results illustrate how emulsions containing only limited loadings of MgO and $CaCO_3$ particle are able to provide long-term pH treatment in columns containing sandy porous media. Models developed and employed herein provide a tool that may aid in designing treatments employing oil-in-water emulsions, as well as providing insight into how to best reach or maintain site specific pH requirements.

DEDICATION

To my father who was always proud of me, my grandfather who primed me to be an engineer from the start, and my mother who showed me what it is be a strong, dedicated, and compassionate individual.

ACKNOWLEDGEMENTS

I would like to thank my friends and family for their continuous support over the course of my long tenure at Tufts University. Their encouragement and understanding proved to be invaluable throughout this process. In particular, I would like to thank Travis Yates, who on numerous occasions was the voice of reason I very much needed; Will Farmer for his friendship (and stats help) that kept me moving forward through hard times; and Doug Walker for his helpful insights, motivating conversations, and pushing me to be a better researcher over the years. I would like to thank Rhiannon Ervin, Brian Thomas, Anna Murray, Amy Hunter, Sandeep Sathyamoorthy, and Matt Becker. I would also like to thank Somayeh Ghazvinizadeh for modeling support. Thank you to Olivia Leach, Eric Wilburn, Tory Sims, Eric Liu, Justina Cheng, John Gill, Eimy Bonilla, and Evan Hallberg for their help in the laboratory. Most importantly, I would like to my advisor Dr. C. Andrew Ramsburg. He has been an excellent mentor. I admire his work ethic, attention to detail, and outlook on life.

Additionally, I would like to acknowledge my committee members, Dr. Steven Chapra (Tufts University), Dr. Robert Viesca (Tufts University), Dr. Hyunmin Yi (Tufts University), Dr. Brent Sleep (University of Toronto), and Dr. C. Andrew Ramsburg (Tufts University) for their guidance and help with this research.

Funding for this research was received from NSF CMMI-1000714 and Tufts University. The content of this document does not necessarily represent the

views of the agency and has not been subject to agency review. Partial funding for conference travel was provided by the Graduate Student Travel Fund and the School of Engineering at Tufts University.

TABLE OF CONTENTS

LIST OF FIGURES

LIST OF TABLES

LIST OF SYMBOLS

A= Hamaker constant [N·m]

A_s = Happel correction factor [-]

$a_{s,I,II}$ = specific interfacial area between the phases [1/L]

adj-R^2 = adjusted R^2

C=aqueous phase concentration [$M \cdot L^{-3}$]

C^*=equilibrium concentration [$M \cdot L^{-3}$]

$\overline{C}$ =average solvent concentration in the finger [$M \cdot L^{-3}$]

C_I^* = equilibrium concentration of the component in phase I [$M \cdot L^{-3}$]

C_0 = initial concentration [$M \cdot L^{-3}$]

Ca = Capillary number

D = diffusion coefficient as computed by Stokes-Einstein [$L^2 \cdot T^{-1}$]

D = distance between the center of two particles [m]

D_{aq}= aqueous molecular diffusion coefficient [$cm^2 \cdot min^{-1}$]

D_{eff} = effective molecular diffusion [$L^2\ T^{-1}$]

D_h = hydrodynamic dispersion [$L^2\ T^{-1}$]

D_m=mechanical diffusion [$cm^2 \cdot min^{-1}$]

D_{vis}=viscous diffusion coefficient [$cm^2 \cdot min^{-1}$]

d_p= particle diameter [L]

d_g= sand grain diameter [L]

d_{50}=median grain size [L]

E= effective mobility ratio [-]

e =charge of an electron

$f(\overline{C})$ = solvent fractional flow of the total volume [-]

f_D = fraction of displacing fluid [-]

f_R = fraction of resident fluid [-]

H= heterogeneity factor [-]

I = ionic strength

K= Koval factor [-]

K_p = partitioning coefficient

K_m =liquid-solid mass transfer rate [T^{-1}]

K_1 = Langmuir binding constant [$L^3 \cdot M^{-1}$]

K_2 =maximum sorption capacity [$M \cdot M^{-1}$]

k = Boltzmann constant

k = number of model parameters

k_d =first order deposition rate coefficient [T^{-1}]

k = intrinsic mass transfer coefficient [L·T-1]

k_L = lumped mass transfer coefficient [T-1]

$k_{I \to II}$ = mass transfer coefficient for phase I to phase II [$L \cdot T^{-1}$]

L = bed length [L]

M=mobility ratio [-]

N = number of samples in dataset or subset

n= porosity [-]

N_A = Avogadro's number

N_A = attractive number [-]

N_I = interception number [-]

N_{Pe} = Peclet number [-]

N_{vdw} = London-van der Waals attractive force number

N_G = gravitational number [-]

N_R = aspect ratio [-]

Pe = Peclet Number = $\frac{v_i L}{D_h}$ [-]

PV_D= Pore volumes of displacing fluid [PV]

∇P = pressure gradient vector [$Pa \cdot L^{-1}$]

q= Darcy velocity [$cm \cdot min^{-1}$]

q= particle charge

$q_{I \to II}$ = mass flux of the component from phase II to phase I [M/L^3-T]

R=radius of particle [m]

R_f = retardation factor [-]

S=solid-phase concentration [M-DP·M-sand^{-1}]

S_{max} = maximum solid phase concentration [$M \cdot M^{-1}$]

$S_{max,tot}$ = overall maximum solid phase concentration [$M \cdot M^{-1}$]

S_w=water saturation [-]

Sc =Schmidt number

s= separation distance [m]

SSA = specific surface area [L^{-1}]

T =fluid temperature [K]

U = fluid velocity [$L \cdot T^{-1}$]

U_i = uniformity index [-]

v_x= pore water velocity [$cm \cdot min^{-1}$]

α= dispersivity [cm]

α'= collision efficient factor [-]

β=depth-dependent exponent [-]

ε_r=relative dielectric constant of the liquid

ε_0 = the permeability in a vacuum (8.99×10^{-12} $C^2 J^{-1} m^{-1}$)

ζ_1= zeta potential of the particle surface

ζ_2=zeta potential of the collector grain

η_0 = collision frequency [-]

θ_{N0} = initial volume fraction of NAPL

θ_N = volume fraction of NAPL

κ= inverse Debye length [m^{-1}]

k_D=relative permeability of the displacing solution

k_R =relative permeability of the resident phase

κ = intrinsic permeability of the media [L^2]

τ = tortuosity as defined by Millington and Quirk (1961) [-]

μ_e=emulsion viscosity [mPa·s]

μ_0=water viscosity [mPa·s]

μ_r=resident fluid viscosity [mPa·s]

μ_d=displacing fluid viscosity [mPa·s]

ρ_e=emulsion density [$g \cdot mL^{-1}$]

ρ_{DP}=dispersed phase density [$g \cdot mL^{-1}$]

ρ_b=bulk density [$g \cdot mL^{-1}$]

Ψ_b= blocking function [-]

Ψ_d= depth-dependent function [-]

Φ_{EDL} = electric double layer force

$\Phi_{EDL,sphere-sphere}$= electric double layer force between two particles

$\Phi_{EDL,sphere-plane}$= electric double layer force between a particle and planar surface

$\Phi_{RES,sphere-sphere}$= Electrostatic repulsive force between two particles

$\Phi_{RES,sphere-plane}$= Electrostatic repulsive force between a particle and planar surface

Φ_{vdW}= van der Waal force

Φ_{Total}= total interaction force

$\Phi_{vdW,sphere-sphere}$= Van der Waals force for particle-particle interactions

$\Phi_{vdW,sphere-plane}$= Van der Waals force for particle-solid interactions

σ_c = surface tension of the continuous phase

μ = dynamic viscosity of the fluid [$M \cdot L^{-2}$]

μ_c = viscosity of the continuous phase

μ_D = viscosity of the displacing phase

μ_R = viscosity of the resident phase

LIST OF ACRONYMS

AIC= Akaike information criterion

AIC_c = sample size corrected Akaike information criterion

$AIC_{c,w}$ = weighed sample size corrected Akaike information criterion

CaO= calcium oxide

$CaCO_3$= calcium carbonate

CTRW= continuous time random walk

DLVO= Derjaguin-Landau-Verwey-Overbeek

DNAPL= dense non-aqueous phase liquid

DP = dispersed phase

GA = gum arabic

LOI=loss on ignition

MgO= magnesium oxide

$Mg(OH)_2$= magnesium hydroxide

NAPL= non-aqueous phase liquid

NSE = Nash-Sutcliffe model efficient coefficient

nZVI= nano zero valent iron

o/w= oil-in-water

PCE=tetrachloroethylene

PV = pore volume

Re=Reynold's number

SBO = soybean oil

Sh=Sherwood number

S_N=NAPL saturation

SSE = sum squared error

SSE_w = weighted sum squared errors

TCE= trichloroethylene

VC= vinyl chloride

vdW= Van der Waals force

EXECUTIVE SUMMARY

Oil-in-water emulsions are also routinely used in environmental applications as means of providing mobility control, as an amendment delivery vehicle, but most commonly as the oil substrate to sustain biotic reactions. Currently, understanding of amendment placement and release for subsurface remediation is rather limited and thus remains highly empirical.

The overall objective of this research was to assess the utility of oil-in-water emulsions for delivery and sustention of remedial amendments. Emulsion design and testing was accomplished using a series of batch and column experiments and subsequent mathematical modeling. Investigations focused specifically on encapsulating alkalinity-releasing particles within oil-in-water emulsion droplets to provide long term pH control as alkalinity slowly releases from the oil droplets retained in the subsurface.

Successful in-situ remediation hinges on the ability to successfully delivery and release remedial amendments which provide treatment. To address the three major components of required for effective remediation, this work was split into three corollary areas: emulsion transport and retention, extent and rate of alkalinity release, and the resulting pH treatment in a flow through system. With improved knowledge related to each of these components, remedial design can work to tailor remediation to fit specific site treatment requirements.

Emulsion transport and retention was evaluated using a series of 1-d column experiments and mathematical models. Existing particle transport models

are able to capture emulsion transport and deposition at low concentrations, but fail to adequately describe droplet transport at high concentration. To capture the experimental data, existing particle transport models were adapted to include two additional dispersive mixing terms. These terms included the influence of the deposited mass on mechanical dispersion and the influence of viscous instabilities on mixing. Inclusion of these additional mechanisms permitted particle transport models to be parameterized with low concentration emulsion transport data and then employed to predict emulsion transport and retention at concentrations that were an order of magnitude greater.

Mineral dissolution and linear driving force models were used to describe release kinetics from bare and emulsion encapsulated particles, respectively. By coupling alkalinity release and complex equilibrium chemistry, models were developed for alkalinity release from both bare particles and particles held within oil-in-water emulsions in batch systems. Long term pH treatment from the emulsion systems was tested experimentally in 1-d column systems. Mathematical models describing the pH over the course of emulsion treatment were validated with experiments. The resulting model offers insight on how to best modify particles and/or emulsions to provide the desired retention and release rates, to increase the ability to control subsurface pH.

[This page is intentionally left blank]

Chapter 1: Background

Within the remediation community there is considerable interest in improving coupled physical, chemical and biological processes for cleanup and stewardship of contaminated sites. Many of these processes require control of pH during treatment and, in some cases, long after. Thus, some of the most common amendments added to groundwater during site remediation are compounds to adjust pH. In fact, when considering strategies to transform or sequester organic and inorganic contaminants, it is the control of pH and redox potential that become critical to the overall success of the remediation technology. Groups of technologies which rely upon biotic or abiotic transformation or sequestration have been applied to treat heavy metals, radionuclides, and organic solvents. Currently, control of subsurface pH is typically completed by adding direct sources of alkalinity (e.g., sodium hydroxide (NaOH), magnesium oxide (MgO), calcium carbonate ($CaCO_3$), and sodium bicarbonate ($NaHCO_3$)) either as a solid or an aqueous solution to the groundwater. However, such methods for pH control in the field are often ineffective and/or costly.

Emulsions are widely utilized in the food, medical and pharmaceutical industries to encapsulate, deliver, and release active ingredients; however, control of amendment placement and release in environmental applications remains highly empirical. The overall objective of this research was to assess the utility of oil-in-water emulsions for delivery and sustention of remedial amendments with a focus on understanding the mechanisms controlling the delivery and release of

alkalinity releasing particles held *within* the oil phase of the emulsion. Encapsulation of particles within in emulsion droplets can provide both in situ pH treatment as well as substrate needed to sustain biotic reactions.

Successful description of alkalinity release from suspensions of bare particles and from particles encapsulated in oil-in-water emulsions will help reveal the controlling parameters in the extent and rate of alkalinity release. With increased knowledge, it may become possible to "tune" particle containing emulsions to provide a specific alkalinity release rate needed for remedial events. By coupling alkalinity release and complex equilibrium chemistry, models can be developed for alkalinity release (rates and extent) from both bare particles and particles held within oil-in-water emulsions. Colloidal particle transport and retention modeling is well established with various model formulations used to provide a mechanistic understanding of the physical and chemical processes governing particle transport and retention. However, when considering oil-in-water emulsion transport there are only a few acceptable models. The most widely accepted model is a modified particle filtration theory model (Soo & Radke, 1986) that mechanistically describes the transport of the emulsion oil droplets. Here, modeling efforts that pair alkalinity release with transport and deposition will provide a complete description of pH control for various particle delivery methods (i.e., particle suspensions, oil-in-water emulsions containing particles). Models validated with experiments will offer insight on how to best modify particles and/or emulsions to provide the desired retention and release rates, to increase the ability to control subsurface pH.

1.1 REMEDIATION BACKGROUND

Subsurface remediation is required at thousands of sites nationwide to reduce the risk posed by subsurface contaminants to human and environmental health. Contaminants found in the subsurface are most commonly due to human activities (e.g., chemical spills, poor disposal techniques, application of pesticides, etc.). Remediation of chemical pollutants is typically grouped into classes based upon process: biological (e.g., enhanced bioremediation); chemical (e.g., chemical oxidation); thermal (e.g., electrical resistive heating); and/or physical (e.g., pump and treat and air sparging). Common to all of these treatment classes is the need to add chemical, mechanical or thermal energy into the subsurface. In situ treatment technologies require successful delivery (and sometimes recovery) of additives to the subsurface. The ability to control amendment delivery to ensure effective contact between remedial amendment and subsurface contaminants is critical, though in practice this control is aspirational (See Table 1.1).

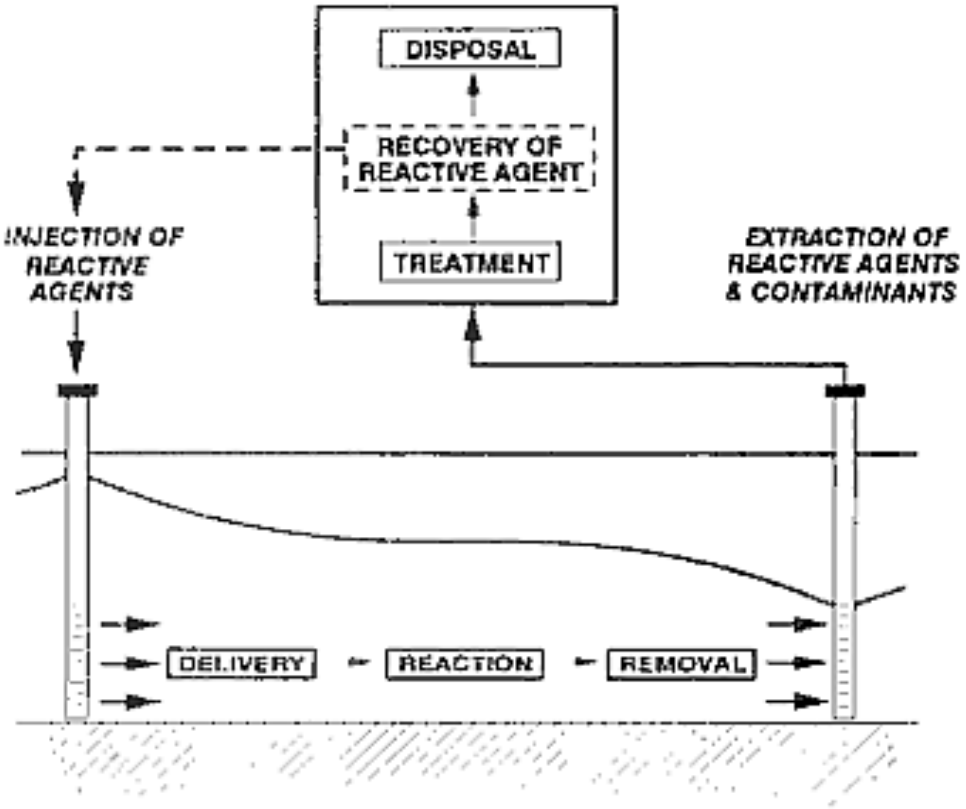

Figure 1.1: Schematic of a pump and treat system paired with the injection active remedial ingredients. (Source: Palmer & Fish, 1992)

Table 1.1: Additives for illustrative chemical remediation technologies.

Remediation Technology	Example Contaminants	Additives	Injection Method
Solidification/ Stabilization	• Radionuclides • Heavy metals • Coal tar	• Cement • Silicate, carbon, phosphates, or sulfur material binders • Clays • Lime	• Vertical auger mixing • Shallow mixing • Injection grouting
Chemical Oxidation	• Chlorinated solvents • BTEX • Phenols • Explosives • Pesticides • PCBs • VOCs • PAHs	• Potassium or sodium permanganate • Fenton's catalyzed hydrogen peroxide • Ozone • Sodium persulfate • Acids to acidify subsurface (required for some oxidants)	• Mixed into soil/ sludge • Gravity feed or injection wells • Pressurized injection • Hydraulic fracturing
Chemical Flushing	• Metals • Chlorinated solvents • Phenols	• Acidic/basic solutions • Surfactants • Chelating agents • Cosolvents	• Injection/ extraction wells
Bioremediation	• Chlorinated solvents • Heavy metals • Nitrate • Perchlorate	• Electron donor • Microbes • Nutrients • Alkalinity sources	• Injection/ extraction wells

Adapted from United States Environmental Protection Agency, 2006

1.2 SUBSURFACE AMENDMENT DELIVERY

The success of remediation technologies relies on the ability to delivery active constituents to the subsurface contamination; whether amendments need to be delivered directly to the contaminants or correctly placed for subsequent dissolution from the emplaced additives.

1.2.1 INJECTED AQUEOUS AMENDMENTS

Amendment delivery can be accomplished with aqueous solutions via injections wells, direct push methods, infiltration galleries, and recirculation wells (Arcadis, 2002). Recirculation systems can be in situ systems, where amendments are directly added to the ambient groundwater thus not requiring additional pumping of groundwater to the subsurface; or ex situ, where amendments are mixed with extracted groundwater aboveground. Injection-extraction wells, circulation wells and tandem recirculating wells can all be used to delivery aqueous amendments. In situ recirculation systems require in-well mixing (e.g., static or inline mixers) to mix chemical amendments with the contaminated groundwater (Goltz & Christ, 2012). However, clogging and fouling of injection/extraction wells can be a major issue during remediation when injecting aqueous solutes that may form precipices when contacting groundwater (e.g., $CaCO_3$).

Even with efforts to enhance mixing and delivery, subsurface heterogeneity (e.g., regions of permeability contrast) can create zones of flow bypass and preferential flow paths, and thus delivery of injected aqueous

amendments, dictated by ambient groundwater patterns, may not successfully reach the intended targeted area. Contaminant treatment in low permeability zones can be difficult to achieve due to the inaccessibility to delivery or emplace amendments; and contaminant rebounding post cleanup is typically cited to be due to incomplete removal from less accessible geological regions.

1.2.2 Solid Amendments

Solid phase materials (e.g., $Mg(OH)_2$, CaO, $CaCO_3$) can be added to the subsurface via directly injecting the solids (as a slurry) into boreholes or by following the solid injection with injection of a slurry material to aid in transport away from the injection site. Transport of solid materials can be increased through physically mixing the injected solid into the subsurface using augers (Borden, et al., 2008; Castelbaum, et al., 2011). Reactive materials can also be added to the subsurface in the form of a permeable reactive barrier (PRB) to treat contaminants. With a PRB a reactive zone or barrier is created in the subsurface where contaminated groundwater will flow through to be treated. Reactive iron particles are commonly employed as a PRB for degradation of organic compounds since injection and targeted delivery of ZVI in the subsurface presents difficulties.

1.3 Importance of Subsurface pH Control

Amendments designed to aid in pH regulation are the most common amendments added to groundwater. Numerous remedial technologies such as

immobilization of heavy metals/radionuclides, enhanced bioremediation of chlorinated solvents, and in situ chemical oxidation/reduction require careful control of subsurface pH for successful contaminant remediation.

1.3.1 Enhanced Anaerobic Bioremediation

In situ bioremediation is a widely used remediation technique to degrade a variety of contaminant types (e.g., chlorinated solvents, heavy metals, nitrate, etc.); however, successful long-term bioremediation requires that the subsurface be held at conditions favorable for microbial degradation to occur (i.e., sufficient carbon sources, nutrient levels, temperature, pH, etc.). Enhanced biodegradation is widely used due to the in situ nature of the technology along with the relatively low cost of treatment. In situ biodegradation involves employing microbes (either naturally occurring on site or added) to degrade contaminants present in the subsurface. In order to promote biodegradation additional microbe consortiums can be injected along with amendments (e.g., compounds to control pH, carbon sources, nutrients, etc.) to create a subsurface with favorable conditions for microbial degradation. Degradation of chlorinated solvents is commonly completed using enhanced biodegradation by reductive dechlorination (microbial degradation pathway shown in Figure 1.2).

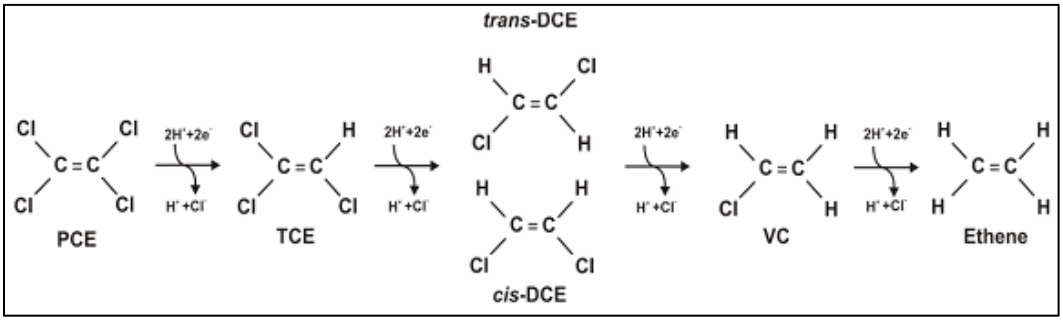

Figure 1.2: Reductive dechlorination of chlorinated ethenes. (Source: Parsons, 2004)

Metabolic reductive dechlorination approaches commonly employ fermentable carbon sources to produce electron donor in the form on hydrogen. The dechlorination processes creates a mole of acid with each mole of chloride removed from the contaminant molecule or its degradation products (Steffan, et al., 2010). This acidity produced from degradation reduces rates of contaminant degradation. Moreover, some of the organisms responsible for the conversion of cis-DCE and VC, already the rate limiting steps in the degradation process, can be most influenced by the decrease in pH (Lacroix, et al., 2014; Adamson, et al., 2004). Thus, maintaining pH near circa neutral is highly important for remedial success via enhanced bioremediation.

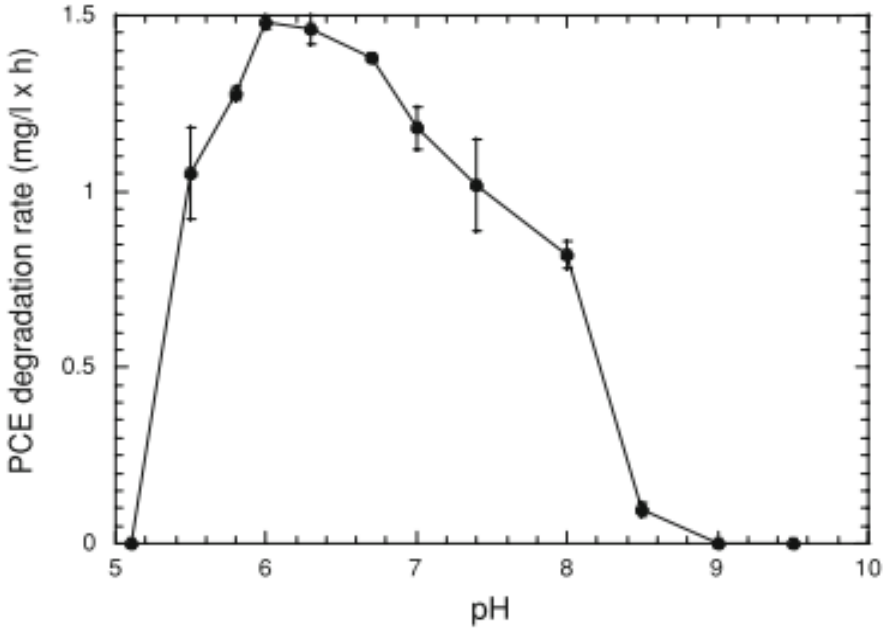

Figure 1.3: The effect of pH on PCE degradation by SDC-9TM. (Source: Vainberg, et al., 2009)

Subsurface pH control becomes critical because microbial contaminant degradation rates are highest at circa neutral pH conditions, with pH 5.5-7.5 found to be ideal for PCE degradation, and degradation rates are substantially lower outside of this range (Vainberg, et al., 2009). In fact, there are many reports of organohalide-respiring bacteria becoming inactivated as the pH drops below 5 (Vainberg, et al., 2009; Robinson, et al., 2009; Lacroix, et al., 2014). Philips et al. (2013) studied the use of a common inoculum, KB-1, and found that dechlorination rates of TCE were highest when the pH was between 7.1-7.5 but TCE degradation was completely inhibited below 6.2. Vainberg et al. (2009) determined that the PCE degradation rate at optimal pH (i.e., pH 6) was 1.5 mg $PCE \cdot L^{-1}$-h. Laxroix et al. (2014) completed dechlorination experiments with various microbial consortia to evaluate the pH inhibition on each step in the reductive dechlorination process. The authors corroborated that degradation from vinyl chloride to ethene was the most pH sensitive reductive dechlorination step, which supports field evidence of degradation stalling creating a buildup of degradation products, mainly vinyl chloride, before complete reduction to ethene

Table 1.2: Optimal pH for reductive dechlorination by mixed cultures.

Source	Optimal pH	Inhibition pH (low; high)*	Contaminant degraded	Microbial Consortium
Philips et al. (2013)	7.1-7.5	6.2	TCE	*KB-1*™ ** (SiREM, Canada)
Lacroix et al. (2014)	6.99	4.3; 9.2	PCE to *cis*-DCE	SL2-PCEa ┼
	6.6	5.3; 7.9	*cis*-DCE to VC	SL2-PCEa ┼
	6.5	5.2; 7.8	VC to ethene	SL2-PCEa ┼
	6.44	4.4; 8.5	PCE to *cis*-DCE	SL2-PCEb ┼
	7.43	4.6; 10.2	*cis*-DCE to VC	AQ-1 ┼
	6.99	5.4; 8.5	VC to ethene	AQ-1 ┼
	6.56	6.1; 7.1	PCE to ethene	AQ-5 ┼
	6.78	5.3; 8.2	PCE to VC	PM ┼┼
	6.78	5.5; 8.0	VC to ethene	PM ┼┼
Vainberg et al. (2009)	6	5; 9	PCE	SDC-9™ ∘

* Inhibition pH was calculated when the pH inhibition function was less than 0.01 (i.e., 99% of degradation was inhibited) based on modeled parameters in Lacroix et al. (2014).

** Commercially available dechlorinating inoculum containing Dehalococcoides sp., Geobacter sp., and Methanomethylovorans sp. grown in dilute salt solution with formate or lactate.

┼ Organohalide-respiring consortia originated obtained from chlorinated ethene contaminated aquifers that were enriched and maintained in the laboratory. (Szynalski, 2003)

┼┼ Consortia originated obtained from Point Mugu Naval Weapon Facility, California enriched under anaerobic conditions with soil and groundwater from site for 1.5 years then enriched with a sterile basal medium with trace nutrients present. (Yu, 2003)

∘ Commercially available dechlorinating inoculum containing Dehalococcoides sp. strains grown under anaerobic conditions on lactate with PCE. Other trade names of this culture include: Bat-9™; RTB-1™; and BDLplus™

Although the natural buffering capacity of the soil can provide some alkalinity, the quantity is highly variable depending on soil type (see Section 1.4.1 Intrinsic Buffering Capacity for further details). Once the natural buffering capacity of the soil is exhausted artificial pH control of the subsurface is required to prevent degradation stalling (Robinson, et al., 2009; Steffan, et al., 2010). The type of electron donor used for bio-stimulation will also determine the alkalinity demand required to maintain acceptable pH levels. McCarty et al. (2007) studied the influence of type of organic electron donor on the amount of alkalinity (as bicarbonate) required to keep pH above 6.5. Their study suggests that formate is more effective as a substrate for a given level of available alkalinity. The reason being that bicarbonate is formed as formate is utilized thereby providing additional alkalinity to help maintain pH in a range suitable for solvent degradation. Although formate can allow more of a sustainable bioremediation process, the rate at which formate is dehydrogenated is slow and may not produce a sufficiently fast rate of alkalinity to prevent acid buildup (Philips, et al., 2013).

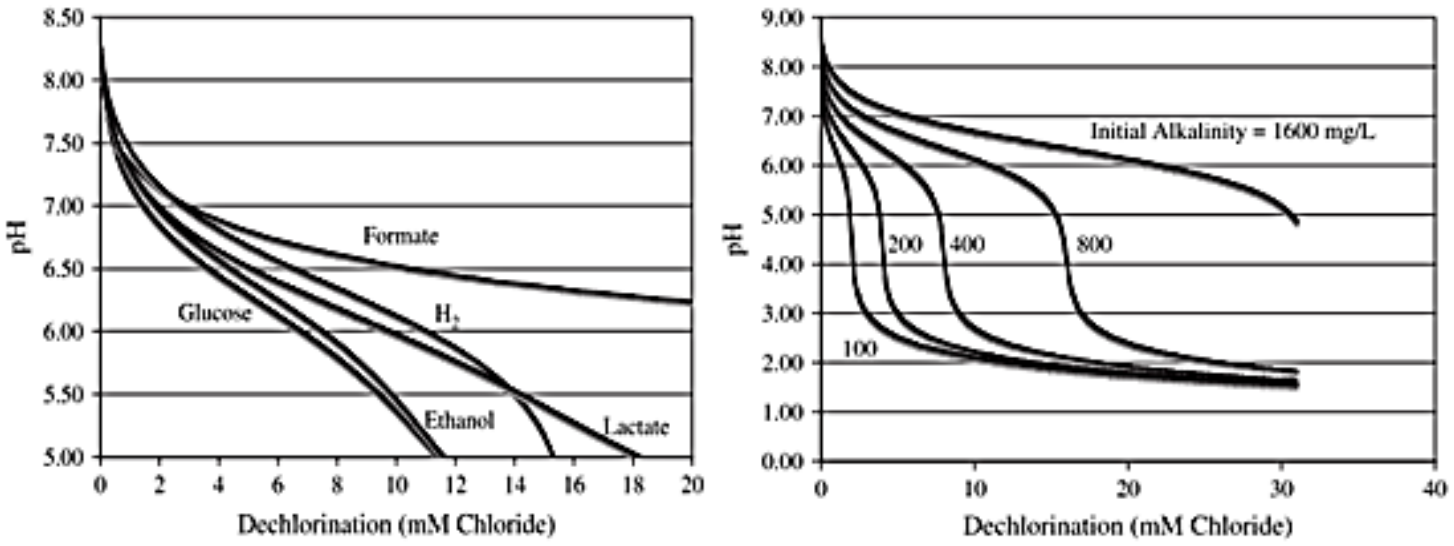

Figure 1.4: (left) Effect of initial alkalinity on pH as reductive dechlorination is occurring. Figure assume hydrogen is the electron donor with an initial dissolved carbon dioxide concentration of $2x10^{-4}$ mM and temperature is 20^0C; (right) effect of reductive dechlorination on pH as a function of electron donor, assumes same assumptions as the left figure and has a starting alkalinity of 800 $mg \cdot L^{-1}$ bicarbonate alkalinity. (Source: McCarty, et al. (2007)

An additional concern is that providing further buffering capacity in the form of bicarbonate can promote other microbial groups (i.e., methanogens and homoacetogens) that compete with organohalide-respiring microbial groups for hydrogen as an electron donor (Delgado, et al., 2012).

1.3.2 Stabilization Techniques

Stabilization is a remediation technology where instead of physical immobilization of the contaminants (solidification), compounds are chemical altered to reduce mobility in the subsurface allowing the soil to be treated instead of the groundwater (Mulligan, et al., 2001) . Heavy metal solubility and thus transport is greatly affected by pH and to a lesser extent by redox potential. Chuan, et al. (1996) found that lead, cadmium, and zinc were present at low solubility under basic conditions, whereas the metal solubility greatly increased as pH was reduced to more acidic conditions. The authors also found that metal solubility increased as redox potential decreased while at constant pH. Due to the influence of pH on metal solubility, these compounds can be precipitated or immobilized by in situ pH adjustments. For example, oxides present in the subsurface can adsorb metal ions, stabilizing heavy metals in the form of metal oxides- again this adsorption process is directly connected to pH and redox potential. Both cations and anions are greatly influenced by subsurface pH (Figures 1.5 and 1.6 for example, adsorption of anions will increase with increasing pH, stabilizing the ionic contaminants (Palmer & Fish, 1992).

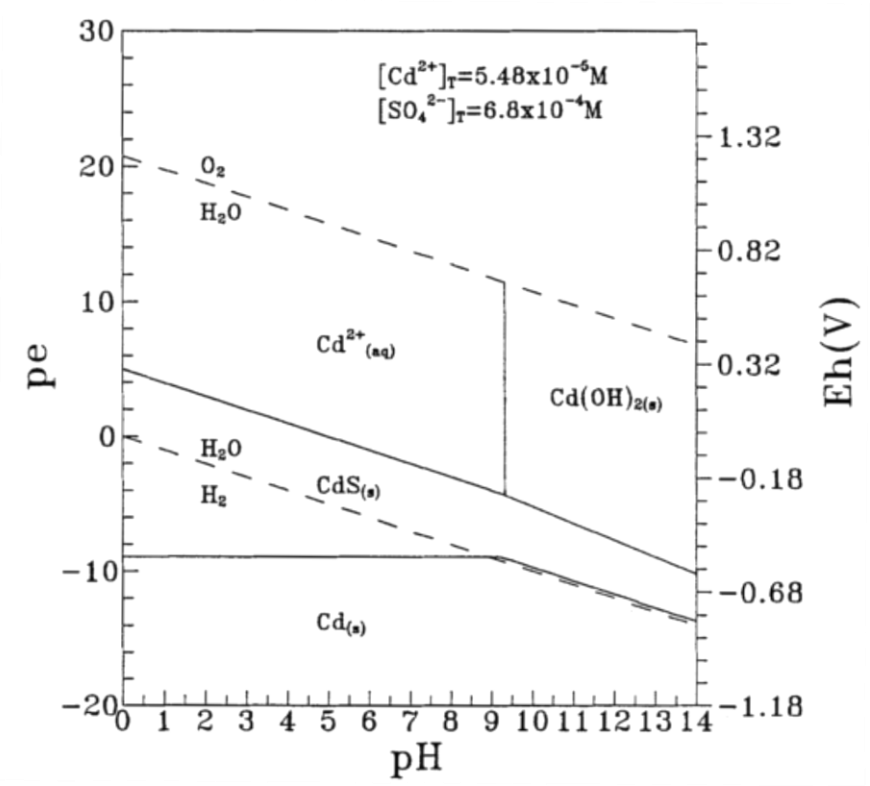

Figure 1.5: Example pE-pH diagram for Cadmium to show influence of pH and redox on metal solubility. $[Cd]_T=5.48x10^{-5}$ M; $[SO_4]_T=6.8x10^{-4}$ M. (Source: Chuan, et al. (1996))

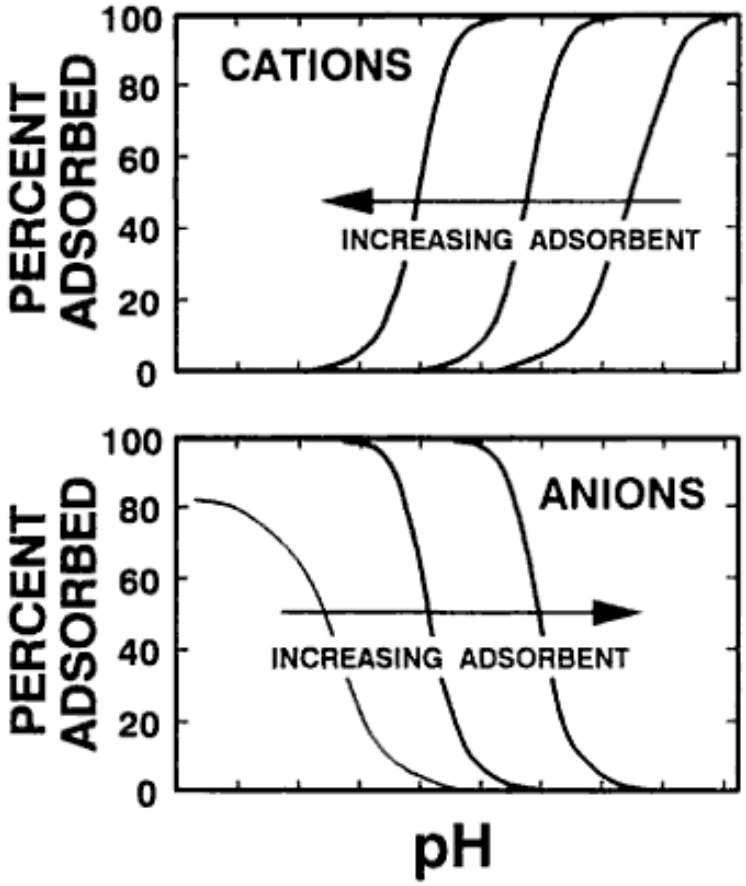

Figure 1.6: Effect of pH on adsorption of cations and anions. (Source: Palmer & Fish (1992))

Additionally, bioimmobilization can effectively reduce the solubility and mobility of radionuclides (e.g., uranium) in the subsurface by utilizing naturally occurring subsurface microbes that release sulfide or phosphate for immobilization (Martinez, et al., 2007). pH control may become important for bio immobilization due to the effect of pH on microbial release of phosphate. It was found that bacteria increased phosphate release by around about 40% when the pH was increased from 5 to 7 helping promote bio immobilization (Beazley, et al., 2007).

1.3.3 Chemical Oxidation

Chemical oxidation treatments can be used to transform toxic contaminants into less harmful compounds. Oxidants supplied to the groundwater (e.g., permanganate, hydrogen peroxide, iron, persulfate, ozone, etc.) can be used to remediate a variety of contaminants; however, for some oxidization reactions the subsurface pH must be held between a specific range of pH levels. In situ chemical oxidation (ISCO) is most commonly completed with base activated persulfate (although persulfate activation can be completed by many mechanisms including heat, UV, and chelated iron) (Furman, et al., 2010). There are limitations of each type of chemical oxidation for example, catalyzed H_2O_2 decomposes rapidly and permanganate tends to react with the reducing species in subsurface (e.g., soil organic matter).

As an illustrative example on how pH affects chemical oxidation, reactions with permanganate as shown below:

$$MnO_4^- + 8H^+ + 5e^- \rightarrow Mn^{2+} + 4H_2O \qquad pH < 3.5 \qquad (1.1)$$

$$MnO_4^- + 2H_2O + 3e^- \rightarrow MnO_2(s) + 4OH^- \qquad 3.5 < pH < 12 \qquad (1.2)$$

$$MnO_4^- + e^- \rightarrow MnO_4^{2-} \qquad pH > 12 \qquad (1.3)$$

For example, Fenton's reagent (i.e., a form of catalyzed hydrogen peroxide (H_2O_2)) is found to be most effective under acidic conditions (i.e., below 3.5) for the removal of dyes and chemical oxidation demand (COD) in wastewaters (Meriç, et al., 2004) and for complete mineralization of the pesticide pentachlorophenol (Watts, et al., 1990) thus requiring treatment step for pH adjustment. Ozone oxidation is also most effective under acidic conditions. Thus oxidation via Fenton's reagent or ozone is not applicable for basic soils or soils with high buffering capacity since it would require a significant amount additives for successful pH modification. Although, in situ permanganate oxidation can successfully occur under typical environmental pH conditions (3.5-12), it is most efficient under acidic conditions when five electrons are transferred (see reactions below-equations 1.4 & 1.5 from Huling & Pivetz, 2006). In situ chemical oxidation can also be used for chlorinated solvent removal, creating non-toxic byproducts by the following reactions (reaction shown below with permanganate as the oxidizing agent for PCE and TCE when pH is between 3.5 and 12, respectively (Strategic Environmental Research and Development Program, 2006)).

$$4MnO_4^- + 3C_2Cl_4 + 4H_2O \rightarrow 4MnO_2(s) + 6CO_2 + 8H^+ + 12Cl^- \quad (1.4)$$

$$2MnO_4^- + C_2HCl_3 \rightarrow 2MnO_2(s) + 2CO_2 + H^+ + 3Cl^- \quad (1.5)$$

Hydrogen ions are a byproduct of chlorinated solvent oxidation, and thus contaminant reduction can drastically reduce the groundwater pH over the course of remediation. Large amounts of carbon dioxide gas can be produced during oxidation which can alter subsurface permeability and thus pH control can become important here as well in order to reduce permeability changes.

The mobility of heavy metals may be enhanced or decreased during chemical oxidation/reduction treatments due to the pH sensitivity of metal solubility and may require some pH treatments to produce either mobilization or immobilization of metals. Also, MnO_2(s) can act as a strong adsorbent for many heavy metals (e.g., Cd, Cr, Zn, etc.) affecting metal mobility during chemical treatments.

1.3.4 Chemical Reduction

Contaminant degradation, of chlorinated solvents and heavy metals in particular, via bimetallic particles (e.g., zero valent iron (ZVI), zinc, nickel, copper, etc.) is a widely studied abiotic destructive technology (e.g., Arnold & Roberts, 2000; Lien & Zhang, 2001; Liu, et al., 2005; review by O'Carroll, et al., 2013). As bimetallic particles become oxidized, reducing conditions are created thus providing favorable conditions for abiotic contaminant reduction (Henn &

Waddill, 2006). For example, the reaction of ZVI and TCE reducing completely to ethylene can be written as (Chen, et al., 2001):

$$Fe^0 \rightarrow Fe^{2+} + 2e^- \quad (1.6)$$

$$C_2HCl_3 + 3H^+ + 6e^- \rightarrow C_2H_4 + 3Cl^- \quad (1.7)$$

However, the electrons produced from oxidizing ZVI can also react with water or with other aqueous constituents in groundwater. When reaction with water a hydroxide ion and hydrogen gas are produced:

$$2H_2O + 2e^- \rightarrow 2OH^- + H_2(g) \quad (1.8)$$

In addition to the more direct surface reduction as written in Equation 1.8, the hydrogen gas produced from the reaction with water can act as the reductant for contaminant degradation.

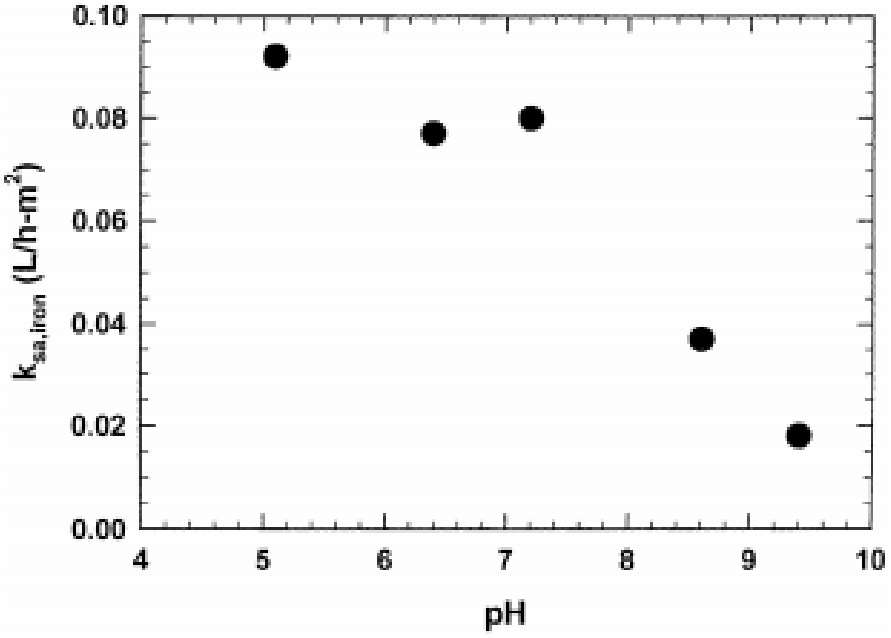

Figure 1.7: Influence of pH on TCE reduction via zero valent iron particles. (Source: Chen, et al., 2001)

Since H^+ and OH^- ions are entering the reduction reactions, degradation will be affected by pH. For example, Chen et al. (2001) investigated the effects of pH on TCE degradation rates by ZVI finding decreasing degradation rates with increasing pH. At low pH levels, iron corrosion is enhanced thus increasing the surface oxidization of the ZVI core; however at high pH levels iron hydroxides form on the surface limiting contamiant degradation (Song & Carraway, 2005).

1.4 Typical Practices for Subsurface pH Control

1.4.1 Intrinsic Buffering Capacity

Soil and groundwater can contain a natural buffering capacity. The buffering capacity of groundwater is measured by the alkalinity present and the U.S. Geological Survey (2010) defines alkalinity as "the capacity of water for neutralizing an acid solution." More specifically, alkalinity is the proton deficiency relative to H_2CO_3*. For most natural waters alkalinity is dominated by the carbonate system and thus the relevant expression for carbonate dominated system is shown below.

$$Alk_T = 2[CO_3^{2-}] + [HCO_3^-] + [OH^-] - [H^+] \qquad (1.9)$$

However, with groundwaters other ions can be present that affect total alkalinity and often the total alkalinity calculation is expanded as follows:

$$Alk_T = 2[CO_3^{2-}] + [HCO_3^-] + [OH^-] + [B(OH)_4^-] + 2[HPO_4^{2-}] \ldots$$
$$\ldots + [SiO(OH)_3^-] - [HSO_4^-] - [H^+] \qquad (1.10)$$

Where: $B(OH)_4^-$ is tetrahyroxyborate

Although alkalinity measurements of the groundwater can provide insight into the overall buffering capacity, the soil and solids present provide the majority of the buffering capacity for the subsurface system. The buffering capacity of solids is similarly defined and is the ability of a solid to bond/sorb and release excess hydrogen ions. Soil buffering capacity is typically high for systems with solids containing bicarbonate, carbonate, and hydroxides minerals (e.g., calcite, dolomite); although some alkalinity can be provided from borates, silicates and phosphates present in soils (Arcadis, 2002). Soil buffering capacity can take the form of mineral dissolution to give off weak acids (e.g., calcium carbonate dissolution); weathering of silicates that release basic cations; ion exchange onto mineral and organic soil surfaces of hydrogen cations; incorporation of hydrogen ions into clay structures and mineral lattices; or via neutralization reactions with oxides and hydroxides (Hajnos, 2011). Soil buffering capacity can be estimated based on the organic carbon and clay content of the soil; with increasing organic carbon content and clay content comes increasing buffering capacity (Weaver, et al., 2004).

Table 1.3: Buffering capacity of soil components (in pH range of 3.5-8.0).

Soil Material	Capacity [meq/g]	Reference
Silicate Clays		
Smectites	0.8-1.5	McBride (1994)
Vermiculite	1.5-2.0	
Illite	0.2-0.4	
Kaolinite	0.01-0.05	Thomas & Hargrove (1984)
Soil Organic Matter (SOM)	2.0	Helling, et al. (1964)
Allophane and Imogolilte	0.2-0.5	Wada (1989)
Iron and Aluminum Hydroxides and Oxides*	0.05-0.4	Borggaard (1983)
Calcium Carbonate ($CaCO_3$)**	20	Stumm & Morgan (1996)

*Based on linear extrapolation between 8 and 3.5 of the data for hematite and goethite
**$CaCO_3$ equilibrium occurs at pH 7 or above
Source: Bloom, 1999

The cationic exchange capacity (CEC) of the soil is the measure of the ability for a soil to hold more cations and is thus directly correlated to the buffering capacity of the soil; as CEC increases the intrinsic buffering capacity of the soil also generically increases. The CEC value of a soil or soil type is commonly known whereas the soil buffering capacity is typically unknown. Additionally, the mineralization of organic matter, nitrogen, sulfur, phosphorous can all be affected by ability of soils to adsorb and release hydrogen ions (i.e., the buffering capacity). Soil acidification occurs when cations are removed from soils and replaced with anions (van Breemen, et al., 1984). Colloidal soil particles can also provide buffering capacity to the subsurface (e.g., humus) (Hajnos, 2011).

1.4.2 Artificial pH Modification

Subsurface pH must be modified artificially when natural buffering capacity is limited or exhausted. Typically, artificial pH control for subsurface remediation is completed via aqueous phase additions of alkaline solutions (e.g., sodium bicarbonate ($NaHCO_3$), sodium or calcium carbonate ($NaCO_3$ or $CaCO_3$), sodium hydroxide (NaOH), etc.), buffered aqueous solutions (e.g., phosphate buffers), or solid phase alkaline materials to the subsurface (see Table 1.4 for pH modification examples). Aqueous phase additions practices have large limitations since aqueous delivery is governed by ambient groundwater flow; thus decreasing the control over spatial and temporal in-situ amendment delivery, which is increasingly problematic in heterogeneous media.

Table 1.4: Common chemical additives to provide alkalinity or acid neutralization.

Chemical	**Capacity [meq/g]**	**Max pH**	**Neutralization Efficiency [%]**	**Mass needed compared to limestone**	**Cost compared to NaOH**
Sodium carbonate (Soda Ash) (Na_2CO_3)	18.9	11.6	95-100 (powder) 60 (briquettes)	1.06	0.56
Calcium Hydroxide ($Ca(OH)_2$)	27.0	12.4-12.5	90-95	0.74	0.17
Calcium oxide (lime) (CaO)	35.7	12.4-12.5	90	0.56	0.11
Sodium Hydroxide (NaOH)	25.0	14	100	0.80	1.00
Magnesium oxide/hydroxide ($MgO/Mg(OH)_2$)	50.0/34.5	Theoretical: 10.2 Actual: 9-9.5	90-95	0.40/0.58	0.22
Calcium Carbonate ($CaCO_3$)	20.0	Theoretical: 9.4 Actual: 6-7.5	30-90	1.00	0.04

Source: Trumm (2009)

Active amendment delivery (including pH modification amendments) can be completed using injections wells, direct push methods, recirculation wells (both in and ex situ systems) and infiltration galleries (Arcadis, 2002). Phosphate buffers can also be employed to provide pH adjustments to the subsurface either as a pretreatment for chemical treatments or as a way to combat changing pH over the course of remediation; however, phosphate salts are not commonly used in the field due to the high cost and creating issues of aquifer clogging (McCarty & Criddle, 2012). Solid phase alkaline materials (e.g., $Mg(OH)_2$, CaO, $CaCO_3$) can be added to the subsurface via directly injecting the solid as a slurry into boreholes or by following the solid injection with injection of a slurry material to aid in transport away from the injection site. Transport of solid materials can be increased by physically mixing the injected solid into the subsurface using augers (Borden, et al., 2008).

1.4.3 Cost Considerations

Active amendment delivery may not be cost effective at some cleanup sites. A cost assessment was completed for field site at Fort Dix, New Jersey to remediate chlorinated solvents via bioaugmentation from 2006-2009 indicating that remediation cost around $875 per cubic yard of contaminated aquifer (Steffan, et al., 2010). Since the natural buffering capacity at the site was low, with pH approximately around 4.5, adjustment of the subsurface pH was required and 16,600 pounds of sodium bicarbonate and sodium carbonate solid buffer were added to the subsurface to help control pH during bioremediation. At this site 49% of the total cost was for capital costs, which included the installation of a

buffer injection system; and 31% of cost was for operation and maintenance of which included pH buffer, lactate, and nutrient amendments. Additional costs were accrued due to fouling and clogging of the injection wells by the buffering additives, as well as due to a spike in pH levels which affected the in situ microbial communities, requiring additional microbes to be added to the subsurface (Steffan, et al., 2010). Still, bioaugmentation with recirculation was determined to be approximately one third the cost of a pump and treat system for this site, and costs could be reduced another 30% if passive bioagumentation techniques were used (Steffan, et al., 2010). Not only are continuous injection operations to control pH expensive to run and maintain, but have also been cited to not effectively control subsurface pH levels at field sites. The same field study as described above found that in some injection wells the pH was greater than 9 where in other subsurface locations the pH was less than 5.5 even after weeks of injecting buffered solutions (Steffan, et al., 2010).

1.4.4 Advanced Control Methods for Subsurface pH

Alternative delivery approaches for controlling pH have been explored. Particle suspensions, particle-containing emulsions, and encapsulated buffering materials are being investigated as a possibly method that allows for better long-term control of amendment delivery to the subsurface. The use of reactive particles for subsurface treatment has been thoroughly investigated with reactive iron particles (i.e., nZVI); however, use of bare particles is limited due to issues of effective delivery. Particle suspensions have been investigated for pH control as

well with insoluble buffering particles (nano to micron size calcium carbonate particles) patented as Neutral Zone™ for subsurface pH control. Surface modification of the Neutral Zone™ particles was completed with food grade additives to give the particles a negative surface charge for enhanced suspension stability and mobility for subsurface injection (Piegat and Newman, 2008). Additionally, Lacroix et al. (2014) used silicate minerals (andradite, diopside, fayalite, forsterite) for passive pH control in systems of laboratory microbial consortia degrading PCE. The authors found that although silicate minerals are able to help control pH during degradation events some of the silicate minerals were not compatible with the microbial consortia, resulting in microbial inhibition, specifically with cis-DCE and VC degradation. No investigations into the aspects of mineral delivery were investigated to assess the applicability of using such particles for subsurface treatment. Pyrite (FeS_2) mineral was also found to be effective for pH control during denitrification in batch and column experiments (Jha & Bose, 2005). In situ pH modifications have also been completed, on the laboratory scale, using an encapsulated phosphate buffer (Vanukuru, et al., 1998; Rust, et al., 2000) and further extended so that buffers were encapsulated in a pH sensitive coating (Rust, et al., 2002; Flora, et al., 2008; Aelion, et al., 2009). Organic compounds have also been the subject of recent study on pH control methods and tertiary amines have been invested as a potential pH buffer via mineralization of CO_2 into carbonate minerals and although the application is presented for CO_2 sequestration (Steel, et al., 2013).

1.5 Delivery of Particle Suspensions to the Subsurface

Although many studies have found that micro and nano-sized particles can successfully supply the active ingredients, including for modifying pH, particle delivery and distribution within the subsurface can control effectiveness of these remedial efforts. Aqueous suspensions or slurries of unmodified particles tend to be unstable, limiting the ability to distribute particles to the subsurface. Basic forms of particle surface modification and particle encapsulation techniques have been explored in an attempt to enhance amendment delivery with such additions as particle coatings, encapsulation and emulsions. Understanding the mechanisms controlling suspension stability, of both unmodified and modified particles, and how particle stability and surface characteristics affect the transport of particles in the subsurface is important for further improvement of remedial technologies.

1.6 Particle Surface Coatings

Surface modification of nanoparticles can increase control over the physical and chemical properties of particles to allow for more targeted use. Recently substantial effort has been directed toward understanding surfactants, polymers and polyelectrolytes to improve stability and transport of nano- and colloid-size particles in the subsurface (e.g., Lowry, et al., 2012; O'Carroll, et al., 2013; Garner & Keller, 2014) for enhanced control during remedial activities. In the realm of environmental remediation, polymers and polyelectrolytes have been used to modify nanoparticles to improve colloidal stability and transport in the

subsurface, most notably with nanoscale zero-valent iron (nZVI) nanoparticles (e.g., via CMC stabilization, although surface coatings have been applied to many other types of nanoparticles such as zinc oxide, silver, gold, cerium oxide, titanium dioxide, quantum dots, and iron oxides (Lowry, et al., 2012)).

Table 1.5: Common nanomaterials and coatings.

	Typical capping agents/coatings	
Nanomaterial	**Inorganic and small organic molecules**	**Synthetic and Organic macromolecules**
Zinc Oxide	2-mercaptoethanol, triethoxycarprylsilane, triethanolamine, acetate	Polyvinylpyrrolidone (PVP), polysaccharides
Silver	Citrate, decanethiol, tannic acid, ethylenediaminetetraacetic acid (EDTA)	Polyethylene glycol (PEG), PVP, Gum Arabic
Gold	Citrate, Octanethiol, Cethltrimethyl Ammonium Bromide (CTAB), cysteine, tannic acid	Biotin, Bovine serum albumin (BSA), polypeptides
Cerium Oxide	Oleic acid	PVP, Poly(acrylic acid)-octyl amine
Titanium Dioxide	Oleic acid	Poly(acrylic acid)
Quantum dots (CdSe, CdS)	Silica (inorganic), zinc sulfide (inorganic), citrate, mercaptopropionic acid	PEG, aminodextran
Iron Oxide	Dodecylamine, oleic acid	BSA, Poly(acrylic acid), poly(methacrylic acid), PEG
Zerovalent Iron (ZVI)	Au, Pd, Pt, Ni	Carboxymethyl cellulose, xanthan gum, polypropylene glycol

Source: Lowry, et al. 2012

Nanoparticles can be successfully stabilized using surfactants by overcoming the attractive van der Waal forces between particles (see Section 1.7 on DLVO Theory); however, surfactant adsorption is reversible and thus subsurface transport can be limited as the surfactant desorbs from the particle surface. Covalently bonding or physical adsorption of polymers can provide a successful and irreversible surface modification. Irreversible surface modification of nanoparticles can been completed using various methods such as via ultrasonic wave irradiation (Nishida, et al., 2005) or by UV-induced graft polymerization (Kim, et al., 2005) to coat nanoparticles with the polymer(s) of interest.

1.7 DLVO THEORY

Derjaguin-Landau-Verwey-Overbeek (DVLO) theory is widely used to model the particle aggregation as well as particle-collector interactions when considering particle transport in porous media. DLVO theory calculates the forces between two charged surfaces over a varying separation distances. The total interaction energy is determined by the sum of the attractive van der Waal force (Φ_{vdW}) and the repulsive electric double layer force Φ_{EDL}:

$$\Phi_{Total} = \Phi_{vdW} + \Phi_{EDL} \qquad (1.11)$$

Van der Waals force (vdW) can be expressed as: (a) for particle-particle interactions (i.e., modeled as two spheres) and as: (b) for particle-planar surface (used for nanoparticle-sand grain interactions).

$$\text{(a)}\ \Phi_{vdW,sphere-sphere} = \frac{-AR_1R_2}{6s(R_1+R_2)} \qquad (1.12)$$

(b) $\Phi_{vdW,sphere-plane} = \frac{-AR}{6s}$ (1.13)

Where: A is the Hamaker constant [N·m], R, R_1, R_2 are the radius of the particles [m], and s is the separation distance between the surfaces [m]. The attractive force increases with increasing particle size but decrease as the separation distance increases.

To assess stability of nanoparticle suspensions, the overall *vdW* forces between two spherical particles can be expressed as (Phenrat, et al., 2007):

$$\Phi_{vdW,sphere-sphere} = \frac{-A}{6}\left[\frac{2R^2}{s(4R+s)} + \frac{2R^2}{(2R+s)^2} + \ln s \frac{4R+s}{(2R+s)^2}\right] \quad (1.14)$$

The vdW forces between a spherical particle on the nanoscale and a flat plane can be expressed as shown in (Dunphy Guzman, et al., 2006):

$$\Phi_{vdW,sphere-plane} = \frac{-A}{6}\left[\frac{R}{s} + \frac{R}{(s+2R)} + \ln\frac{s}{(s+2R)}\right] \quad (1.15)$$

Electrostatic repulsion between the two surfaces can be described as:

(a) $\Phi_{RES,sphere-sphere} = 2\pi\varepsilon_r\varepsilon_0 R\zeta_1^{\,2}\ln[1+e^{-\kappa s}]$ (1.16)

(b) $\Phi_{RES,sphere-plane} = \pi\varepsilon_r\varepsilon_0 R[2\zeta_1\zeta_2\ln[\frac{1+e^{-\kappa s}}{1-s}] + (\zeta_1^{\,2}+\zeta_2^{\,2})\ln(1-e^{-\kappa s})]$ (1.17)

Where: ε_r is the relative dielectric constant of the liquid, ε_0 is the permeability in a vacuum ($8.99\text{x}10^{-12}$ $C^2J^{-1}m^{-1}$), ζ_1 is the zeta potential of the particle surface, ζ_2 is

the zeta potential of the collector grain, κ is the inverse Debye length, *R* is the particle radius, and *s* is the separation distance.

Electrostatic repulsion (i.e., electric double layer forces, EDL) as a function of separation distance between two spherical particles can be determined by the following equation (Dunphy Guzman, et al., 2006):

$$\Phi_{EDL,sphere-sphere} = \frac{-q_1 q_2 e^{-\kappa^{-1}} s}{4\pi\varepsilon_0\varepsilon_r D(1+2\kappa^{-1}r_p)} \qquad (1.18)$$

Where: q_1, q_2 are the charge of the particles, and *D* is the distance between the center of the two particles.

Electrostatic repulsion (i.e., electric double layer forces, EDL) as a function of separation distance between a spherical particle and a plane (large collector grain is assumed to be best represented as a plane at small separation distances) can be determined by the following equation (Dunphy Guzman, et al., 2006):

$$\Phi_{EDL,sphere-plane} = \pi\varepsilon_0\varepsilon_r\kappa^{-1}(\psi_s{}^2+\psi_p{}^2)\int_0^{r_p}(-\coth[\kappa^{-1}(s+r_p-r_p\sqrt{1-(\frac{r}{r_p})^2})]+\ldots$$

$$\coth[\kappa^{-1}(s+r_p-r_p\sqrt{1-(\frac{r}{r_p})^2})]+\frac{2\psi_s\psi_p}{\psi_s{}^2+\psi_p{}^2}\{\operatorname{csch}[\kappa^{-1}(s+r_p-r_p\sqrt{1-(\frac{r}{r_p})^2})]-\operatorname{csch}[\kappa^{-1}(s+r_p-r_p\sqrt{1-(\frac{r}{r_p})^2}]\}rdr$$

(1.19)

Where: ψ_s , ψ_p is the surface potential of the sphere and plane, respectively.

The characteristic thickness of the diffuse electrostatic double layer, κ, is defined by Equation 1.20. The double layer becomes compressed with increasing ionic strength.

$$\kappa = \sqrt{\frac{\varepsilon_0 \varepsilon_r kT}{2N_A e^2 I}} \qquad (1.20)$$

Where: e is the charge of an electron, N_A is Avogadro's number, and I is the ionic strength for a monovalent salt. The Debye length κ^{-1} is parameter that changes with environmental conditions such as background salt concentration and potentially changing pH (due to changes in ionic strength).

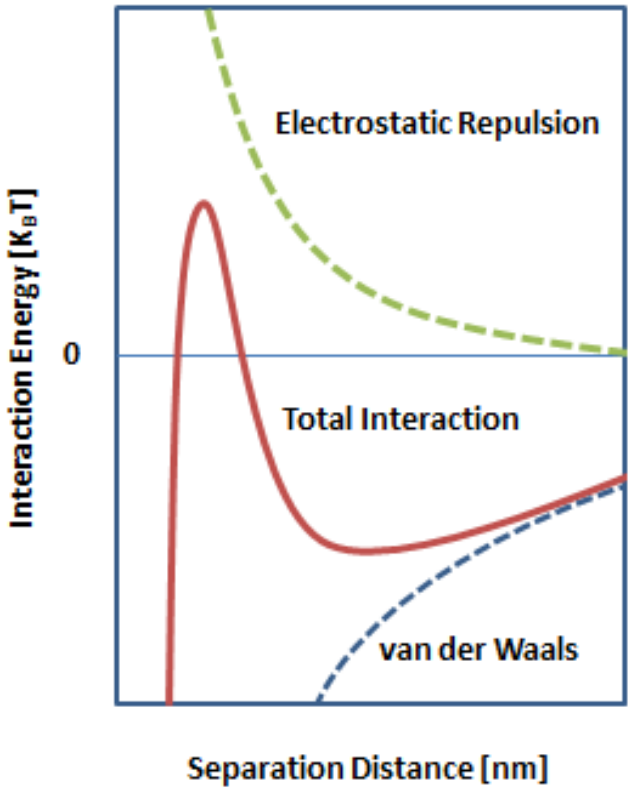

Figure 1.8: Example of a typical energy barrier plot over separation distance to help assess colloidal interaction energies using DLVO theory.

Total interaction curves typically have a primary and secondary minimum with an energy barrier separating the two minimums. The primary minimum is the most stable configuration and the secondary minimum corresponds to a separation distance at which the system is kinetically stable. If the energy barrier is overcome, then the charged particles will be able to reside in the primary, absolute minimum, at very close separation distances. The total interaction energy between two particles (to assess colloidal suspension stability) or between a particle and a charged surfaced (to assess colloidal deposition) can be calculated over separation distances (d). An example is shown in Figure 1.8.

1.7.1 Solution Chemistry Effects on Particle Suspension Stability

As salt concentration increases, the Debye length κ^{-1} decreases, allowing charged particles reach shorter separation distances due to the decreased energy barrier. As the separation distance decreases the attractive forces will dominate the system decreasing the overall stability of the particle suspension or increasing particle deposition. DLVO interaction energy curves change with: 1) particle radius (r); 2) ionic strength of the aqueous medium (I); 3) electrolyte type (i.e., monovalent or divalent electrolytes); and 4) surface potentials of the particle(s) and the collector $\frac{\psi_s}{\psi_p}$.

The influence of ionic strength on interaction energies is illustrated in Figure 1.9. As the ionic strength of the background solution increases the energy barrier to reach the primary minimum decreases allowing for increased particle aggregation.

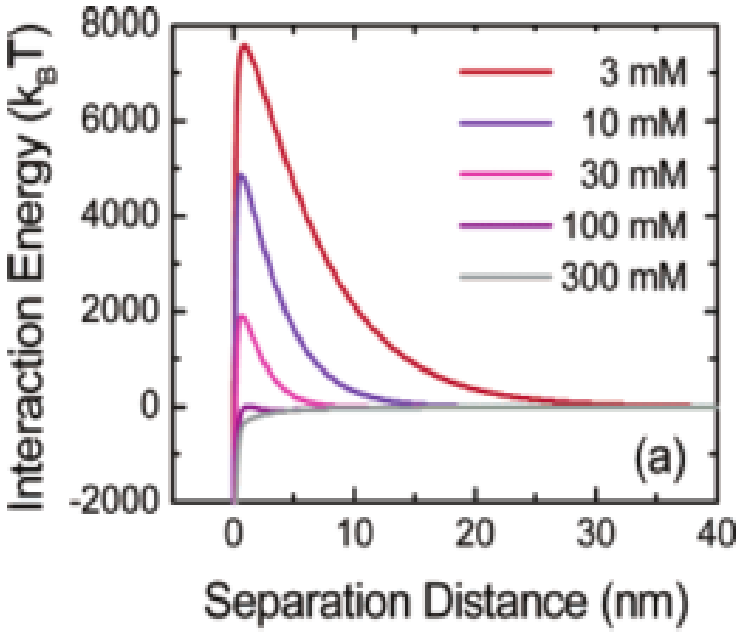

Figure 1.9: Example of the influence of salt concentration on DLVO total interaction curves. (Source: Tufenkji & Elimelech, 2005)

Both uncoated and coated particles will be affected by solution chemistry (e.g., ionic strength, salt type, solution pH) which alters the stability of a particle suspension. Zeta potential values can be loosely used to indicate suspension stability and zeta potentials between -20 and 20 mV are typically thought of as representing unstable suspensions. For example, the zeta potential of uncoated and coated with various stabilizing agents (i.e., citrate, polyvinylpyrrolidone (PVP), sodium borohydride ($NaBH_4$) and branched polyethyleneimine (BPEI)) silver nanoparticles was measured under two ionic strength and over pH values of 2 to 10 (El Badawy, et al., 2010). El Badawy, et al. (2010) found experimentally that increasing pH had the strongest effect on zeta potential for the BPEI coated particles, where zeta potentials decreases towards zero from around 60 mV with increasing pH. This is expected because BPEI will undergo surface charge changes with changing solution pH due to the functional groups present in BPEI. A similar trend was seen with the uncoated silver nanoparticles, although to a lesser extent; and little or no effect of pH was found to the other coated particles.

1.8 MECHANISMS OF PARTICLE TRANSPORT

DLVO interactions between a particle and a collector grain can be applied to understand processes governing particle transport and retention. Particle transport in porous media is governed by three mechanisms: (1) interception; (2) sedimentation due to gravity, and (3) diffusion via Brownian motion **(Yao, et al., 1971)** as depicted in Figure 1.10.

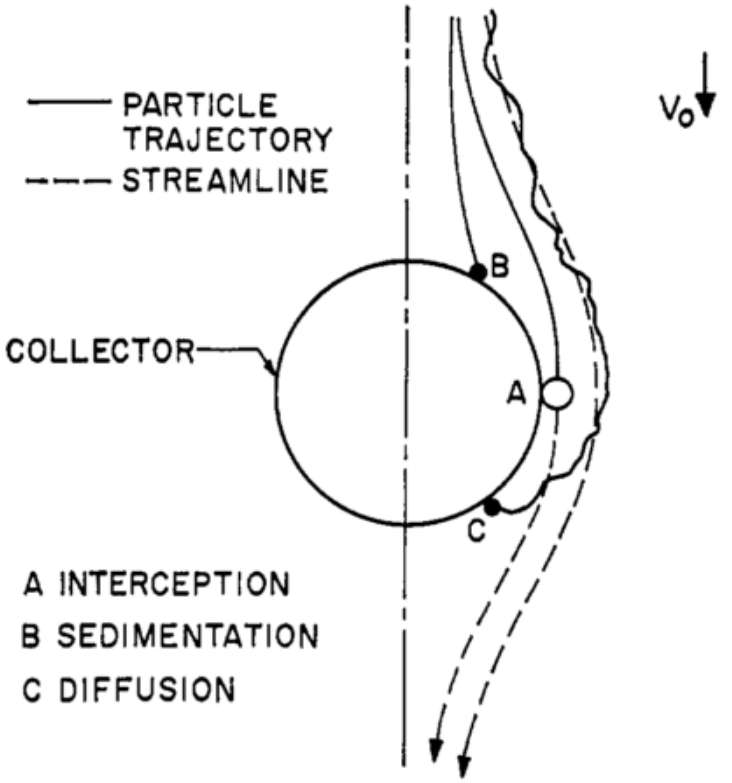

Figure 1.10: Mechanisms of particle transport in porous media. (Source: Yao, et al., 1971)

1.8.1 Mechanisms of Particle Transport: Interception, Sedimentation and Diffusion

Particle interception in porous media is governed be the relative sizes of the suspended particle and the size of the porous media (i.e., interception parameter):

$$(\frac{d_p}{d_m})^2 \qquad (1.21)$$

Where: d_p is the diameter of the particle [L]; and d_m is the diameter of the collector media [L].

Differences in density between suspended particles and the flowing fluid will allow for gravitational sedimentation of particle on to solid media (i.e., collectors). The controlling parameter for gravitational sedimentation is the Stokes settling velocity for a spherical particle as defined as:

$$v_s = \frac{g}{18\mu}(\rho_p - \rho_f)d_p^{\,2} \qquad (1.22)$$

Where: v_s is the Stokes settling velocity, g is the gravitational acceleration, μ is the fluid viscosity, ρ_p is the density of the particle, and ρ_f is the density of the fluid.

Brownian motion is characterized by the particle diffusivity, defined as, D_p, by Einstein:

$$D_p = \frac{kT}{3\pi\mu d_p} \qquad (1.23)$$

Where: k is the Boltzmann constant ($1.38064852 \times 10^{-23}$ $m^{2} \cdot kg \cdot s^{-2} \cdot K^{-1}$), and T is absolute temperature [K].

1.8.2 Mechanisms of Particle Attachment

Although particles may collide with a sand grain collector due to sedimentation, interception, or Brownian motion, they may or may not attach to the surface due to electrostatic, chemical and hydrodynamic forces occurring between the particle and the grain surface (Yao, et al., 1971). Electrostatic interactions tend to dominate particle attachment and can be characterized by the surface potentials of the particle (ψ_p) and the collector surface (ψ_m). It should be noted that experimentally, the zeta potential (ζ) of the surface of interest instead of the surface potential itself is often measured and subsequently used in many interaction equations as a surrogate for surface charge.

1.9 Particle Transport Equations

The 1-d ADR equations can be modified to include straining, deposition (attachment) and remobilization (detachment) of particles on the sand grain surface to model particle transport in porous media (Tufenkji & Elimelech, 2004). If the contribution of a process to particle transport and retention is negligible it can be eliminated from the transport and deposition equations.

1.9.1 Deposition Equations

Mathematically, particle deposition needs to be accounted for in both the aqueous- and solid-phase transport equations. Total deposition is the summation of diffusion, interception, and gravitational effects and is a function of the aqueous particle concentration and can also be a function of the maximum retention capacity of the porous media. For small particles (i.e., nanoscale particles) the diffusion component will account for the majority of particle deposition. As particle concentrations in the aqueous phase increase, particle retention on the solid grains will increase. The rate at which particles are deposited is typically assumed to be first order with respect to aqueous phase concentration. The first order deposition rate coefficient, k_d, can be calculated using the following equation:

$$k_d = \frac{3(1-n)v_x}{2d_c}\alpha'\eta_0 \qquad (1.24)$$

Where: d_c is the diameter of the sand grain collector [L]; α' is the collision efficient factor (i.e., the fraction of particles that remain attached to the sand grain after a collision) [-]; η_0 is the frequency of collisions between particles and sand grains.

Diffusion, interception, and sedimentation processes are all included in calculation of the collision frequency (η_0). The frequency of particle-collector collisions can be calculated by the following equation:

$$\eta_0 = \eta_D + \eta_I + \eta_G \qquad (1.25)$$

$$\eta_0 = 2.4A_s^{1/3}N_I^{-0.081}N_{Pe}^{-0.715}N_{vdw}^{0.052} + 0.55A_sN_R^{1.675}N_A^{0.125} + 0.22N_I^{-0.24}N_G^{1.11}N_{vdw}^{0.053} \quad (1.26)$$

Where: A_s is the Happel correction factor; N_I is the interception number; N_{Pe} is the Peclet number; N_{vdw} is the London-van der Waals attractive force number; N_G is the gravitational number; N_A is the attractive number; N_R is the aspect ratio.

$$A_s = \frac{2(1-\gamma^5)}{2-3\gamma+3\gamma^5-2\gamma^6} \quad (1.27)$$

Where: $\gamma = (1-n)^{1/3}$

$$N_I = \frac{3}{2}\cdot\left(\frac{d_p}{d_c}\right)^2 \quad (1.28)$$

$$N_G = \frac{2}{9}\cdot\frac{r_p^{\,2}(\rho_p-\rho_f)g}{\mu\cdot v_x n} \quad (1.29)$$

$$N_R = \frac{d_p}{d_c} \quad (1.30)$$

$$N_{Pe} = \frac{v_x\cdot n\cdot d_c}{D} \quad (1.31)$$

Where: D is the diffusion coefficient [$L^2\cdot T^{-1}$] as computed by Stokes-Einstein Equation 1.23) and μ is the viscosity of the fluid.

$$N_{vdw} = \frac{A}{kT} \quad (1.32)$$

Where: k is the Boltzmann constant, T is fluid temperature

$$N_A = \frac{A}{12 \cdot \mu \cdot v_x n \cdot r_p^{\,2}} \qquad (1.33)$$

The theoretical collision frequency can be calculated when values of the particle, collector and hydrodynamics of the system are known.

1.9.2 Colloidal Remobilization

In general, attached particles are assumed only to detach from a collector surface due to variations in solution chemistry. Typically, an energy barrier model is used to describe the kinetics of colloid detachment where the height of the detachment energy barrier (Arrhenius relationship) dictates release rates. Particle remobilization consists of two steps, first the colloid must detach from the grain surface and then it must diffuse away from the grain surface before getting remobilized in the bulk fluid. Thus, mechanistically remobilization can be divided into two limiting cases: (1) detachment limited; or (2) diffusion limited remobilization. Colloidal remobilization via detachment limited is applicable for systems when the rate of detachment is much slower than diffusion; and remobilization in a diffusion limited system is when diffusion rates are much slower than detachment. In a diffusion limited system (e.g., hematite-quartz system at pH 11 explored experimentally by Ryan and Gschwend (1994)) the hydrodynamics of flow in the system will dictate remobilization kinetics. Ryan and Gschwend (1994) found that remobilization rates as a function of flow rate

(for the system described above) closely followed the theoretical derivation for the diffusion rate (i.e., $k_r = \frac{kT}{6\pi\mu_f a_c}^{1/3} \cdot a_g^{3/4} \cdot U^{2/3}$ where μ_f is the fluid viscosity, a_c is the radius of the colloid, a_g is the radius of the collector grain, U is the pore water velocity).

1.9.3 Influence of Water Chemistry

Solution chemistry changes can alter the attachment and detachment behavior of colloids since changes in pH and ionic strength modify the electrostatic interactions between colloids and the collector surface (i.e., interaction energies as described by 1.7 DLVO Theory).

1.9.3.1 Particle Attachment

The influence of ionic strength on particle transport can be rather significant with many experimental and modeling studies focused on quantifying the effects of changing ionic strength. As given by DLVO theory, an increase in ionic strength decreases the thickness of the double layer, resulting (in general) in increased particle retention. Particle deposition is greatly affected by background salt concentration and at high salt concentrations, deposition is considered to be a fast reaction and reaches a constant maximum rate; at lower salt concentrations the deposition rate becomes a function of salt concentration and type (Grolimund, et al., 2001). Particle deposition can also dependent on salt type (i.e., monovalent versus divalent ions) with deposition occurring at a much lower background ion

concentration with divalent ions present versus monovalent (Grolimund, et al., 1998). Saleh, et al. (2008) and Bradford, et al. (2012) employed an empirical relationship between the ionic strength of the system and the sticking coefficient or deposition efficiency, α (α is fraction of particle-solid collisions that result in particle deposition). Ionic strength changes can also affect the surface charge on both the particle of interest as well as the porous media surface. Saleh, et al. (2008) found that the zeta potential of nZVI became less negative (note this trend is system specific) as the ionic strength increased via additions of sodium and calcium ions, respectively.

1.9.3.2 Particle Detachment

Additionally, increasing pH has been found to release attached colloids from natural sediments until the increasing ionic strength (due to increasing pH) starting to increase particle attachment to the point where it become the dominant mechanism (Bunn, et al., 2002).

Ryan and Gschwend (1994) found that the surface potential of the charged colloids was not well represented by the zeta potential especially under high ionic strength and high surface charge and instead used a surface complexation/double layer method to calculate the surface potentials. Also, the surface potential of mineral oxides as a function of pH can be estimated by using the Nernst Equation:

$$\Psi_{0,i} = \frac{2.303kT}{e}(pH_{zpc,i} - pH) \qquad (1.34)$$

Where: $pH_{zpc,i}$ is the pH at the point of zero charge for the mineral oxide of interest.

1.9.4 STRAINING EQUATIONS

Physically straining of particles on porous media can become an important process affecting particle transport and retention. For particles sizes approaching the magnitude of the pore throats of the porous media, the effect of straining becomes increasingly important for modeling transport behavior. If particles, colloids, or droplets are injected into a porous media with a similar characteristic size, a reduction in porosity and aquifer permeability can occur to partial or full clogging of the particles in the porous media. If clogging occurs, the average pore size (or throat size) is reduced, thus decreasing the overall aquifer permeability and creates increased pressure gradients.

$$\psi_{str}(x) = \left(\frac{d_{50} + x}{d_{50}}\right)^{-\beta} \qquad (1.35)$$

Where: β is a fitting parameter as defined in Bradford et al. (2003) to fit the shape of the retention profile, where straining effects are greatest near the column inlet.

$$\psi_{att} = \frac{S_{\max} - S}{S_{\max}} \qquad (1.36)$$

Where: S_{max} is the maximum solid phase concentration [$M \cdot M^{-1}$].

These effects of clogging can have a great influence on the transport and retention behavior of the particles or droplet. Clogging is typically experienced in

the waste water sector with deep bed filtration methods used to improve water quality by removing solids from the liquid stream (e.g., slow and fast sand filtration) with these filters require backwashing processes to remove the buildup for solids to allow for continued fluid flow over time.

1.10 PARTICLE TRANSPORT MODELS

Transport and deposition of colloidal particles in porous media has been widely studied with various models used to describe particle behavior. Particle transport models based from the adjective-dispersion reaction equations with additional processes (i.e., particle attachment, remobilization, straining) to help describe specific aspects of transport behavior, routinely used to describe nanoparticle transport. Particle transport can exhibit a wide range of deposition behavior from hyper-exponential retention profiles, attributed to aggregation of particles depositing near the column inlet, to linearly decreasing, to nonmonotonic or monotonically increasing retention profiles (Goldberg & Scheringer, 2014).

Table 1.6: Particle Transport Models.

Model	Processes Modeled	Governing Mass Balance Equation	Fitted Parameters	References
Colloid filtration theory (CFT)	Deposition	$\frac{\partial C}{\partial t} = -v_x \frac{\partial C}{\partial x} - \frac{\rho_b}{nS_w}\frac{\partial S^*}{\partial t}$ (1.37) $\frac{\rho_b}{nS_w}\frac{\partial S}{\partial t} = k_d C$ (1.38) $k_d = \frac{3(1-nS_w)}{2d_c}\alpha v_x \eta_0$ (1.39)	α	Yao, et al., 1971; Tufenkji & Elimelech, 2004
Dual deposition mode CFT	Fast Deposition Slow Deposition	$\frac{\partial C}{\partial t} = -v_x \frac{\partial C}{\partial x} - \frac{\rho_b}{nS_w}\frac{\partial S^*}{\partial t}$ $\frac{\rho_b}{nS_w}\frac{\partial S}{\partial t} = f \cdot k_{d,f} C + (1-f)\cdot k_{d,s} C$ (1.40)	f $k_{d,f}$ $k_{d,s}$	Tufenkji & Elimelech, 2004; Tufenkji & Elimelech, 2005; Foppen, et al., 2007
Single-site deposition remobilization	Deposition Remobilization	$\frac{\partial C}{\partial t} = -v_x \frac{\partial C}{\partial x} - \frac{\rho_b}{nS_w}\frac{\partial S^*}{\partial t}$ $\frac{\rho_b}{nS_w}\frac{\partial S}{\partial t} = k_d C - \frac{\rho_b}{nS_w} k_r S$ (1.41)	k_d k_r	Kretzschmar, et al., 1999
Dual-site deposition remobilization	Deposition Remobilization	$\frac{\partial C}{\partial t} = D_h \frac{\partial^2 C}{\partial x^2} - v_x \frac{\partial C}{\partial t} - \frac{\rho_b}{nS_w}\frac{\partial S_1}{\partial t} - \frac{\rho_b}{nS_w}\frac{\partial S_2}{\partial t}$ (1.42) $\frac{\rho_b}{nS_w}\frac{\partial S_1}{\partial t} = k_{d,1} C - \frac{\rho_b}{nS_w} k_{r,1} S_1$ (1.43) $\frac{\rho_b}{nS_w}\frac{\partial S_2}{\partial t} = k_{d,2} C - \frac{\rho_b}{nS_w} k_{r,2} S_2$	k_d $k_{d,2}$ k_r $k_{r,2}$	Schijven, et al., 2002

Single-site deposition remobilization and blocking	Deposition Remobilization Langmuirian blocking	$\frac{\partial C}{\partial t} = D_h \frac{\partial^2 C}{\partial x^2} - v_x \frac{\partial C}{\partial t} - \frac{\rho_b}{nS_w} \frac{\partial S}{\partial t}$ $\frac{\rho_b}{nS_w} \frac{\partial S}{\partial t} = k_d \psi_b C - \frac{\rho_b}{nS_w} k_r S$ (1.44) $\psi_b = 1 - \frac{S}{S_{\max}}$ (1.45)	k_d k_r S_{max}	Johnson & Elimelech, 1995; Kasel, et al., 2013
Single-site deposition remobilization and depth-dependent retention (straining)	Deposition Remobilization Straining	$\frac{\partial C}{\partial t} = D_h \frac{\partial^2 C}{\partial x^2} - v_x \frac{\partial C}{\partial t} - \frac{\rho_b}{nS_w} \frac{\partial S}{\partial t}$ $\frac{\rho_b}{nS_w} \frac{\partial S}{\partial t} = k_d \psi_s C - \frac{\rho_b}{nS_w} k_r S$ $\psi_s(x) = (\frac{d_{50} + x}{d_{50}})^{-\beta}$	k_d k_r β	Johnson & Elimelech, 1995; Bradford, et al., 2003; Bradford, et al., 2004; Gargiulo, et al., 2007
Single-site deposition remobilization, blocking, and depth-dependent retention (straining)	Deposition Remobilization Langmuirian blocking Straining	$\frac{\partial C}{\partial t} = D_h \frac{\partial^2 C}{\partial x^2} - v_x \frac{\partial C}{\partial t} - \frac{\rho_b}{nS_w} \frac{\partial S}{\partial t}$ $\frac{\rho_b}{nS_w} \frac{\partial S}{\partial t} = k_d \psi_b \psi_s C - \frac{\rho_b}{nS_w} k_r S$ (1.46) $\psi_b = 1 - \frac{S}{S_{\max}}$ $\psi_s(x) = (\frac{d_{50} + x}{d_{50}})^{-\beta}$	k_d k_r S_{max} β	Bradford, et al., 2003; Gargiulo, et al., 2007; Kasel, et al., 2013

Reproduced after that appearing in Goldberg & Scheringer (2014)

[*] n is replaced with $n \cdot S_w$

Where: C is the aqueous particle concentration [$kg \cdot m^{-3}$]; S is the solid phase concentration [$kg_{part} \cdot kg_{soil}^{-1}$]; v_x is the pore water velocity [$m \cdot s^{-1}$]; t is time [s]; x is the distance from column inlet [m]; ρ_b is the bulk density [$kg \cdot m^{-3}$]; D_h is the longitudinal dispersion coefficient [$m^2 \cdot s^{-1}$]; n is the porosity [-]; α is the attachment efficiency [-];α_f, α_s is the fast, slow attachment efficiency [-]; f_f, f_s is the particle population fraction associated with α_f, α_s [-];η_0 is the single-collector contact efficiency [-];k_d, $k_{d,2}$ is the primary/secondary site deposition rate constant [s^{-1}]; k_r, $k_{r,2}$ is the primary/secondary site remobilization rate constant [s^{-1}]; ψ_b is the Langmuirian blocking function [-]; ψ_s is the depth dependent retention function [-]; $k_{d,f}$, $k_{d,s}$ is the rate constant of deposition associated with α_f, α_s, respectively [s^{-1}]; β is the empirical depth-dependent retention parameter [-]

1.11 Encapsulation of Active Ingredients

Solids, liquids and gases have been encapsulated to control release or shield the core from the external environmental conditions. Encapsulation is widely used for pharmaceutical delivery with chitosan-alginate microcapsulation commonly used for encapsulation of a variety of biologically active structures (e.g., proteins, enzymes, cells, etc.) partly because of it is biodegradable and non-toxic (Silva, et al., 2006; Luo, et al., 2014). Chitosan-alginate has been used to encapsulate nZVI aimed at remediation of Pb (II). Microbead encapsulation of bacterial in gellan gum (16-53 μm diameter) has been investigated for use in subsurface bioremediation of gasoline contamination (Moslemy, et al., 2002). Encapsulation of the bacteria provided a physical barrier between the bacteria and toxic hydrocarbons present, resulting in more effective degradation rates by decreasing the bacteria adaptation timeframe to the subsurface conditions. Laboratory column experiments investigated the subsurface transport and retention of the gel-encapsulation microbeads (10-40 μm diameter) finding that effective transport and retention could be completed in sandy porous media to create sufficient a bioaugmentation zone (Moslemy, et al., 2003). TCE oxidation via potassium permanganate ($KMnO_4$) was completed by slow release from microcapsules (60-2000 μm diameters) with either a single or multiple $KMnO_4$ grains cores encapsulated with various polymers (Ross, et al., 2005).

Solid acidic phosphate (K_2HPO_4 phosphate buffer) was encapsulated with a pH-sensitive polymer (Eudragit^{TM} S-100 methacrylic acid polymer) that

degrades when the pH is greater than 7 to decrease pH during denitrification (Vanukuru, et al., 1998; Rust, et al., 2000; Rust, et al., 2002). A stochastic model using a Monte Carlo analysis was employed to account for a distribution of mass loading in the macrocapusle core as well as the mass of the polymer wall to describe the release kinetics. Aelion et al. (2009) encapsulated the same phosphate buffer but here in a pH- sensitive polymer (Eudragit® E-PO) that degrades under acidic conditions, allowing for control of acidic groundwaters. Liu et al. (2008) used similar macrocapsules (here, 1.3 cm diameter, 80% Eudragit™ S-100 methacrylic acid polymer) containing an acidic phosphate buffer ($Ca(H_2PO_4)_2$) for pH control. The release kinetics from said macrocapsules in a batch system was successfully modeled using a first order rate expression (that varies with pH) with respect to the mass of polymer and equilibrium chemistry that included the possible complexation and precipitants with calcium and phosphate (Liu, et al., 2008). However, due to the large size of the microcapsules, the microcapsules could only be employed in the subsurface in the form of a line or point source addition.

Table 1.7: Summary table: particle surface modifications for environmental remediation applications.

Surface Modification	Core	Application	Reference
Poly(methacrylic acid)-poly(methyl methacrylate)-poly(styrenesulfonate) (PMAA-PMMA-PSS)	nZVI	Increase colloidal suspension stability for enhanced subsurface delivery. Polymer coating designed to transport to oil-water interface.	Saleh et al., 2005
Olefin-maleic acid copolymer	nZVI	Increase colloidal suspension stability for enhanced subsurface delivery to target entrapped NAPL.	Phenrat et al., 2011
Poly(styrene sulfonate) (PSS), Carboxymethyl cellulose (CMC), Polyaspartate (PAP)	nZVI	Use anionic polyelectrolytes to decrease aggregation and sedimentation of nZVI	Phenrat et al., 2008
Gellan gum	Bacteria	Encapsulation of bacteria to physically shield consortium from toxic contaminants	Moslemy et al., 2002
Waxy polymer blends (e.g., Boler wax, Piccolyte resin S115, Epolene C-16)	$KMnO_4$	Slow release of KMnO4 for TCE oxidation	Ross et al., 2005
Eudragit™ S-100 methacrylic acid polymer	KH_2PO_4	pH control during denitrification via the pH-sensitive polymer encapsulation	Vanukuru et al., 1998, Rust et al., 2000, Rust et al., 2002
Eudragit® E-PO	K_2HPO_4	pH control of acidic groundwater using a pH-sensitive polymer macrocapsule	Aelion et al., 2009
Eudragit™ S-100 methacrylic acid polymer	$Ca(H_2PO4)_2$	pH control using a pH-sensitive polymer macrocapsule	Liu et al., 2008
Alginate microcapsules (with Span 85) water-in-soybean oil microemulsion	nZVI	Removal of Pb(II) contamination	Luo et al., 2014
Corn oil, Span 85 (nonionic surfactant) oil-in-water emulsion	ZVI	Enhanced subsurface delivery of ZVI particles using an oil-in-water biodegradable emulsion	Quinn et al., 2005
Soybean oil-nonionic surfactants (Span 80/oleic acid)- water emulsions	Coated RNIP	Enhanced subsurface delivery of surface modified ZVI particles using an oil-in-water biodegradable emulsion	Berge and Ramsburg, 2009

1.12 OIL-IN-WATER EMULSIONS

Emulsions are widely utilized in the food, medical and pharmaceutical industries to encapsulate, deliver, and release active ingredients. Emulsions are created by stabilizing a mixture of two or more immiscible fluids (e.g., water and oil) with a stabilizing agent such as a surfactant that typically form spherical droplets of one phase in the other. Many types of emulsion systems can be created such as conventional emulsions (i.e., oil-in-water (o/w); water-in-oil (w/o) emulsion); multiple emulsions (i.e., water-in-oil-in-water (w/o/w) emulsion); solid liquid particles; and hydrogels) (McClements, et al., 2007).

The emulsion droplets characteristics determine the bulk emulsion properties and thus the transport behavior of the emulsion as well as the release behavior of the encapsulated ingredients. Important droplet properties of the emulsion include: droplet concentration, droplet size distribution, droplet charge (e.g., surface charge, zeta potential), and properties of the droplet interface (e.g., interfacial tension, surface active species), all of which can affect the release rate and extent of active ingredients from the emulsion. Bulk emulsion properties including viscosity and emulsion stability play a role in emulsion transport.

Emulsions have been used in environmental remediation as means of: (a) mobility control due to the viscous nature of many emulsions (e.g., Costa & Lobo, 2001; Zhong, et al., 2011); b) enhanced contaminant recovery (e.g., Kwon, et al., 2005, Lee, et al., 2007) and as a contaminant stabilization technique (e.g., Fox &

Medina, 2005); c) as an amendment itself to promote remedial events such as contaminant biodegradation (e.g., Borden, 2007); and d) as a delivery vehicle to provide active ingredients to the subsurface (e.g., Berge & Ramsburg, 2009; Shen, et al., 2011; Ramsburg, et al., 2003).

1.13 EMULSIONS FOR MOBILITY CONTROL

To combat issues of incomplete spatial amendment delivery, viscous fluids, first widely applied in the enhanced oil recovery sector, have been used to aid in successful subsurface delivery in heterogeneous porous media. Mobility control techniques involve forcing viscous solutions to flow through both low and high permeability regions by increasing pore pressures such that cross-flow occurs (Jackson, et al., 2003). Polymers and surfactants can be added to aqueous solutions to increase the viscosity to aid in NAPL mobilization. Many viscous fluids can be directly injected to help provide a more thorough "sweep" of remedial amendments to the subsurface such as: emulsified oils, emulsions, liquid suspensions, polymer solutions, and molasses. Oil-in-water emulsions provide mobility control via a different mechanism than viscosity difference between phases, by capillary driven mobility control- the trapping of oil droplets in the pore throats of the porous media that creates flow bypass due to altering local pressure gradients (Cobos, et al., 2009; Guillen, et al., 2012) . The capillary number (i.e., the ratio of viscous forces to surface tension) can be used to determine the ability of an emulsion for mobility control. Capillary number is calculated as:

$$Ca = \frac{\mu_c v_x}{\sigma_c} \quad (1.48)$$

Where: μ_c is the viscosity of the continuous phase, v_x is the pore water velocity; and σ_c is the surface tension of the continuous phase. Guillen, et al. (2012) found that at low capillary numbers emulsions provided mobility control.

Unlike for oil recovery where the intent is to mobilize DNAPL from the subsurface, viscous fluids can also be used to help ensure contact between the additives injected and the contaminants in heterogeneous media. For example, mobility control using solutions of xanthan polymers can be used to provide amendments for enhanced bioremediation to lower permeability regions to help limit contaminant rebounding via diffusion (Jackson, et al., 2003) or for delivery of the chemical oxidant sodium permanganate ($NaMnO_4$) for TCE removal in a heterogeneous media (Kananizadeha, et al., 2015). Uniform delivery of remedial amendments has been accomplished using emulsions, foams, and shear thinning fluids in highly heterogeneous media in both saturated and unsaturated zones while limiting contaminant mobilization (Zhong, et al., 2008) (Zhong, et al., 2011). Foams (as oil-in-water emulsions) can also be utilized for mobility control by clogging up the low permeability zones to re-direct flow through higher permeability regions (Li, et al., 2010).

1.14 EMULSIONS FOR ENHANCED CONTAMINANT SOLUBILIZATION AND STABILIZATION

Surfactant enhanced solubilization is a widely known remediation technique for NAPL; however, has some limitations (e.g., high cost and loss of surfactant to uncontaminated subsurface regions) (Sabatini, et al., 1996). The injected surfactant is able to decrease the interfacial tension between the hydrophobic contaminant and the aqueous phase making it more water soluble and in some cases creating microemulsions (i.e., a thermodynamically stable emulsion) to aid in contaminant removal. Above the critical micelle concentration (CMC), colloidal sized micelles will be formed with a hydrophobic (i.e., oil) interior surrounded by surfactant molecules allowing organic contaminants to partition into the micellar core and making the micelles themselves water soluble (Shiau, et al., 1994)- this system is deemed a Winsor Type I. When the proportions of the oil and water phases are similar (i.e., a Winsor Type III system) microemulsions can be formed allowing for increased removal efficiencies through ultralow interfacial tensions. If the ratio of oil to aqueous phase is high then reverse micelles will be formed creating a Winsor Type II condition (i.e., hydrophilic interior and oil exterior) increasing water solubilization in the hydrophobic phase (Winsor, 1948; 1954). In addition to phase ratios, micelle formation is also affected by other factors such as surfactant type and concentration, hydrophobic chain length, temperature, and salt concentration.

Contaminant solubilization can also be enhanced with the addition of an emulsified hydrophobic phase; for example up to 11,000 ppm of TCE or 18,000 ppm of PCE was found to be adsorbed into an emulsion and subsequently flushed out of a column with a 2% (v/v) oil-in-water emulsion (corn and olive oils) without generation of a contaminant NAPL phase while still removing more than 98% of the emplaced contaminant mass (Lee, et al., 2007). Kwon et al., (2005) also successfully removed DNAPL contaminants through enhanced solubilization with 0.5-2% (v/v) silicone oil emulsions. Contaminant-NAPL migration is a concern with surfactant and emulsion remediation technologies and mobilization should be investigation when adding additional NAPL to the subsurface (Pennell, et al., 1996).

One characteristic of hydrophobic edible oils (typical material of oil-in-water emulsions) to note is their ability to sequester aqueous phase contaminants (e.g., chlorinated solvents, and their degradation daughter products (i.e., PCE, TCE, cis-DCE, and VC)), into the oil-NAPL phase. An experimental study found that food-grade soybean oil had oil: water partitioning coefficients (K_p) to be from 22 to 1200 for PCE down to VC (Pfeiffer, et al., 2005). Contaminants with low aqueous solubility (e.g., chlorinated solvents) will undergo reversible partitioning back into the NAPL source zone phase present (Ramsburg, et al., 2010). Sequestration of such contaminants into NAPL can reduce mobile, aqueous contaminant levels in the groundwater significantly, thus affecting reducing the available contaminant mass for degradation. Partitioned contaminants into the

emplaced edible oil phase will be re-released from the oil phase as the oil degrades and must be taken into account in a remediation plan. For example, neat SBO was directly injected via injection wells at an industrial field site; down gradient monitoring indicated that initially the chlorinated solvents present partitioned into the SBO and slowly dissolved back out into the groundwater over time where the contaminates underwent reductive dechlorination (Borden & Lee, 2002).

1.15 Edible Oils as Amendments for Enhanced Bioremediation

Edible oils are widely used to promote anaerobic degradation that aid in degrading many types of subsurface contaminants such as: perchlorate, explosives, dissolved metals, nitrates, sulfates, and chlorinated solvents. Injection of edible oil can be done by injecting a neat NAPL phase or by creating a water-in-oil emulsion (e.g., vegetable oil, emulsified vegetable oil, emulsified edible oil, etc.) to provide substrate and create anaerobic conditions to aid in microbial degradation (Air Force Center for Engineering and the Environmental , 2007). Oil-in-water emulsions (e.g., of commercially available products: EOS® (Borden & Lee, 2004; Borden & Lee, 2009)) are used to provide long-term support for sustained subsurface anaerobic biodegradation for a variety of contaminants such as: nitrate (Hunter, 2001); chlorinated solvents (Long & Borden, 2006; Borden & Rodriguez, 2006; Lee, et al., 2007; Hiortdahl & Borden, 2014; Harkness & Fisher, 2013); explosives (e.g., TNT) (Fuller, et al., 2004); perchlorate (Hunter, 2002);

acid mine drainage (i.e., sulfate and heavy metals) (Lindow & Borden, 2005); Uranium (Watson, et al., 2013) and even herbicides (e.g., Atrazine) (Hunter & Shaner, 2009) by supplying sufficient long-term electron donor derived from a carbon source or immobilizing the contaminant. The edible oil(s) (e.g., soybean oil) contained in the oil-in-water emulsion provide a slow release of carbon to promote contaminant degradation. Electron donor can be added to the subsurface in a variety of forms such as acetate, lactate, glucose, and hydrogen to promote aerobic contaminant degradation. Acid mine drainage containing sulfate (SO_4^{2-}) and heavy metals were significantly reduced when emulsified soybean oil was injected into column experiments along with additional amendments including ammonium phosphate dibasic ($(NH_4)_2HPO_4$), microbial inoculum, molasses, and yeast extract (Lindow & Borden, 2005). The degradation of neat PCE-NAPL was able to enhanced by flushing of emulsified edible oil for electron donor, colloidal $Mg(OH)_2$ buffer for pH control, and inoculum to supply the microbial consortiums (Hiortdahl & Borden, 2014). Many studies have investigated the potential of using either neat edible oil or emulsified oil to provide electron donor to the subsurface, both with and without additional amendments injections, for enhanced bioremediation without attempted to delivery additional amendments held *within* the oil phase (Hunter, 2002; Coulibaly & Borden, 2004; Fuller, et al., 2004; Lindow & Borden, 2005; Coulibaly, et al., 2006; Borden, 2007).

1.16 EMULSIONS USED TO DELIVER REMEDIAL AMENDMENTS

Macro emulsions have been employed to deliver remedial amendments to the subsurface (Berge & Ramsburg, 2009; Ramsburg, et al., 2003). Amendment stability, delivery and transport can be enhanced through an emulsification process. Oil-in-water emulsions containing food grade biodegradable oil and a stabilizing agent have been created to improve delivery of amendments (e.g., ZVI) to subsurface (e.g., Berge & Ramsburg, 2009; Quinn, et al., 2005). Shen et al. (2011) have investigated delivering of amendments, in the form of nanoparticles, held within foam for remediation. The authors found that the transport of surrogate latex microspheres when held within surfactant foams was significantly enhanced compared to an injected suspension of microspheres through the vadose zone.

1.17 EMULSION STABILITY

Emulsions are only kinetically stable- thermodynamically the interfacial area between the two phases present in an emulsion want to be at a minimum (i.e., phase separation). The use of emulsifiers and stabilizing agents will decrease the interface tension between phases allowing for the emulsion to stable over longer periods of time by inhibiting droplet coalescence (e.g., by creating a physical barrier/film to coalescence at the interface), increasing the energy barrier to reach the primary energy minimum, or enhancing stability via steric stabilization. Emulsion stability is often assessed using DLVO theory to determine the total interaction energy between emulsion droplets. See equations in DLVO theory section. Ionic strength, temperature (because of the influence on interfacial

tension), pH (i.e., surface charge and interfacial tension dependence on pH) and surface active agents all play a role in emulsion stability (Kokal, et al., 1992). McAuliffe (1973) found that by adding NaOH (i.e., changing the pH) to the aqueous phase of a highly concentrated emulsion (70% oil), the droplet size distribution varied due to the neutralization of surface active acids. The author found that the droplet size decreased with increasing NaOH, thus increasing emulsion stability.

1.18 MODELING EMULSION TRANSPORT IN POROUS MEDIA

For dilute stable emulsions, researcher have found that transport through porous media is typically characterized by the following attributes: (1) monotonically permeability decrease over the course of emulsion injection; (2) droplets are retarded, eluding later than at one pore volume; (3) permeability reduction increases with increasing droplet size-pore size ratio; (4) increase in flow rate tends to increase reduction of permeability; (5) steady state conditions are reached over time; and (6) if the emulsion is followed by a water flush, emulsion droplets will elute for about one pore volume but the original permeability reduction will persist (McAuliffe, 1973; Devereux, 1974b; Alvarado & Marsden, 1979; Soo & Radke, 1984a).

Three models have been formulated to explain the transport behavior of oil-in-water emulsions in porous media: (a) continuum bulk viscosity model; (b) droplet retardation model; and (c) a modified filtration model.

1.18.1 Bulk Viscosity Model

For concentrated emulsions, a simple bulk viscosity model was developed by Alvarado & Marsden (1979) based on Darcy law's that can be modified for viscous fluids if needed (i.e., for non-Newtonian fluids). Darcy's law that can be utilized for Newtonian fluids is shown in Equation 1.49.

$$q = \frac{-\kappa}{\mu}\nabla P \qquad (1.49)$$

Where: q is the Darcy flux [L/T]; κ is the intrinsic permeability of the media [L^2]; μ is the fluid viscosity [Pa·T]; ∇P is the pressure gradient vector [Pa·L^{-1}].

This model treats the flowing emulsion as a single continuous phase instead of handling droplet transport and thus does not predict any loss of mass to the porous media in the form of droplet retention. This model does not consider any permeability loss- predicting emulsion breakthrough occurring at one pore volume after injection. The bulk viscosity model can be applied to both Newtonian and non-Newtonian fluids where it is assumed that emulsions follow Newtonian behavior at concentrations below 50% oil (Kokal, et al., 1992). Many models exist for flow of non-Newtonian fluids in porous media that use a relationship to describe how viscosity changes with shear stress (e.g., power law model, shear thinning models, etc.).

For dilute emulsions (i.e., Newtonian fluids) the value of viscosity has only minor effects on emulsion transport (3 μm droplet size) in porous media.

Kokal, et al. (1992) found that emulsion transport was similar for emulsions with comparable droplet sizes but having an order of magnitude difference in viscosity.

1.18.2 Droplet Retardation Model

Conceptually the droplet retardation model assumes that droplets larger than pore throats will undergo deformation in order to squeeze through a pore contraction. Any permeability losses due to droplet deformation will be reversed once water is flushed in the system (Kokal, et al., 1992). As a droplet encounters a pore constriction the velocity of the moving droplet decreases (as compared to the continuous phase due to capillary resistance) resulting in permeability loss. When a droplet is held in the porous media by straining, if enough permeability change occurs around the strained droplet it can be re-suspended squeezed through the blocked pore throat or the droplet can be broken up into smaller droplets that can pass through the pore throat. Breaking up of droplets during transport in porous media will change the distribution of droplet sizes from the influent to the effluent. This model can only account for retardation in emulsion transport and reversible permeability losses but cannot account for any droplet retention onto the porous media.

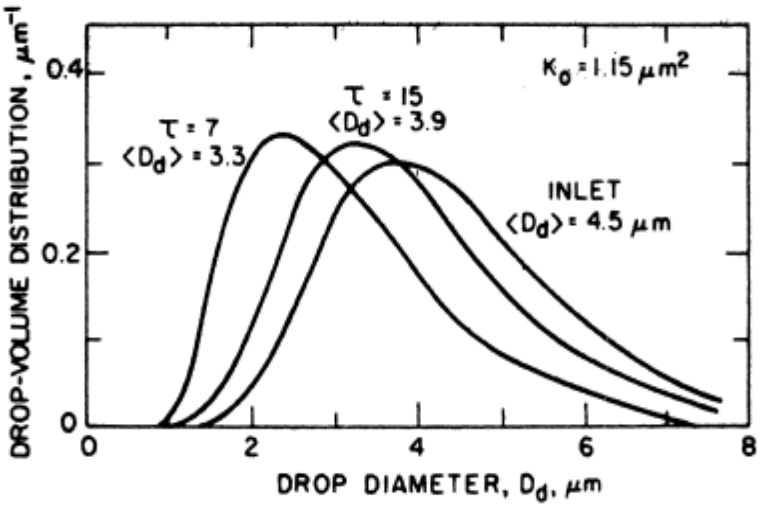

Figure 1.11: Influent and effluent droplet size distributions.
(Source: Soo & Radke, 1984a)

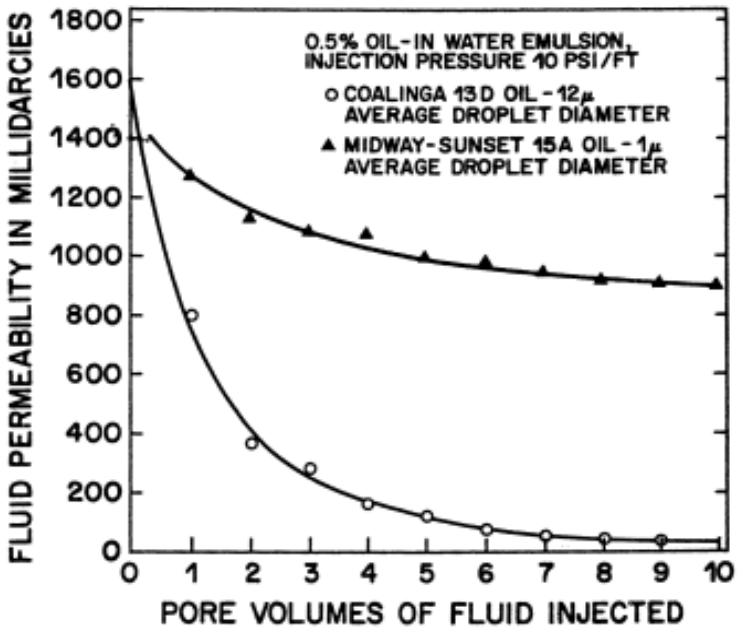

Figure 1.12: Effect of droplet size on permeability reduction.
(Source McAuliffe, 1973)

Hofman & Stein (1991) found significant permeability loss (reduction down to 35% of initial permeability) when flowing a 1% (v/v) stabilized emulsion (droplet size approx. 5-9 µm) through glass beads (grain size 40-60 µm). Cobos et al. (2009) described emulsion flow by droplet blockage of pore throats to describe the flow of oil-in-water emulsions in capillary tubes.

1.18.3 Filtration Model

Adaption of the deep bed filtration model has been applied to dilute emulsion transport most notably by Soo & Radke (1984, 1986) where emulsion droplets can be retarded via straining as well as interacting with the porous media allowing for droplet capture and remobilization (i.e., principles of colloid transport and retention). However, there are some notable difference between emulsion droplet transport and traditional particle transport. For example, changes in local permeability alter flow paths in emulsion transport when the droplet sizes are of similar scale to pore diameters; in typical particle transport models the alteration of local permeability is often negligible and disregarded. Soo & Radke (1984) define two droplet retention regimes to enhance the mechanistic view of droplet transport in porous media; the first regime is when droplets are captured predominately via straining and the second via interception mechanisms. The rate of droplet capture via straining has been found to be directly proportional to the flow rate and can be described by a straining filtration theory for deformable drops. Soo & Radke (1984, 1986) derive mathematical expressions for filtration modeling of dilute emulsion droplets with the assumption that emulsions are one

droplet size (although the model can be updated to include a distribution of droplet sizes) but that the porous media has a range of grain sizes and pore throats. This model handles the transient changes in permeability and local flow redistribution that affect deformable droplet transport using three parameters: a filter coefficient, a pore flow redistribution factor, and a local flow restriction factor.

1.18.4 Droplet Sorption Models

The oil droplets of the oil-in-water emulsions will be retained on porous media depending on the affinity and capacity of the droplets for the subsurface materials as well as properties of the groundwater flow. Coulibaly and Borden (2004) found that oil droplet retention is proportional to the clay content in the soil, with increasing retention in higher clay porous media. Clayton and Borden (2009) modeled oil droplet retention to solid particles using a rate-limited isotherm to describe the "reaction term" in the standard advection-dispersion-reaction (ADR) transport equation through the equilibrium concentration (C^*) in the linear driving force model for mass transfer being defined as the standard aqueous phase expression (Equation 1.50) and the solid phase concentration is then determined by the following equation:

$$\frac{\partial S}{\partial t} = K_m \frac{nS_w}{\rho_b}(C - C^*) \qquad (1.50)$$

Where: K_m is the liquid-solid mass transfer rate and C^* is defined as:

$$C^* = S(K_1K_2 - K_1S)^{-1} \qquad (1.51)$$

Where: K_1 is the Langmuir binding constant [$L^3 \cdot M^{-1}$] and K_2 is the maximum sorption capacity [$M \cdot M^{-1}$]. The authors used this modeling method to predict oil retention in a 3-d heterogeneous domain with previously calibrated sorption isotherm parameters and mass lumped transfer coefficient.

1.18.5 Viscous Fingering

Density and viscosity differences between two fluids (regardless if fluids are fully miscible or immiscible) in porous media can create instabilities in flow. When a less dense and/or less viscous fluid is injected after a more dense/more viscous fluid, the less viscous solution tends to penetrate the other fluid causing "viscous fingering" (Homsy, 1987).

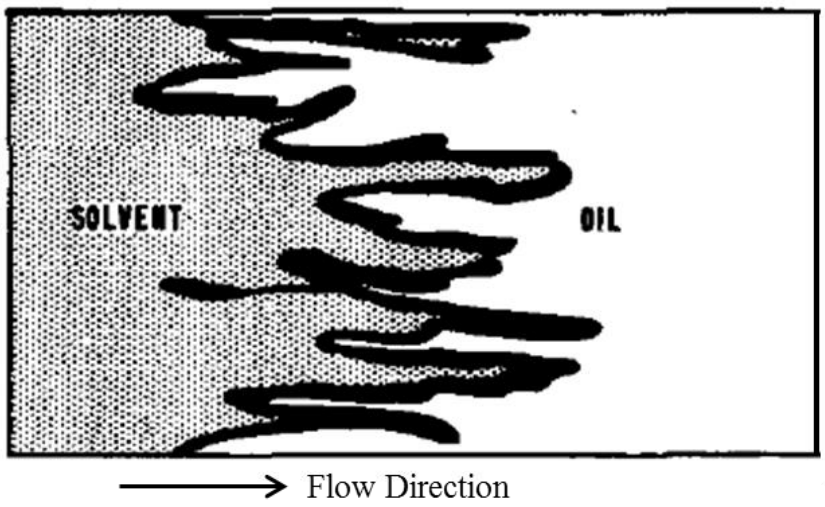

Figure 1.13: Example of viscous fingering of a less viscous solvent into a more viscous oil phase. (Source: Koval, 1964)

Viscous fingering alters the flow front making the standard assumptions of transport being dominated by advective and dispersive forces invalid at the front between the two fluids. For miscible fluids, the effect of viscous fingering on transport can be accounted for using averaged models or with direct numerical simulations of the physical fingering process (e.g., Koval, 1963; Sorbie, et al., 1995).

1.18.5.1 Koval averaging method

The first averaged model was developed by Koval (1963) where the average solvent concentration in the fingers is denoted, $\overline{C}$ with the solvent fractional flow of the total volume $f(\overline{C})$ modeled assuming viscous fingering growth is linear with time. Several models have been used to describe the fractional solvent flow $f(\overline{C})$ (e.g., Koval, 1963; Todd & Longstaff, 1972, etc.). The Koval (1963) model is widely used due to the model simplicity (e.g., Sorbie et al., 1994; Tchelepi, 1994).

The flow front where vicious instability occurs (i.e., where a less viscous solution is penetrating into the more viscous solution) can be derived from a material balance (Koval 1963). In the work of Koval, the less viscous phase is deemed the solvent displacing phase; and the more viscous, the resident phase. When addressing displacements involving oil-in-water emulsions, the emulsion is typically the more viscous phase, though it should be recognized that the viscosity of either phase can be manipulated using thickening agents such as xanthum gum.

$$\frac{1}{PV_D} = \frac{df(\overline{C})}{d\overline{C}} \qquad (1.52)$$

Using the expression for fractional solvent volume as defined by Koval (1963) the equation can be rewritten in terms of $f(\overline{C})$

$$f(\overline{C}) = \frac{K\overline{C}}{1+(K-1)\overline{C}} \qquad (1.53)$$

Where the derivative with respect to $(\overline{C})$ is:

$$\frac{df(\overline{C})}{d\overline{C}} = \frac{K}{(1+(K-1)\overline{C})^2} \qquad (1.54)$$

Since $\overline{C}$ is difficult to determine experimentally, it can be eliminated from the equation and instead written in terms of $f(\overline{C})$ and PV_D by plugging and rearranging in resulting in:

$$f(\overline{C}) = -\frac{K+\sqrt{\frac{K}{PV_D}}}{K-1} \qquad (1.55)$$

Since pore space is either occupied by solvent or oil (i.e., $f_D + f_R = 1$); the fractional flow in terms of f_R can be described for $PV_D \le \frac{1}{K}$ and $PV_D > K$, as:

$$f_R = 1 - f(\overline{C}) = \frac{\sqrt{\frac{K}{PV_D}+1}}{K-1} + 2 \qquad (1.56)$$

The mobility ratio, *M*, is defined as the mobility of the displacing phase compared to the mobility of the displaced phase. The mobility ratio is widely used in engineering literature to determine the resistance to flow at a given fluid saturation.

$$M = \frac{k_D}{k_R}\frac{\mu_R}{\mu_D} \qquad (1.57)$$

Where: k_D ,k_R are the relative permeability of the less viscous displacing solution and the more viscous resident phase, respectively; μ_D , μ_R are the viscosity of the displacing and resident phases, respectively.

Typically it is assumed that relative permeabilites are equal and constant; simplifying the mobility ratio to the ratio of the solution viscosities.

However, mixing occurs at the displacing front between the solvent and the oil and thus an effective mobility ratio, *E*, is needed to correct for this mixing font. Koval (1964) examined experimental data acquired from Blackwell, et al. (1960) and estimated the mixing ratio was approximately 78% displacing fluid and 22% displaced or resident fluid in heterogeneous systems that limit flow effects. Thus, Koval computes the effective mobility ratio, *E*, as:

$$E = [0.78 + 0.22M^{0.25}]^4 \qquad (1.58)$$

Koval also applies a heterogeneity factor, *H*, to account for channeling and dispersion effects and alludes to the fact that *H* may be a property of the porous media and independent of the mobility ratio.

$$K = H \cdot E \qquad (1.59)$$

Transport can then be modeled in the fingering region as the spatial average solvent concentration, $\overline{C}$. However, it should be noted that since $\overline{C}$ is the spatial average solvent concentration it is directly comparable to experimental results but not directly applicable when considering other mechanisms affecting transport behavior (e.g., attachment, detachment, straining processes) since these processes occur based on the actual concentration, *C*, not the averaged concentration, $\overline{C}$. When the dispersed phase of the emulsion is conceptualized as a solute (as in colloid filtration theory), viscous instabilities manifest as dispersive mixing. In fact, the Koval model has be directly linked to solute dispersion by relating the flux averaged expression to the analytical solute transport solution to produce an empirical expression describing instabilities as dispersive mixing (Flowers and Hunt, 2007).

Viscous effects were incorporated by adapting the method of Flowers and Hunt (2007) which relates viscous mixing to effective dispersion. Koval (1963) described the normalized effluent concentration resulting from viscous fingering using Equation 1.60.

$$\frac{C(PV_D)}{C_0} = \frac{E \cdot H - \sqrt{\frac{E \cdot H}{PV_D}}}{E \cdot H - 1} \qquad (1.60)$$

Where: C is the effluent concentration during displacement [$M \cdot L^{-3}$]; PV_D is the volume of displacing fluid introduced normalized by the pore volume of the medium [-]; C_0 is the initial concentration of the viscous (i.e., resident) solution [$M \cdot L^{-3}$]; and H is a heterogeneity factor [-] to account for channeling and dispersion (i.e., physical heterogeneities).

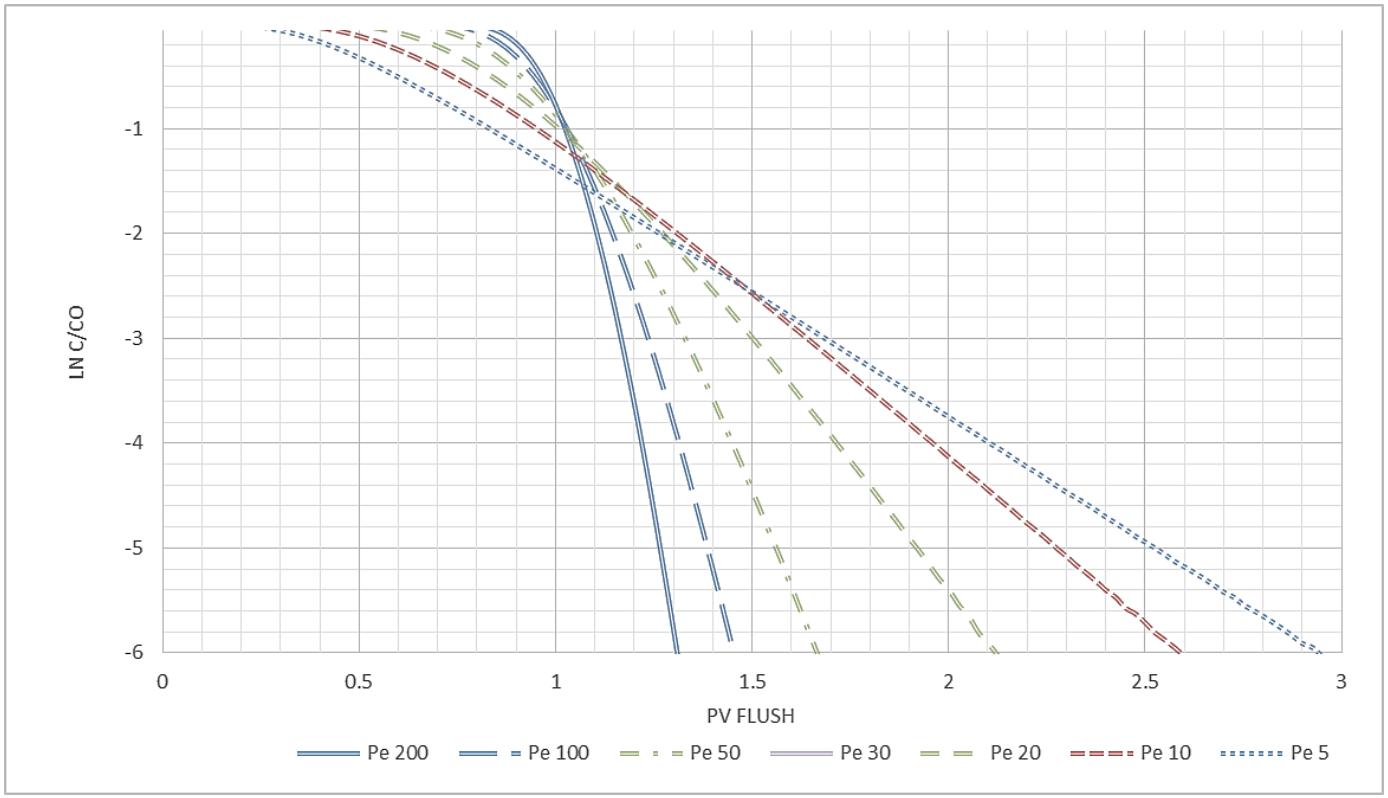

Figure 1.14: An illustration of tailing based on Koval's equation for various Pelect numbers (i.e., various dispersive mixing conditions). Increased dispersive mixing (decreasing *Pe*) gives an early fall of the 'backside' of breakthrough curve and extended tailing.

Flowers and Hunt (2007), suggest rearranging Equation 1.60 for PV_D in order to substitute the expression into a dimensionless form of the approximate analytical solution (Freeze and Cherry, 1979). The validity of the approximate analytical solution is highest at high Peclet number (*Pe*). Viscous instabilities, however, create conditions effectively increase mixing (i.e., effectively decrease *Pe*). Thus, the Koval solution can be linked to the more robust Ogata and Banks (1961) solution to the advection-dispersion equation. This method produces an expression for a dispersion-like term, D_{vis} that can be added to existing formulations of D_m to capture the influence of viscous effects on mixing when assessing the applicability of colloid transport models across a wide range of emulsion concentration. Substitution of Equation 1.60 (rearranged to be in terms of PV_D) into the dimensionless analytical solution of Ogata and Banks produces an expression that can be solved iteratively to determine the dependence of *Pe,* and thus D_{vis}, on the product E·H. The solution, for $\frac{C}{C_0}$ of 0.9 as per Flowers and Hunt (2007), is shown in Equation 1.61, respecting the bounds Koval placed on his solution in terms of PV_D.

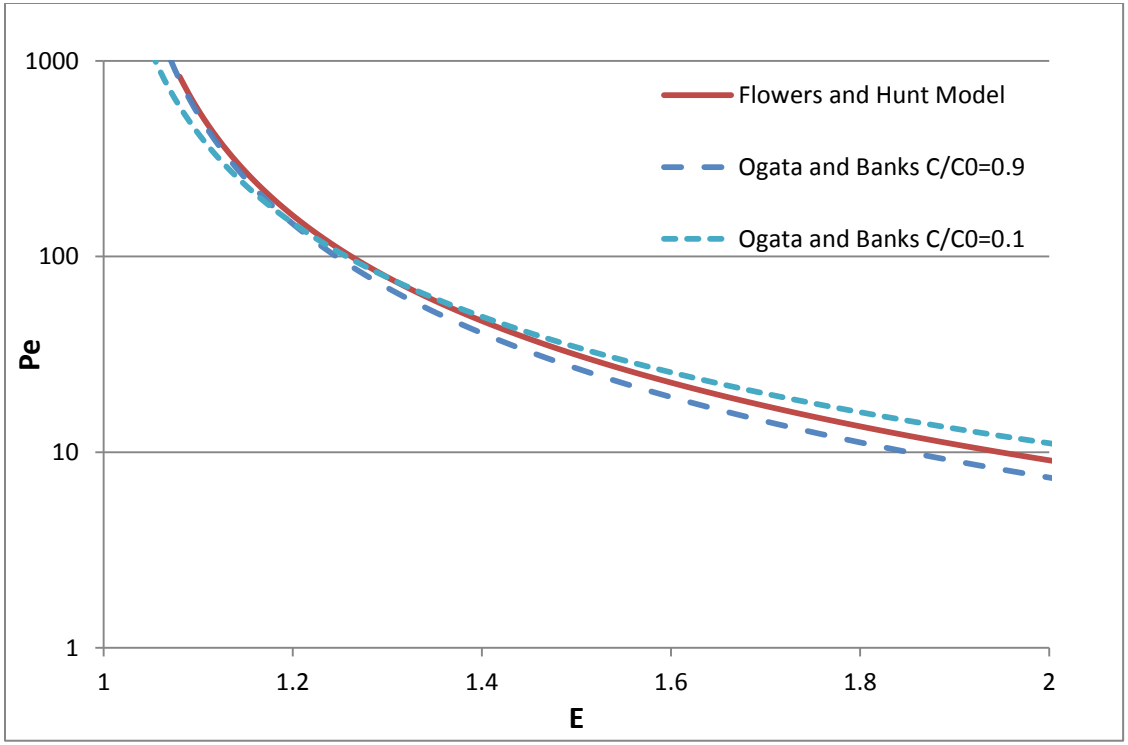

Figure 1.15: Functionality of *Pe* and effective mobility ratio (*E*). (solid line) Flowers and Hunt (2007) expression listed as: $\frac{1}{Pe} = 0.11(E-1)^{1.79}$; (long dashed line) Ogata and Banks (1961) analytical solution solved at C/C_0=0.9 of: $\frac{1}{Pe} = 0.13(E-1)^{1.86}$ and (short dashed line) at C/C_0=0.1 of: $\frac{1}{Pe} = 0.09(E-1)^{1.65}$.

Figure 1.15 illustrates the difference between the both the analytical solution used in Flowers and Hunt (2007) and the Ogata and Banks (1961) solution which provides higher accuracy in high diffusion systems (i.e., low *Pe*) as well as the potential difference of the solution as a function of concentration (i.e., C/C_0=0.1 vs C/C_0=0.9). Here, the expression for C/C_0=0.9 was selected for further use in describing the effect of viscous fingering on emulsion transport. Although outside the scope of this work, further investigations may benefit in understanding any potential role of concentration on these correlations (i.e., concentration dependent functionality of *Pe* and *E*).

The final Ogata and Banks (1961) correlation limited by the bounds defined by Koval is shown in Equation 1.61. This expression gives the additional dispersive mixing term from the viscous instabilities in terms of D_h which can be added directly to an ADR expression.

$$D_{vis} = \begin{cases} 0.13\dfrac{qL}{ns_{aq}}\left(E\cdot H-1\right)^{1.86} & \left(E\cdot H\right)^{-1} < PV_D < E\cdot H \\ 0 & PV_D < \left(E\cdot H\right)^{-1} \;\&\; PV_D > E\cdot H \end{cases} \tag{1.61}$$

1.19 Oil and Emulsion Subsurface Transport and Retention Behavior

In order for edible oils to be utilized for remediation efforts adequate transport, delivery and retention of the oil droplets needs to occur over the target zone of treatment. Oil droplets can be envisioned to be retained in porous media by similar mechanisms as govern particle deposition or as ultimately coating the

sand surface and filling the pore space. Laboratory experiments are typically completed with a homogenous porous media; however, heterogeneities exist in the fluid. In heterogeneous media, droplet retention can be increasingly complex, creating less uniform droplet retention due to different permeability zones throughout the subsurface (Clayton and Borden, 2009). Emulsion retention in laboratory experiments and in the field is highlighted in Table 1.8. With neat oils a significant amount of oil will be retained in the pore space - Coulibaly and Borden (2004) found between 1 and 20 lb-oil·ft^{-3} of neat oil was retained and 0.1 to 1 lb-oil·ft^{-3} retained when injected as an oil-in-water emulsion. See Table 1.8 for experimental retention behavior of oil-in-water emulsions.

Table 1.8: Oil-in-water emulsion retention in various porous media.

Porous Media	Maximum Emulsion Retention (Column Experiment) [g/g]	Effective Emulsion Retention [g/g]	Reference
Sandy mixture with 7% silts and clay	0.0054	0.0066 (Box experiment)	Coulibaly & Borden, 2004
Sandy mixture with 9% silts and clay	0.0061	0.0035 (Box experiment)	Coulibaly & Borden, 2004
Sandy mixture with 12% silts and clay	0.0095	0.0037 (Box experiment)	Coulibaly & Borden, 2004
Aluvium, clayey sand (Maryland field site)	0.0037	0.0013 (Field test)	
Sandy clay with rock fractures, low permeability (Burlington, NC field site)	Not Measured	0.0017	
Gravelly sand with high permeability (Indiana field site)	Note Measured	0.002	

Source: AFCEE, 2007

Investigation into the delivery behavior of both neat and emulsified oils found that injection of neat oil created moderate to high permeability loss in typical subsurface materials, whereas stable oil-in-water emulsions have more desirable delivery characteristics (Coulibaly & Borden, 2004). Injection of neat soybean oil is only successful for course sands and otherwise has been shown to result in large permeability loss and ineffective oil distribution. Clay content was found to play a role in oil retention with more retention for soils with higher clay contents (Coulibaly & Borden, 2004). However, injecting emulsified oils has been shown to give an effective distribution with limited permeability loss (Coulibaly, et al., 2006; Long & Borden, 2006). When emulsion droplets (0.7 to 1.2 μm mean diameter) were injected into a 3-d aquifer cell and followed by a water chase, effective and uniform distribution was achieved that could be successfully modeled using a colloid transport model with a Langmuirian blocking function in both homogenous and heterogeneous porous media (Jung, et al., 2006). A different experimentally based study modeled the retention of emulsion oil droplets in porous media using a rate limited Langmuir isotherm (Clayton & Borden, 2009).

Many of the emulsion retention experiments were completed with the aim of adding edible oils to the subsurface to support remedial activities. The amount of degradable oil needed to supply sufficient electron donor for microbial degradation is typically much less than the amount of oil retained in porous media when attempt to achieve uniform oil retention (Air Force Center for Engineering

and the Environmental, 2007). Such oil-in-water emulsions can be employed in the subsurface as a permeable reactive barrier (PRB) where contaminated groundwater flows through the emulsion zone for treatment, via injection wells into the source zone, or in a recirculation type system (AFCEE, 2007). Laboratory experiments investigated the use of soybean oil coated sand grains (1% g-oil/g-sand) in a permeable barrier to promote denitrification, finding that the hydraulic conductivity reduced with increasing oil content (Hunter, 2001). Injection of pure edible oils into existing on-site wells can be completed by an oil injection followed by a water flush or via a push-pull technique. For example, an injection of pure soybean oil followed with a water chase was employed at the Naval Support Activity Mid-South, Tennessee (Air Force Center for Engineering and the Environmental, 2007).

1.20 Reaction of Amendments and Contaminants

Transport and retention of active ingredients is only one part of successful use of amendments for remedial efforts. The reaction mechanisms between amendments and contaminants must also be considered. With any subsurface contaminants, reaction can be dictated by chemical or mass transfer limitations of active compounds once delivered to the contaminants. Although, much emphasis has been placed on emulsion transport and retention the mechanisms governing the rate of reaction and potential alkalinity release from these oil-in-water emulsions are not well studied.

Release and chemical reactions can be limited by either: 1) the chemical reaction rates of the species (e.g., slow reaction rate between two compounds); and 2) by mass transfer of the reactive species (e.g., transfer across a phase, diffusion away from a dissolving surface). Many aqueous reactions are essentially instantaneous and so it is often assumed that mass transfer rates limit the overall reaction rather than the chemical reaction rates. However, mass transfer can dictate in many systems due to such processes as the kinetics of particle/mineral dissolution and rates leading to the partitioning of solutes between phases.

1.21 MASS TRANSFER AT THE OIL-WATER INTERFACE

The transfer of mass across an interface (e.g., liquid-liquid interface, solid-liquid interface, etc.) can be described using several models. Many models can be used to conceptualize diffusive mass transfer across an interface including equilibrium distribution, film theory, and surface renewal models.

1.21.1 EQUILIBRIUM PARTITIONING

Contaminant partitioning assumes that the concentration of a component in one phase is proportional to the concentration of that component in a different phase connected via an interface. This model is commonly applied to systems of low concentration assuming that local equilibrium has been reached. Typically, the proportionally is assumed to be linear as is described as follows:

$$c_j^{\,1} = Kc_j^{\,2} \qquad (1.62)$$

Where: the subscript indicates the component, *j*, and the superscript the phase, and *K* is the equilibrium partitioning coefficient. Many groundwater models assume equilibrium partitioning between NAPL and aqueous phases (e.g., (Pinder & Abriola, 1986).

1.21.1.1 Local equilibrium approximation/assumption

Local equilibrium models are widely used in transport modeling to account for the mass exchange between two phases of interest (e.g., sorption to solid surfaces, mass transfer between aqueous and NAPL phases, etc.). Local equilibrium assumes that the processes (chemical and/or physical) are sufficiently fast compared to the bulk fluid flow rate; however, if these processes are not fast enough then the system is considered to be at either physical or chemical nonequilibrium conditions. Valocchi (1985) derives conditions for homogenous soils when the local equilibrium assumption (LEA) is valid for kinetic mass transfer models (both physical and chemical limiting cases). When LEA is not valid, then local equilibrium models will incorrectly predict mass transport. For the case of dissolution from NAPL droplets, if LEA is not valid then models using this assumption will over predict effluent concentrations (See Figure 1.16)

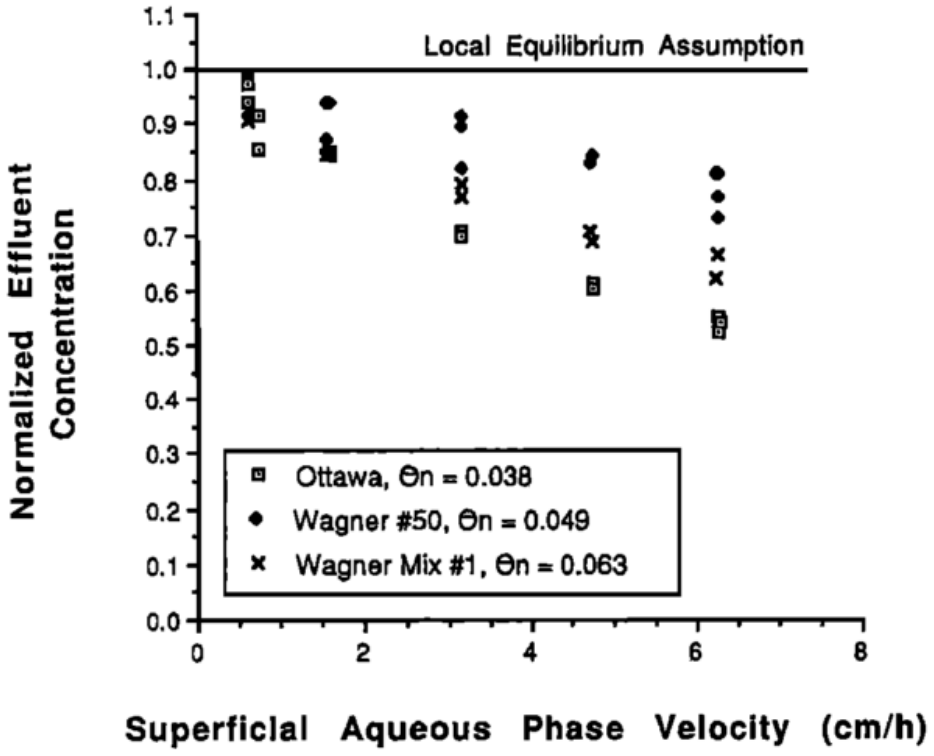

Figure 1.16: Influence of flow velocity on deviation from local equilibrium assumption (LEA) for steady state NAPL dissolution in varying porous media. (Source: Powers, et al., 1992)

When the local equilibrium assumption is not valid then a chemical or physical process is limiting mass exchange in the system. If transport of solutes or reactive species is the limiting step, then the system is considered to be in physical nonequilibrium and the kinetics of transport must be considered when developing a transport model with mass transfer between phases, most commonly conceptualized using film theory, a surface renewal model, or penetration theory.

1.21.2 Film Theory

Film theory assumes that mass transfer of a component between phases is controlled by diffusion over the two thin films of phase interface. The bulk phases are assumed to be well mixed (i.e., mixing within each bulk phase is sufficiently fast in comparison to transfer between phases) and the thin films at the interface are stagnant layers controlled by quasi-steady state diffusion. By definition there must be two films at an interface; however, typically one side is assumed to control the overall mass transfer rate.

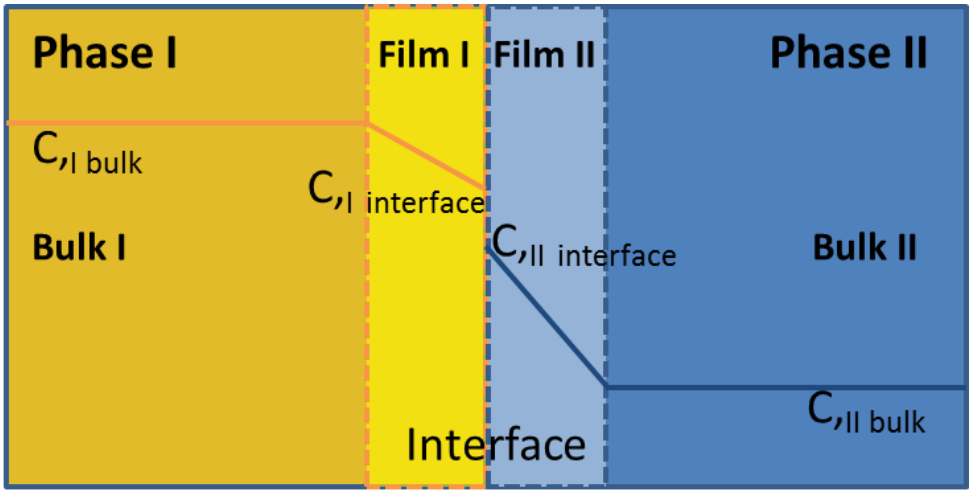

Figure 1.17: Graphic representation of two thin-film model for interphase mass transfer.

Mass flux (from phase *I* to phase *II*) across a film can be expressed as:

$$q_{I\to II} = k_{I\to II} a_{s,I,II} (C_I^* - C_I) \quad (1.63)$$

Where: $q_{I\to II}$ is the mass flux of the component from phase II to phase I [M/L^3-T]; $k_{I\to II}$ is the mass transfer coefficient for phase I to phase II [L·T^{-1}]; $a_{s,I,II}$ is the specific interfacial area between the phases [1/L]; C_I^* is the equilibrium concentration of the component in phase I [M·L^{-3}].

The specific interfacial area is a difficult value to measure or estimate especially in porous media when only a portion of the NAPL interface may be in contact with the flowing aqueous phase, with the remaining surface area in contact with soil grains. Still, the interfacial area can be estimated using either geometric considerations or thermodynamics. A shape factor (ψ) can be applied to the interfacial area for geometric estimates to account for any shape irregularities (i.e., variations from spherical shape), where ψ is the ratio of the measured mass transfer coefficient to the mass transfer coefficient calculated from an applicable correlation. There are shape factor corrections for non-spherical solid particles, etc. in the literature. Additionally, interfacial area can be predicated thermodynamically using capillary pressures, the degree of NAPL saturation, and interfacial tension (Rose & Bruce, 1949; Grant & Gerhard, 2007). Kokkinaki, et al. (2013) found that thermodynamic models for estimating temporal interfacial area over the course of NAPL dissolution required less system calibration than geometric models for estimating specific surface area. The

authors were able to correlate mass transfer coefficients calculated using Sherwood correlations and soil properties. However, if the specific interfacial area is assumed to be constant with time, then it can be combined with the mass transfer coefficient to give a lumped mass transfer coefficient $k_{L,I\rightarrow II}$ [1/T] (Miller et al., 1990; Powers et al. 1992, 1994; Imhoff et al. 1994; Zhang and Schwartz 2000). Additionally, the stagnant thin film model assumes mass transfer is solely a product of diffusive transport when in fact mass can be transferred between phases by diffusive, adjective, and other phenomena (e.g., chemical kinetics) (Miller, et al., 1990). To describe mass transfer in a more mechanistic form, the impact of local velocities and the differences in flow around a single sphere versus flow through porous media needs to be considered; and thus many empirical correlations have been developed to estimate the mass transfer coefficient for a variety of conditions and interphases.

In porous media, correlations employing the Sherwood number, grain size, and the molecular diffusivity have been developed (e.g., Miller et al., 1990; Powers et al., 1992, 1994a) for liquid-liquid interphase mass transfer. The theoretical idea of the thin film model can then be extended and written in terms of the Sherwood number, *Sh* [-] with the characteristic length specific for porous media based on grain size as follows:

$$k_{L,I\rightarrow II} = Sh\frac{D_I}{d_{50}^{\ 2}} \qquad (1.64)$$

Where: d_{50} is the mean grain size of the porous media [L]

When considering mass transfer from an organic liquid or non-aqueous phase liquid (NAPL), the Sherwood number can then be empirically related to Reynold's number (*Re*) and NAPL saturation (S_N) by the following relationship format:

$$Sh = \alpha \cdot \mathrm{Re}^{\beta} \cdot S_N{}^{\gamma} \quad (1.65)$$

Where: α, β and γ are dimensionless fitting parameters; Peclet number (*Pe*) is the ratio of advective to diffusive rates (i.e., $Pe=L \cdot U/D$ where: L is the characteristic length [L], U is the fluid velocity [$L \cdot T^{-1}$] and D is the diffusivity [$L^2 \cdot T^{-1}$]); Reynolds number (*Re*) is the ratio of inertial forces to viscous forces (i.e., $Re=U\rho L/\mu$ or for porous media $Re=v_x \rho d_p/\mu$) where v_x is the pore water velocity [$L \cdot T^{-1}$]; ρ is the density of the flowing fluid [$M \cdot L^{-3}$]; d_p is the grain size diameter of the porous media [L]; and μ is the dynamic viscosity of the fluid [$M \cdot L^{-2}$]. Still, here three fitting parameters are required to give insight into a single lumped parameter.

Many Sherwood number mass transfer correlations have been developed for various applications and specific conditions. The correlations that are relevant to NAPL dissolution from entrapped ganglia are presented in Table 1.9.

Table 1.9: Sherwood number mass transfer rate correlations based on experimental data.

Dissolution from Entrapped NAPL			
	Range of Applicability	**Correlation**	**Reference**
Oil dissolution in porous media (pools)	$0.5 < Pe < 50$	$Sh = 0.55 + 0.25Pe^{1.5}$	Pfannkuch, 1984
NAPL droplet in porous media	$1 < Pe < 200$	$Sh = 77.6 \cdot \mathrm{Re}^{0.658}$	Powers, et al., 1994b
		$Sh = 44 \cdot \mathrm{Re}^{0.526} Sn^{0.937}$	Nambi & Powers, 2003
	$0<\theta_N<0.04$ $1<Pe<25$ $1.4 \le \frac{x}{d_{50}} \le 180$	$Sh = 340 \cdot \theta_N^{0.87} \cdot \mathrm{Re}^{0.71} \cdot (\frac{x}{d_{50}})^{-0.31}$	Imhoff, et al., 1994
	$10 < Pe < 250$	$Sh = 57.7 \cdot \mathrm{Re}^{0.61} d_{50}^{0.64} U_i^{0.41}$	Powers, et al., 1992
NAPL blobs with changing surface area as dissolution occurs	$10 < Pe < 170$	$Sh = 4.13 \cdot \mathrm{Re}^{0.589} (\frac{d_{50}}{d_M})^{0.673} U_i^{0.369} (\frac{\theta_N}{\theta_{N0}})^{\beta}$ $\beta = 0.518 + 0.144(\frac{d_{50}}{d_M}) + 0.10U_i$	Powers, et al., 1994a

U_i is the uniformity index(d_{60}/d_{10}); n is porosity; Sc is Schmidt number defined as: $Sc=\mu/\rho \cdot D_m$; D_m is the molecular diffusion coefficient of the NAPL source solute in the aqueous phase (Miller, et al., 1990); d_M is the diameter of a "medium" sand grain (0.05 cm); θ_{N0} is the initial volume fraction of NAPL; θ_N is the volume fraction of NAPL; (x/d_{50}) is the dimensionless distance into the region of residual NAPL

Mass transfer of various acidic and basic crude oil molecules from oil to water was investigated using a simplified system with oil-water partitioning coefficients dictating the interface mass transfer. No investigation into the temporal response but rather forced solely on the equilibrium state of the system to evaluate the acid/basic effects of the crude oil on the aqueous environment. The authors did note that interfacial tension at the oil-water interface was decreased at low and high pHs due to the ionization of interfacial groups effectively creating surfactants at the interface (Hutin, et al., 2014).

1.22 DISSOLUTION OF SOLIDS

Dissolution of solids has been extensively studied particularly when related to mineral dissolution. Modeling the release kinetics from solid particles has been done successfully using a variety of models- some with a more mechanistic approach and others using empirical models. Release kinetics have been extensively within the context of environmental engineering aquatic chemistry and soil science as well as by the pharmaceutical industry to determine drug release rates from solid forms (e.g., tablets). Some of the most common kinetic models include zero and first-order release kinetics; however, more empirical fits have been able to capture the release kinetics and are also widely used. Zero-order dissolution kinetics can be successful in describing simple release scenarios, typically applicable for modeling of low soluble drug dissolution. Such a model does not account for changing surface area and is not dependent on the aqueous concentration of the releasing compound and thus is

only valid for slow release rates or for complete sink conditions (Costa & Lobo, 2001). Other models, for example, base release by the amount of the compound still available for release (i.e., first order with respect to the solid rather than to the aqueous concentration) and can be expressed using the Hixson and Crowell Equation. Costa and Lobo (2001) completed an overview of dissolution model, both mechanistic and empirical models, in the context of drug release via dissolution from solids (Table 1.10).

Table 1.10: Mathematical models for dissolution.

Model	Equation	Details
Zero Order	$\frac{dC}{dt} = -K_0$	Assumes: 1) area does not change; 2) perfect sink conditions
First Order	$\frac{dC}{dt} = -K_1(C^* - C)$	K_1 is the lumped mass transfer coefficient ; C^* is the aqueous solubility First order with respect to aqueous concentration
Second Order	$\frac{dC}{dt} = K_2(C^* - C)\cdot C^*$	
Hixson-Crowell	$\frac{dC}{dt} = -3K(C_0{}^{1/3} - K\cdot t)^2$	First order with respect to the solid. Dissolution from a planar surface (i.e., solid tablet)
Weibull	$\frac{dC}{dt} = -abC\cdot t^{b-1}\cdot \exp(a\cdot t^b)$	Strictly empirical curve fitting. a is a scale parameter, b is a shape parameter
Higuchi	$\frac{dC}{dt} = 0.5k\cdot t^{-0.5}$	Release of a water soluble compound from a solid or semi-solid matrix based on diffusion processes.
Baker-Lonsdale	$\frac{3}{2}[1-(-(\frac{C_t}{C^*})^{2/3}]-(\frac{C_t}{C^*}) = k\cdot t$	Release from a spherical matrix, has been used to model release from microcapsules.
Korsmeyer-Peppas	$\frac{dC}{dt} = C\cdot n\cdot K_{KP}\cdot (t^{n-1})$	Semi-empirical; n is the release exponent ; n=0.5 to model as Fickian diffusion; $0.5<n<1.0$ to model as non-Fickian behavior
Quadratic	$\frac{dC}{dt} = 200\cdot K_1\cdot t + K_2$	
Gompertz	$\frac{dC}{dt} = -AK\cdot \exp(-e - K(t-y))$	
Hopfenberg	$\frac{dC}{dt} = \frac{nKC^*}{a\cdot C_0}(1-\frac{K\cdot t}{a\cdot C_0})^{n-1}$	Dissolution from surface-eroding matrices. Generic form to include all geometries.

Adapted from Costa and Lobo (2001)

1.23 SOLUTE TRANSPORT MODELS

Modeling release of active ingredients from retained additives a basic solute transport model can be used and the reaction term can be changed to represent the reaction/release behavior (e.g., linear partitioning, linear driving force model, etc.). For single phase 1-d solute transport, a form of the advection-dispersion-reaction (ADR) equation is used to model solute transport. The generic form can be expressed as:

$$Rf\frac{\partial C_I}{\partial t} = -v_x\frac{\partial C_I}{\partial x} + D_h\frac{\partial^2 C_I}{\partial x^2} + \frac{\partial C_I}{\partial t}_{rxn} \qquad (1.66)$$

Where: Rf is the retardation factor [-]; v_x is porewater velocity [$L\cdot T^{-1}$]; D_h is the dispersion coefficient [$L^2\cdot T^{-1}$]; and $\frac{\partial C_I}{\partial t}_{rxn}$ is the generic reaction source or sink term. Equilibrium contaminant partitioning between two phases can be incorporated into the ADR equation by the retardation factor, Rf. Rf is generically defined as:

$$Rf = 1 + \frac{\rho_b}{nS_w}\left(\frac{\partial C_{II}}{\partial C_I}\right) \qquad (1.67)$$

With $\frac{\partial C_{II}}{\partial C_I}$ representing the slope of the isotherm (or distribution plot). If the system does not follow the local equilibrium assumption, then a kinetic mass transfer term between phases can be introduced. Here, the $\frac{\partial C_I}{\partial t}_{rxn}$ can be equated

to a description of the interface mass transfer rate. For example, if the mass transfer is assumed to be described by a linear driving force model then:

$$\left(\frac{\partial C_I}{\partial t}\right)_{rxn} = kA_s(C_I^* - C_I) \qquad (1.68)$$

Where: k is the mass transfer coefficient; A_s is the specific surface area; C_I^* is the concentration of I at equilibrium; and C_I is the concentration of I at time, t.

However, if the assumption that the bulk phases are well mixed is violated, then interphase diffusion can also play a role in the rate of mass transfer between phases and needs to be accounted for in the mass transfer equation.

Chapter 2: Research Objectives

The overall objective of this research was to assess the utility of oil-in-water emulsions for delivery and sustention of remedial amendments. Emulsion design and testing was accomplished using a series of batch and column experiments. Experimental results were used to parameterize and assess mathematical models employed to test the conceptual models developed related to droplet transport and the amendment release processes. Overall the research consisted of five specific objectives: (i) develop kinetically stable particle containing oil-in-water emulsions; (ii) mathematically model the transport and retention of emulsions within sandy porous media; (iii) investigate the droplet retention, as well as fluid saturation, on mechanical dispersion; (iv) elucidate mechanisms of alkalinity release from particle suspensions and particle-containing emulsions; and (v) develop mathematical models to describe long-term pH treatment from particle-containing emulsions introduced in flow-through systems.

OBJECTIVE 1: DEVELOP KINETICALLY STABLE PARTICLE CONTAINING OIL-IN-WATER EMULSIONS

This research focused on supplying alkalinity to the subsurface through dissolution of magnesium oxide (MgO) and calcium carbonate ($CaCO_3$) particles. A central hypothesis of this work is that encapsulation of these particles within the dispersed phase of an oil-in-water emulsion could control rates of alkalinity

release. Particle mass held in the emulsion must, therefore, remain accessible for release, albeit at rates that are slower than that provided during mineral dissolution. For effective delivery, oil-in-water emulsions need to be stable for a minimum period of several hours (i.e., to inject and distribute). Objective 1a focused on developing formulations to encapsulate alkalinity-releasing nanoparticles (either MgO or $CaCO_3$) within the droplets of soybean oil. Desired emulsion properties include having a density and viscosity that allow for effective subsurface delivery. Emulsion densities and viscosities near that of the resident water limit the pressure required for injection and limit the potential for flow instabilities which can lead to non-uniform distribution of amendment. Objective 1b concentrated on the development of a conceptual model for alkalinity release from the particle-containing oil-in-water emulsions. This conceptual model formed the basis for research objectives related to the modeling of the alkalinity release process. Results related to this objective are described primarily in Chapter 3, with the conceptual model presented in Chapter 6.

OBJECTIVE 2: MATHEMATICALLY MODEL THE TRANSPORT AND RETENTION OF EMULSIONS WITHIN SANDY POROUS MEDIA

Oil-in-water emulsions are routinely used in subsurface remediation, although without mechanistic insights into the transport and deposition of concentration emulsions, remedial design is limited. Field applications employ either neat edible oil or emulsified oil at concentrations ranging upwards from 1% upwards towards 20% wt. However, most particle and emulsion transport

concepts and models have been created and evaluated for low concentrations. Here, the goal was to assess the applicability of existing transport models (applicable for dilute systems) to describe the transport and retention of concentrated emulsions (i.e., realistic concentrations of dispersed phase). Specifically, existing particle and emulsion transport model formulations were evaluated on their ability to capture experimental emulsion transport and retention behavior at various input concentrations in a sandy porous media. *It is hypothesized that transport and retention of highly concentrated emulsions are governed by additional mechanisms not considered in dilute transport models*. *Due to substantial emulsion deposition and/or the viscous nature of concentrated emulsions, it is hypothesized that these additional processes influence the transport behavior by altering the dispersive mixing conditions.* Modeling efforts focused on relating existing particle transport model formulations, parameterized with low concentration data, to predict emulsion transport and deposition at much higher concentrations. The predictive quality of this approach can help support system design when employing oil-in-water emulsions for remediation. Additionally, the dependence of mixing conditions on deposited mass and viscous instabilities can be applied more broadly to systems where water saturation is temporal and spatial (specifically when large quantities of mass are deposited on the porous media) and viscosity contrasts exist between fluids. Results related to Objective 2 can be found in Chapter 5.

OBJECTIVE 3: INVESTIGATE THE DROPLET RETENTION, AS WELL AS FLUID SATURATION, ON MECHANICAL DISPERSION

Injection of concentrated emulsions can result in large quantities of oil mass being retained on the porous media (e.g., 20% phase saturation). Saturations of non-aqueous phases (i.e., air and NAPL) have been shown to result in larger values of dispersivity. Yet, models capable of predicting these changes remain elusive, thus requiring α to by fit with a non-reactive tracer test. In unsaturated (air-water) systems the literature suggests that dispersivity is a function of both porous media properties and water content. Water saturation can also be altered by the presence of residual oil. Residual oil can be present in the subsurface as either the NAPL contaminant or alternatively as a remedial amendment (e.g., edible oils). *It is hypothesized that dispersive mixing is dependent on water saturation in both air-water and water-NAPL systems.* This hypothesis was tested through by analyzing existing literature data for both saturated and unsaturated laboratory column experiments with uniform water saturation. Data was regressed against the physical properties of the porous media and water saturation to give a poly-parameter model for dispersivity. *Furthermore, it is hypothesized that the developed model can be used to estimate dispersivity in systems where water saturation is changing is space and time (i.e., non-uniform water saturation).* The ability of developed correlations for uniform saturation are tested for applicability to predict mixing in spatially variant water saturation systems (i.e., concentrated emulsion experiments). Results related to Objective 3 are presented in Chapter 4.

OBJECTIVE 4: ELUCIDATE MECHANISMS OF ALKALINITY RELEASE FROM PARTICLE SUSPENSIONS AND PARTICLE-CONTAINING EMULSIONS

Elucidation of the extent and rates of alkalinity release from particle suspensions and particle-containing emulsions will permit release to be tailored to site-specific requirements for pH control. Objective 4a will focus on assessing and modeling non-encapsulated particles within an aqueous suspension. *It is hypothesized that particle surface area will be the controlling factor for release from these particle suspensions* The ability of empirical mineral dissolution models to describe the release behavior from bare particle is evaluated in Chapter 6. There the dissolution models are coupled with aqueous chemistry to predict pH through the dissolution (i.e., release) process in batch systems.

Objective 4b focused on modeling the release of alkalinity from particles encapsulated within the oil droplets of an oil-in-water emulsion. *It is hypothesized that particle and oil loadings influence the rate of alkalinity release from the emulsion, thereby providing an ability to tailor release rates on a site-specific basis.* The influence of emulsion properties on release rates was investigated in an attempt to help improve emulsion design for tuning alkalinity release rates. Release data collected in batch experiments was modeled in Chapter 6 using a linear driving force model to account for the mass transfer resistant across the oil-water interface.

OBJECTIVE 5: DEVELOP MATHEMATICAL MODELS TO DESCRIBE LONG-TERM PH TREATMENT FROM PARTICLE-CONTAINING EMULSIONS INTRODUCED IN FLOW-THROUGH SYSTEMS

Objective 5 aimed to relate the alkalinity release models (Objective 4) with the emulsion retention processes (Objective 2). Together these provide the constitutive relationships required to simulate the entire process of emulsion transport and subsequent alkalinity release from the retained emulsion fraction. *It is hypothesized that the alkalinity release mechanism found in Objective 4 can be used when modeling pH treatment in a 1-d column flow-through system.* Successful modeling of alkalinity release may identify points of control for the release rate and extent that can better fulfill specific alkalinity requirements for subsurface pH control. Deposited alkalinity from retained particle-containing oil-in-water emulsion, is evaluated on the ability to provide desired subsurface pH levels by extended controlled release of alkalinity. This evaluation is presented in Chapter 7. The effluent pH in these column experiments is modeled using solute transport equations which employed the rate of release expressions developed as a part of Objective 4.

Chapter 3: Development of kinetically stable particle containing oil-in-water emulsions

3.1 ABSTRACT

Oil-in-water emulsions were developed and evaluated for potential use in aiding aquifer remediation. Alkalinity releasing particles (i.e., MgO or $CaCO_3$ particles) were encapsulated in soybean oil to create an oil-in-water emulsion. Emulsion suitability was assessed via determination of the physical properties (i.e., density, viscosity, and droplet size distribution) and kinetic stability. Emulsions had desirable properties for subsurface injection: density near that of water, a manageable viscosity, and kinetic stability of greater than 20 hours. Expressions to describe emulsion density and viscosity as a function of soybean oil in the emulsion were developed here. 20% soybean oil emulsions were identified as the optimal emulsion formation and used in subsequent experimentation.

3.2 INTRODUCTION

For successful pH control via emulsions, alkalinity-releasing particles must be encapsulated within emulsion oil droplets; however, the particle encapsulation must not block alkalinity release from the oil phase to the aqueous phase. Ideally, emulsions have a density near that of water to remove any

potential buoyancy affects in the aquifer, and have a manageable viscosity as to limit backpressure during injection. Soybean oil was selected for the oil phase because of its wide usage in environmental remediation applications and low cost. Gum Arabic (GA) was selected for the stabilizing agent because GA: (1) is a natural, non-toxic compound (harvested from the acacia tree); (2) can form solutions at high concentrations (i.e., more than 50% concentration); and (3) acts as an excellent emulsifier and colloid protector. The alkalinity-releasing particles considered in this work are magnesium oxide (MgO) and calcium carbonate ($CaCO_3$) particles. These two particles types were selected because manufactured as nanoparticle, deemed safe for environmental use, relatively inexpensive, and because they are widely in current practice to provide alkalinity to the subsurface.

3.3 MATERIALS AND METHODS

3.3.1 MATERIALS

Magnesium oxide particles were obtained from Nanostructured & Amorphous Materials, Inc. in varying nano-sized diameters (nMgO) (99% + purity, ACS grade). Nano calcium carbonate particles ($nCaCO_3$) (60 nm) were obtained from Arcos Organic (99% + purity, ACS grade); micron-sized calcium carbonate particles were obtained from Sigma-Aldrich (reported size as <#40 mesh); soybean oil from MP Biomedicals (Laboratory grade); and Gum Arabic from Fisher Scientific (>99% purity). Additional material details are provided in Table 3.1. Soybean oil (SBO) contains both unsaturated and saturated fatty acids.

Although the exact amount of fatty acids may vary the major components are linoleate acid and oleic acid. See for Table 3.2 for typical soybean oil composition ranges and Table 3.3 for physical properties.

Table 3.1: Properties of alkalinity releasing particles.

Particle	Manufacture	Purity [%]	Diameter*	Density* [$g \cdot m^{-3}$]	Specific surface area (SSA)* [$m^2 \cdot g^{-1}$]
nMgO	Nanostructured and Amorphous Materials	99+%	100 nm	3.58	7
			50 nm		~20
			20 nm		50
MgO	Sigma-Aldrich	99+%	~44 µm (~325 mesh)	not reported	not reported
$nCaCO_3$	Acros Organics	99+% (ACS grade)	60 nm	2.83	not reported
$CaCO_3$	Sigma-Aldrich	99+% (ACS grade)	not reported (listed at 10µm in Leach, 2011)	2.93	not reported

*As reported by manufacturer

Table 3.2: Typical composition of commercially available soybean oil.

Methyl Ester	Typical Value [%]	Typical Range [%]
Linoleate	54.51 ± 1.54	35.2–64.8
Oleate	22.98 ± 2.01	8.6–79.0
Palmitate	10.57 ± 0.43	3.2–26.4
Linolenate	7.23 ± 0.78	1.7–19.0
Stearate	4.09 ± 0.34	2.6–32.6

Source: Hammond, et al., 2005 where data was collected from 21 samples of commercially available soybean oils

Table 3.3: Physical properties of soybean oil.

	Measured Value	**Literature Value(s)**
Density [$g \cdot mL^{-1}$]	0.920±0.001 (22°C)	0.9165 - 0.9261 (20°C)
Viscosity [cP]	72.2±0.53 (22°C)	32.2 - 58.5 (20°C)
Surface Tension (at 30°C) [dyne/cm]	not measured	27.6 (decreases 0.077 dyne/cm °C)

± indicates the standard deviation
Source: Hammond, et al., 2005. Details on viscosity measurements were not provided (i.e., shear rate, rheometer geometry, etc.)

Gum Arabic is a mixture of many components and has been found to have molecular weights varying between 250,000 to 580,000 with molecules shaped as short spirals with many side chains where the length of a spiral molecule is approximately 1050 nm (NPCS Board of Consultants & Engineers, 2009). The viscosity of aqueous solutions of GA is a function of pH with viscosity peaking at around pH 6 and 7 and falling to the lowest viscosity at both very acid and basic conditions (pH 2 and 13). Also, the addition of electrolytes tends to decrease the viscosity of a GA solution. GA contains potassium, calcium, and magnesium salts and can provide some buffering capacity (NPCS Board of Consultants & Engineers, 2009).

3.3.2 Experimental Methods

The process used to create oil-in-water emulsions was specifically designed to promote particle encapsulation within the oil droplets of the emulsion. Emulsions were prepared by first suspending the alkalinity releasing particles (i.e., MgO or $CaCO_3$ particles) in soybean oil (SBO) via Fisher Scientific Sonic Dismembrator (model 500) sonicator at 100% amplitude for one minute. The particle-oil dispersion was then used to make oil-in-water emulsions via a phase inversion process. The particle containing oil was mixed using a standard kitchen blender while a solution of 3.5% (wt.) Gum Arabic in MilliQ water (water resistivity>18.2 mΩ/cm and total organic carbon <10 ppb, Millipore Inc.) was slowly added until the target fraction of oil in the emulsion is reached. Gum Arabic (GA) was used as an emulsifying agent because it is a natural, non-toxic

material that is frequently employed in the food industry for structural stabilization and encapsulation.

Emulsions containing between 0.1 and 1.0% wt. particles and between 10-30% soybean oil stabilized with 3.5% (wt.) GA and MilliQ solution were evaluated. Emulsions were characterized by density, viscosity, droplet size, and droplet zeta potential, with all characterization completed at a 22.0±0.2°C. Emulsion density was measured using a 2 mL glass pycnometer (Ace Glass) calibrated with MilliQ water and verified with isopropanol. Approximately 20 mL of emulsion were used for viscosity measurements via a TA Instruments AR-G2 rheometer with concentric cylinder geometry over a range of shear rates (1 - 100 s^{-1}) with reported values at a shear rate of 20 s^{-1} unless stated otherwise. Performance of the rheometer was monitored using MilliQ water for each geometry/sensor on each day of use. Geometry was tested with water prior to each day of use and verified with MilliQ water to be near that of 1cP. Droplet sizes were characterized using light microscopy (Ziess Axiovert S100) coupled with MetaMorph (Molecular Devices) image analysis, as well as with dynamic light scattering (Malvern Zetasizer NanoZS). The zeta potential of emulsion droplet was assessed after dilution with MilliQ water (1:200 or 1:500) using the Malvern Zetasizer NanoZS. Zeta potential measurements were determined by measuring the electrophoretic mobility and converting to zeta potential via the Smoluchowski equation. The zeta potential of emulsions containing MgO, $CaCO_3$, and no particles were measured at the equilibrium pH. Zeta potentials for

emulsions containing particles were only able to be measured at the equilibrium pH since at any other pH the particles release alkalinity to bring the pH to equilibrium not allowing for accurate measurement of zeta potential at a specific pH. Kinetic stability of emulsions was assessed by a previous investigator in our laboratory via light transmission stability/sedimentation experiments using a PerkinElmer UV/VIS spectrophotometer monitoring at a wavelength of 580 nm (Leach, 2011). The light transmission data was then used to fit a settling and non-settling fraction using the assumption that light adsorption is linearly related to particle concentrat ion.

3.4 RESULTS AND DISCUSSION

The examined emulsions contained 0.1-1% wt. particles in 10-30% soybean oil stabilized with 3.5% (wt.) GA and MilliQ solution. In general, such emulsions are characterized by kinetic stability in excess of 20 hr, densities between 0.98 and 1.01 g/mL, viscosities between 10 and 20 cP, mean droplet diameters between 1.0 and 1.4 μm, and droplet zeta potentials between -30 and -35 mV. Previous kinetic stability results indicated that ~60 nm $CaCO_3$, 50 nm MgO, and 100 nm MgO particles in unamended soybean oil exhibit sufficient stability for emulsion encapsulation (Leach, 2011). The phase inversion process used to create the emulsion was specifically used to promote particles remaining in the oil phase of the emulsion. This, in concert with droplet imaging and emulsion stability results suggest that particles are held in the oil phase through the emulsification process. Emulsions were conceptualized as having alkalinity-

releasing particles within the soybean oil core of the emulsion droplets where the droplets are encapsulated with a gum Arabic wrapping as noted by Long and Ramsburg (2011) and shown in Figure 3.1.

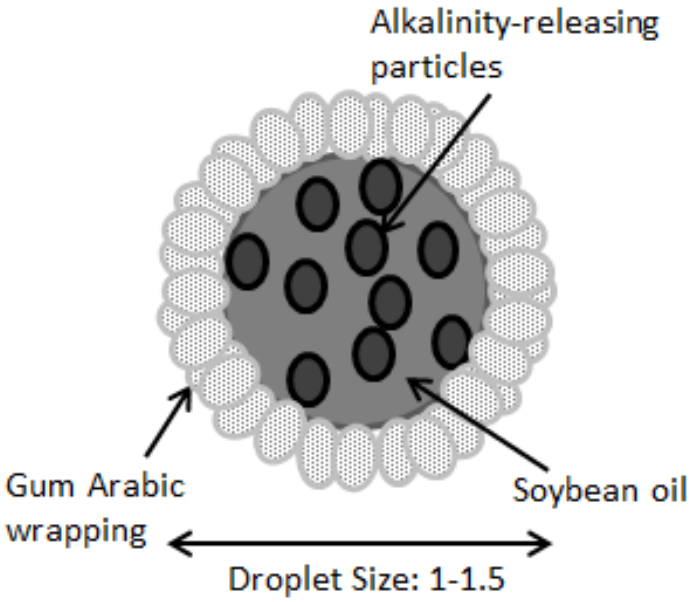

Figure 3.1: Conceptual model of oil-in-water emulsion.

The density of the oil-in-water emulsions as a function of soybean oil content was determined using the same oil dispersion of 0.1% (wt. particle/ wt. oil) $CaCO_3$ particle content and 3.5% (wt./ wt. total) of GA. The neat soybean oil-particle dispersion had a density of 0.92±0.0 g/mL and a viscosity of 72.2±0.53 cP. The density of the dispersed phase was calculated to be approximately 0.965 $g \cdot mL^{-1}$ using the following expression of density of a slurry:

$$\rho_{mix,A-B} = \frac{1}{\frac{f_A}{\rho_{s,A}} + \frac{f_B}{\rho_{s,B}}} \quad (3.3)$$

Where: $f_A+f_B=1$ for a solid comprised of only *A* and *B* solids. f_A, f_B is the mass fraction of component *A* and *B* in the solid mixture, respectively; and $\rho_{s,A}, \rho_{s,B}$ is the solid bulk density of component *A* and *B*, respectively. Here, the mass fraction of GA was held constant at 0.175 g GA/g SBO; $\rho_{s,GA}$ was found to be approximately 1.36 $g \cdot mL^{-1}$; with $\rho_{s,SBO}$=0.92 $g \cdot mL^{-1}$.

Emulsion viscosity was modeled after the expression presented in Sibree (1930) and Broughton and Squires (1937) where the approximation factor, *h*, was fitted for the particular emulsion.

$$\mu_e = \frac{\mu_0}{1-(h \cdot C \cdot \frac{\rho_e}{\rho_{DP}})^{1/3}} \quad (3.4)$$

Where: ρ_e and μ_e are the emulsion density [$g \cdot mL^{-1}$] and viscosity [mPa·s], respectively; μ_0 is the fluid viscosity when no dispersed phase is present (μ_0 =0.954 mPa·s (i.e., properties of water at 22 °C)).

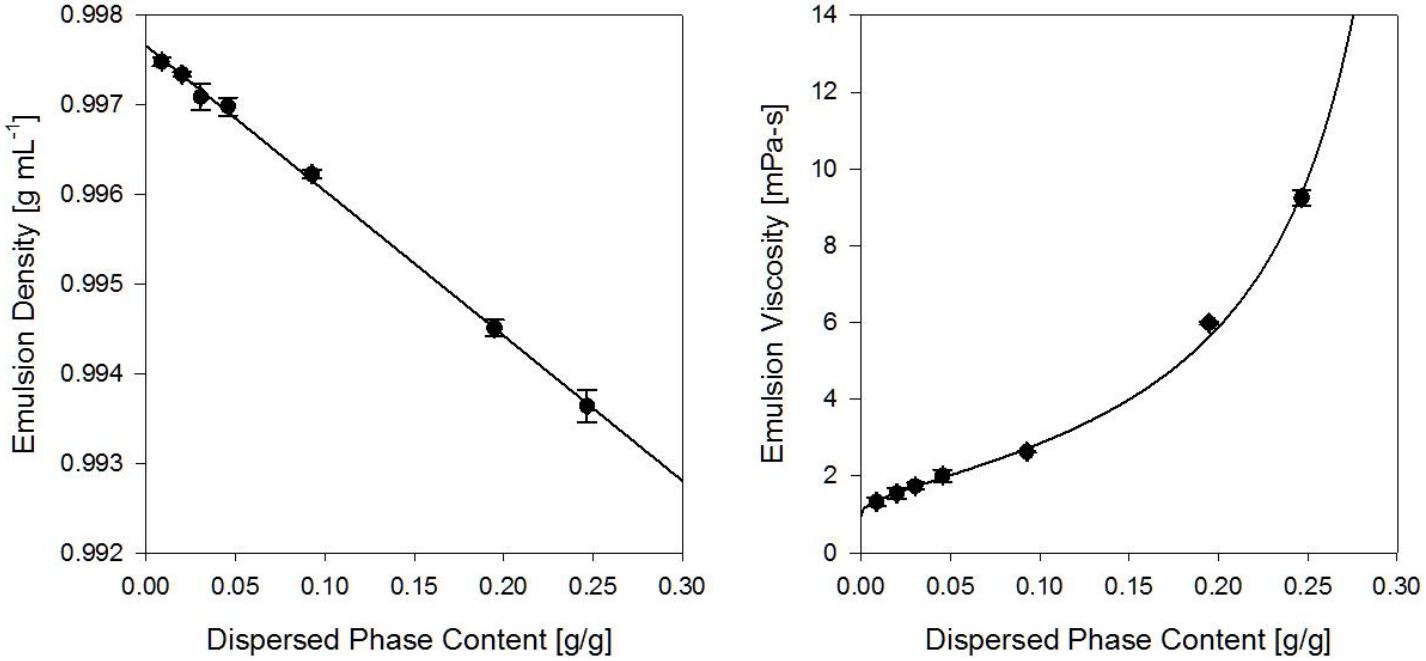

Figure 3.2: Emulsion density (left) and viscosity (right) as a function of the dispersed phase content at 22°C. Circles represent measured values (error bars indicate standard deviation); and lines represent fitted models. Emulsion composition: 2.5% Gum Arabic (wt % in total emulsion); with varying soybean contents and the remainder as MilliQ water.

The expression for emulsion density (model line in Figure 3.2) was described by the following equation (R^2=0.999):

$$\rho_e = -0.0162 \cdot C + 0.9977 \qquad (3.5)$$

And emulsion viscosity by the following equation (R^2=0.997):

$$\mu_e = \frac{\mu_0}{1-(2.85 \cdot C \cdot \frac{\rho_e}{\rho_{DP}})^{1/3}} \qquad (3.6)$$

Given the density and viscosity results, 20% oil content emulsion was deemed to have optimal physical properties for subsurface remediation. Thus the majority of further investigations into emulsion properties were completed at 20% oil content. Selected emulsion properties are shown for in Table 3.4.

Table 3.4: Properties of particle-containing oil-in-water emulsions for emulsions with 20% oil content.

Emulsion Composition	**Density [g·mL^{-1}]**	**Viscosity [cP]**	**Measured Zeta Potential [mV]**	**Equilibrium pH**
0.02% MgO 20% SBO 3.5% GA	0.995±2.27e^{-3}	8.96±0.14	-31.43±1.01	10.5
0.02% $CaCO_3$ 20% SBO 3.5% GA			-32.79±0.90	9.8
No Particle 20% SBO 3.5% GA			-34.82±0.78	4.5

± indicate standard deviation

3.5 CONCLUSIONS

Kinetic stability of the oil-in-water emulsion indicated that a wide range emulsion compositions (i.e., all tested emulsion formulations) were kinetically stable for greater than 20 hours, giving sufficient time for injection into the subsurface for remedial activities. Emulsion viscosity was determined to be a function of oil content. Oil content can be altered if a lower viscosity is needed for successful aquifer injection and effective amendment distribution. A 20% oil content emulsion was selected for future experimentation because: emulsion density is near that of water; the emulsion viscosity is manageable for subsurface injection; and emulsion viscosity seems to be a linear related to oil content when less than 20%, permitting extrapolation where required.

Chapter 4: Influence of Water Saturation on Solute Transport and Mixing

4.1 ABSTRACT

Quantification of dispersive mixing is critically important to characterizing and predicting reactive transport behavior in porous media. Dispersion is often estimated by fitting a transport model to data collected from a non-reactive, conservative tracer test. While this approach may provide quality estimates, the estimate is specific to the site, soil, or experimental conditions in which the test occurred. The goal of this research was to ascertain if dispersion occurring under both fully and partially water saturated conditions could be correlated to easily obtainable properties of a porous medium. The data set employed in this research was assembled by considering available data related to Fickian dispersion in sandy porous media. Results suggest that predictors such as median grain size, uniformity index, porosity, and water saturation can be used to provide meaningful predictions of dispersivity under a set of limiting conditions (water saturation > 0.4 and transport length < 100 cm). Model performance was increased by linking dispersivity in partially saturated media to those values obtained for the same medium but under fully water saturated conditions. The resulting simple dispersivity model may have utility for systems with transient water saturation, such as those experienced during infiltration and irrigation

events, chemical or biological reactions occurring within porous media, NAPL source depletion, and delivery of foams and emulsions used in site remediation.

4.2 INTRODUCTION

The magnitude of dispersive mixing can be critically important when describing or engineering the physical, chemical and biological processes affecting solutes in the subsurface (e.g., Vanderborght and Vereecken, 2007; Jimenez-Martinez et al., 2015). In partially saturated porous media, many studies report a change in the extent of dispersive mixing due to the presence of a second fluid (i.e., air or non-aqueous phase liquid (NAPL)). However, these changes are rarely well predicted, and more often than not, studies examining reactive processes occurring in partially or variably saturated media either neglect the phenomena all together or employ system-specific fits of longitudinal hydrodynamic dispersion (D_h). Our interest in quantifying the effects of saturation on hydrodynamic dispersion stems from the use of oil-in-water emulsions to deliver and release remediation amendments (e.g., Borden, 2007; Long and Borden, 2006; Berge and Ramsburg, 2008; Long and Ramsburg, 2011; Muller et al., 2015). Here, the delivery of the amendment (or a carrier phase) can influence dispersive mixing. While similar physics occur during infiltration and source-zone remediation, there is no uniform approach to describe these changes in mixing. Consequently, less is understood about the implications of changes in water saturation on solute interactions and reactions occurring in porous media.

In fully saturated systems, D_h is assumed to be proportional to magnitude of the pore water velocity (v_i) with the coefficient of proportionality termed the dispersivity (α) (e.g. Scheidegger, 1960; Bear, 1961; Bear, 1972) Many studies suggest a functional form of $D_h \propto v_i^{\beta}$ with $1 \leq \beta \leq 2$ (e.g., Bear, 1972; Scheidegger, 1961; Legatski and Katz, 1967; Yule and Gardner, 1978; Freeze and Cherry, 1979; Fattah and Hoopes, 1985; Sahimi et al., 1986; Blackwell et al., 1962).

While the dependence of D_h on v_i, remains open to study (De Smedt et al., 1986; De Smedt and Wierenga, 1979; Sahimi et al., 1986; Hassanizadeh, 1996; Maraqa et al., 1997; Padilla et al., 1999; Lee et al., 2000) there is arguably less known about how properties of a porous medium influence α. Dispersion has been linked to grain size, with some postulating a direct relationship between α and median grain size (d_{50}) (e.g., Perkins and Johnson, 1963; Fried and Combarnous, 1971) (example correlations shown in Table 4.1), notwithstanding the observation of scale dependent dispersivities (Gelhar et al., 1992). By and large, dispersivity remains a property that is determined for each specific study by fitting the transport equation to non-reactive, conservative tracer test data.

Table 4.1: Literature models for dispersivity.

	Source	Notes
Fully Saturated Systems		
$\alpha = c_1 \cdot d_{50}$ $c_1 = 1.75^a$	[a]Perkins and Johnston (1963); Fried and Combarnous (1971)	
Air-Water Systems		
$\alpha = -a \cdot \theta_w + b$	Maciejewski (1993)	a=0.197 cm; b=0.087cm for sandy soil
$\alpha = \frac{a \cdot L}{2} \cdot \theta_w^{\ b}$	Nützmann et al. (2002)	For coarse-textured sands: a=0.00431133; b=-2.25046 For glass beads: a=0.00395; b=-2.89689
$\alpha = \frac{d_{50}}{Pe} = \frac{d_{50}}{a \cdot S_r^{\ b}}$	Sato et al. (2003)	*a* and *b* are textual parameters as defined by: $a = \frac{d_{50}}{\alpha_{Sw=1}} = \frac{d_{50}}{6.0(\frac{\alpha^*}{n^*}) + 0.015}$ (Sato et al., 2003) correlation to van Genuchten (1980a) textural parameters $S_r = \frac{1}{[1+(\alpha^* h)^{n^*}]^{1-\frac{1}{n^*}}}$
$\alpha_{unsat} \approx 4 \cdot \alpha_{sat}$	Szenknect et al. (2008)	
NAPL-Water Systems		
No models found		

Entrapped and mobile non-aqueous phase liquids are noted to alter transport properties including α, which has been found to increase with decreasing S_w (Pennell et al., 1993; Pennell et al., 1994; Rogers and Logan, 2000; Zhang, et al., 2014). While the NAPL saturations in many of these studies remained low (entrapped saturations that generally produce S_w>0.8), large increases in α have been observed. Entrapped saturations commonly result in values of α that are twice that quantified for the same medium when completely water saturated (i.e., comparison between tracer test conducted before and after NAPL entrapment). Still, little research has been conducted to understand the relationship between S_w and α in NAPL-water systems. Zhang et al. (2014) examined diesel fuel and engine oil ($0.6 \leq S_w \leq 1.0$) and found that the magnitude of increase in α depended on the type of non-aqueous phase. Though the reason for the difference between the results using diesel fuel and engine oil is unclear, Zhang et al. (2014) reported that the spatial non-uniformity of saturation increased with increasing NAPL saturation. Spatially variable water content suggests that some regions of the porous medium may contribute areas of greater mixing than the overall saturation (or average) saturation would otherwise suggest. The results from Zhang et al. (2014) also suggest that fluid type influences dispersion through the pore-scale NAPL architecture. Effective globule size has been linked to medium and fluid properties, though most typically with d_{50}, uniformity index (U_i), volumetric water content (θ_w) and maximum-entrapped NAPL saturation (e.g., Brusseau et al., 2009; Ramsburg et al., 2011).

Considerably more work has been directed at understanding the influence of θ_w on D_h (and α) within the context of partially saturated air-water systems (e.g., Nielsen and Biggar, 1962; De Smedt and Wierenga, 1984; De Smedt et al., 1986; Conca and Wright, 1992; Maciegewski, 1993; Maraqa et al., 1997; Padilla et al., 1999; Vanderborght and Vereecken, 2007). Many properties have been correlated with dispersion in unsaturated systems including: grain size, water content, water saturation, porosity, angularity or roughness of grains, uniformity index, and the parameters from the van Genuchten model (van Genuchten, 1980a) (e.g., Klotz and Moser, 1974; Haga et al., 1999; Padilla et al., 1999; Sato et al., 2003; Toride et al., 2003). Findings from these investigations suggest that α is a property of both the porous media and S_w, but there is less agreement on what properties best describe the portion of α ascribed to the porous medium. What is somewhat better articulated through these studies is a power law dependence of α on S_w (Haga et al., 1999; Padilla et al., 1999; Nützmann et al., 2002; Sato et al., 2003). Studies employing a power-law model at $S_w > 0.4$ generally resolve the exponent between 1 and 2. Still, it is important to note that there is not universal agreement on this concept as non-monotonic relationships between S_w (or θ_w) and α have been observed (Haga et al., 1999; Toride et al., 2003; Raoff and Hassanizadeh, 2013).

To date, studies that aimed to develop or parameterize descriptions of α have focused on a limited number of experimental results, usually in air-water systems. In many cases results are compared to data presented in a selected

number of other studies, with data obtained from packed columns. The objective of this study is to explore the utility of polyparameter models to describe α. To do this, we aggregate and assess available data related to dispersion in columns containing homogenous packings of porous media. Relationships are then explored for fully and partially water saturated media separately, as well as in combination, with the goal of establishing a predictive capability for dispersive mixing that can be applied to describe porous media undergoing spatial or temporal changes in water content.

4.3. METHODS

4.3.1 ESTABLISHMENT OF THE DATASET

The dataset used herein is compiled from studies available in the peer reviewed literature. The dataset comprises both fully and partially saturated experiments. Partially saturated data encompass air-water and NAPL-water systems. All studies included quantify dispersive mixing by fitting the hydrodynamic dispersion coefficient (D_h), Peclet number (Pe), or α to the advection-dispersion equation (ADE) (Equation 4.1). Use of the ADE implies Fickian transport behavior.

$$\frac{\partial C}{\partial t} = D_h \frac{\partial^2 C}{\partial x^2} - v_i \frac{\partial C}{\partial x} \qquad (4.1)$$

Where: D_h is the hydrodynamic dispersion coefficient [$L^2 \cdot T^{-1}$] and v_i is the pore water velocity [$L \cdot T^{-1}$].

The overall hydrodynamic dispersion (D_h) is defined as the sum of molecular diffusion and mechanical dispersion (Equation 4.2)

$$D_h = D_{eff} + D_{mech} \qquad (4.2)$$

Where effective molecular diffusion is described as:

$$D_{eff} = D_{ab}\tau \qquad (4.3)$$

Here, tortuosity (τ) was calculated using the Millington and Quirk (1961) expression:

$$\tau = \frac{\theta_w^{7/3}}{(n \cdot S_w)^2} \qquad (4.4)$$

and mechanical dispersion as:

$$D_{mech} = \alpha \cdot v_i^{\beta} \qquad (4.5)$$

Often the overall dispersion is simplified to $D_h = \alpha \cdot v$ as the β coefficient is set to 1. Under these assumptions some authors will fit the Peclet number directly:

$$Pe = \frac{v_i \cdot L}{D_h} \qquad (4.6)$$

With: L= characteristic length [L] (typically column length is used as L).

To ensure consistency between studies, reported values of D_h or Pe were converted to values of α using:

$$\alpha = \frac{(D_h - D_{eff})}{v_i} \qquad (4.7)$$

Study selection was limited to laboratory scale (L<100 cm) column experiments using mainly sandy porous media (i.e., glass bead experiments were excluded). In addition, the following properties were required through either

direct reporting or inclusion of data that enabled calculation: pore water velocity (v_i), water saturation (S_w), volumetric water content (θ_w), mean grain size diameter (d_{50}), porosity (n), uniformity index (U_i), column length (L), hydrodynamic dispersion coefficient (D_h) and dispersivity (α). The resulting data set comprised a total of 133 experiments, 63 of which were conducted under fully saturated conditions and 70 under partially saturated conditions. The data set established in this study is shown in Table 4.2. The type of fit used in each study is coded to correspond to classes shown in Table 4.3. Table 4.4 provides a summary of the data used for the analysis.

Table 4.2: Description of data set.

Fully saturated Sw=1

Experimental Study	**Fit Type/ Fit Method**	**Tracer**	**Porous Media**	**Column Length**	**Inner Diameter**	**Darcy Velocity**	**Porewater Velocity**	**Peclet Number**	**Porosity**	**Median grain size**	**Uniformity Index**	**Volumetric Water Content**	**Water Saturation**	**Tortuosity**	**Hydrodynamic Dispersion Coefficient**	**Diffusion Contribution**	**Dispersivity**
				L	d	q	v_i	Pe	n	d_{50}	U_i	θ_w	S_w	τ	D_h	D_{eff}/D_h	α
				[cm]	[cm]	[cm·min^{-1}]	[cm·min^{-1}]	[-]	[-]	[cm]	[-]	[-]	[-]	[-]	[cm^2·min^{-1}]		[cm]
Padilla, et al. (1999)	A/†	Cl	Silica Sand	25	4.8	0.06	0.13	761.9	0.45	0.025	1.25	0.45	1.00	0.77	0.004	16%	0.03
						0.06	0.13	750.0	0.45	0.025	1.25	0.45	1.00	0.77	0.004	16%	0.03
						0.01	0.03	589.3	0.45	0.025	1.25	0.45	1.00	0.77	0.001	49%	0.04
Pennell et al. (1993)	B/*	$^3H_20$	20-30	6.5	4.8	0.08	0.25	106.6	0.32	0.071	1.16	0.32	1.00	0.69	0.015	6%	0.06
				6.4		0.08	0.25	105.8	0.33	0.071	1.16	0.33	1.00	0.69	0.015	6%	0.06
Pennell et al. (1994)	B/*	$^3H_20$	20-30	10.6	4.8	0.06	0.17	364.8	0.34	0.071	1.16	0.34	1.00	0.69	0.005	20%	0.03
			40-120	10.4		0.05	0.14	578.9	0.37	0.016	1.36	0.37	1.00	0.71	0.002	40%	0.02
			F-95	12.2		0.05	0.14	169.4	0.36	0.018	1.46	0.36	1.00	0.71	0.010	10%	0.07
Taylor (1999)	B/†	I	20-30	10.5	4.8	0.11	0.32	388.9	0.34	0.071	1.16	0.34	1.00	0.70	0.009	10%	0.03
				10.5		0.11	0.31	250.0	0.35	0.071	1.16	0.35	1.00	0.70	0.013	7%	0.04
				10.2		0.11	0.32	340.0	0.35	0.071	1.16	0.35	1.00	0.70	0.010	9%	0.03
				10.4		0.11	0.32	288.9	0.35	0.071	1.16	0.35	1.00	0.70	0.011	8%	0.04
		Br		10.2		0.06	0.16	178.0	0.35	0.071	1.16	0.35	1.00	0.71	0.009	11%	0.06
				9.8		0.06	0.16	237.9	0.35	0.071	1.16	0.35	1.00	0.70	0.007	15%	0.04
				8.6		0.06	0.16	137.8	0.35	0.071	1.16	0.35	1.00	0.70	0.010	10%	0.06
				9.2		0.06	0.17	135.5	0.33	0.071	1.16	0.33	1.00	0.69	0.012	8%	0.07
				9.3		0.06	0.16	105.0	0.34	0.071	1.16	0.34	1.00	0.70	0.014	7%	0.09

Table 4.2 Cont. Fully saturated S_w=1

Study	*Fit*	*Tracer*	*Porous Media*	*L*	*d*	*q*	v_i	*Pe*	*n*	d_{50}	U_i	θ_w	S_w	τ	D_h	D_{eff}/D_h	α
Taylor et al. (2001)	B/†	I	20-30	10.2	4.8	0.05	0.16	364.3	0.34	0.071	1.16	0.34	1.00	0.70	0.004	19%	0.03
				9.6		0.14	0.39	309.7	0.35	0.071	1.16	0.35	1.00	0.70	0.012	7%	0.03
				9.9		0.01	0.04	341.4	0.35	0.071	1.16	0.35	1.00	0.70	0.001	75%	0.03
				10		0.07	0.20	243.9	0.34	0.071	1.16	0.34	1.00	0.70	0.008	10%	0.04
				10		0.08	0.24	277.8	0.35	0.071	1.16	0.35	1.00	0.70	0.008	10%	0.04
Taylor et al. (2004)	B/†	I	20-30	10.3	4.8	0.05	0.16	367.9	0.35	0.071	1.16	0.35	1.00	0.70	0.004	19%	0.03
				10		0.14	0.40	303.0	0.34	0.071	1.16	0.34	1.00	0.70	0.013	7%	0.03
				9.7		0.01	0.04	269.4	0.34	0.071	1.16	0.34	1.00	0.70	0.001	60%	0.04
				9.7		0.08	0.22	277.1	0.34	0.071	1.16	0.34	1.00	0.70	0.008	11%	0.04
				10.0		0.01	0.04	250.0	0.35	0.071	1.16	0.35	1.00	0.70	0.002	56%	0.04
				10.1		0.14	0.40	280.6	0.34	0.071	1.16	0.34	1.00	0.70	0.014	6%	0.04
				10.4		0.06	0.16	297.1	0.35	0.071	1.16	0.35	1.00	0.70	0.006	16%	0.04
				9.8		0.14	0.40	264.9	0.34	0.071	1.16	0.34	1.00	0.70	0.015	6%	0.04
				9.9		0.06	0.16	253.8	0.35	0.071	1.16	0.35	1.00	0.70	0.006	14%	0.04
				10.2		0.01	0.04	291.4	0.34	0.071	1.16	0.34	1.00	0.70	0.001	62%	0.04
Berge and Ramsburg (2009)	B/NR	Br	FF	11.6	4.8	0.03	0.08	127.5	0.36	0.031	1.65	0.36	1.00	0.71	0.007	14%	0.09
				11.0		0.03	0.08	203.7	0.37	0.031	1.65	0.37	1.00	0.72	0.004	24%	0.05
			F-95	9.8		0.03	0.08	65.3	0.37	0.018	1.46	0.37	1.00	0.72	0.011	9%	0.15
				11.8		0.03	0.08	176.1	0.37	0.018	1.46	0.37	1.00	0.72	0.005	20%	0.07
Wang (2009)	B/†	Br	20-30	15.0	2.5	0.07	0.20	272.7	0.35	0.071	1.16	0.35	1.00	0.70	0.011	9%	0.06
						0.56	1.61	234.4	0.35	0.071	1.16	0.35	1.00	0.70	0.103	1%	0.06
			40-50			0.07	0.19	263.2	0.37	0.036	1.20	0.37	1.00	0.71	0.011	9%	0.06
						0.56	1.52	234.4	0.37	0.036	1.20	0.37	1.00	0.71	0.097	1%	0.06
			80-100			0.07	0.18	223.9	0.39	0.016	1.09	0.39	1.00	0.73	0.012	8%	0.07
						0.56	1.42	238.1	0.39	0.016	1.09	0.39	1.00	0.73	0.090	1%	0.06
			100-140			0.07	0.18	288.5	0.39	0.013	1.20	0.40	1.00	0.76	0.009	11%	0.05
						0.56	1.39	230.8	0.4	0.013	1.20	0.40	1.00	0.73	0.090	1%	0.07
Zhang, et al. (2014)	B/*	Cl	Silty Sand	30.0	5	0.04	0.12	263.2	0.35	0.010	5.31	0.35	1.00	0.70	0.014	7%	0.11
Taghavy et al. (2013)	B/†	Br	40-50	16.0	2.55	0.071	0.20	243.0	0.36	0.036	1.20	0.36	1.00	0.71	0.013	8%	0.07
				12.0	2.7	0.063	0.18	175.0	0.36	0.036	1.20	0.36	1.00	0.71	0.012	8%	0.07
				12.1	2.7	0.065	0.18	185.0	0.37	0.036	1.20	0.37	1.00	0.72	0.011	9%	0.07
				16.0	2.55	0.072	0.20	160.0	0.37	0.036	1.20	0.37	1.00	0.72	0.020	5%	0.10

Table 4.2 *Cont. Fully saturated S_w=1*

Study	*Fit*	*Tracer*	*Porous Media*	*L*	*d*	*q*	v_i	*Pe*	*n*	d_{50}	U_i	θ_w	S_w	τ	D_h	D_{eff}/D_h	α
Maraqa et al. (1997)	A/†	$^3H_20$	Oakville A Horizon	30.2	5.45	0.215	0.53	45.7	*0.41*	0.031	2.68	0.41	1.00	0.74	0.348	0%	0.66
				30.2		0.043	0.11	35.4	*0.41*	0.031	2.68	0.41	1.00	0.74	0.090	0%	0.85
				30.2		0.004	0.01	85.1	*0.41*	0.031	2.68	0.41	1.00	0.74	0.004	11%	0.35
			Pipestone B Horizon	30.2		0.214	0.56	54.0	0.38	0.031	2.68	0.38	1.00	0.73	0.313	0%	0.56
				30.2		0.043	0.11	70.0	0.38	0.031	2.68	0.38	1.00	0.73	0.048	1%	0.43
				30.2		0.004	0.01	127.3	0.38	0.031	2.68	0.38	1.00	0.73	0.003	16%	0.24
			Oakville B Horizon	30.2		0.215	0.61	61.1	0.35	0.031	2.68	0.35	1.00	0.71	0.301	0%	0.49
				30.2		0.043	0.12	67.2	0.35	0.031	2.68	0.35	1.00	0.71	0.055	1%	0.45
				30.2		0.004	0.01	108.6	0.35	0.031	2.68	0.35	1.00	0.71	0.003	12%	0.28
Muller	B/°	Br	FF	10.4	4.8	0.03	0.09	185.0	0.38	0.031	1.65	0.38	1.00	0.72	0.005	19%	0.06
			FF	10.2		0.04	0.10	186.0	0.37	0.031	1.65	0.37	1.00	0.72	0.006	18%	0.06
			20-30	10.4		0.07	0.20	187.0	0.36	0.071	1.16	0.36	1.00	0.71	0.011	9%	0.06
			FF	10.5		0.06	0.15	188.0	0.37	0.031	1.65	0.37	1.00	0.72	0.008	12%	0.06
			60-80	10.2		0.05	0.13	189.0	0.41	0.021	1.10	0.41	1.00	0.74	0.007	15%	0.05

Table 4.2 Cont. *Partially saturated $S_w \neq 1$*

Study	*Fit*	*Second Fluid*	*Tracer*	*Porous Media*	*L*	*d*	*q*	v_i	*Pe*	*n*	d_{50}	U_i	θ_w	S_w	τ	D_h	D_{eff}/D_h	α
Padilla, et al. (1999)	A/†	AIR	Cl	Silica Sand	25.0	4.8	0.06	0.18	167.3	0.45	0.025	1.25	0.31	0.69	0.32	0.028	1%	0.15
							0.06	0.19	167.3	0.45	0.025	1.25	0.31	0.69	0.32	0.028	1%	0.15
							0.06	0.18	171.7	0.45	0.025	1.25	0.32	0.71	0.35	0.027	1%	0.14
							0.04	0.21	50.9	0.45	0.025	1.25	0.20	0.44	0.12	0.105	0%	0.49
							0.03	0.16	50.1	0.45	0.025	1.25	0.18	0.40	0.09	0.082	0%	0.50
							0.02	0.11	53.3	0.45	0.025	1.25	0.16	0.36	0.07	0.050	0%	0.47
							0.01	0.08	51.9	0.45	0.025	1.25	0.15	0.33	0.06	0.038	0%	0.48
							0.03	0.15	62.4	0.45	0.025	1.25	0.19	0.42	0.10	0.061	0%	0.40
							0.05	0.21	123.8	0.45	0.025	1.25	0.24	0.53	0.18	0.042	0%	0.20
							0.04	0.20	110.6	0.45	0.025	1.25	0.22	0.49	0.14	0.044	0%	0.23
							0.02	0.10	85.1	0.45	0.025	1.25	0.18	0.40	0.09	0.028	0%	0.29
							0.06	0.21	147.9	0.45	0.025	1.25	0.27	0.60	0.23	0.036	1%	0.17
							0.05	0.20	92.0	0.45	0.025	1.25	0.25	0.56	0.19	0.055	0%	0.27
Sato et al. (2003)	G/¤	AIR	Cl	Toyoura Sand	12.0	5.0	0.04	0.33	29.9	0.38	0.017	1.60	0.12	0.32	0.05	0.131	0%	0.40
							0.04	0.38	34.8	0.38	0.017	1.60	0.12	0.31	0.05	0.131	0%	0.34
							0.05	0.51	30.2	0.38	0.017	1.60	0.10	0.26	0.03	0.201	0%	0.40
							0.07	0.59	28.0	0.38	0.017	1.60	0.11	0.31	0.05	0.251	0%	0.43
							0.02	0.11	52.1	0.38	0.017	1.60	0.16	0.44	0.11	0.025	1%	0.23
							0.10	0.53	42.2	0.38	0.017	1.60	0.18	0.49	0.14	0.151	0%	0.28
							0.12	0.73	43.8	0.38	0.017	1.60	0.16	0.43	0.10	0.201	0%	0.27
							0.14	0.74	51.6	0.38	0.017	1.60	0.19	0.50	0.14	0.171	0%	0.23
							0.08	0.30	88.1	0.38	0.017	1.60	0.26	0.70	0.32	0.040	1%	0.13
							0.11	0.34	81.9	0.38	0.017	1.60	0.31	0.82	0.46	0.050	1%	0.14
							0.13	0.44	58.5	0.38	0.017	1.60	0.29	0.78	0.40	0.090	1%	0.20
							0.13	0.48	95.3	0.38	0.017	1.60	0.27	0.73	0.34	0.061	1%	0.12
							0.18	0.56	216.4	0.38	0.017	1.60	0.33	0.88	0.54	0.031	2%	0.05
							0.21	0.65	110.8	0.38	0.017	1.60	0.32	0.85	0.49	0.071	1%	0.11
							0.24	0.77	101.4	0.38	0.017	1.60	0.31	0.82	0.45	0.091	1%	0.12
Pennell et al. (1993)	B/*	Dodecane	$^3H_20$	20-30	6.5	4.8	0.08	0.29	42.2	0.32	0.071	1.16	0.26	0.80	0.40	0.045	1%	0.15
					6.4		0.08	0.28	45.7	0.33	0.071	1.16	0.27	0.84	0.46	0.038	2%	0.14
					6.4		0.08	0.29	56.4	0.32	0.071	1.16	0.26	0.80	0.41	0.033	2%	0.11

Table 4.2 Cont. *partially saturated $S_w \neq 1$*

Study	*Fit*	*Second Fluid*	*Tracer*	*Porous Media*	*L*	*d*	*q*	v_i	*Pe*	*n*	d_{50}	U_i	θ_w	S_w	τ	D_h	D_{eff}/D_h	α
Taylor et al. (1999)	B/†	Dodecane	Br	20-30	10.2	4.8	0.05	0.15	107.9	0.35	0.071	1.16	0.30	0.85	0.48	0.015	5%	0.09
					9.8		0.05	0.16	74.1	0.35	0.071	1.16	0.30	0.85	0.48	0.021	3%	0.13
					8.6		0.05	0.16	100.0	0.35	0.071	1.16	0.31	0.89	0.54	0.014	5%	0.08
Ervin et al. (2011)	B/†	TCE	Br	45-50	5.0	4.8	0.10	0.32	15.6	0.39	0.033	1.09	0.32	0.83	0.48	0.102	1%	0.32
					4.9		0.03	0.09	32.7	0.39	0.033	1.09	0.34	0.87	0.53	0.014	5%	0.14
Pennell et al. (1994)	B/*	PCE	$^3H_20$	20-30	10.6	4.8	0.06	0.20	160.3	0.34	0.071	1.16	0.28	0.85	0.47	0.013	5%	0.06
				40-120	10.4		0.06	0.18	306.5	0.37	0.016	1.36	0.32	0.87	0.51	0.006	12%	0.03
				F-95	12.2		0.06	0.19	86.5	0.36	0.018	1.46	0.30	0.82	0.45	0.026	2%	0.14
Taylor (1999)	B/†	PCE	I	20-30	5.2	4.8	0.06	0.21	25.7	0.36	0.071	1.16	0.26	0.72	0.33	0.043	1%	0.20
					10.5		0.11	0.42	121.0	0.34	0.071	1.16	0.26	0.77	0.38	0.036	1%	0.09
					10.5		0.11	0.34	224.8	0.35	0.071	1.16	0.32	0.91	0.57	0.016	4%	0.04
					10.2		0.11	0.36	204.0	0.35	0.071	1.16	0.31	0.89	0.53	0.018	4%	0.05
					10.4		0.11	0.37	150.9	0.35	0.071	1.16	0.30	0.87	0.50	0.025	2%	0.07
Taylor et al. (2001)	B/†	PCE	I	20-30	10.2	4.8	0.05	0.18	268.4	0.34	0.071	1.16	0.30	0.89	0.53	0.007	10%	0.03
					9.6		0.14	0.43	168.4	0.35	0.071	1.16	0.32	0.90	0.56	0.025	3%	0.06
					9.9		0.01	0.05	183.3	0.35	0.071	1.16	0.30	0.86	0.50	0.002	25%	0.04
					10.0		0.07	0.22	155.8	0.34	0.071	1.16	0.30	0.89	0.54	0.014	5%	0.06
					10.0		0.08	0.26	153.8	0.35	0.071	1.16	0.31	0.89	0.54	0.017	4%	0.06
Taylor et al. (2004)	B/†	PCE	I	20-30	10.3	4.8	0.05	0.18	251.2	0.35	0.071	1.16	0.31	0.89	0.54	0.007	9%	0.04
					10.0		0.14	0.45	185.2	0.34	0.071	1.16	0.30	0.89	0.53	0.024	3%	0.05
					9.7		0.01	0.04	161.7	0.34	0.071	1.16	0.31	0.90	0.55	0.003	26%	0.04
					9.7		0.08	0.25	151.6	0.34	0.071	1.16	0.31	0.89	0.54	0.016	4%	0.06
					10.0		0.01	0.04	151.5	0.35	0.071	1.16	0.31	0.90	0.55	0.003	24%	0.05
					10.1		0.14	0.45	148.5	0.34	0.071	1.16	0.31	0.89	0.53	0.030	2%	0.07
					10.4		0.06	0.18	136.1	0.35	0.071	1.16	0.30	0.87	0.51	0.014	5%	0.07
					9.8		0.14	0.46	130.1	0.34	0.071	1.16	0.30	0.87	0.51	0.035	2%	0.07
					9.9		0.06	0.18	167.5	0.35	0.071	1.16	0.30	0.87	0.51	0.011	6%	0.06
					10.2		0.01	0.05	136.2	0.34	0.071	1.16	0.30	0.88	0.51	0.003	19%	0.06
Ramsburg et al. (2011)	B/†	PCE	Br	50-60	3.5	4.8	0.11	0.34	19.9	0.39	0.027	1.10	0.32	0.83	0.47	0.060	1%	0.17
				45-50	3.5		0.11	0.34	42.4	0.38	0.033	1.09	0.33	0.87	0.52	0.027	3%	0.08
				20-30	3.5		0.11	0.35	10.4	0.36	0.071	1.16	0.32	0.89	0.54	0.116	1%	0.33

Study	*Fit*	*Second Fluid*	*Tracer*	*Porous Media*	*L*	*d*	*q*	v_i	*Pe*	*n*	d_{50}	U_i	θ_w	S_w	τ	D_h	D_{eff}/D_h	α
Zhang, et al. (2014)	E/*	Diesel	Cl	Silty Sand	30.0	5.0	0.02	0.07	135.8	0.35	0.010	5.31	0.34	0.98	0.67	0.016	6%	0.21
							0.02	0.06	112.7	0.35	0.010	5.31	0.33	0.95	0.63	0.016	5%	0.25
							0.01	0.05	81.9	0.35	0.010	5.31	0.32	0.91	0.56	0.017	5%	0.35
		Engine oil					0.03	0.07	135.6	0.35	0.010	5.31	0.34	0.98	0.67	0.017	6%	0.21
							0.02	0.07	111.1	0.35	0.010	5.31	0.32	0.91	0.56	0.019	4%	0.26
							0.02	0.06	95.4	0.35	0.010	5.31	0.29	0.82	0.44	0.019	3%	0.30
							0.01	0.05	98.7	0.35	0.010	5.31	0.22	0.63	0.24	0.016	2%	0.30

Fit type codes are shown in Table 4.3.

†CXTFIT (Toride et al., 1995);°CFITM (van Genuchten, 1980b); ¤ Ogata and Banks (1961); *unspecified analytical solution

NR=Not Reported

D_a [cm^2 min^{-1}] for Cl=1.25e-3; Br=1.22e-3; I=1.23e-3 (Lide, 1999); $^3H_20$=1.38e-3 (Krynicki, et al., 1978)

Table 4.3: Types of fits in data set.

Code	Fitted Parameter	D_{eff} Included?	Values given for D_{eff}	calculated α	Re-calculated parameters?
A	D_h	Yes	$\tau_w = 0.85; D_w = 8 \cdot 10^{-3}$ cm^2 min^{-1}	$\alpha = \frac{(D_{h,r} - D_{eff,r})}{v_x}$	Yes*
A (Padilla)	D_h	Yes	$\tau_{sat} = 0.85;\ S_r = 0.17;$ $D_w = 8 \cdot 10^{-4}$ cm^2 min^{-1} $\tau_w = \tau_{sat} \frac{(S - S_r)}{(1 - S_r)}$	$\alpha = \frac{(D_{h,r} - D_{eff,r})}{v_x}$	Yes*
B	Pe	No	No	$\alpha_r = \frac{L}{Pe_r}$ $D_h = \alpha_r \cdot v_i$ $\alpha = \frac{(D_{h,r} - D_{eff,c})}{v_x}$	No
C	D_h	No	No	$\alpha = \frac{(D_{h,r} - D_{eff,c})}{v_x}$	No
D	α	unknown	No	$D_h = \alpha_r \cdot v_i$ $\alpha = \frac{(D_{h,r} - D_{eff,c})}{v_x}$	No
E	D_h	No	No	$D_h = \alpha_r \cdot v_i$ $\alpha = \frac{(D_{h,r} - D_{eff,c})}{v_x}$	No

Subscripts used with D_h & D_{eff}: r indicates that the value as reported in the literature; c indicates that the value was calculated.
*Millington and Quirk (1961) used to calculate tortuosity

When assessing the data, it became necessary to down-select for the purposes of assuring quality in the data set. Experiments in which: (i) high *Pe* introduced uncertainty into values of D_h or α; and/or (ii) the effective diffusion contributed appreciably to D_h, were excluded from the analysis. Two thresholds were employed for each of these criteria ($Pe < 300$ & $Pe < 200$, and $D_{eff}/D_h<25\%$ & $D_{eff}/D_h<10\%$), creating the 3x3 matrix shown in Table 4.4. The development of the *Pe* criteria is explained in more detail below. Final polyparameter models were produced by enforcing the strictest set of criteria (i.e., $Pe<200$ and $D_{eff}/D_h<10\%$). The influence of enforcing these criteria on the quantity of studies in the data set is shown in Table 4.4.

Table 4.4: Summary of number of data by type of study.

		All *Pe*	***Pe*<300**	***Pe*<200**
All D_{eff}/D_h	S_w=1	63	56	33
	S_w<1	70	70	64
	NAPL-water	42	41	37
	air-water	28	28	27
	total	133	126	97
D_{eff}/D_h<25%	S_w=1	57	51	31
	S_w<1	69	68	63
	NAPL-water	41	40	36
	air-water	28	28	27
	total	126	119	94
D_{eff}/D_h<10%	S_w=1	34	30	18
	S_w<1	64	64	59
	NAPL-water	36	36	32
	air-water	28	28	27
	total	98	94	77

4.3.2 Model Development and Evaluation

4.3.2.1 Predictor Selection

Selection of predictors for use in the polyparameter model development focused on identifying commonly reported properties of saturated and unsaturated porous media. Porosity, median grain diameter and uniformity index were selected as dispersivity has been linked to these routinely quantified properties of a medium (e.g., Perkins and Johnston, 1963; Fried and Combarnous, 1971; Menzie and Dutta, 1988). Water content was represented within the polyparameter models as either water saturation or volumetric water content. Tortuosity was included through the use of a tortuosity factor (Millington and Quirk 1961). The Millington and Quirk tortuosity factor is a non-linear combination of porosity and water saturation. Distributions of these properties, as well as *Pe*, D_h, α, and v_i are provided in Figure 4.1.

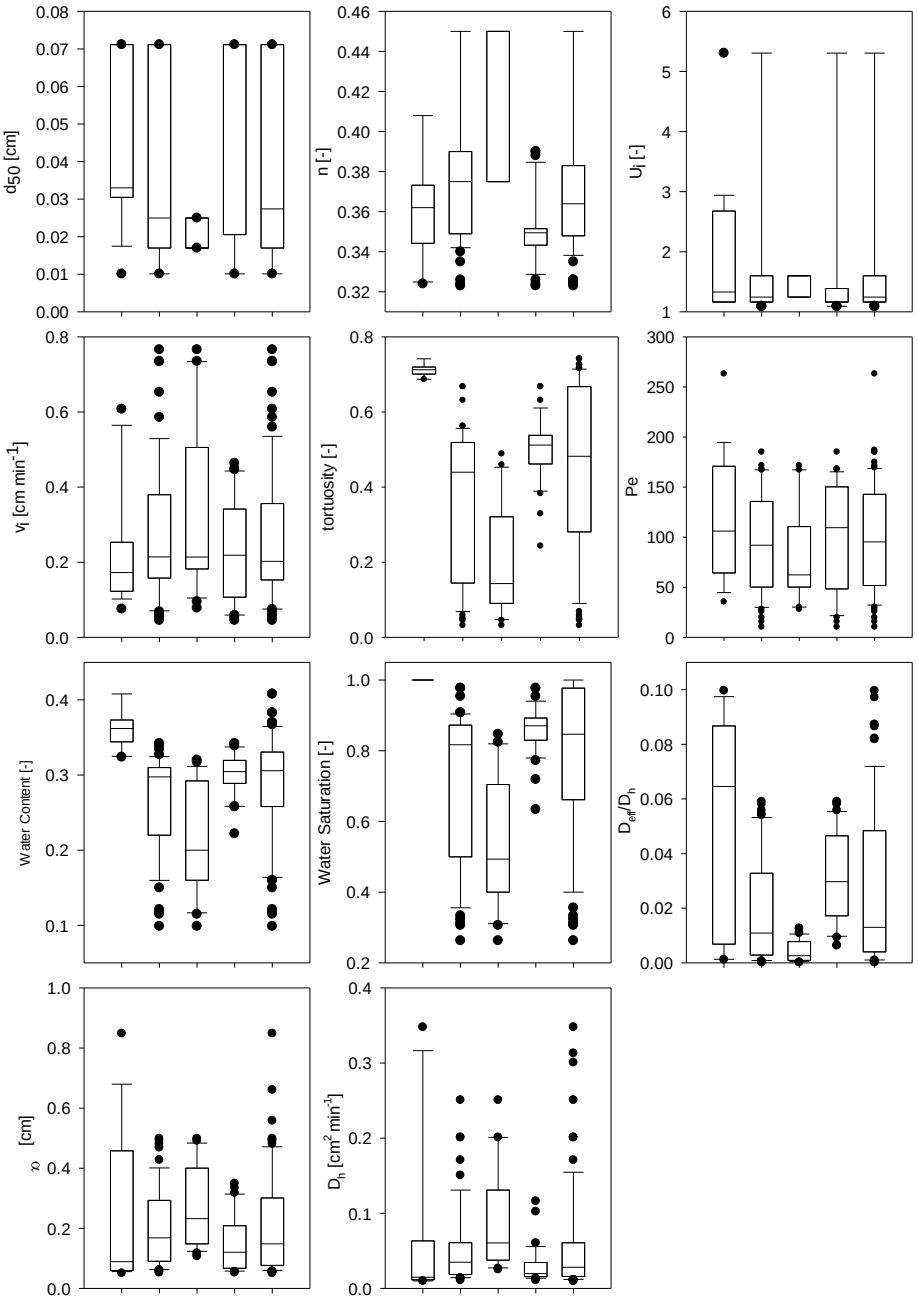

Figure 4.1: Distribution of properties in data set. Each panel shows (left to right): fully saturated (S_w=1); partially saturated (S_w<1); air-water systems; NAPL-water systems; and all data. Boxes denote the 25th and 75th percentiles. Median values are shown as the horizontal line within each box. 10th and 90th percentiles are shown with whiskers, and outliers noted by the filled circles.

4.3.2.2 Polyparameter Model Fitting

Polyparameter models were fit using MATLAB R2014a (The Mathworks, Natick, MA). The governing equation was linearized in order to capitalize on the robustness of the MATLAB linear fitting routine (*fitlm*) to minimize the sum squared errors. The resulting equation in its most general form (including all possible predictors) is shown in Equation 4.8.

$$\log(\hat{\alpha}) = a \cdot \log(d_{50}) + b \cdot \log(n) + c \cdot \log(U_i) + d \cdot \log(S_w) + e \cdot \log(\theta_w) + f \cdot \log(\tau) + \chi \quad (4.8)$$

Here $\hat{\alpha}$ is the modeled dispersivity and *a-f* are fitted model parameters. A model coefficient (χ) was also fit as the omission of this coefficient would imply that α can be entirely described by the predictor variables - a result that has limited physical meaning. Polyparameter models of increasing complexity were systematically developed by adding a new predictor until the addition of another predictor was not statistically significant (i.e., $p > 0.05$). Model residuals were checked for normality (Anderson-Darling test) and homoscedasticity (Breusch-Pagan test), and multicollinearity between predictors was evaluated (variance inflation factor).

4.3.3 Model Evaluation

The developed polyparameter models were evaluated on the basis of three goodness of fit metrics: sample size corrected Akaike information criterion (AICc); Nash-Sutcliffe model efficient coefficient (NSE), and the adjusted R^2 (adj-R^2). AICc was used to select models within the subset of data being

described by evaluating goodness of fit with penalties for additional fitting parameters (Equation 4.9) (Akaike, 1974).

$$AICc = \left[N \cdot \ln\left(\frac{SSE}{N}\right) + 2k \right] + \frac{2k(k+1)}{N-k-1} \qquad (4.9)$$

Where: N is the number of observations, SSE is the sum squared error, and k is the number of model parameters plus one. Note that the number of model parameters is the number of predictors plus one since χ is also fit. *NSE* was calculated as shown in Equation 4.10 (Nash and Sutcliffe, 1970)

$$NSE = 1 - \frac{\sum(\alpha_i - \hat{\alpha}_i)^2}{\sum(\alpha_i - \bar{\alpha})^2} \qquad (4.10)$$

Where: α is the observed dispersivity, $\hat{\alpha}$ is the modeled dispersivity and $\bar{\alpha}$ is the averaged observed dispersivity.

4.3.4 Transport Simulations

Transport of a one pore volume pulse of a nonreactive, conservative tracer was simulated using STANMOD v.2.07 (Simunek, et al., 2005), specifically the CFITM equilibrium transport code for a semi-finite system with a third type boundary condition (van Genuchten, 1980b). Simulations were conducted for $50 \leq Pe \leq 400$. To produce discretized, simulated data, effluent concentrations from the tracer simulations were averaged over a given sampling period. Sampling frequencies of 10 and 18 samples per pore volume were assessed. Fits of the transport equation to the synthetic data were conducted using CFTIM under the

same conditions as described above. Where noted below, experimental uncertainty was approximated by adding 2% Gaussian noise to the synthetic data.

4.4 RESULTS AND DISCUSSION

4.4.1 LENGTH SCALE

Studies have found longitudinal dispersion is a function of the length scale (e.g., de Jong, 1958; Saffman, 1959) especially on a field scale (e.g., Gelhar et al. 1992). Here, the focus was on mixing at the laboratory scale with datasets ranging from L=0.03 to 0.3 m. The complied dataset was checked for any length scale dependence. With this small range of lengths in the column experiment data used, no influence of length scale on dispersivity was found (Figure 4.2).

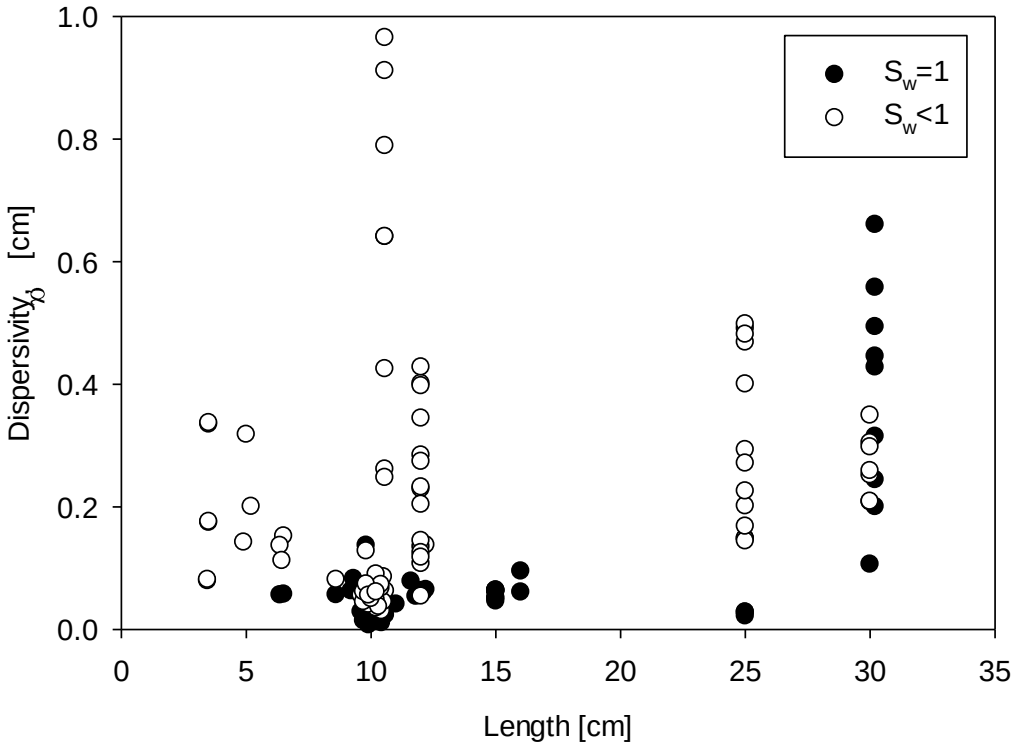

Figure 4.2: Dispersivity versus length scale for fully (S_w=1) and partially (S_w<1) saturated column experiments. Only studies with Pe<200 and D_{eff}/D_h<10% included.

4.4.2 Influence of Peclet Number on Estimation of Alpha

The reliability of α obtained through fitting of tracer breakthrough curves depends both on the quality and quantity of data, as well as the appropriateness of the transport model. This analysis is restricted to those studies for which the ADE was used to describe tracer transport through the porous medium. This restriction does not preclude utility of other descriptions of solute transport such as mobile-immobile (e.g., van Genuchten and Wierenga, 1976) or continuous time random walk (e.g., Cortis and Berkowitz, 2004) models; rather, it provides a uniform basis from which to examine a set of data.

Within the context of the ADE, *Pe* serves as the critical description of dispersive mixing. Effective measurement of dispersion in systems comprising a disproportionate amount of advection, however, can be difficult. For example, non-reactive, conservative tracer tests are routinely conducted through collection of 10-12 effluent samples per pore volume. The concentration of tracer in these samples was quantified and subsequently used to fit the ADE by adjusting a parameter that represents dispersive mixing (*Pe*, D_h or α). As *Pe* increases, this fitting approach is increasingly reliant upon just a few data points corresponding to the rise and fall of the breakthrough curve. Shown in Figure 4.3 are synthetic data which illustrate this point.

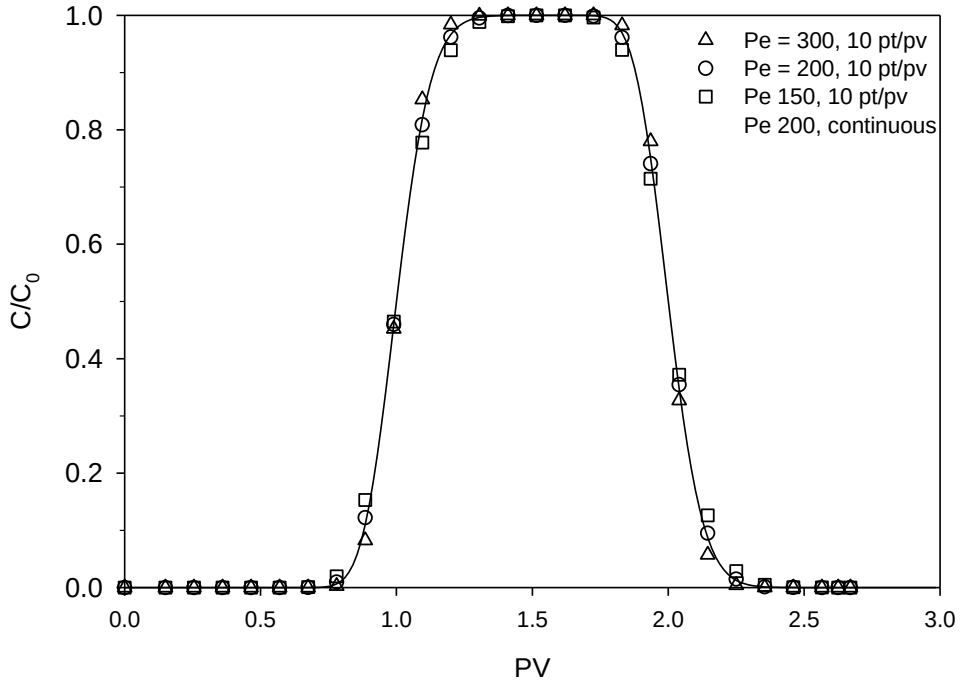

Figure 4.3: Influence of experimental sampling (i.e., discretization) on simulated tracer transport.

For each *Pe* the BTC was simulated and then discretized to 10 'observations' per pore volume by calculating the cumulative solute mass in the effluent over a sampling period and dividing by the cumulative phase volume in the effluent over that period. The tracer simulation for *Pe* = 200 is shown to illustrate the similarity in the data. These 'observations' are then used to produce estimates of *Pe* using CFTIM which where compared to the known values of *Pe* used in the original forward simulation. Results using a 10 sample per pore volume discretization suggest that the percent difference between fitted and known *Pe* scales linearly with *Pe* (slope = $(4.0\pm0.1) \times 10^{-2}$ for $Pe > 50$), and is approximately 8% at *Pe* = 200. Use of 18 samples per pore volume increases the accuracy of the fits by roughly a factor of three (Table 4.5) with percent difference versus *Pe* producing a slope of $(1.4\pm0.1) \times 10^{-2}$ (for $Pe > 50$).

Table 4.5: Uncertainty when fitting simulated data after discretization.

	fitted *Pe* (95% CI) percent difference with known	
	Discretized 10 pts/PV	**Discretized 18 pts/PV**
400	337.5 (334.1,340.9) 16%	378.5 (377.6,379.4) 5%
300	263.6 (261.3, 266.0) 12%	287.8 (287.2, 288.4) 4%
250	224.3 (222.4, 226.1) 10%	241.4 (241.0, 241.9) 3%
200	183.3 (181.9, 184.6) 8%	194.5 (194.2,194.8) 3%
150	140.4 (139.5, 141.3) 6%	146.9 (146.7,147.1) 2%
125	118.3 (117.5, 119.0) 5%	122.8 (122.7,123.0) 2%
100	96.0 (95.1, 96.2) 4%	98.6 (98.5, 98.7) 1%
50	48. 9 (48.7,49.1) 3%	49.7 (49.6,49.7) 1%

4.4.3 Fitting of Noisy Synthetic Data

Values of *Pe* and *Rf* fit to simulated breakthrough curve data were also analyzed to discern the influence of potential experimental or measurement error. 2% Gaussian noise was added to simulated data as to represent experimental or measurement error. Three scenarios were considered: (i) no noise (Table 4.5); (ii) 2% noise in dimensionless concentration (C/C_0) values; and (iii) 2% noise in both C/C_0 values and dimensionless time (PV). The influence of the added noise on the fitted values of *Pe* and R_f is shown in Table 4.6 for two sampling frequencies (10 and 18 samples/PV).

Table 4.6: Influence of 2% noise on fits obtained with discretized synthetic data.

Known *Pe*	Noise Added	fitted *Pe* (95% CI) fitted R_f (95% CI) Discretized 10 pts/PV	fitted *Pe* (95% CI) fitted R_f (95% CI) Discretized 18 pts/PV
400	None	337.5 (334.1,340.9) 1.00 (1.00, 1.00)	378.5 (377.6,379.4) 1.00 (1.00, 1.00)
	2% C/Co	311.8 (270.7, 352.9) 1.00 (1.00, 1.00)	395.5 (353.9,437.1) 1.00 (1.00, 1.00)
	2% PV & 2% C/Co	442.7 (305.1,580.4) 1.06 (1.06, 1.07)	327.2 (205.6, 448.8) 1.00 (0.99,1.01)
300	None	263.6 (261.3, 266.0) 1.00 (1.00, 1.00)	287.8 (287.2, 288.4) 1.00 (1.00, 1.00)
	2% C/Co	262.7 (245.3, 278.0) 1.00 (1.00, 1.00)	299.3 (279.7, 318.8) 1.00 (1.00, 1.00)
	2% PV & 2% C/Co	239.1 (203.9, 274.3) 1.01 (1.01, 1.02)	411.8 (316.2, 507.4) 1.01 (1.00, 1.01)
250	None	224.3 (222.4, 226.1) 1.00 (1.00, 1.00)	241.44 (241.0, 241.9) 1.00 (1.00, 1.00)
	2% C/Co	233.8 (213.4, 254.2) 1.00 (1.00, 1.00)	229.3 (211.9, 246.8) 1.00 (1.00, 1.00)
	2% PV & 2% C/Co	263.3 (139.2, 387.3) 0.98 (0.97, 0.99)	206.1 (154.9, 257.4) 0.98 (0.97, 0.99)
200	None	183.3 (181.9, 184.6) 1.00 (1.00, 1.00)	194.5(194.2,194.6) 1.00 (1.00, 1.00)
	2% C/Co	186.1 (165.9,206.4) 1.00 (1.00, 1.01)	188.4 (174.9, 201.9) 1.00 (1.00, 1.00)
	2% PV & 2% C/Co	309.4 (188.5, 430.2) 0.98 (0.97, 0.99)	202.3 (164.7, 240.0) 1.00 (0.99, 1.00)
150	None	140.4 (139.5, 141.3) 1.00 (1.00, 1.00)	146.9 (146.7, 147.1) 1.00 (1.00, 1.00)
	2% C/Co	142.1 (133.8, 150.4) 1.00 (1.00, 1.00)	144.4 (133.0, 155.8) 1.00 (1.00, 1.00)
	2% PV & 2% C/Co	125.0 (81.2, 168.7) 1.00 (0.98, 1.01)	211.8 (142.3,281.3) 1.00 (0.99, 1.01)
125	None	118.3 (117.6,119.0) 1.00 (1.00, 1.00)	122.8 (122.7, 123.0) 1.00 (1.00, 1.00)
	2% C/Co	109.3 (101.9, 116.8) 1.00 (1.00, 1.00)	119.5 (113.8,125.2) 1.00 (1.00, 1.00)
	2% PV & 2% C/Co	108.4 (46.1, 170.8) 0.97 (0.95, 1.00)	114.9 (93.7, 136.1) 1.01 (1.00, 1.02)

Table 4.6 Cont.

Known *Pe*	Noise Added	fitted *Pe* (95% CI) fitted R_f (95% CI)	
		Discretized 10 pts/PV	**Discretized 18 pts/PV**
100	None	95.8 (94.9, 96.6) 1.00 (1.00, 1.00)	98.6 (94.5, 98.7) 1.00 (1.00, 1.00)
	2% C/Co	90.3 (84.1, 96.5) 1.00 (1.00, 1.00	98.1 (93.0, 103.1) 1.00 (1.00, 1.00)
	2% PV & 2% C/Co	98.2 (79.1, 117.2) 1.01 (1.00, 1.02)	107.4 (74.2, 140.7) 1.01 (0.99, 1.02)
50	None	48.9 (48.7, 49.1) 1.00 (1.00, 1.00)	49.6 (49.6, 49.7) 1.00 (1.00, 1.00)
	2% C/Co	49.2 (46.3, 52.1) 1.00 (1.00, 1.01)	49.6 (47.7, 51.4) 1.00 (1.00, 1.00)
	2% PV & 2% C/Co	46.3 (38.4, 54.2) 1.01 (1.00, 1.03)	54.0 (49.1, 58.8) 1.01 (1.00 1.01)

These results suggest that tracer experiments conducted at high *Pe* may produce less reliable estimates of α. Studies having *Pe* > 200 were therefore excluded, unless the study was determined to use a higher rate of sampling (i.e., greater than 10 samples per pore volume). Only three such studies were identified in the data set: Pennell et al. (1993 & 1994) with ~15 samples per pore volume, and Zhang et al. (2014) with ~30 samples per pore volume.

With respect to tracer test design, it appears as though estimates of α become more reliable when *Pe* <200 and/or higher sampling frequencies are employed. It is important to note that the presented results exclude experimental or measurement error, which will only serve to increase the need to employ moderate *Pe* or higher frequency sampling. With shorter or thinner columns high frequency sampling may be made difficult by the sample volume required for analysis (usually, one to several mL for ion-specific probes or ion chromatography). Reliability in the estimated α can also be enhanced by limiting effective diffusion to be <10% of the overall hydrodynamic dispersion. This essentially diminishes the influence of model selection for calculation of the tortuosity factor as diffusion coefficients for most tracer solutes are relatively well established (Lide, 1999).

The extent to which measurement error may exacerbate the effects of data quantity when fitting the ADE to determine α was investigated here. Results suggest that where the fits improve (Table 4.6), it is due to an expansion of the confidence interval about the fitted *Pe* value. Certainly the data set used to

establish the polyparameter models described herein contains uncertain estimates of α, although which values are more or less uncertain cannot ascertained here. This highlights the need to place greater emphasis on capturing and understanding the uncertainty in fitted values of α.

4.4.4 Influence of Exclusion Criteria on Model Development

Model performance (as defined by AICc, NSE, and adj-R^2) for the best one, two, and three parameter models under varying *Pe* and D_{eff}/D_h exclusion criteria is shown in Table 4.7 for the fully saturated and Table 4.8 for the partially saturated subsets. Exclusion criterion are also shown in graphically form for the fully saturated dataset in Figure 4.4 where the best model for the fully saturated subset is plotted for (i) all points (i.e., no exclusion criteria enforced); (ii) for $Pe<200$; (iii) for D_{eff}/D_h <10% and (iv) both $Pe<200$ and D_{eff}/D_h <10%. Fully saturated systems were most effected by the $Pe<200$ criteria, leaving only a few studies applicable for analysis.

Table 4.7: Influence of applying the exclusion criteria in model development.

Fully Saturated Systems (S_w=1)

		all *Pe*			*Pe*<300			*Pe*<200		
		AIC_c	*NSE*	*adj-*R^2	AIC_c	*NSE*	*adj-*R^2	AIC_c	*NSE*	*adj-*R^2
all D_{eff}/D_h	U_i	24.1	0	0.56	20.0	0.03	0.56	22.3	0	0.53
	U_i, d_{50}							16.6	0.34	0.62
	-									
D_{eff}/D_h <0.25	U_i	22.3	0	0.53	5.0	0.09	0.61	15.1	0	0.56
	-									
	-									
D_{eff}/D_h <0.10	U_i	9.0	0	0.61	6.6	0	0.61	11.9	0	0.52
	U_i, d_{50}	2.3	0.51	0.69	1.7	0.48	0.69	7.5	0.63	0.66
	U_i, n, d_{50}	0.90	0.76	0.72	-3.1	0.80	0.75	4.6	0.82	0.74

A blank indicates that no model was statistically significant ($p<0.1$)

Table 4.8: Influence of applying the exclusion criteria in model development

Partial Saturated Systems (S_w<1)

		all *Pe*				*Pe*<200		
		AIC_c	*NSE*	*adj-*R^2		AIC_c	*NSE*	*adj-*R^2
all D_{eff}/D_h	S_w	8.28	0.45	0.50	S_w	-2.57	0.47	0.52
	S_w, U_i	-14.55	0.63	0.52	S_w, U_i	-28.99	0.66	0.56
	n, S_w, U_i	-21.14	0.68	0.74	*n*, S_w, U_i	-37.41	0.70	0.75
D_{eff}/D_h <0.25	S_w	7.31	0.45	0.50	S_w	4.62	0.44	0.50
	S_w, U_i	-14.63	0.63	0.52	S_w, U_i	-16.78	0.62	0.53
	n, S_w, U_i	-20.68	0.67	0.73	*n*, S_w, U_i	-23.08	0.67	0.73
D_{eff}/D_h <0.10	S_w	-6.22	0.45	0.51	S_w	-14.55	0.47	0.53
	S_w, U_i	-27.70	0.64	0.55	S_w, d_{50}	-41.77	0.68	0.61
	n, S_w, U_i	-34.27	0.69	0.72	*n*, S_w, U_i	-49.21	0.72	0.74

A blank indicates that no model was statistically significant ($p<0.1$)

No studies in this subset were excluded by Pe<300 criteria. Pennell et al. (1994) experiments were run at Pe ~300, but had sufficient sampling frequency to justify inclusion

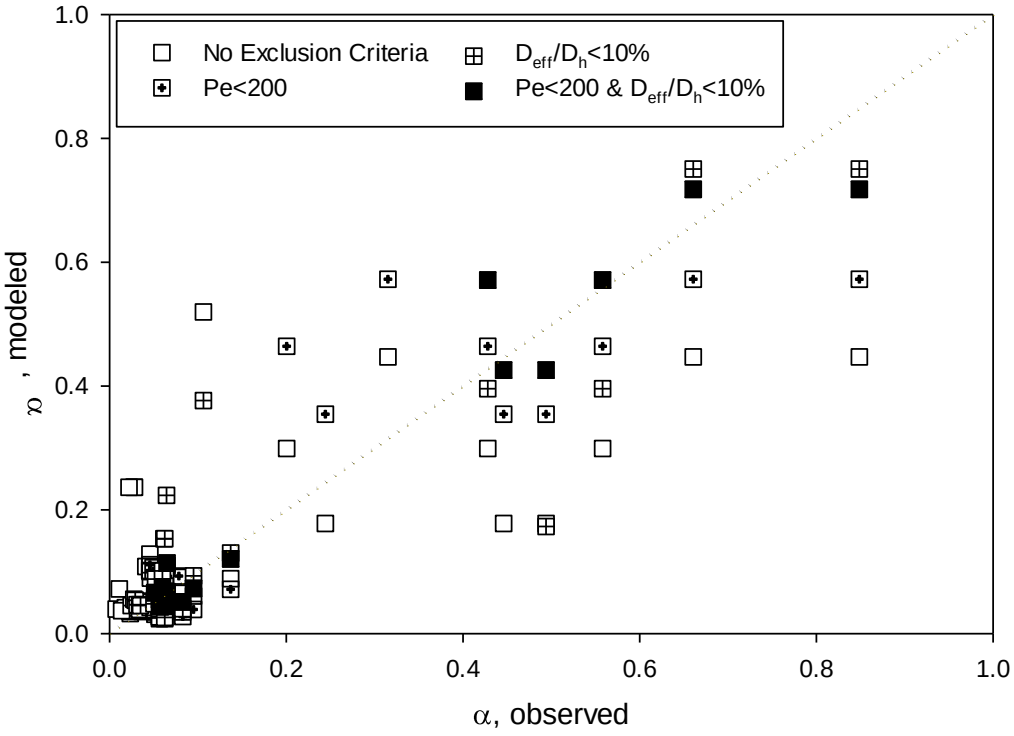

Figure 4.4: Fully saturated models for $\hat{\alpha} = K \cdot n^a U_i^{\ b}$. The entire dataset (i.e., no exclusion criteria) is shown with the open squares. Studies with *Pe*<200 are shown with dotted squares. Studies where $D_{eff} / D_h < 10\%$ are shown with crossed squares. Studies that passed all exclusion criteria (i.e., *Pe*<200 and $D_{eff} / D_h < 10\%$ are shown with filled squares.

4.4.5 Polyparameter Models

4.4.5.1 Fully Saturated Media

The single best predictor for fully saturated systems is U_i (AIC_c = 11.9, adj-R^2 = 0.52), though the NSE = 0 for this model suggests that the mean of the measurements is an equally good predictor. The best two-predictor model includes U_i and n (AIC_c = 7.6, adj-R^2 = 0.66, NSE = 0.63). The identification of U_i is well aligned with other studies that suggest the distribution of grain or pore sizes can influence dispersion (Klotz and Moser, 1974; Menzie and Dutta, 1988). The overall best fit model is the three-predictor model shown as Equation 4.11 (AIC_c = 4.6, adj-R^2 = 0.74, NSE = 0.82).

$$\alpha(cm) = 10^{3.4} \cdot d_{50}^{0.8} \cdot n^{7.9} \cdot U_i^{1.8} \qquad (4.11)$$

The best fit model includes predictors that characterize the median and distribution of grain sizes.

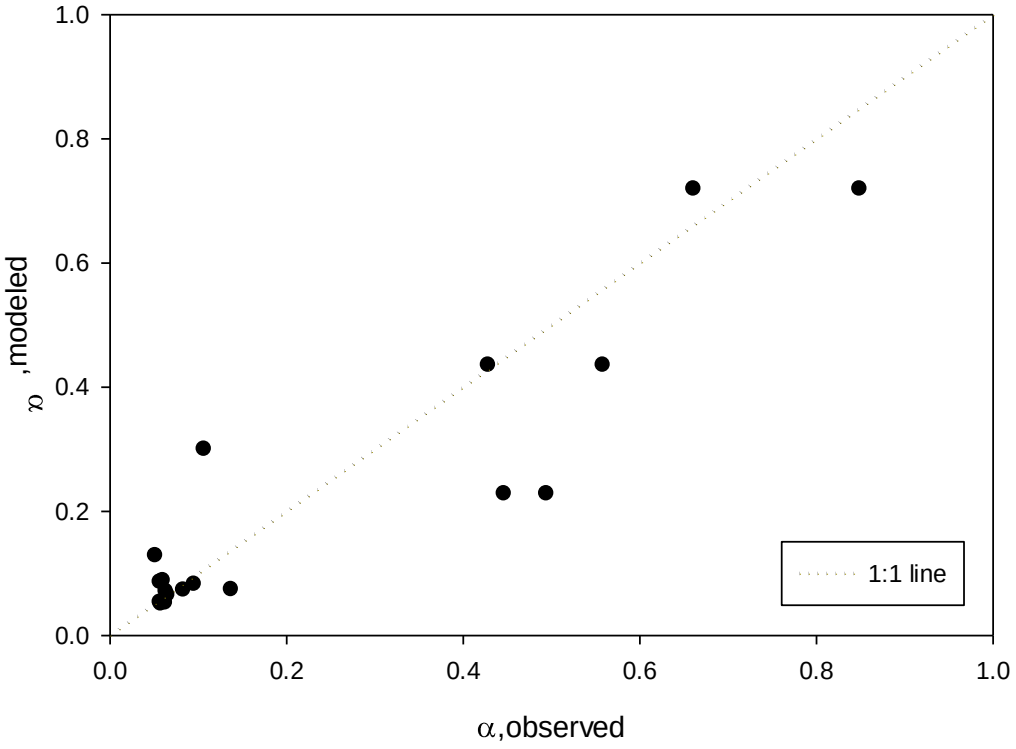

Figure 4.5: Performance of best fit model for dispersity in fully saturated porous media (reported in cm) using Equation 4.11.

This model offers comparable performance to that developed by Sato et al. (2003) for fully saturated systems. The Sato model (adj-R^2 = 0.79, NSE = 0.78) uses parameters from the van Genuchten model (1980a) of the capillary pressure - saturation relationship as predictors in their polyparameter model describing α. Important to note here is that the van Genuchten (1980a) parameters can be interpreted as representing the average pore size (or the entry pressure for that pore size) and the distribution of pore sizes. The combination of d_{50} and U_i offers similar information through established links between particle size distributions and pore size distributions (Barr, 2001). The value in using d_{50} and U_i in this capacity is the relative ease by which the predictors are determined.

4.4.5.2 Partially Saturated Media

The partially saturated experiments in the data set comprise both NAPL-water and air-water systems. The single best predictors for the NAPL-water system and air-water systems are d_{50} (AIC_c = -12.1, adj-R^2 = 0.51, NSE = 0.49) and S_w (AIC_c = -46.0, adj-R^2 = 0.79, NSE = 0.66), respectively. Both of these single predictor models offer strong performance. The selection of S_w as the best single predictor for the air-water system is well aligned with the many studies identifying a dependence of dispersive mixing on S_w (or θ_w) (Conca and Wright, 1992; Haga et al., 1999; Sato et al., 2003). The air-water model suggests an inverse relationship between S_w and α. In contrast, S_w is not statistically significant as a single predictor for the NAPL-water subset of data.

The partially saturated dataset was split into NAPL-water and air-water systems. For the NAPL water system Equation 4.12 was the best fit model (AIC_c=-13.80; adj-R^2=0.55; NSE=0.43).

$$\alpha_{NAPL-water}(cm) = 0.01 \cdot d_{50}^{-0.58} S_w^{-1.83} \quad (4.12)$$

For the air-water system Equation 4.13 was the best fit model (AIC_c=-47.53; adj-R^2=0.81; NSE=0.76).

$$\alpha_{air-water}(cm) = 0.23 \cdot n^{2.2} \theta_w^{-1.27} \quad (4.13)$$

NAPL-water and air-water system best model fits are shown in Figure 4.6.

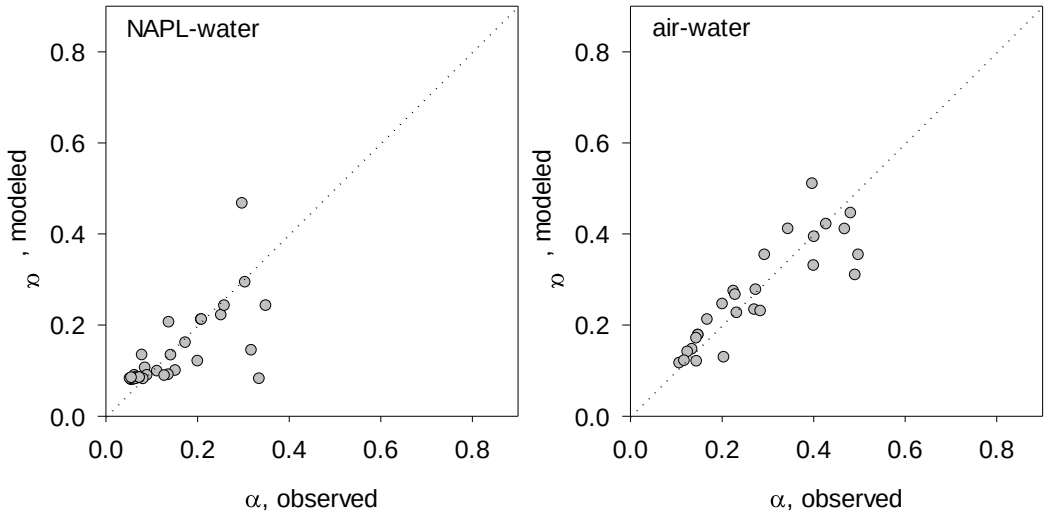

Figure 4.6: Performance of best models for partially saturated systems. (left) NAPL-water (Equation 4.12); (right) air-water (Equation 4.13).

It is suspected that this relates to the relatively narrow range of S_w created by the entrapped NAPL saturations that comprise the NAPL-water subset (see Figure 4.1). The NAPL-water single predictor model suggests an inverse relationship with d_{50}, which is in contrast with the direct relationship identified for the fully saturated data. It is hypothesized that d_{50} is contributing information related to the pore-scale architecture of the entrapped NAPL as shown in correlations relating d_{50} to effective size of NAPL ganglia (e.g., Brusseau et al., 2009; Ramsburg et al., 2011). For the NAPL-water system the best two-predictor model couples d_{50} and S_w (AIC_c = -13.8, adj-R^2 = 0.55, NSE = 0.43). The best three-predictor model includes d_{50}, S_w and n (AIC_c = -13.7, adj-R^2 = 0.57, NSE = 0.46), though the addition of the third parameter cannot be fully justified given the modest gain in model performance. Multiple two-predictor models offer similar performance for the air-water system (AIC_c = -47.5, adj-R^2 = 0.81, NSE = 0.76), though the model comprising θ_w and n was selected based on the level of significance of all coefficients ($p<0.01$). These results suggest that combination of the NAPL-water and air-water systems may yield a predictive capability that is broadly applicable.

When the partially saturated data subsets are combined, S_w is seen to be the single best predictor (AIC_c = -14.6, adj-R^2 = 0.47, NSE = 0.53), with d_{50} and S_w comprising the best two-predictor model (AIC_c = -41.7, adj-R^2 = 0.68, NSE = 0.61). The best fit model comprises S_w, n and U_i (AIC_c = -49.2, adj-R^2 = 0.72, NSE = 0.74) and is shown as Equation 4.14.

$$\alpha(cm) = 10^{-0.32} \cdot S_w^{-1.1} n^{1.8} U_i^{0.68} \quad (4.14)$$

The resulting model represents an important result, as it combines data from NAPL-water and air-water systems into a single model that offers similar predictive performance to that develop for the air-water data alone (note that the NSEs are 0.74 and 0.76, respectively). The best fit model for all partially saturated systems is shown in Figure 4.7.

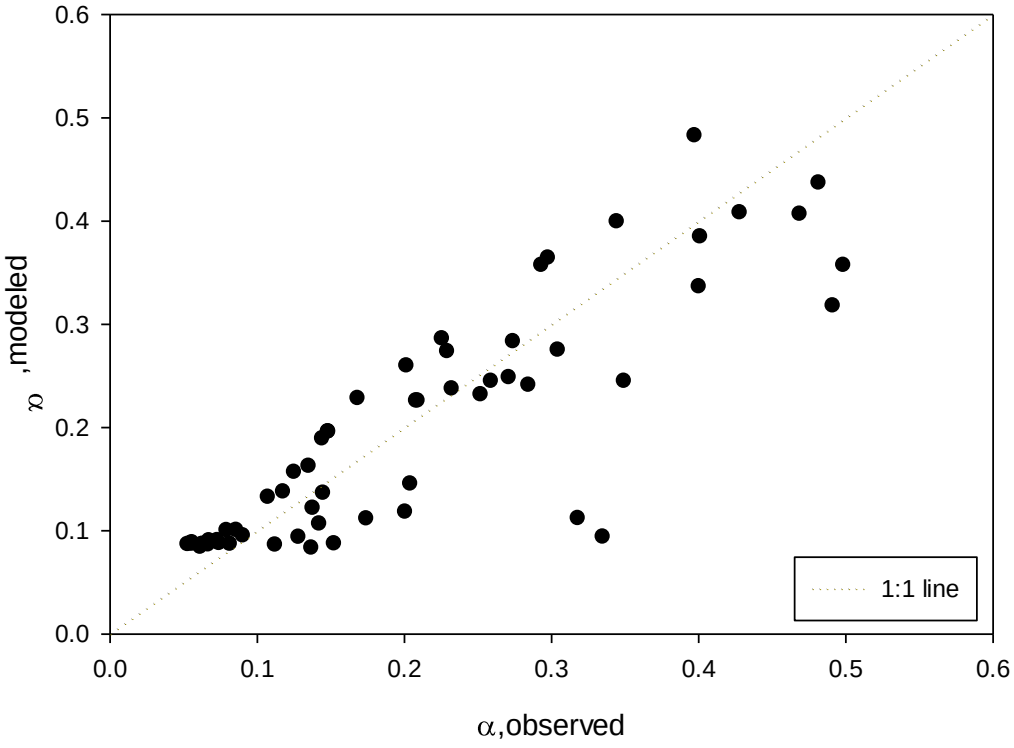

Figure 4.7: Performance of best model for partially saturated systems (both NAPL-water and air-water systems).

Both the fully saturated (Equation 4.11) and partially saturated (Equation 4.14) models include U_i and n, though the coefficients are statistically different (Table 4.9). Combination of the air-water and NAPL-water systems moves the NAPL-water model away from d_{50}, in favor of other predictors (U_i, n, S_w) that have been used in correlations of pore-scale NAPL architecture (e.g., Brusseau et al., 2009; Ramsburg et al., 2011). It is in this way that the model appears to be capturing the role of the interconnectedness of the non-wetting phase on mixing, which aligns with previous findings related to how the saturation and interconnectedness of the saturation influences tortuosity and mixing (e.g., Wildenshchild and Jensen, 1999; Rossi et al., 2007). The statistical differences between the coefficients on U_i and n for the fully and partially saturated models also suggest that these predictors provide information on both the porous medium and the distribution of the water within the porous medium.

4.4.5.3 Combined Model

To explore the possibility of obtaining a model capable of describing transitions between fully saturated and partially saturated conditions, we combined the data and developed a best-fit four-parameter model (Equation 4.15, AIC_c = -27.2, adj-R^2 = 0.65, NSE = 0.52).

$$\alpha(cm) = 10^{1.01} \cdot d_{50}^{0.38} S_w^{-1.0} n^{3.8} U_i^{1.3} \qquad (4.15)$$

The model resulting from use of the entire data set represents degraded predictive capability from those models produced for the fully saturated and partially saturated subsets.

Table 4.9: Comparison of best-fit model parameters across subsets of the data.

	d_{50}	U_i	n	S_w
fully saturated	0.80 ± 0.33	1.8 ± 0.4	7.9 ± 2.2[c]	-
partially saturated	-	0.68 ± 0.10[b]	1.8 ± 0.6[d]	-1.1 ± 0.2
air-water systems[a]	-	-	0.89 ± 0.19[d]	-1.3 ± 0.1
NAPL-water systems	-0.58 ± 0.09[b]	-	-	-1.9 ± 0.9
all data	0.38 ± 0.15	1.3 ± 0.2	3.8 ± 0.7[c]	-1.0 ± 0.2

[a] based on values of n and Θ_w in best fit model;
[b] statistically different than other entries ($p<0.05$);
[c,d] use of the same letter indicates a pair that is statistically similar, but that is statistically different from other entries ($p<0.05$)

It is, however, worth noting here similarities between the model coefficients. For example, the model coefficients associated with predictors that relate to properties of the porous medium (d_{50}, U_i, and n) are not statistically different (at p = 0.05) between the fully saturated and all data models (Table 4.9). Haga et al. (1999) correlated *Pe* to S_w in partially saturated system. In doing so, the authors selected d_{50} to represent the length scale used in *Pe*. When viewed from the perspective of our study, the approach used by Haga et al. (1999) (which is also employed by Sato et al., (2003)) essentially sets the model coefficient on *Pe* to unity. Results from the fully saturated model (Equation 4.11) suggest the Haga et al. (1999) approach may hold utility for fully saturated systems. However, the exponent found for d_{50} in the combined model (Equation 4.15) offers a point of contrast when using the approach of Haga et al. (1999) for partially saturated systems. The coefficient related to S_w is not statistically different (*p*-value = 0.05) between the partially saturated and all data models. Studies examining power-law models suggest the value of the exponent on S_w is near one which agrees well with results described herein (e.g., Maraqa et al., 1997; Haga et al., 1999). Thus, it appears that the model developed using all of the data cannot resolve descriptors that have been shown to contribute to describing both the porous medium and interconnectedness of S_w. Because this limitation arises from the number of available predictors, future studies may wish to develop new predictors that can better differentiate fully and partially saturated media. One option may be to consider interfacial area or a similar parameter that

can be theoretically estimated if the capillary pressure - saturation parameters are known (e.g., Grant and Gerhard, 2007).

4.5 IMPLICATIONS FOR TRANSIENT WATER SATURATION

Efforts to link fully saturated and partially saturated models were motivated by a need to describe changes in dispersive mixing as S_w decreases from unity. Decreases in S_w often relates to the delivery of emulsified oil as a remediation amendment. However, understanding mixing when a porous medium transitions to/from fully saturated is relevant in other areas (e.g., infiltration, artificial recharge, NAPL removal/dissolution). Mixing through this transition requires greater understanding at both the pore and Darcy scales (e.g., Jimenez-Martinez et al., 2015). This behavior was examined by analyzing the data set for studies that conducted a tracer test within a given porous medium under both fully and partially saturated conditions. Dispersivity values obtained under fully and partially saturated conditions were directly compared to identify a model that relates α through the transition from full to partial saturation. 54 experiments were identified, 28 of which were conducted in air-water systems and 26 of which were conducted in NAPL-water systems. The model developed to relate $\alpha_{Sw<1}$ to $\alpha_{Sw=1}$ is shown as Equation 4.16. The basis for this single parameter model, where K is the fitted coefficient, are observations that: (i) the single best predictor of the partially saturated data was found to be S_w, and (ii) coefficients for all other predictors are statistically different between the Equations 4.11 and 4.15.

$$\alpha_{Sw<1}(cm) = K \cdot \alpha_{sw=1} \cdot S_w^{-1.0} \qquad (4.16)$$

The formulation shown in Equation 4.16 can be justified by experimental evidence that finds large changes in dispersive mixing for small changes in S_w. For example, Zhang et al. (2014) found a 2% reduction in S_w increased α by a factor of 2. Fits of Equation 4.16 to the data produced a model coefficient of 2.0 ± 0.1 (adj-R^2 = 0.82, NSE = 0.82). During the fitting process it was realized that the fits of the coefficient were being adversely affected by a single set of experiments (Padilla et al. (1999)). When fit separately the Padilla data are well described by Equation 4.16, albeit with a different coefficient (K = 6). This suggests the reported value of $\alpha_{sw=1}$ for their experiments are a factor of 3 lower than would be otherwise expected with this model. This discrepancy may likely be explained by the fact that the fully saturated tracer tests reported in Padilla et al. (1999) were conducted at $570 \leq Pe \leq 750$. The easily corrected outlier nature of the values points to the discussion above regarding the accuracy of mixing parameters obtained at high Pe and reinforces the recommendation that tracer tests be designed to ensure moderate values of Pe (<200), where D_h or α may be more reliably fit to experimental data. Overall, the simple model (Equation 4.16) provides a good description of the data irrespective of saturation level or type of non-wetting phase (Figure 4.8), and is therefore recommended for use when describing solute transport in media where water saturation is dynamic and dispersion is known (or estimated) at a reference water saturation.

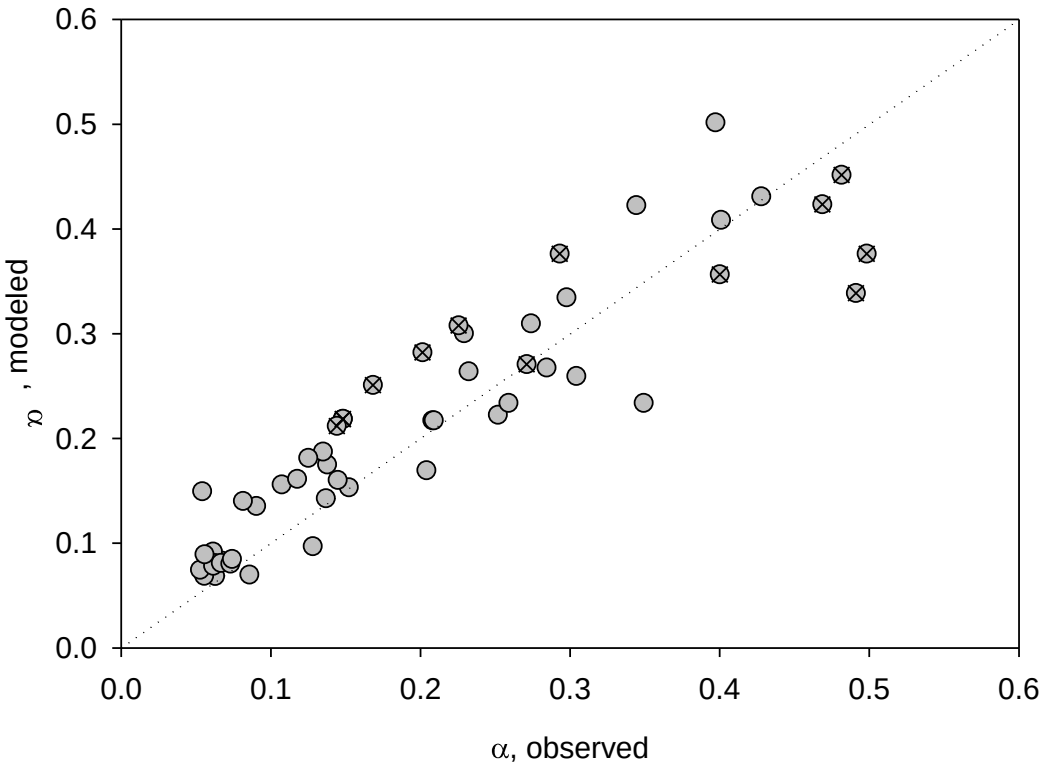

Figure 4.8: Performance of model (Equation 4.16) relating $\alpha_{Sw<1}$ to $\alpha_{Sw=1}$. ⊗ denotes data of Padilla et al. (1999) where the model coefficient was adjusted.

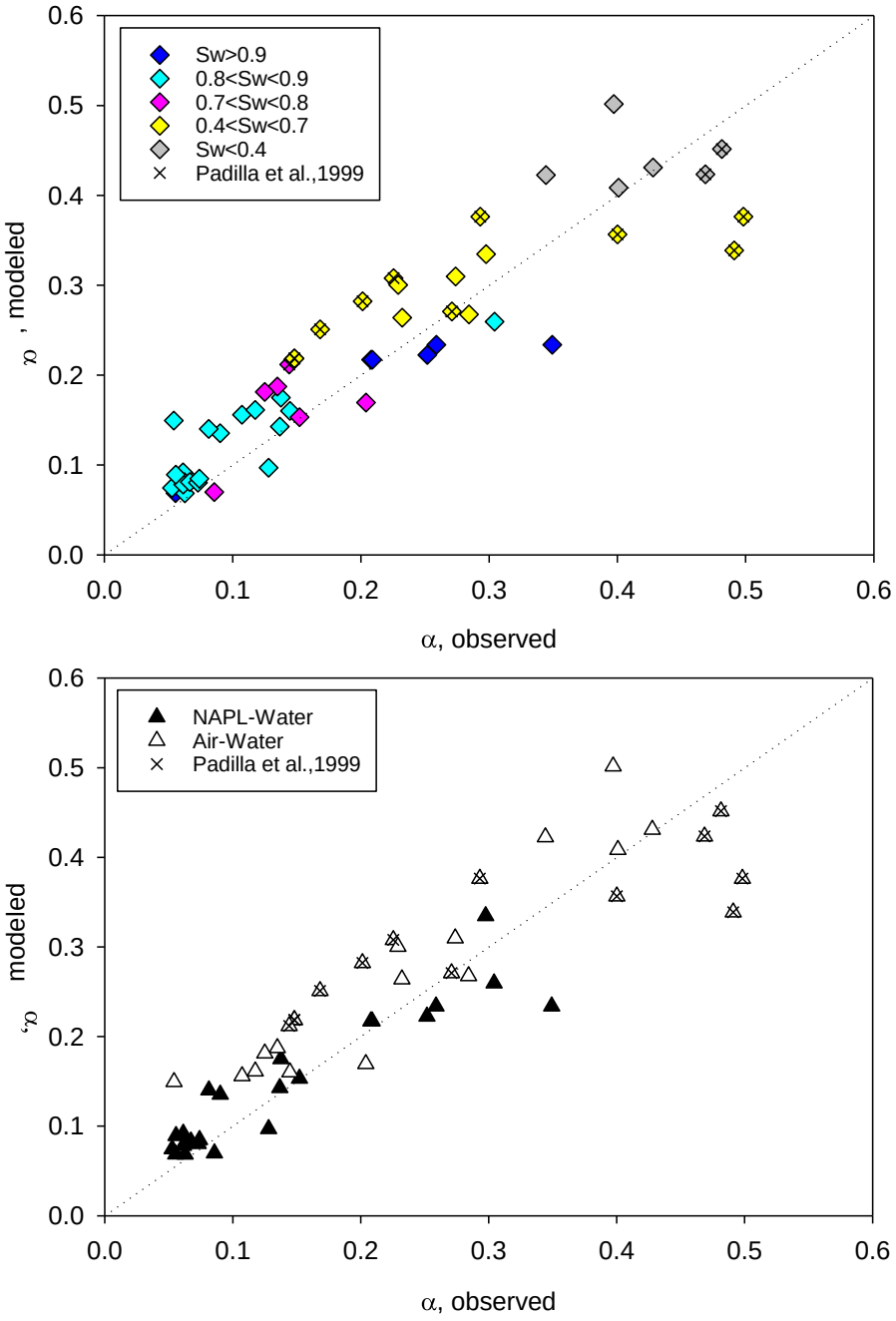

Figure 4.9: Performance of Equation 4.16 that relates $\alpha_{Sw<1}$ to $\alpha_{Sw=1}$. Crosses denote data of Padilla et al. (1999). K = 2 for all studies (expect Padilla et al. (1999)); K = 6 for Padilla et al. (1999). (top) data shown as a function of S_w; (bottom) data shown by fluid type for NAPL-water (closed triangles) and air-water (open triangles) systems.

It is recognized that Equation 4.16 possesses a discontinuity at $S_w = 1$. An alternative model developed to be continuous through $S_w = 1$ was found to offer similar performance (see Figure 4.9). An alternative model that was developed to be continuous through $S_w = 1$ is shown as Equation 4.17.

$$\alpha_{Sw<1} = \alpha_{Sw=1} + K \cdot \alpha_{Sw=1}(1 - S_w)^b \qquad (4.17)$$

Where: K and b are fitted model parameters. Note that this model uses $(1\text{-}S_w)$ and thus fitted parameter values are not directly comparable with the other equations presented above. Values of $K = 5.5$ and $b = 0.78$ were fit using all studies except that of Padilla et al. (1999). As noted earlier, the data of Padilla et al. (1999) were obtained at high Pe and quite likely represent overestimation of the $\alpha_{Sw=1}$. The Padilla et al. (1999) data were therefore fit separately ($K = 39.9$; $b = 1.9$). The overall model has an adj-$R^2 = 0.82$ and NSE = 0.83. Model performance is shown in Figure 4.10 and delineated by saturation level and NAPL type in Figure 4.11.

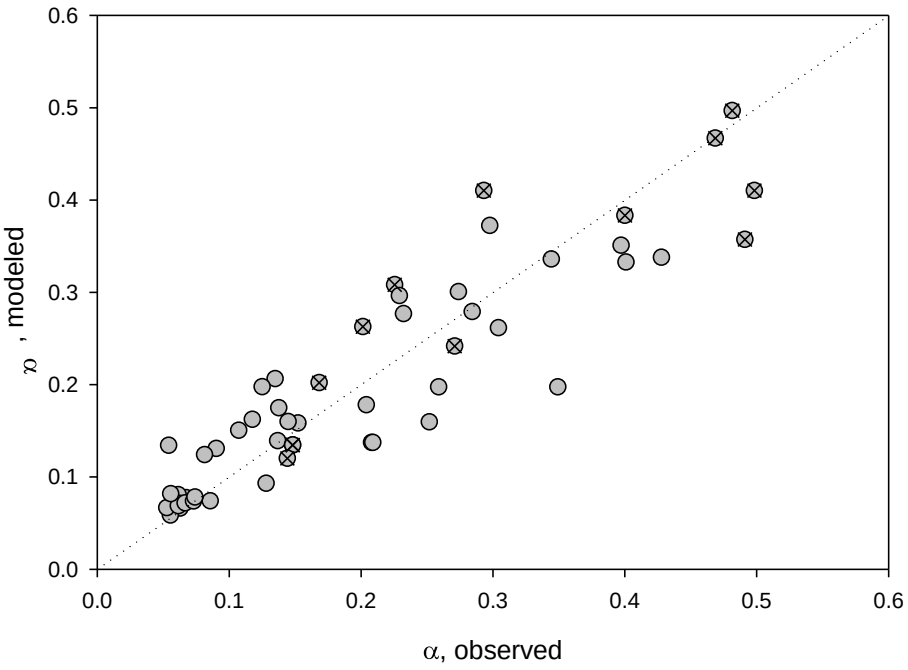

Figure 4.10: Performance of model (Equation 4.17) relating $\alpha_{Sw<1}$ to $\alpha_{Sw=1}$.

⊗ denotes data of Padilla et al. (1999) where the model coefficient was adjusted.

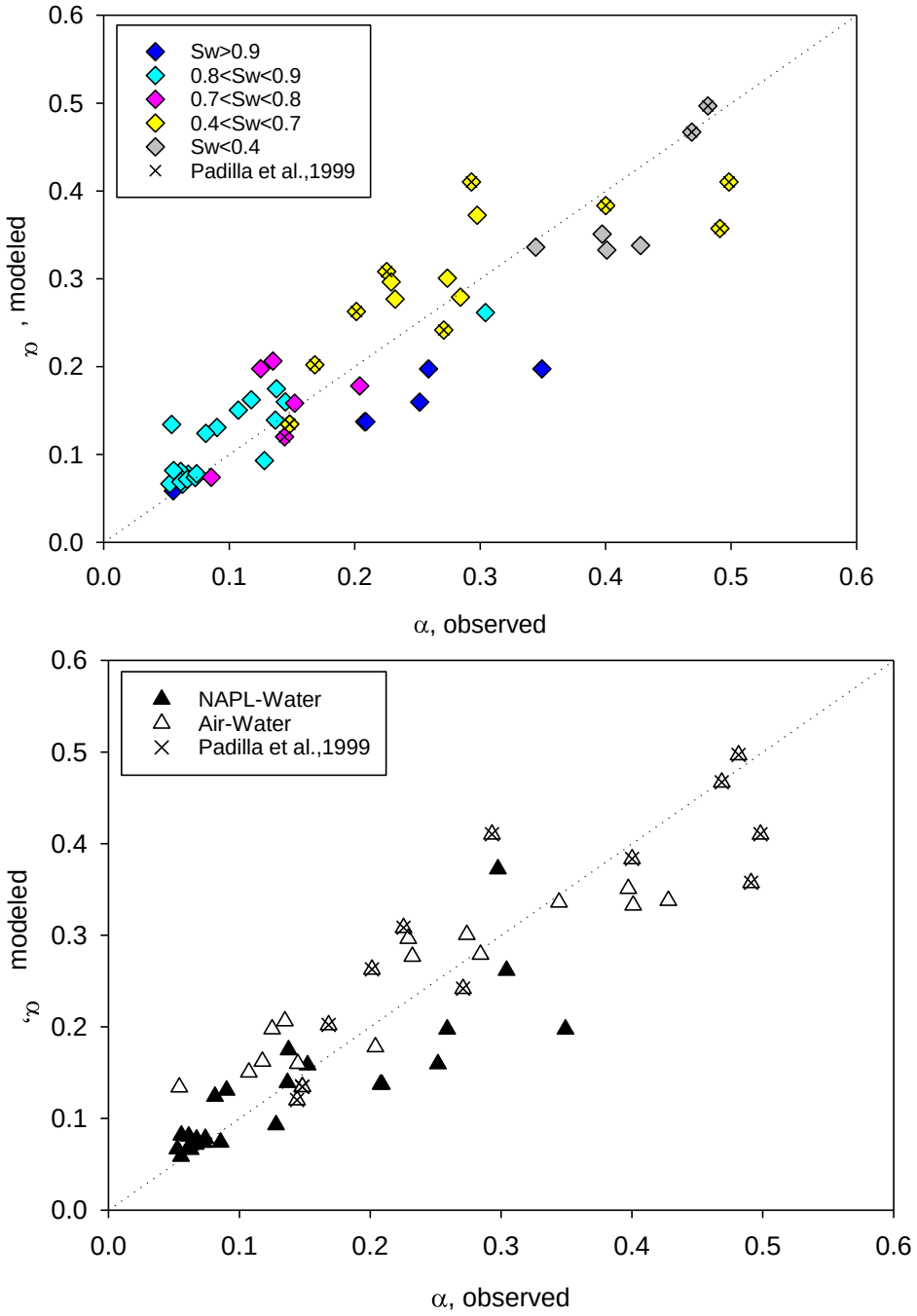

Figure 4.11: Performance of Equation 4.17 relating $\alpha_{Sw<1}$ to $\alpha_{Sw=1}$. Crosses denote data of Padilla et al. (1999). (top) data shown as a function of S_w; (bottom) data shown by fluid type for NAPL-water (closed triangles) and air-water (open triangles) systems.

4.6 IMPLICATIONS AND CONCLUSIONS

Predictors such as median grain size, uniformity index, porosity, and water saturation were able to provide meaningful predictions of dispersivity under a set of limiting conditions (water saturation > 0.4 and transport length < 100 cm). All models are based on standard porous media properties.

The main finding was that even low to moderate saturations of non-wetting phase were found to greatly influence dispersivity in partially saturated media (i.e., for both NAPL-water and air-water system) with water saturation found to be the best overall predictor of dispersivity. Additionally, values of dispersivity obtained under saturated conditions were found to scale for an improved estimate of mixing under partially saturated conditions. This resulting simple dispersivity model (Equation 4.16) may have utility for systems with transient water saturation (e.g., infiltration and irrigation events, chemical or biological reactions occurring within porous media, NAPL source depletion, and delivery of foams and emulsions used in site remediation). These finding have appreciable significance for many applications where the influence of saturation on solute transport behavior is often neglected. All developed predictive models were formulated for easy incorporation into flow and transport simulations.

Chapter 5: Emulsion Transport and Retention

5.1 ABSTRACT

Oil-in-water emulsions are routinely used in subsurface remediation, although remedial design can be limited by the empirical nature of descriptions for droplet transport. Field applications of injectable, edible oils employ either neat oil or emulsified oil at concentrations ranging upwards towards 20% wt. Emulsion transport and retention was therefore investigated over a range of input concentrations (1.3%, 2.3% and 23% wt.) via a series of 1-d column experiments conducted in Ottawa sands. Existing particle transport models were able to capture the transport and hyper-exponential retention behavior of the lower concentration emulsions, but not that of the higher concentrated emulsions. Breakthrough curves for the higher concentration emulsions exhibited an early fall on the backside of the breakthrough curve along with extending tailing. Both of these features cannot be captured by existing models for emulsion transport. Thus the objective of this chapter was to examine the role of additional mixing processes associated with the transport of concentrated emulsions. Focus is placed on the influence of the retained fraction on dispersivity and the influence of viscous instabilities on the pulse of emulsion introduced to the columns. The developed model extends existing particle transport model formulations (parameterized with low concentration data) to describe emulsion transport and

deposition at concentrations that are an order of magnitude greater. The predictive quality of the approach can help support system design when employing oil-in-water emulsions, as well as to provide insight into how fluid saturation and viscosity influence mixing behavior.

5.2 INTRODUCTION

Oil-in-water emulsions have been used in environmental remediation for a variety of applications including enhanced contaminant recovery (e.g., Kwon, et al., 2005, Lee, et al., 2007), contaminant stabilization (e.g., Fox & Medina, 2005), fermentable substrate delivery (e.g., Borden, 2007, Watson et al., 2013), mobility control (e.g., McAulifee, 1973; Cobos et al., 2009; Guillen et al., 2012) and to deliver active ingredients to the subsurface (e.g., Ramsburg et al., 2004; McClements et al., 2007; Berge & Ramsburg, 2009; Shen, et al., 2011). Utilization of emulsions for in situ remediation efforts requires a balance between retention and distribution of remedial amendments and ease of delivery/injection. When remedial amendments are held within emulsions (i.e., alkalinity releasing particles), modeling of emulsion transport and retention in porous media is needed to provide a complete description of treatment. Effective amendment delivery systems must balance the ability to infiltrate a wide treatment area (i.e., transport) while providing sufficient retention to supply desired amendment mass. Here, the duration of alkalinity release (i.e., treatment capacity) from particle-containing emulsions is directly proportional to the extent of emulsion oil droplet retention in porous media (i.e., all particle mass is assumed to be held in droplets). Long term

pH control via emulsions hinges on slow release from these retained droplets holding the alkalinity-releasing particles, making understanding emulsion transport and deposition models key to successful pH control. Highly concentrated emulsions or neat edible oils are frequently required to reach remediation outcomes. For example, a 12% (v/v) SBO emulsion was used to sustain biodegradation of perchlorate and chlorinated solvents (Borden, 2007) and uranium (Watson et al., 2013) and a 20% (wt./wt.) emulsion was employed at the pilot study at Altus Air Force Base in Altus, Oklahoma (Lee et al., 2003). Currently concentrated emulsion transport and retention is highly empirical. A more mechanistic understanding and description of the processes controlling emulsion mobility and the spatial entrainment in porous media may aid in remedial design.

These models conceptualize the emulsion into a single-phase flow process. That is, the models do not model droplets as a component, and thus are incapable of describing the distribution of droplets within the domain. Colloid filtration theory provides an approach to modeling droplet concentrations. Filtration theory has been adapted and applied to describe the transport of kinetically stable, dilute (i.e., <1% v/v) macro emulsions. The most notable application of this approach is by Soo & Radke (1984, 1986a, 1986b). These authors assume droplets are retained via straining as well as droplet capture and remobilization. Applications of colloid filtration models typically assume the permeability of the medium is constant - uninfluenced by any particle retention. In contrast, Soo & Radke

(1986a&b) found that deposition processes such as pore clogging and straining influenced the flow behavior when droplet-pore size ratio nears unity. Soo & Radke (1986a&b) restructured the filtration model formulation to account for the impact of droplet straining and interception by describing the permeability and flow behavior as a transient processes captured with a reducing filter coefficient and flow restriction and redistribution parameters. While these experiments focused on emulsions where the droplets were on the scale of pore throats, straining processes have been cited to occur even when droplets are orders of magnitude smaller than pore throats (e.g., Bradford et al. (2006) suggest straining occurs when ratio of particle diameter to the sand grain diameter $(\frac{d_p}{d_g}) > 0.008)$.

In an alternative approach to modeling emulsion droplet transport, Coulibaly et al. (2006) account for mass deposition via a surface capacity (S_{max}) that modifies the attachment rate to describe concentrated emulsion transport (11% v/v; μ_e=1.44 mPa·s) in column experiments characterized by substantial retention and limited breakthrough. In addition, the authors reported no evidence of droplet retardation or droplet remobilization, and thus excluded these processes when formulating the transport model. Cortis and Ghezzehei (2007) examined the extended tailing observed in the Coulibaly et al. (2006) experiments using a continuous time random walk (CTRW) model. The model of Cortis and Ghezzehei included two types of transport processes and added a film flow component to the more typical retention and remobilization processes.

A common theme among models employed to describe the transport of emulsion droplets is the need to incorporate changes to the droplet retention characteristics over the course of the deposition event (e.g., through a reduction of the filter coefficient (Soo and Radke, 1986a), introduction of surface capacity (Coulibaly et al., 2006), or conceptualization of film flow component (Cortis and Ghezzehei, 2007). Although the particle and emulsion models described above can be fit to experimentally obtained breakthrough curves, the corresponding retention data is often overlooked - either when conducting the experiment or modeling the observations. Many reports detail difficulty in inferring transport mechanisms when examining breakthrough curves alone -that is, without consideration of the corresponding retention data (e.g., Bradford and Bettahar, 2006; Goldberg et al., 2014). Additionally, colloid transport models are often specific to the narrow range of experimental conditions to which the model is fit, thereby limiting the predictive power of the resulting model formulation and parameters (Goldberg et al., 2014).

Largely absent from these investigations is a discussion of the role of input concentration, emulsion viscosity, and droplet retention on mixing and tailing, despite the prevalence of tailing in studies of emulsion transport (e.g., Coulibaly et al. 2006, Borden, 2007; Crocker et al. 2008, Berge and Ramsburg 2009). The influence of input concentration has been explored within the solid-colloid literature finding that colloid mobility increased with increasing input concentration. Such studies have attributed these findings to decreases in the

surface area available for solid-phase accumulation or alteration of collector surface charge with mass deposition (e.g., Tan et al., 1994; Liu et al., 1995; Foppen et al., 2005; Bradford & Bettahar, 2006; Kasel et al., 2013). Still, knowledge on the influence of input concentration especially in the emulsion literature is rather limited. For example, although Soo & Radke tested a 2.5% (v/v) emulsion, these results were not included in the final model- potentially indicating the model provides a less reliable description of droplet transport at higher emulsion concentration. Emulsion concentration largely dictates emulsion viscosity since viscous is highly dependent on oil fraction (i.e., concentration of the dispersed phase), thus permitting viscosities to vary over orders of magnitude. While colloid filtration theory does include hydrodynamic arguments, the influence of viscosity is restricted to estimation of attachment parameters (e.g., Brownian diffusion, clean bed filter coefficient, adhesion number (McDowell-Boyer et al., 1986)) and is incapable of describing the observed tailing and Coulibaly et al. (2006) recognize a deficiency in their model formulation when emulsion density and viscosity deviate from that of water.

Many remediation techniques employing emulsions introduce a viscous emulsion (or perhaps even neat oil (e.g. Parson 2002)) to the subsurface. Following the introduction of the emulsion water flow through the 'treated' region is reestablished through a water flood used to chase the emulsion or as local groundwater re-invades the injection zone (e.g., Borden 2007). The reestablishment of water flow creates non-negligible viscosity contrasts leading to

the potential for viscous instabilities. In porous media, viscosity differences between fluids, regardless if fluids are fully miscible or immiscible, can create instabilities in flow where the less viscous displacing solution tends to penetrate the resident viscous fluid causing "viscous fingering" (Homsy, 1987). The influence of viscous fingering on transport during miscible displacements, such as those experienced during emulsion delivery, can be accounted for using either averaged models or direct numerical simulations of the physical fingering process (e.g., Koval, 1963; Sorbie, et al., 1995). Koval's fluxed averaged model is widely used given its simplicity and accuracy in predicting how viscous instabilities influence the fraction of each fluid in the effluent. Viscous fingering alters the flow front and can degrade applicability of standard formulation for mechanical dispersion (Flowers and Hunt, 2007); however, when the dispersed phase of the emulsion is conceptualized as a solute (as in colloid filtration theory), viscous instabilities manifest as dispersive mixing. In fact, the Koval model has be directly linked to solute dispersion by relating the flux averaged expression to the analytical solute transport solution to produce an empirical expression describing instabilities as dispersive mixing (Flowers and Hunt, 2007).

Given the available evidence, spatial and temporal variations to mixing may influence droplet transport, particularly in the case of concentrated emulsions. Thus, the overall objective of this work was to explore the role of concentration when considering emulsion transport. Specifically, the work aimed to: (i) understand the roles of mass deposition and viscosity contrast on emulsion

transport and retention in porous media, and (ii) ascertain whether or not incorporating these effects enables prediction of high concentration (i.e., 20-25% wt.) emulsion transport using colloid-filtration models parameterized at low concentration (i.e., 1.3-2.3% wt.).

5.3 MATERIALS

Soybean oil (SBO, MP Biomedicals, Laboratory grade), Gum Arabic (GA, >99% purity), sodium bromide (NaBr, 99.9% purity, ACS grade), and sodium chloride (NaCl, 99.5% purity, ACS grade) were purchased from Fisher Scientific. High purity water, denoted MilliQ water, (resistivity > 18.2 mΩ-cm and total organic carbon <10 ppb obtained from a Millipore Inc. Gradient A-10) was used to make all solutions. Federal fine (FF) Ottawa sand (30-140 mesh) from U.S. Silica was used as a representative medium-grain sandy medium; 60-80 mesh sand was sieved from Federal fine to give only that specific mesh size fraction; F-95 Ottawa silica sand was obtained from U.S. Silica; and 20-30 Accusand was obtained from Agsco corporation. The physical properties of the sands are listed in Table 5.1.

Table 5.1: Properties of the Ottawa sands employed for the porous media in this study.

Sand	Mesh size	Median grain size	Uniformity Index	Porosity*
		d_{50}	U_i	n
		[cm]	[-]	[-]
FF[a,d]	30-140	0.031	1.65[a,d]	0.37
20-30[b]	20-30	0.071	1.16[b]	0.36
F-95[c,d]	70-200	0.018	1.46[c,d]	0.40
60-80[d]	60-80	0.021	1.10[d]	0.41

[a] calculated from Berge and Ramsburg (2009) and Suchomel et al. (2007)
[b] calculated from Ramsburg et al. (2011) and Bradford and Abriola (2001)
[c] calculated from Berge and Ramsburg (2009) and Wang (2009)
[d] value from sieve analysis (data not shown)
[*]porosity depends on packing. The listed value is an estimate based on reported values for column experiments.

5.3.1 Experimental Methods

1-d column experiments were conducted (several in duplicate) to assess emulsion transport and retention. Kontes borosilicate glass columns (4.9 cm i.d. x 13 cm) were dry packed with various quartz sands. Federal Fine Ottawa quartz sand (U.S. Silica) was selected for the majority of column experiments to act as a representative medium sand. Columns were packed in one centimeter lifts and topped with a flow adapter to a packed height of approximately 10 cm. After dry packing, columns were flushed with CO_2 (top-down flow direction) for approximately 20 minutes. After CO_2 flushing, the column was preconditioned with a 10 mM NaCl electrolyte solution. A pre-injection non-reactive tracer test (10 mM NaBr) was used to determine the pore volume (PV) and dispersivity (α) by fitting experimental data in CFITM (van Genuchten, 1980b) within STANMOD v.2.07 (Simunek, et al., 2005). Oil-in-water emulsions were introduced at a constant upward (i.e., opposite the direction of gravity) Darcy flux (maintained by either a Varian ProStar HPLC pump or a Masterflex L/S Cole Palmer cartridge pump) for approximately 2.5 PV. Flow was then switched to a 10 mM NaCl solution at the same Darcy flux until the effluent was free of quantifiable dispersed phase (approximately 2.5-3.0 PV). Dispersivity in the presence of retained dispersed phase mass was assessed using a second conservative, non-reactive tracer test. At the conclusion of each experiment, columns were destructively sampled in one centimeter sections to determine the dispersed phase retention profile.

Effluent (aqueous) dispersed phase content was quantified gravimetrically via loss on ignition (LOI) at 105°C for 12+ hours to determine the water content of the sample. Volatilization of SBO and GA at 105°C was immeasurable in control tests. Dispersed phase content was verified via LOI at 550 °C for 2 hours. Dispersed phase retained on the porous media (*S*) in column sections was quantified by LOI at 550 °C.

Seven columns (experiments 1-4) were used to examine transport and retetion of three concentrations of an oil-in-water emulsions: 1.3% wt, 2.3% wt and 23% wt. (Table 5.3) on Federal Fine Ottawa Sand. Most experiments comprised of simultaenously conducted duplicate columns except experiment 4, with experiment 4 being employed in this section to aid assessment of predictive models on FF sand. Additional emulsion transport and deposition experiments (experiments 5-7) were conducted on other porous media (20-30, F-95, and 60-80). The focus of this chapter is placed on experiments 1-4 for analysis of emulsion transport and deposition behavior.

5.3.2 Modeling Approach

All models employed the following 1-d base formulation:

$$\frac{\partial S_w C}{\partial t} = \frac{\partial}{\partial x}\left(S_w\left(D_m + D_{aq}\tau\right)\frac{\partial C}{\partial x}\right) - \frac{q}{n}\frac{\partial C}{\partial x} + \frac{\rho_b}{n}\frac{\partial S}{\partial t} \qquad (5.1)$$

Where: S_w is the aqueous-phase saturation [-], C is the aqueous-phase concentration [$M \cdot L^{-3}$], D_m is mechanical dispersion [$L^2 \cdot T^{-1}$], D_{aq} is the aqueous-phase diffusion coefficient [$L^2 \cdot T^{-1}$], τ is the tortuosity factor calculated using Millington and Quirk (1961) [-], q is the Darcy flux ($L \cdot T^{-1}$), n is porosity [-], ρ_b is the bulk density [$M \cdot L^{-3}$], and S is the solid-phase concentration [$M \cdot M^{-1}$].

In all cases q, n, and ρ_b are assumed not to vary in time and space. Several alternative modeling approaches are explored herein by employing different formulations for D_m and the exchange term (i.e., $\frac{\rho_b}{n}\frac{\partial S}{\partial t}$). Boundary conditions were of type three and two for the inlet and outlet, respectively; irrespective of the D_m and exchange term formulation. Equation 5.1 was solved numerically in MATLAB R2014a (The MathWorks, Natick, MA) using a finite difference scheme that is fully implicit and central differencing in space (Δx=0.1 cm). The transport and solid-phase interaction equations were solved sequentially by iterating within each time step (Δt=0.04 min, convergence criterion = 10^{-6}). Model discretization parameters were selected after a step size analysis. Fits of model parameters were obtained using *lsqcurvefit* in MATLAB using the objective

functions noted below. Model equations, discretization, and solving details are presented in greater detail in Appendix I: Emulsion Transport Modeling Details.

A hyper-exponential expression (Equation 5.2) was fit to each retention profile to provide a continuous description of the solid phase DP concentration along the column. The model output was used to directly input *S(x)* for the post-injection tracer test fitting.

$$S(x) = S_{\min} + c_1 c_2 e^{-c_2 x} \qquad (5.2)$$

Where: *S(x)* is the solid phase concentration [mg DP·g-sand^{-1}] at distance *x*; S_{min} is the minimum solid phase concentration (at *x=L*); *x* is the distance from the column inlet. S_{min}, c_1 and c_2 are fitted coefficients. The water saturation can be directly related to the solid dispersed phase mass in this system by:

$$S_w = 1 - \frac{S \cdot \rho_b}{\rho_{DP} \cdot n} \qquad (5.3)$$

Where: ρ_b is the bulk density of the porous media [M·L^{-3}]; and ρ_{DP} is the dispersed phase density [M·L^{-3}].

Non-reactive conservative tracer test data were used to quantify D_m before and after emulsion retention by fitting Equation 1 with the exchange term equal to zero. All tracer test simulations employed 1.22×10^{-3} cm^2·min^{-1} for the diffusivity of bromide in water (D_{aq}) (Lide, 1999).

In recognition that D_m may be a function of S_w, the correlations developed in Chapter 4 were tested for applicability for emulsion retention. It is important to note that the models developed in Chapter 4 were based on uniform saturations of entrapped fluids. In contrast, emulsion deposition is thought to be more associated with interactions with the solid phase (deposition and straining) and was found to have spatially variant solid phase concentrations (i.e., hyper-exponential retention). Additionally, the previously developed α correlations employed a single, thus representative, S_w value and thus may not directly applicable for spatial variant water saturations. Hence, for emulsion retention, three more spatially flexible approaches were tested on their ability to describe the influence of retention on dispersivity.

(i) constant α

$$D_m = \alpha \frac{q}{nS_w} \qquad (5.4)$$

(ii) linear saturation dependence

$$D_m = \left(\alpha_0 + M_1\left(1 - S_w\right)\right)\frac{q}{nS_w} \qquad (5.5)$$

(iii) non-linear saturation dependence

$$D_m = \left(\alpha_0 + M_2\left(1 - S_w\right)^N\right)\frac{q}{nS_w} \qquad (5.6)$$

For cases of no saturation dependence (i.e., constant α), Equation 5.1 was fit to the tracer breakthrough curve by adjusting α. When evaluating the saturation-dependent formulations, α_0 was fit to the tracer test data obtained prior to the introduction of the emulsion. Then model parameters (either M_1 or M_2 & N) were adjusted to permit Equation 5.1 to fit the tracer test data obtained after emulsion retention. In these cases, the known retention profiles were input as a hyper-exponential function of dispersed-phase saturation (i.e., $S_w(x)$ was known from the experiments.

5.3.2.1 Modeling Emulsion Transport

Four particle transport model formulations were selected to evaluate the emulsion transport results described herein. In addition two emulsion-specific models were also evaluated. The exchange terms for all six models are described in Table 5.2. Exchange of colloids between the aqueous and solid phases is commonly modulated by either:

(1) a blocking function

$$\psi_b = \left(1 - \frac{S}{S_{\max}}\right) \qquad (5.7)$$

based on the idea that sand grains have a maximum surface capacity (S_{max}) for a given colloid (e.g., Coulibaly et al., 2006; Johnson & Elimelech, 1995; Kasel et al., 2013) or;

(2) depth-dependent function

$$\psi_d = \left(\frac{d_{50} + x}{d_{50}} \right)^{-\beta} \qquad (5.8)$$

Where: β is a fitted parameter to describe the shape of the retention profile with depth and d_{50} is the median grain size (e.g. Bradford et al., 2003; Bradford et al., 2004).

Molecular diffusion of the droplets, as calculated via the Stokes-Einstein equation, was found to contribute < 0.01% to the total dispersion in all cases. Thus, D_{aq} neglected when simulating droplet transport.

Preliminary modeling investigations assessed the difference when fitting models to: (a) breakthrough curve data only, (b) retention profile data only, or (c) to both the breakthrough & retention data simultaneously (results presented in Appendix III). From this analysis, fitting simultaneously to both the BTC and RP data was deemed the best fitting approach and this method was used for all presented model fits hereafter. One interesting finding from this preliminary assessment was as model structure improved, the descriptions of the data provided by the three fitting approaches converged (i.e., fits to the BTC only, RP only, and both BTC and RP offered similar modeled concentrations and fitted parameters). In other words, performance of the model formulations having better descriptions of the underlying physical mechanisms was independent of the fitting approach. It is unclear whether this observation can be generalized into robust indicator for model selection beyond the experiments reported here.

Models were fit to both the breakthrough curve and retention profiles using a an objective function designed to provide equal weight to the breakthrough and retention data as well as each column when a single, simultaneous fit to multiple experiments was conducted (Equation 5.9).

$$Obj = \sum_{i=1}^{r}[0.5\frac{n_{BTC,i}}{n_{BTC,tot}(\frac{C}{C_{0n}})_i^2}\sum_{j=1}^{n_{BTC,i}}(\frac{C}{C_0}_{E_{i,j}} - \frac{C}{C_0}_{M_{i,j}})^2 + ... \\ ...0.5\frac{n_{RP,i}}{n_{RP,tot}(S_n)_i^2}\sum_{k=1}^{n_{RP,i}}(S_{E_{i,k}} - S_{M_{i,k}})^2] \quad (5.9)$$

Where: r is the number of experiments included in the simultaneous fit; i is the experiment index; j is the data point index for BTC; k is data point index for RP; E indicates the experimental measured value whereas M indicates the corresponding modeled value; n_{BTC} is number of data points in BTC; n_{RP} is number of data points in RP; $n_{BTC,tot}$ is number of BTC data points in fit; $n_{RP,tot}$ is total number of RP data points in fit; $(\frac{C}{C_{0n}})$ is normalizing $\frac{C}{C_0}$ value; and S_n is normalizing S value.

$$\frac{C}{C_{0n}} = \frac{m_{BTC}}{PV_T \cdot PV \cdot \frac{C_0}{100} \cdot \rho_e} \quad (5.10)$$

and

$$S_n = \frac{m_{RP}}{m_{sand}} \quad (5.11)$$

Where: m_{BTC} *is* total dispersed phase mass collected in effluent [g]; PV_T is the total number of pore volumes the BTC is collected over [PV]; PV is the column

pore volume [mL]; C_0 is the weight percentage of DP per weight emulsion [g DP·(g total·100)$^{-1}$]; ρ_e= emulsion density [g·mL^{-1}]; m_{RP} is the total dispersed phase mass retained on solids [g]; and m_{sand} is the total mass of sand in column [g].

Emulsion transport model fits were assessed by simultaneously fitting experiments 1 and 2 to each of the specified models to identify the formulation that most accurately describes low concentration emulsion transport and deposition. The SSE_w and the AIC_c were used as statistical measures of model performance. The weighted sum of the squared errors (SSE_w) was computed for each model fit as:

$$SSE_w = \sum_{i=1}^{r}\left[\frac{n_{BTC,i}}{n_{BTC,tot}\left(\frac{C}{C_{0n}}\right)_i^2}\sum_{j=1}^{n_{BTC,i}}\left(\frac{C}{C_{0\ E_{i,j}}}-\frac{C}{C_{0\ M_{i,j}}}\right)^2+\frac{n_{RP,i}}{n_{RP,tot}(S_n)_i^2}\sum_{k=1}^{n_{RP,i}}(S_{E_{i,k}}-S_{M_{i,k}})^2\right] \quad (5.12)$$

Table 5.2: Particle and emulsion transport models selected for evaluation.

Model No.	Processes Modeled	Exchange Term in Equation 5.1	Parameters Typically Fit	Application to Emulsion Transport	Illustrative Applications to Particle Transport
M-1	DEPOSITION WITH LANGMUIRIAN BLOCKING (ONE-SITE)	$\frac{\rho_b}{n}\frac{\partial S}{\partial t} = s_{aq} k_d \psi_b C$ (5.13)	k_d S_{max} (in ψ_b)	Coulibaly et al., 2006	Johnson & Elimelech, 1995 Kasel et al., 2013
M-2	DEPTH-DEPENDENT RETENTION (ONE-SITE)	$\frac{\rho_b}{n}\frac{\partial S}{\partial t} = s_{aq} k_r \psi_d C$ (5.14)	k_r β (in ψ_d)	No emulsion applications found	Bradford, et al., 2003; Bradford, et al., 2004
M-3	DEPTH-DEPENDENT RETENTION WITH LANGMUIRIAN BLOCKING (ONE-SITE)	$\frac{\rho_b}{n}\frac{\partial S}{\partial t} = s_{aq} k_d \psi_d \psi_b C$ (5.15)	k_d S_{max} (in ψ_b) β (in ψ_d)	No emulsion applications found	Kasel et al., 2013

Table 5.2 Cont.

MODEL NO.	PROCESSES MODELED	EXCHANGE TERM IN EQUATION 5.1	PARAMETERS TYPICALLY FIT	APPLICATION TO EMULSION TRANSPORT	ILLUSTRATIVE APPLICATIONS TO PARTICLE TRANSPORT
M-4	DEPOSITION WITH LANGMUIRIAN BLOCKING + DEPTH-DEPENDENT RETENTION (TWO-SITE)	$\frac{\rho_b}{n}\frac{\partial S}{\partial t} = s_{aq}\left(k_r\psi_d + k_d\psi_b\right)C$ (5.16)	k_d k_r S_{max} (in ψ_b) β (in ψ_d)	No emulsion applications found	Gargiulo, et al., 2007
M-5	DEPOSITION (ONE-SITE, EQ 5.1 WITHOUT DISPERSION)	$\frac{\rho_b}{n}\frac{\partial S}{\partial t} = \frac{\lambda_{SI} q}{n}\left(1 - \frac{\alpha^*}{n s_{aq}}\frac{\rho_b}{\rho_{DP}}S\right)C$ (5.17)	λ_{SI} α^*	Soo & Radke, 1986 a,b	
M-6	DEPOSITION WITH SURFACE CAPACITY ISOTHERM (ONE-SITE)	$\frac{\rho_b}{n}\frac{\partial S}{\partial t} = k\left[\frac{S}{K\left(S - S_{\max}\right)} - C\right]$ (5.18)	k K S_{max}	Clayton and Borden, 2009	

5.3.2.2 Modeling Viscous Effects

Viscous effects were incorporated by adapting the method of Flowers and Hunt (2007) which relates viscous mixing to effective dispersion. Koval (1963) described the normalized effluent concentration resulting from viscous fingering using Equation 5.19.

$$\frac{C(PV_D)}{C_0} = \frac{E \cdot H - \sqrt{\frac{E \cdot H}{PV_D}}}{E \cdot H - 1} \quad (5.19)$$

Where: C is the effluent concentration during displacement [$M \cdot L^{-3}$]; PV_D is the volume of displacing fluid introduced normalized by the pore volume of the medium [-]; C_0 is the initial concentration of the viscous (i.e., resident) solution [$M \cdot L^{-3}$]; and H is a heterogeneity factor [-] to account for channeling and dispersion (i.e., physical heterogeneities). E in Equation 5.19 is the effective mobility ratio [-], and defined for miscible solutions as:

$$E = \left[K_a + (1 - K_a)\left(\frac{\mu_r}{\mu_d}\right)^{0.25} \right]^4 \quad (5.20)$$

Where: K_a is the mixing ratio in the fingering zone [-], which was approximated by Koval to be 0.78; μ_r and μ_d are the resident and displacing solution viscosities [$M \cdot L^{-1} \cdot T^{-1}$]. Note that Koval specifies that this equation is only valid during the breakthrough of the less viscous solution - a period Koval defined as being between $(H \cdot E)^{-1}$ and $H \cdot E$.

Flowers and Hunt (2007), suggest rearranging Equation 5.19 for PV_D in order to substitute the expression into a dimensionless form of the approximate analytical solution (Freeze and Cherry, 1979). The validity of the approximate analytical solution is highest at high Peclet number (*Pe*). Viscous instabilities, however, create conditions effectively increase mixing (i.e., effectively decrease *Pe*). Thus, here the Koval solution is linked to the more robust Ogata and Banks (1961) solution to the advection-dispersion equation. The goal here was to produce an expression for a dispersion-like term, D_{vis} that can be added to existing formulations of D_m to capture the influence of viscous effects on mixing when assessing the applicability of colloid transport models across a wide range of emulsion concentration. Substitution of Equation 5.19 (rearranged to be in terms of PV_D) into the dimensionless analytical solution of Ogata and Banks produces an expression that can be solved iteratively to determine the dependence of *Pe*, and thus D_{vis}, on the product E·H. The solution, for $\frac{C}{C_0}$ of 0.9 as per Flowers and Hunt (2007), is shown in Equation 5.21, respecting the bounds Koval placed on his solution in terms of PV_D. Additional details on equation development are given in background Section 1.18.5.1.

$$D_{vis} = \begin{cases} 0.135\frac{qL}{ns_{aq}}(E\cdot H-1)^{1.85} & (E\cdot H)^{-1} < PV_D < E\cdot H \\ 0 & PV_D < (E\cdot H)^{-1} \;\&\; PV_D > E\cdot H \end{cases} \quad (5.21)$$

All terms in Equation 5.21 other than *L*, the column length [*L*], have been previously defined.

5.4 RESULTS AND DISCUSSION

5.4.1 EMULSION PROPERTIES

GA-stabilized oil-in-water emulsions were examined at dispersed phase contents between 1.3 and 23% wt. Emulsion droplets have a d_{50} between 1.0 and 1.5 μm, and zeta potentials from -30 and -35 mV. The kinetically-stable, oil-in-water emulsions empolyed in the column experiments had densities between 0.992 and 0.998 g/mL and viscosities between 1 and 10 mPa·s. Emulsion density varies less than 0.6% across approximately an order of magnitude of dispersed phase content. This suggests that phase density can be assumed to be independent of the amount of deposition occuring during transport or the influent emulsion content (i.e., temporal and spatial derivitatives of phase density can be assumed to be zero). In constrast, emulsion viscosity varies by an order of magnitude over the same range of dispersed phase content, suggesting viscous instabilities may influence emulsion transport (i.e., mobility ratio greater than 1).

5.4.2 EMULSION RETENTION

Over the length of the laboratory columns, droplet retention was found to follow a hyper-exponential pattern with signficiant mass retained nearest the column inlet and decreasing rapidly to a minium concentration plateau (Figures 5.1 and 5.2). A hyper-exponential expression was successfully fit to all columns. Fitted model parameters are noted in Table 5.4.

When considering deposition on Federal Fine Ottawa sand (i.e., experiments 1-4), the influence of input concentration is clear. For the dilute columns maximum retention did not exceed 8 mg DP·g-sand^{-1} and the plateau minimum concentration values were around 2 mg DP·g-sand^{-1} (although it is possible that that the plateau concentration may have increased slightly between experiments 1 and 2 following an increased input concentration). As compared to concentrated emulsions where the maxium solid phase conentrations reached 50 mg DP·g-sand^{-1} with plataeu concentrations at around 20 mg DP·g-sand^{-1}. This influence of input concentration on solid phase concentrations (at further distances away with from the injection point) is an important finding and will be investigated further in this chapter.

Experiments conducted on different porous media or size fraction (i.e., experiments 5-7) suggest that retention may be effected by the physical properties of the sand (i.e., d_{50} and U_i). Droplet retention on 20-30 mesh sand was found to have limited retention (Figure 5.2), possibly releated to the larger median grain size of 0.071 cm. Retention on the more graded F-95 Ottawa sand had similar retention (max retention = 60 mg DP·g sand^{-1}; constant plateau concentration=20 mg DP·g sand^{-1}) to that of the graded Federal Fine sand. Although F-95 has the smallest median grain size (d_{50}=0.018 cm) of the media examined herein, it was found to have similar retention characteristics to FF (Figure 5.2). Both of these materials are similarly graded ($U_{i,F\text{-}95}$ =1.46; $U_{i,FF}$ =1.65) and represent broader particle size distributions than do the 20-30 or 60-80 fractions. The greatest retention occurred on the 60-80 fraction (Figure 5.2) where porosity was greatest.

While not definative, results suggest that retention processes sensitive to the pore size distribution (e.g., straining) may have a key role in the transport of these concentrated emulsions.

Table 5.3: Experimental column parameters and results.

experiment	porous media	porosity	bulk density	packed length	pore volume	measured flow rate	initial dispersivity	dispersed phase content	measured viscosity	modeled viscosity [c]	mobility ratio	emulsion introduced	recovered in effluent	retained in column	mass balance	nBTC	nRP
		n	ρ_b	L	PV	Q	α_0	C_0	μ	μ_e	M				MB		
		[-]	[g·cm^{-3}]	[cm]	[mL]	[mL·min^{-1}]	[cm]	[% wt.]	[mPa·s]	[mPa·s]	[-]	[PV]	[g]	[g]	[%]		
1A	FF	0.38	1.65	9.8	67.7	1.05	0.028	1.25 (±0.1)	n.m.[a]	1.4	1.5	2.6	1.42	0.65	98	32	11
1B	FF	0.38	1.65	9.8	67.2	1.03	0.034					2.6	1.36	0.75	101	32	11
2A	FF	0.36	1.70	10.4	68.1	1.06	0.042	2.32 (±0.0)	1.6 (±0.1)	1.6	1.7	2.3	2.77	0.89	102	28	10
2B	FF	0.36	1.71	10.3	66.6	1.02	0.052					2.3	2.65	0.94	104	24	10
3A*	FF	0.38	1.64	10.4	71.9	1.03	0.084	22.7 (±0.4)	7.9[b]	7.5	7.9	2.4	28.3	5.91	98	32	10
3B*	FF	0.37	1.68	10.2	67.8	1.03	0.072					2.5	30.5	5.73	100	32	10
4	FF	0.36	1.69	10.4	68.6	1.00	0.021	23.0 (±0.1)	7.8 (±0.1)	7.8	8.2	3.0	38.1	7.44	100	65	10
7	20-30	0.36	1.69	10.4	68.9	0.75	0.073	23.0 (±0.1)	7.8 (±0.1)	7.8	8.2	2.3	29.3	3.10	100	77	9
8	F-95	0.40	1.59	9.8	71.4	1.01	0.044	23.4 (±0.2)	9.0 (±0.1)	8.1	8.5	2.5	31.3	6.4	100	74	10
9	60-80	0.41	1.58	10.2	75.0	0.96	0.021					2.3	25.2	10.5	98	74	10

* alkalinity-releasing particles were present in emulsion

[a] not measured due to insufficient sample volume

[b] single measurement

[c] emulsion viscosity modeled using expression presented in Chapter 3 based on Sibree (1930) and Broughton and Squires (1937) μ_d is the displacing fluid viscosity. These experiments used water as the displacing fluid; μ_d =0.954 mPa·s (i.e., the viscosity of water at 22°C)

± indicates standard deviation

Table 5.4: Emulsion deposition parameters and corresponding hyper-exponential model fits.

Column	S_w **at column inlet**	$S_{,min}$	c_1	c_2	***SSE***
	measured[a]/ modeled[b]	[mg DP·g sand^{-1}]			
1A	0.98/0.96	1.16	1.06	7.62	0.8
1B	0.97/0.95	1.37	1.17	8.06	1.6
2A	0.84/0.80	1.82	1.13	2.99	0.3
2B	0.84/0.80	2.08	0.95	5.17	0.2
3A	0.77/0.68	15.36	4.45	6.44	1.6
3B	0.98/0.96	14.08	5.12	5.37	1.6
4	0.97/0.95	14.04	11.05	4.84	4.7
7	0.93/0.91	3.69	4.08	3.90	26.7
8	0.77/0.70	26.78	14.89	5.48	17.4
9	0.67/0.55	14.28	11.44	4.93	4.5

[a] water saturation measured from the column section nearest to the column inlet. Section distances varied for each experiment but were taken at approximately at x=0.5 cm.
[b] water saturation values extrapolated to x=0 cm (i.e., column inlet) from the fit hyper exponential models (retention profile fits are shown in Figures 5.1 and 5.2.
n.c. post injection tracer tests was not conducted.

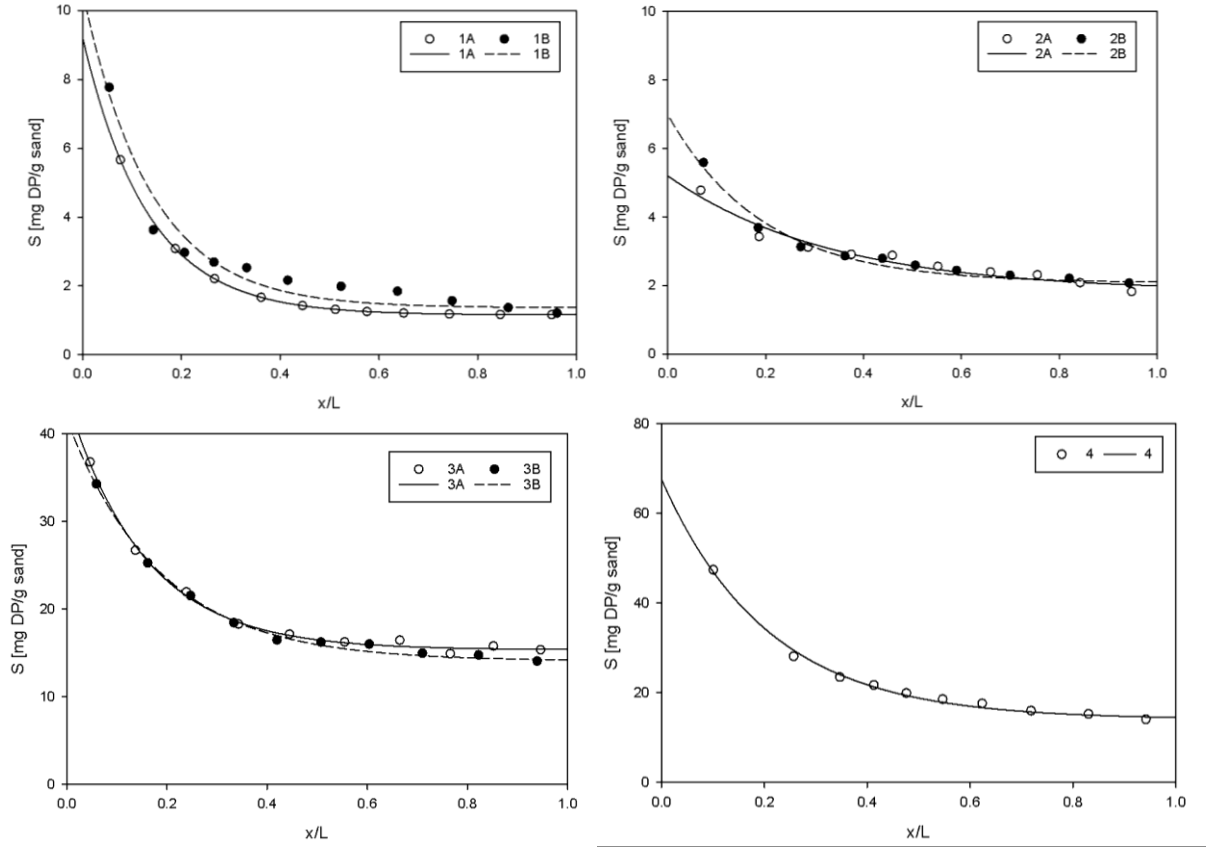

Figure 5.1: The effect of input concentration on emulsion retention on Federal Fine Ottawa sand. Experiment data is shown with circle and the corresponding hyper-exponential model fits with lines. Influent concentrations were 1.25, 2.32, 22.7 and 23.0 % (wt.) for experiments 1-4, respectively.

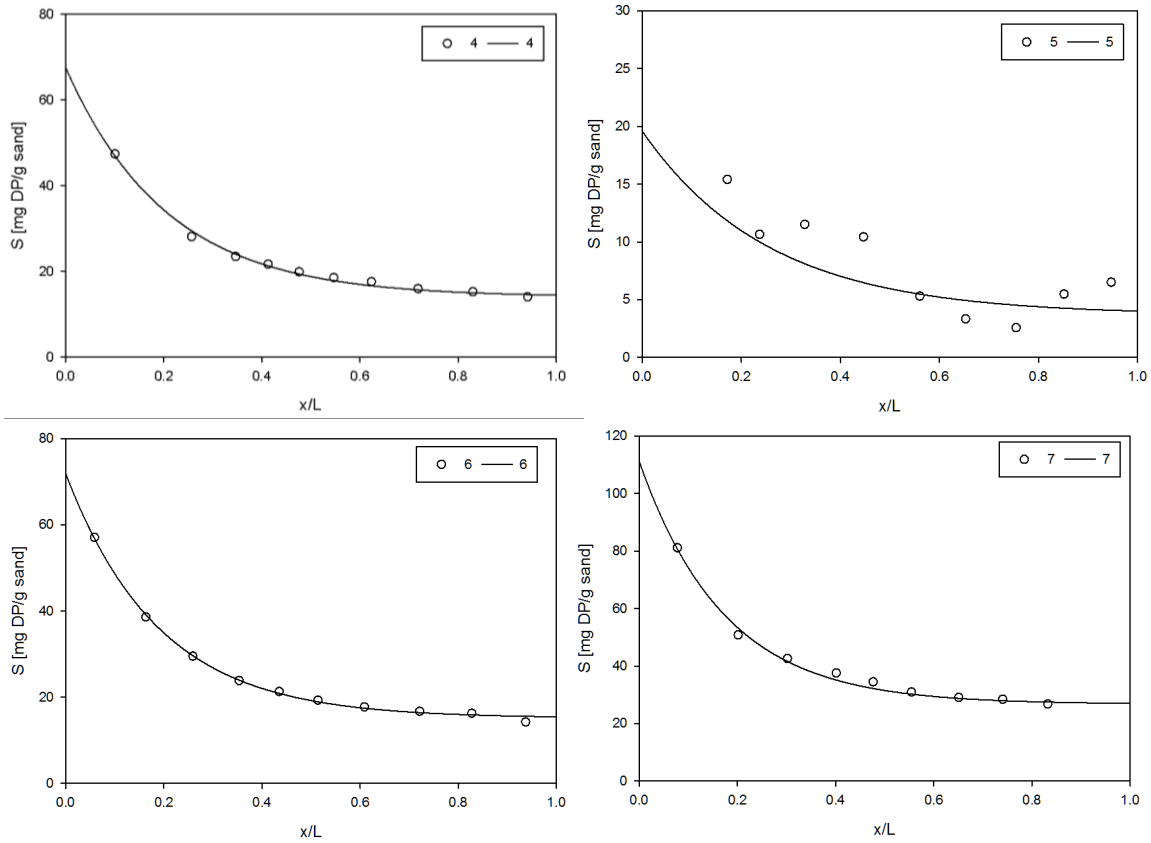

Figure 5.2: The effect of porous media on emulsion retention (C_0~23% wt.). Experimental data is shown with circles and corresponding hyper-exponential model fits with lines. Emulsion retention profiles shown for Federal Fine (top-left experiment 4); 20-30 sand (top-right, experiment 5); F-95 Ottawa sand (bottom-left, experiment 6); and 60-80 mesh Ottawa sand (bottom-right, experiment 7).

5.4.3 DISPERSIVITY

Changes in S_w alter the average pore-water velocity and, consequently, the amount of mechanical dispersion. Mechanical dispersion was found to increase by an order-of-magnitude between the pre- and post-emulsion tracer tests, and could not be accounted for through velocity alone. Unlike in the complied literature dataset (Chapter 4), here, water saturation varied along the length of the experimental column. The partially saturated dataset experiments (i.e., the experiments the Chapter 4 correlations were developed on), both the air-water or NAPL-water systems were uniformly saturated in space. This is a stark contrast from the emulsion column experiments where the distribution of retained oil droplets was strongly spatially variant (i.e., hyper-exponential deposition). Additionally, the pre-emulsion tracer test α value were used (following the method used in Chapter 4) to predict mixing through the fitting on K to the emulsion column dataset. The functionality of Equation 4.16 between $\alpha_{sw=1}$ and S_w holds, albeit with a different constant of proportionality (K). For the non-uniform emulsion deposition, K=2.9 was fit to the experiment data when using the measured S_w values nearest the inlet (adj-R^2 =0.27 and NSE =0.27) and K=3.0 using the hyper-exponential modeled S_w values at x=0 (adj-R^2 =0.33 and NSE =0.33). Recall that the value of K for the uniform saturation experiments was 2 (Section 4.5). The reason for the different coefficient is not immediately apparent; though the initial tracer tests for these emulsion experiments were

conducted at relatively high *Pe* (125-400) (see Section 4.4.2 for additional discussion).

Table 5.5: Dispersivity (shown in cm) changes resulting from emulsion retention.

Column	$\alpha_{,sw=1}$ [a]	$\alpha_{,sw<1}$ [a]	$\alpha_{,sw<1}$ *predicted using Eq 4.16*	
			measured S_w	modeled S_w
1A	0.03	0.03	0.09	0.08
1B	0.04	0.04	0.11	0.12
3A	0.08	0.29	0.29	0.31
3B	0.07	0.26	0.25	0.27
4	0.02	0.29	0.09	0.10
5	0.06	0.13	0.19	0.20
6	0.03	0.17	0.12	0.13
7	0.01	0.54	0.04[d]	0.06[d]

[a] fit using developed finite difference model for non-reactive transport in MATLAB. The effect of molecular diffusion is accounted for directly in the model formulation and α is solved for directly in the ADR

[b] excluded from model fit of Equation 4.16 ($\alpha_{Sw<1}(cm) = K \cdot \alpha_{sw=1} \cdot S_w^{-1.0}$) that produced K=2.9 and K=3.0 when using the measured and modeled values of S_w. Modeled values refer to the hyperexponential fits.

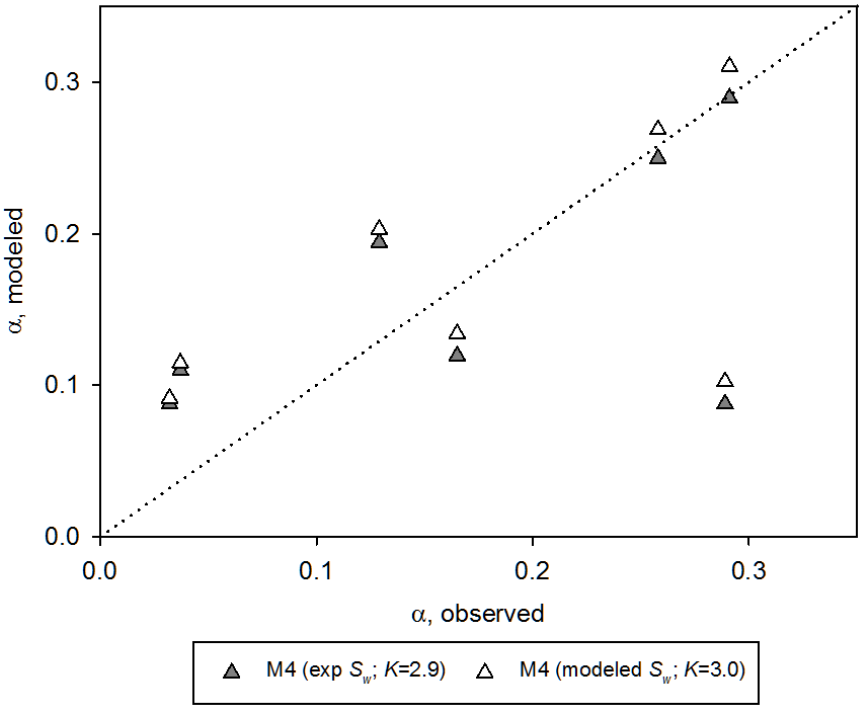

Figure 5.3: Performance of Equation 4.16 for describing changes in dispersivity resulting from emulsion retention. Measured and modeled values of S_w are described in Section 5.6.2.

Although, it is possible to fit (or predict) a constant dispersivity (α) value from pre and post deposition tracer tests, this approach is better suited for systems with constant water saturation. Thus, in attempt to describe dispersive mixing resulting from non-uniform emulsion retention linear and nonlinear formulations linking mechanical mixing to emulsion retention were explored. First individual columns were fit to the dispersion models, followed by simultaneous fits of only the FF columns (1A, 1B, 3A, 3B) (Figure 5.4). Simultaneous fits of each D_m model to experiments 1 and 3 suggest that both the linear (AIC_c = -155.1) and nonlinear (AIC_c = -156.5) models provide very similar value in describing the non-reactive tracer transport (Figure 5.4). Moreover, model parameters fit to data from experiments 1 and 3 (M_1=19.6; M_2=37.6, N=1.26) provide good predictions for the post-emulsion tracer data obtained from experiment 4 which was conducted at high input concentration and independent of those used in the fitting. While either the linear or nonlinear model appears well capable of providing the desired predictive capability (Figure 5.4f), the nonlinear model was selected for subsequent use given the slightly lower AIC_c.

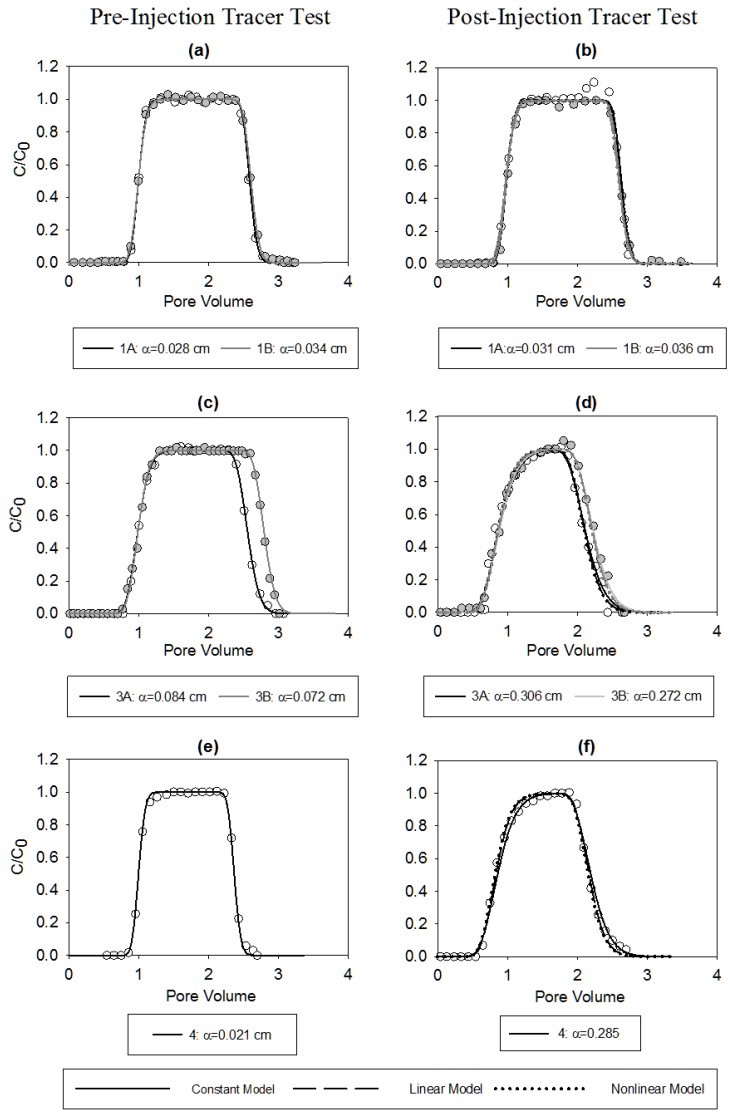

Figure 5.4: Non-reactive tracer test results before (left) and after (right) emulsion injection. (a) pre-injection and (b) post-injection tracer tests with corresponding constant, linear, and nonlinear models for experiment 1 (c) pre-injection and (d) post-injection tracer tests for experiment 3 (e) pre-injection and (f) post-injection tracer tests for experiment 4. Circles indicate the experimental data for the A replicate (open) and the B replicate (closed) of each experiment. The constant alpha model fits are indicated by solid lines with the fitted α value given for each column respectively; the linear model is shown with dashed lines; and the nonlinear model shown with the dotted lines. (f) Gives the prediction of the linear and nonlinear models for column 4. Column 4 data is not included in the linear and nonlinear model fits.

5.4.4 Emulsion Transport

Results from experiment 1 (1.3 % wt.) show a rise across the 'top' of the breakthrough curves (BTCs) and hyper-exponential retention profiles (RPs) (Figure 5.5 a-b). While the RPs in experiment 2 (2.3% wt.) are also hyper-exponential, the rise in the BTCs appears more muted and rounded (Figure 5.5 c-d). Results from experiment 3 (23% wt.) also show hyper-exponential retention, but the influence of retention on the BTC appears limited. More noticeable in the BTC are the approach of the effluent concentration to that of the influent, an early fall (i.e., early breakthrough of the post-emulsion flush), and pronounced tailing of the emulsion pulse. Remobilization of the retained mass was found to be insignificant even after periods of extended flushing (data shown in Chapter 7). The fraction of mass retained in experiments 1, 2 and 3 was approximately 0.33, 0.25, and 0.17, respectively. While these fractions and the BTCs suggest an increasingly more limited role of retention with increasing influence concentration, there is substantial mass retained in all cases (Figure 5.5). At lower influent concentrations (experiments 1 and 2), maximum retention is <10 $mg \cdot g^{-1}$, which corresponds to <3% of the pore space (Figure 5.6). The limited influence of retention on aqueous-phase saturation suggests that the widely employed assumption of $S_w = 1$ (and it being spatially and temporally invariant) may be reasonable when describing the emulsion transport at low concentration and over short pulse duration. In contrast, solid phase concentrations between 35 and 50 $mg \cdot g^{-1}$ were observed near the column inlet in experiment 3 and 4. Note

that retention was greater with the longer duration pulse used in experiment 4. Near-inlet solid-phase concentrations in experiments 3 and 4 represent a decrease in the aqueous-phase pore space of 15 to 23%. Moreover, S_w was less than 0.9 over the first 2 cm of the 10 cm column (Figure 5.6). Thus, caution should be used when attempting to model the transport of concentrated emulsions (or very long duration injections of lower concentration of emulsions) without considering the influence retention may have on the validity of a selected transport model.

Two major distinctions occurred as input concentrations were increased from dilute to high concentrations: 1) mechanical mixing conditions went from relatively constant to highly variable in space and time, as evidenced by the comparison of the pre and post-injection tracer tests (Figure 5.4); and 2) the visual evidence of viscous fingering was seen at high concentration (Figure 5.8). These two additional mechanisms are hypothesized to be increasingly important with increasing concentration were added directly to the particle transport model formulation fitted to the dilute systems. The influence of input emulsion concentration on tailing is shown in Figure 5.7 and compared to model simulations for tracer transport conducted using a uniform value of dispersivity. Experimental breakthrough curves showed extended tailing behavior at high emulsion concentrations as evidenced through the stark contrast to the corresponding forward model simulation. The influence of mass deposition was taken into account by employing the updated aqueous transport expression to allow for temporal and spatial variations in water saturation and mechanical dispersion. The effect viscous instabilities can be seen visually in high

concentration column experiments (experiments 3 and 4) when the emulsion pulse is followed by an aqueous 10 mM NaCl flush solution (Figure 5.8) show the less viscous aqueous flush solution penetrating the emulsion creating a non-uniform flow front as the emulsion exits the column. The effect of viscous instabilities was modeled through the additional viscous dispersion term.

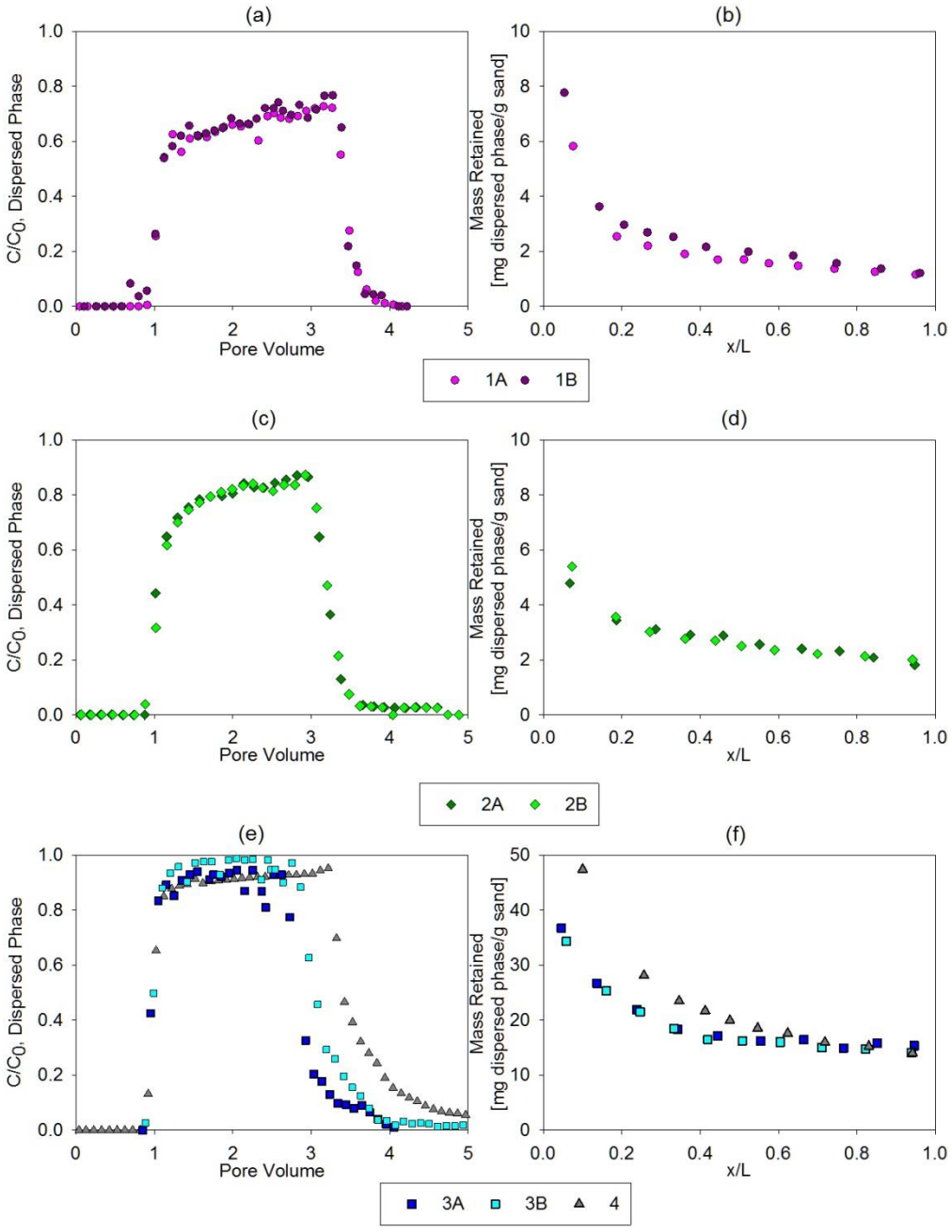

Figure 5.5: Emulsion breakthrough curves (left) and retention profiles and (right). Note the change in y-axis ranges used in panels a-d are different from that used in panels e and f.

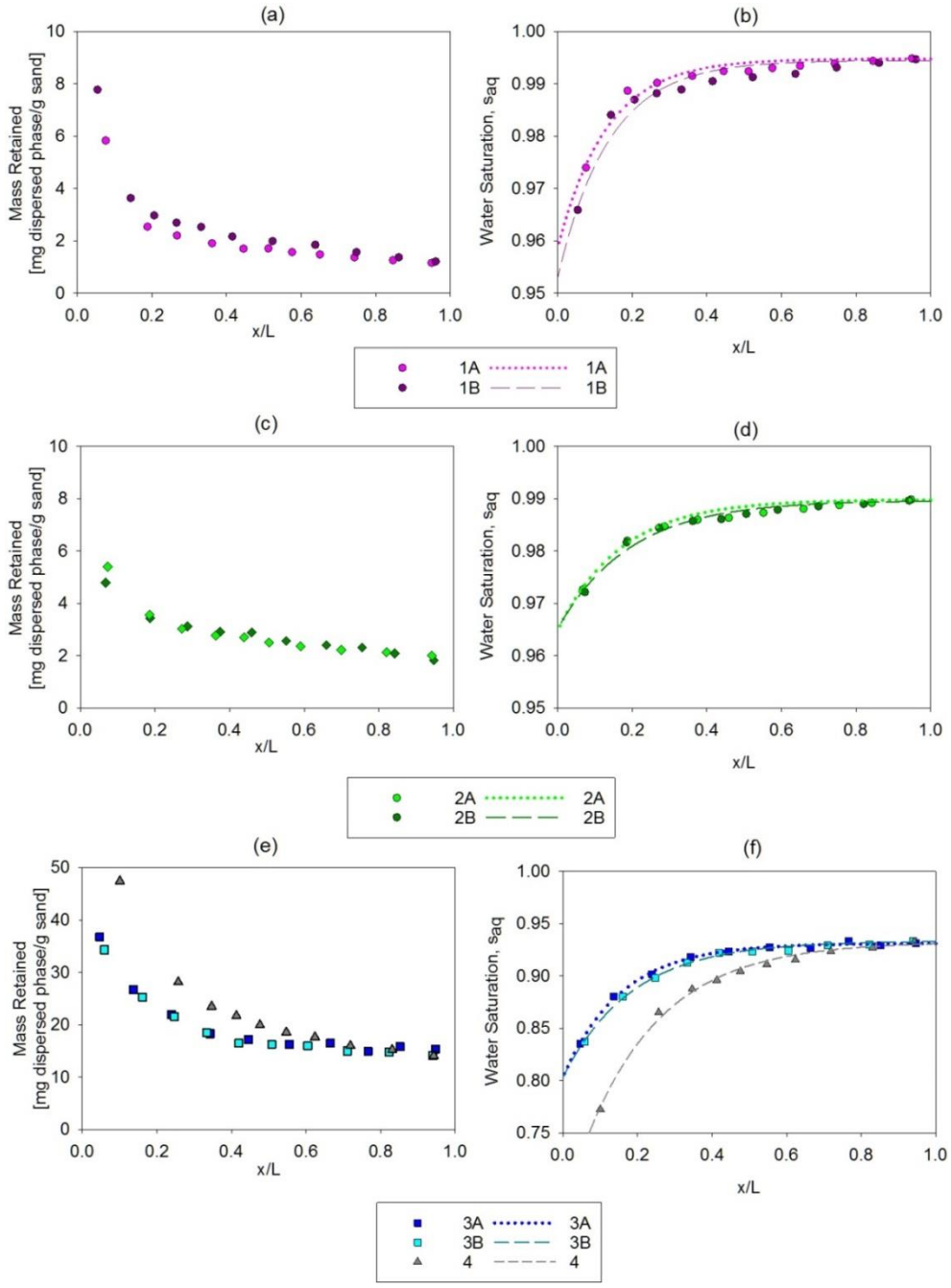

Figure 5.6: Influence of emulsion deposition on water saturation. (left) retention profiles and (right) corresponding water saturation. Circles represent measured values and lines represent hyper-exponential fitted models using Equation 5.2.

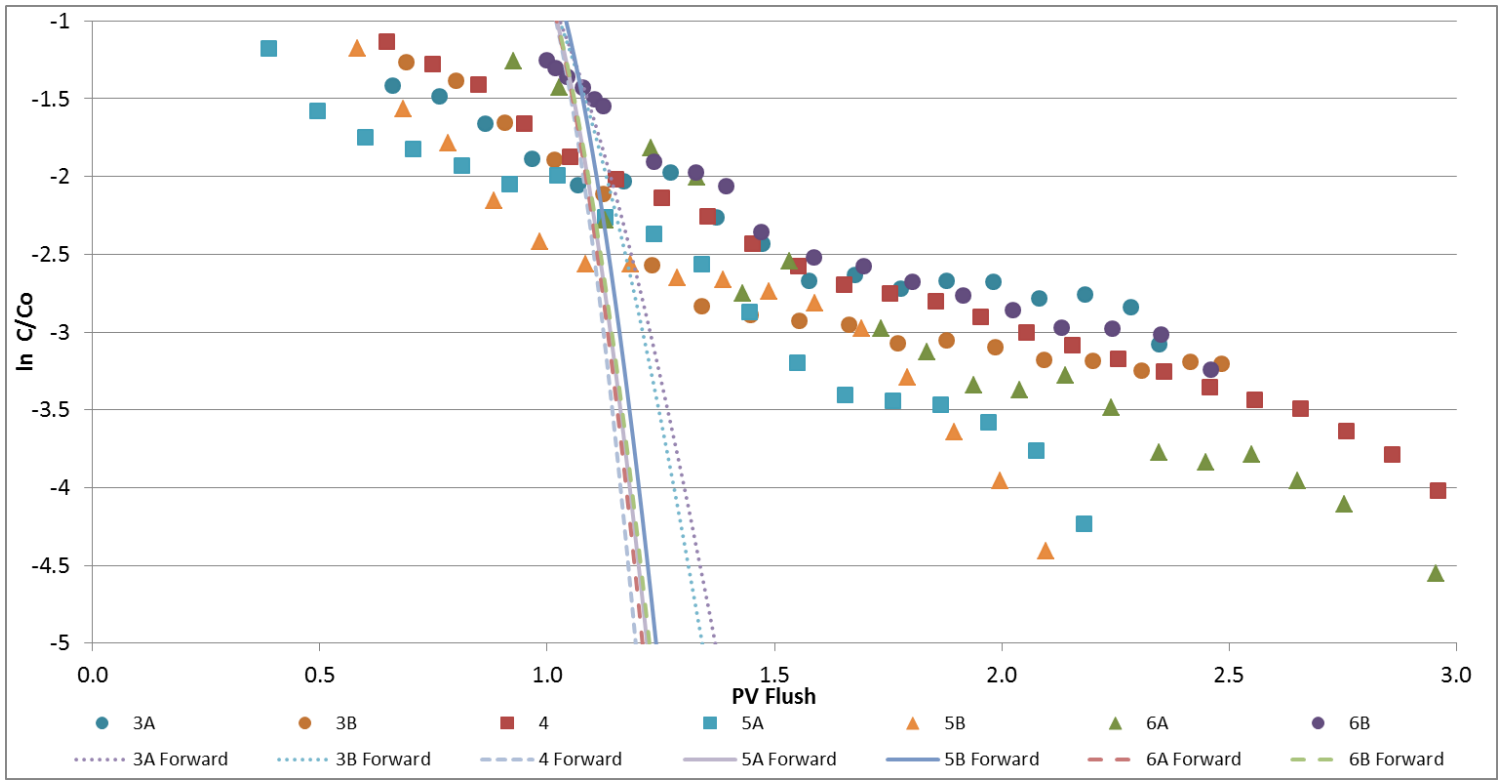

Figure 5.7: Tailing analysis for highly concentrated column experiments conducted in FF sand. Lines represent CXTFIT simulations of a non-reactive tracer with a uniform dispersity equal to that obtained from the post emulsion tracer tests.

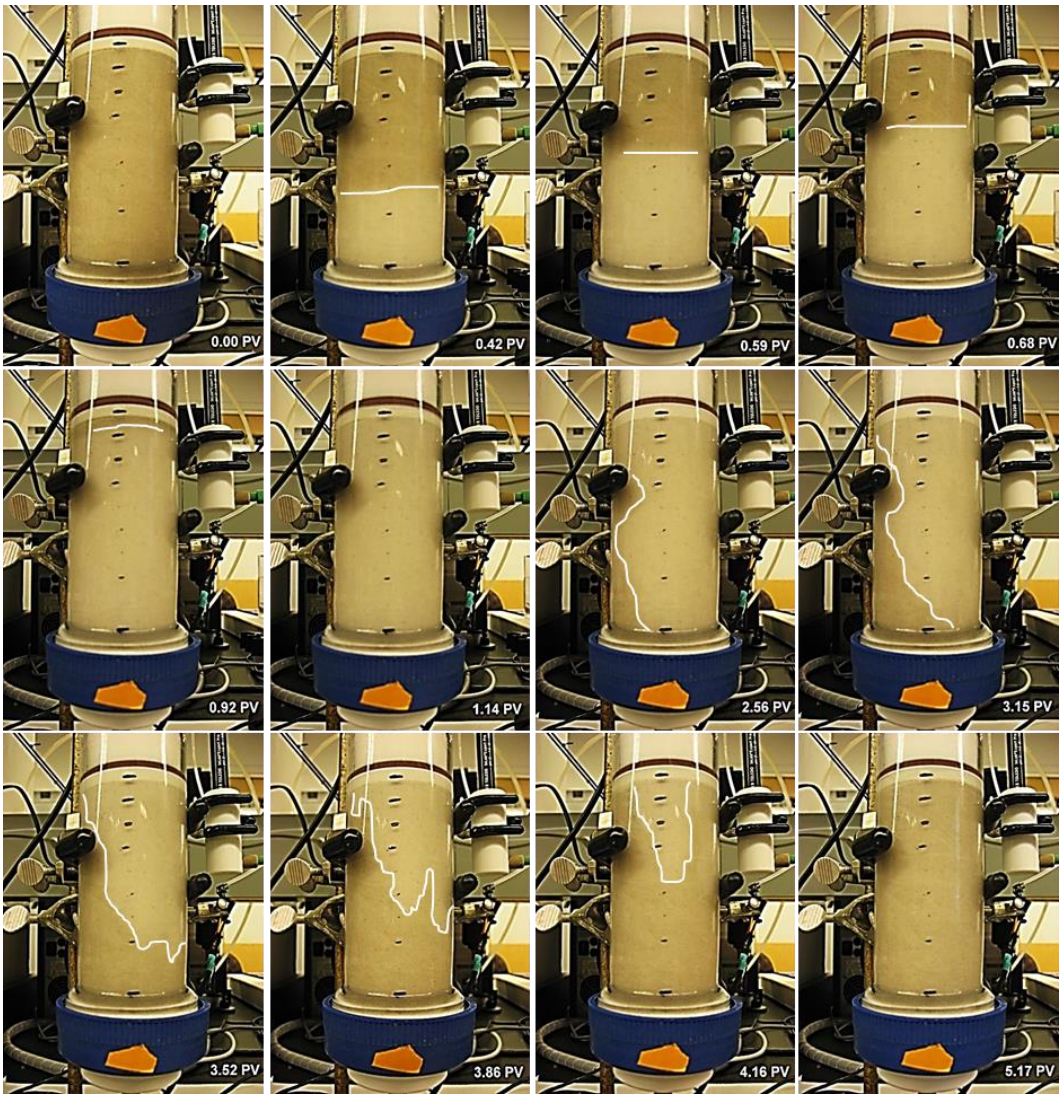

Figure 5.8: Injection of emulsion and subsequent flush. (left to right starting at the top) photos taken at 0.00, 0.42, 0.59, 0.68, 0.92, 1.14, 2.56, 3.15, 3.52, 3.86, 4.16, and 5.17 pore volumes. PV emulsion injected=2.42. Lines are drawn in to illustrate flow front.

Experimental observations noted above provide insight into selection of an appropriate exchange term for use in Equation 5.1. The lack of difference between RPs quantified after 5 and 50+ pore volumes (representative results shown in Chapter 7) of flushing suggests remobilization can be neglected. In fact, preliminary fits allowing for droplet remobilization to occur also suggest remobilization is negligible. In terms of retention processes, the typical first-order processes that exclude surface capacity cannot produce the rise observed in experiment 1. This suggests inclusion of ψ_b may be necessary; however, this term alone is insufficient to modify the first-order retention process as evidenced by the hyper-exponential RPs (i.e., depth-dependent retention). Therefore, the experimental observations suggest the need to consider both ψ_b and ψ_d when evaluating the exchange term in Equation 5.1. The need for both ψ_b and ψ_d also becomes apparent when examining results of fitting the six models to experiments 1 and 2 (see Table 5.2 for additional description of models). Best fits of models M-1, M-2, M-5 and M-6 all fail to produce key features in the BTCs and RPs (Figures 5.9-5.14). Thus, focus was placed on evaluating models M-3 and M-4 (Figures 5.11 and 5.12).

M-3 and M-4 both employ a maximum retention capacity and depth-dependent retention. The key distinction between these models lies in how these terms are combined. M-3 is a one-site model where total retention is modulated by both ψ_b and ψ_d. M-4 conceptualizes retention as resulting from two processes occurring simultaneously: (i) depth dependent retention likely resulting from droplet straining; and (ii) attachment of the droplets to sand particles that is

limited by a surface capacity. The linear combination of the two processes permits the modeled BTCs to show evidence of S_{max} at lower influent concentrations (1-2 % wt. for these column lengths). At higher influent concentrations the fraction of mass retained due to attachment is small relative to the overall masses input and retained. Thus, there is little evidence of S_{max} at high concentration. Importantly, this effect can lead to misidentification of transport processes and model parameters if transport of only higher concentration transport is examined (i.e., fitting of model M-4 requires the maximum relative concentration in the experimentally determined BTC be much less than one).

Although, the selected models are able to describe low concentration behavior, none of the tested models (along with the other model formulations for colloid transport) are able to describe: 1) the early fall of the backside of the breakthrough curve; nor 2) the extended tailing seen at high emulsion concentrations (See Figures 5.15 and 5.16).

5.4.4.1 Low Concentration Emulsion Transport Modeling

At low concentration, emulsion columns exhibited a rising plateau on the breakthrough curve and hyper-exponential retention (Figure 5.5). These experimental characteristics were used when identifying potential model formulations (Goldberg et al., 2014). The six potential model (M1-6) were assessed on the ability to describe relatively dilute emulsion transport (i.e., defined here as when dispersed phase accounts for 1-3% of total emulsion).

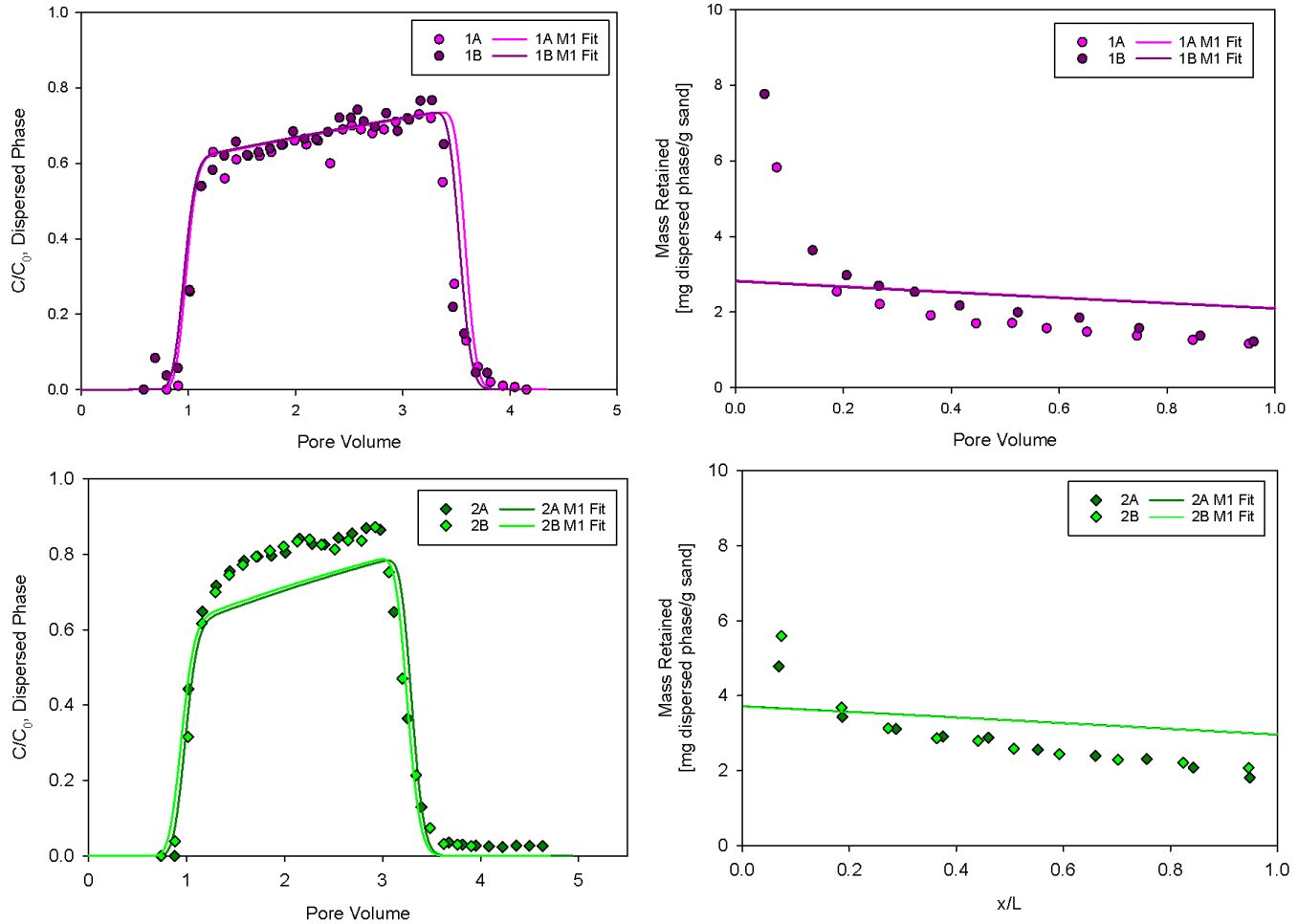

Figure 5.9: M-1 emulsion transport and retention fits to dilute experiments 1&2.

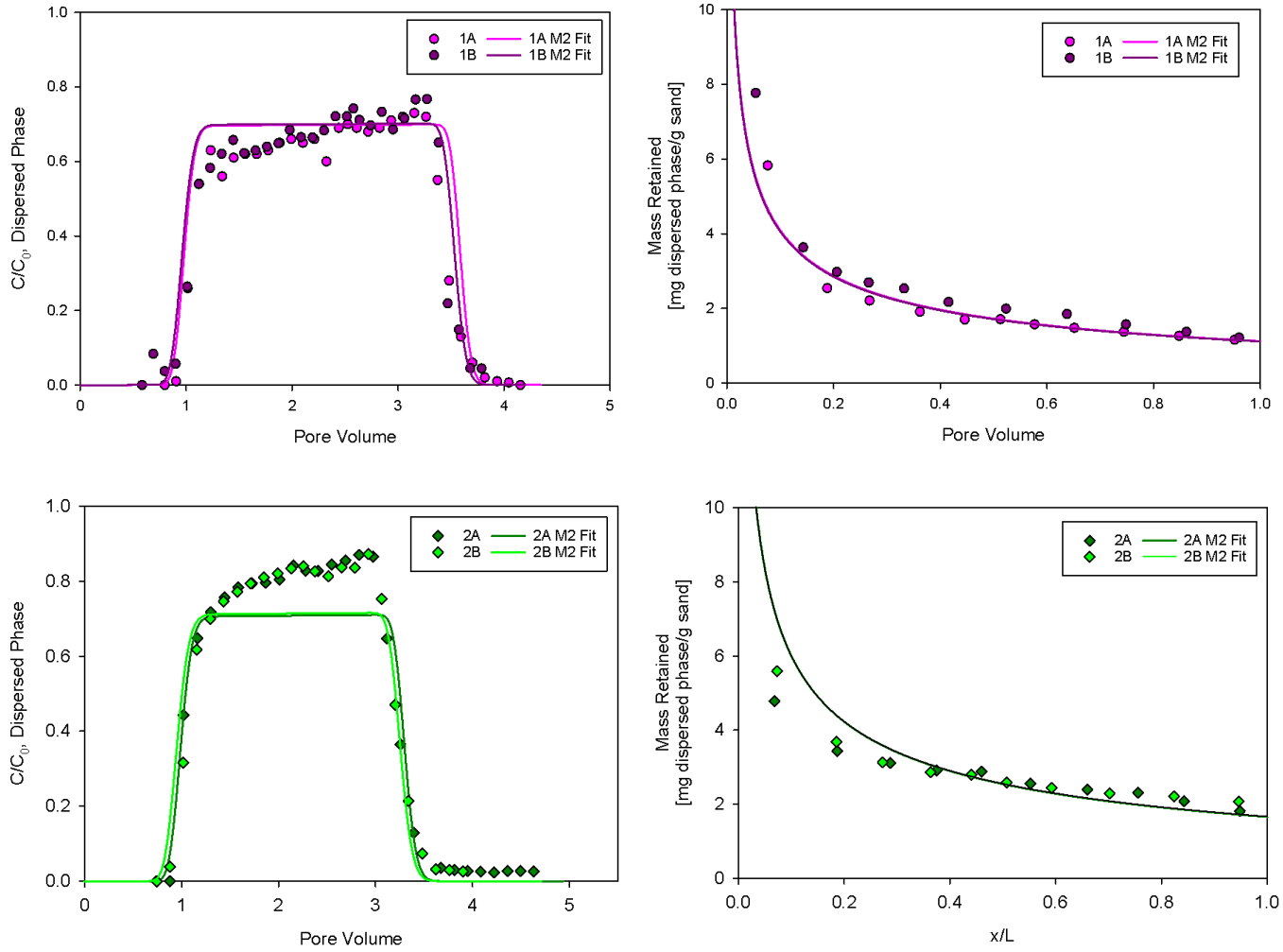

Figure 5.10: M-2 emulsion transport and retention fits to dilute experiments 1&2.

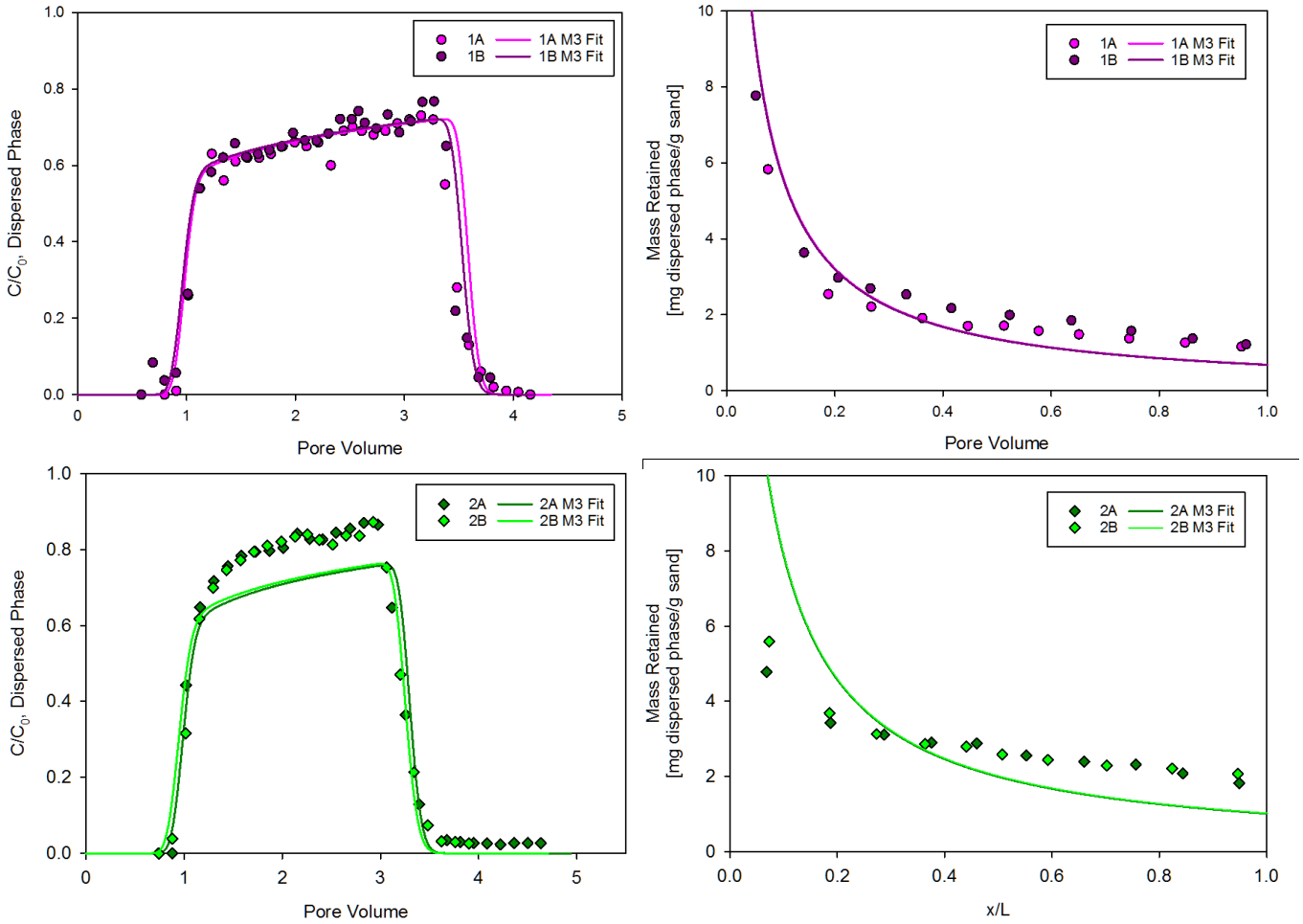

Figure 5.11: M-3 emulsion transport and retention fits to dilute experiments 1&2.

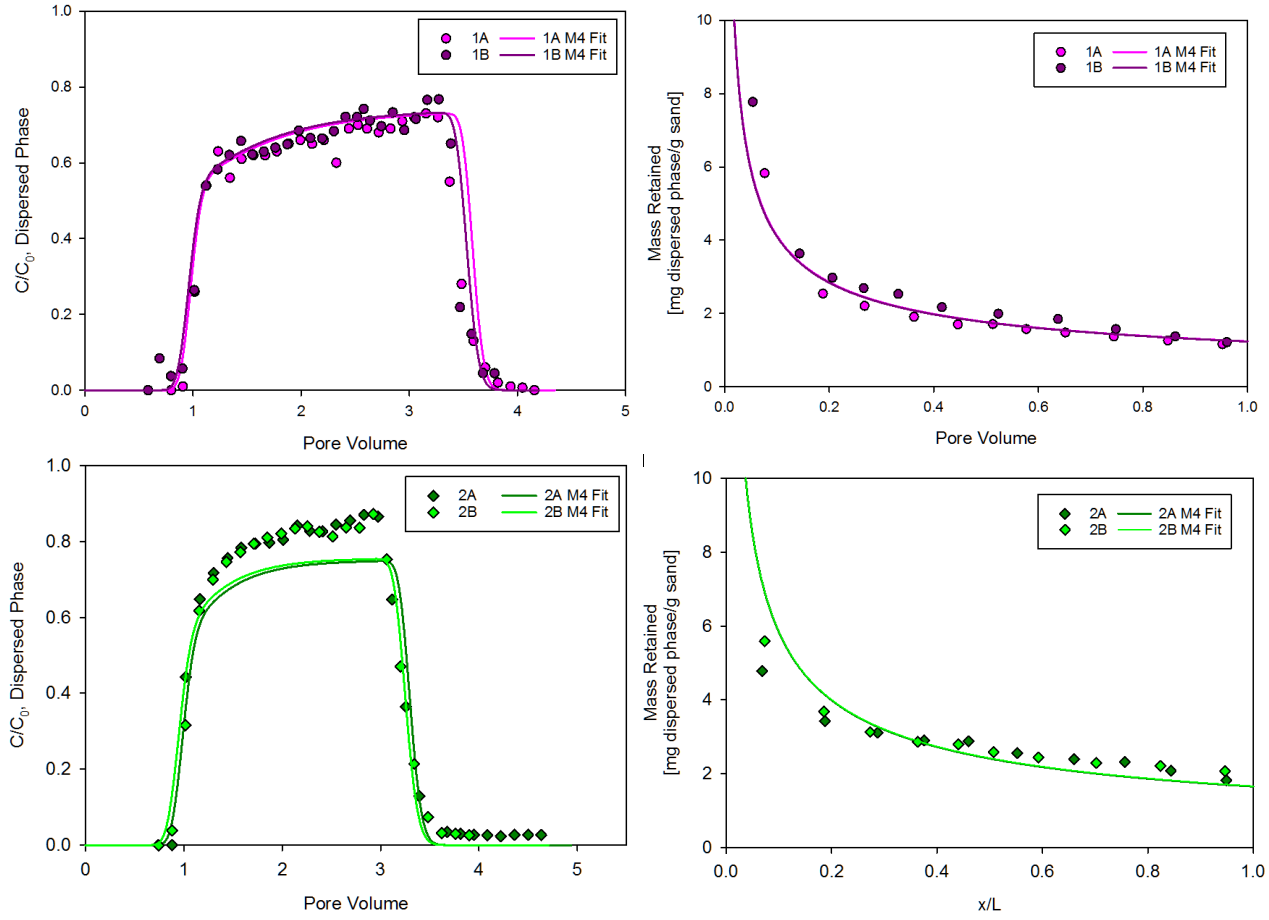

Figure 5.12: M-4 emulsion transport and retention fits to dilute experiments 1&2.

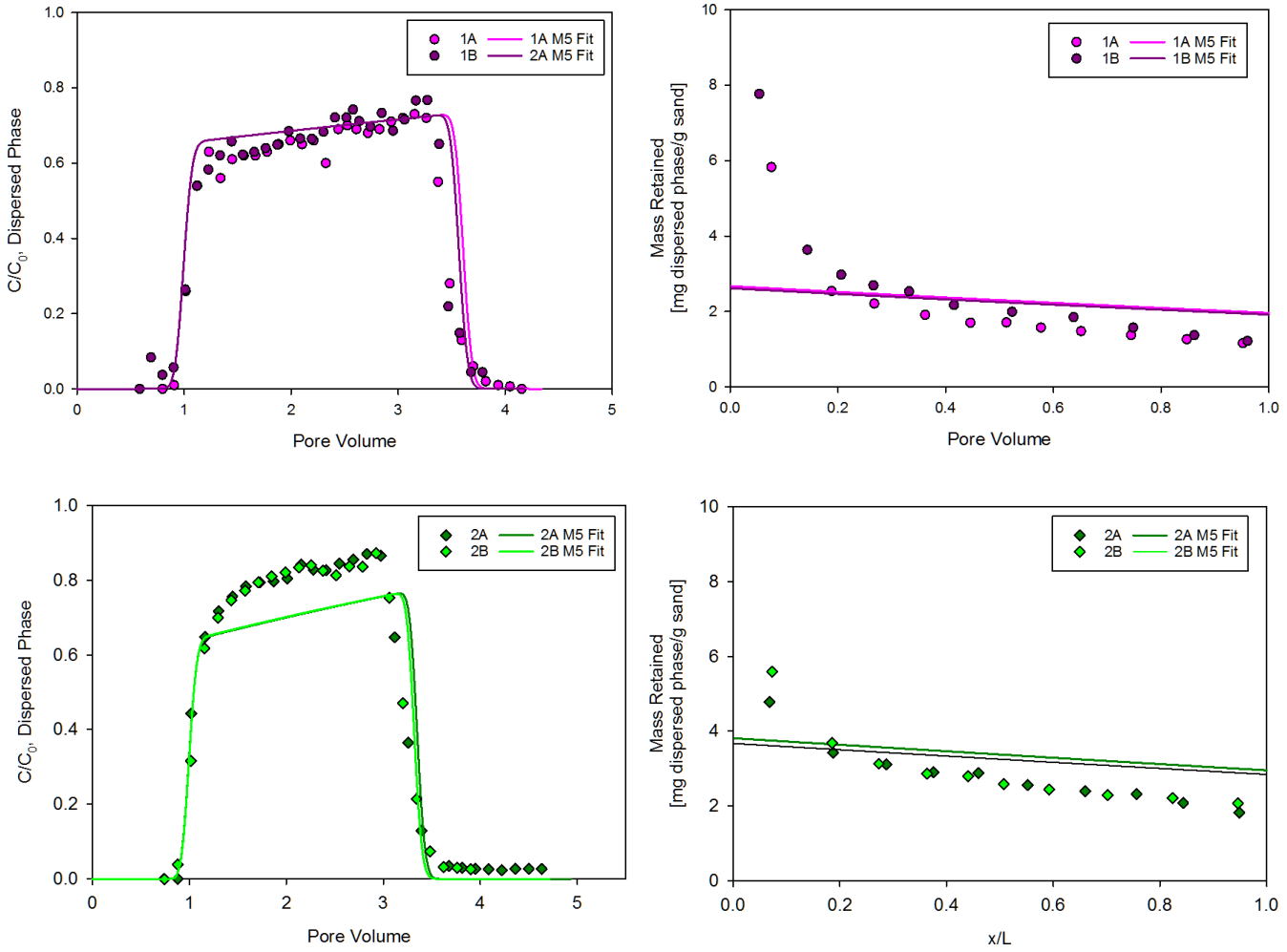

Figure 5.13: M-5 emulsion transport and retention fits to dilute experiments 1&2.

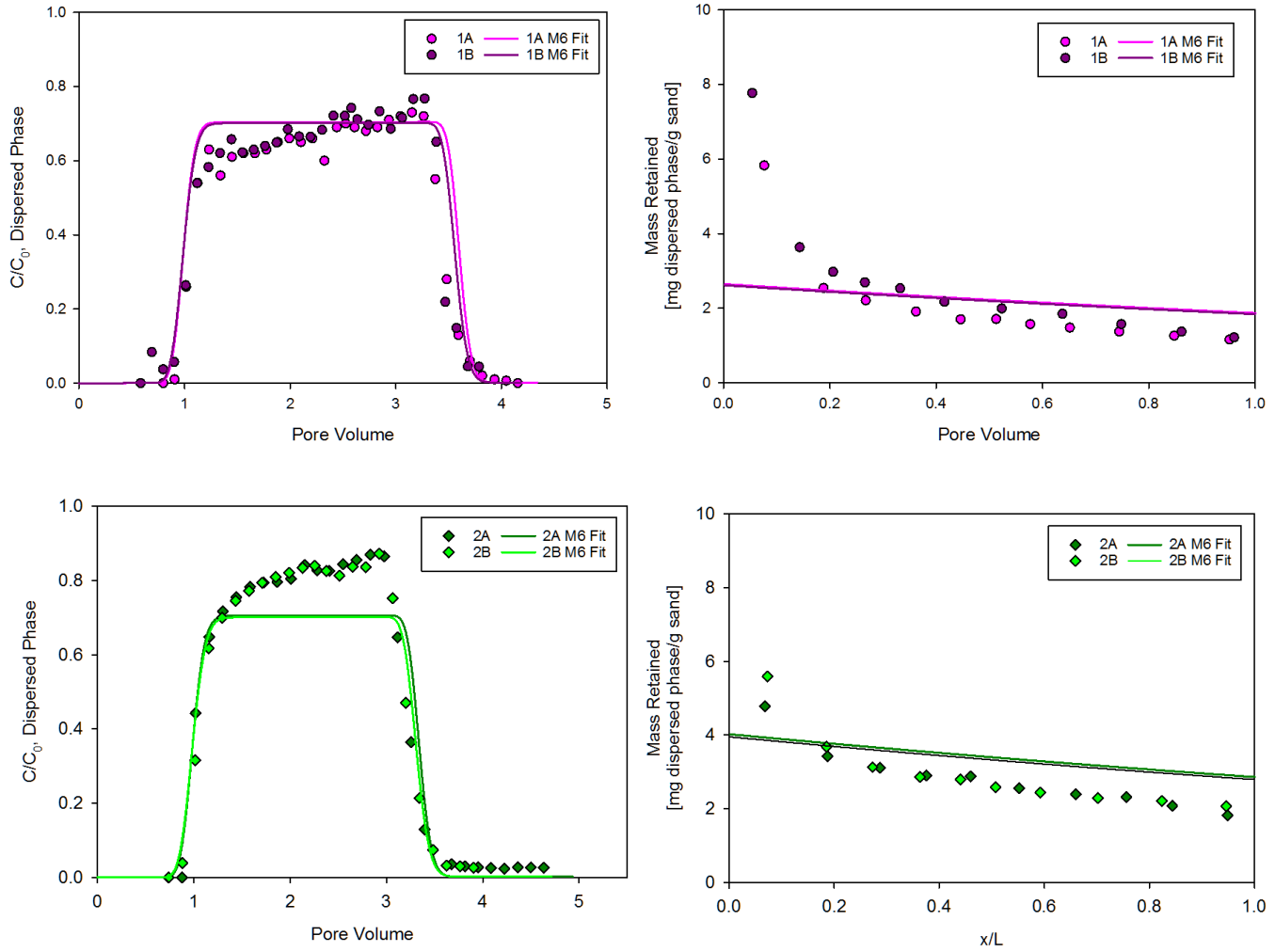

Figure 5.14: M-6 emulsion transport and retention fits to dilute experiments 1&2.

Table 5.6: Model fits to dilute column experiments 1-2.

Model No.		k_d	k_r	β	S_{max_attach}	SSE_w	$AIC_{c,w}$
		[min^{-1}]	**[min^{-1}]**	**[-]**	**[$mg \cdot g^{-1}$]**		
M-1		0.008	-	-	6.2	15.4	-362.2
M-2		0.044	-	0.45	-	9.73	-434.2
M-3		-	0.370	0.90	19.2	14.5	-366.2
M-4		0.005	0.056	0.55	480	7.64	-468.3
Model No.	λ	α	k	K	$S_{max,attach}$	SSE_w	$AIC_{c,w}$
	[min^{-1}]	**[-]**	**[min^{-1}]**	**[$mL \cdot g^{-1}$]**	**[$mg \cdot g^{-1}$]**		
M-5	0.0043	26.34	-	-	-	18.02	-336.8
M-6	-	-	0.0055	102.3	5.75	16.62	-347.6

SSE_w= combined weighted sum of the squared errors for 1A,1B,2A & 2B

$AIC_{c,w}$= combined weighted sample size corrected Akaike information criteria for 1A,1B,2A & 2B

The rising plateau of the breakthrough curve is only captured when a maximum surface retention term (S_{max}) is employed (i.e., M-1, M-3, M-4) and hyper-exponential retention can only be replicated via a depth dependent model formulation (i.e., M-2, M-3, M-4). Thus, M-3 and M-4 were selected as potential models capable of capturing the transport and retention behavior of low concentration oil-in-water emulsions. Although M-3 and M-4 both employ depth-dependent retention with a maximum retention capacity, the distinction between these models is that M-3 is a one-site model where retention is modulated by S_{max} and β, whereas M-4 allows solid mass accumulation on two-sites each limited independently by S_{max} and β, respectively. The hypothesis with M-4 is that high concentrations (i.e., above S_{max}) will effectively swamp out the surface sites leading to a misidentification of transport mechanisms and model parameters if only fit under high retention conditions (i.e., when retention is above S_{max}).

5.4.4.2 Concentrated Emulsion Transport Modeling

Although, the selected models are able to describe low concentration behavior, none of the tested models (along with the other model formulations for colloid transport) are unable to describe: 1) the early fall of the backside of the breakthrough curve; nor 2) the extended tailing seen at high emulsion concentrations. Figures 5.15 and 5.16 show M-3 and M-4 predictions for the concentrated emulsion experiments 3 and 4.

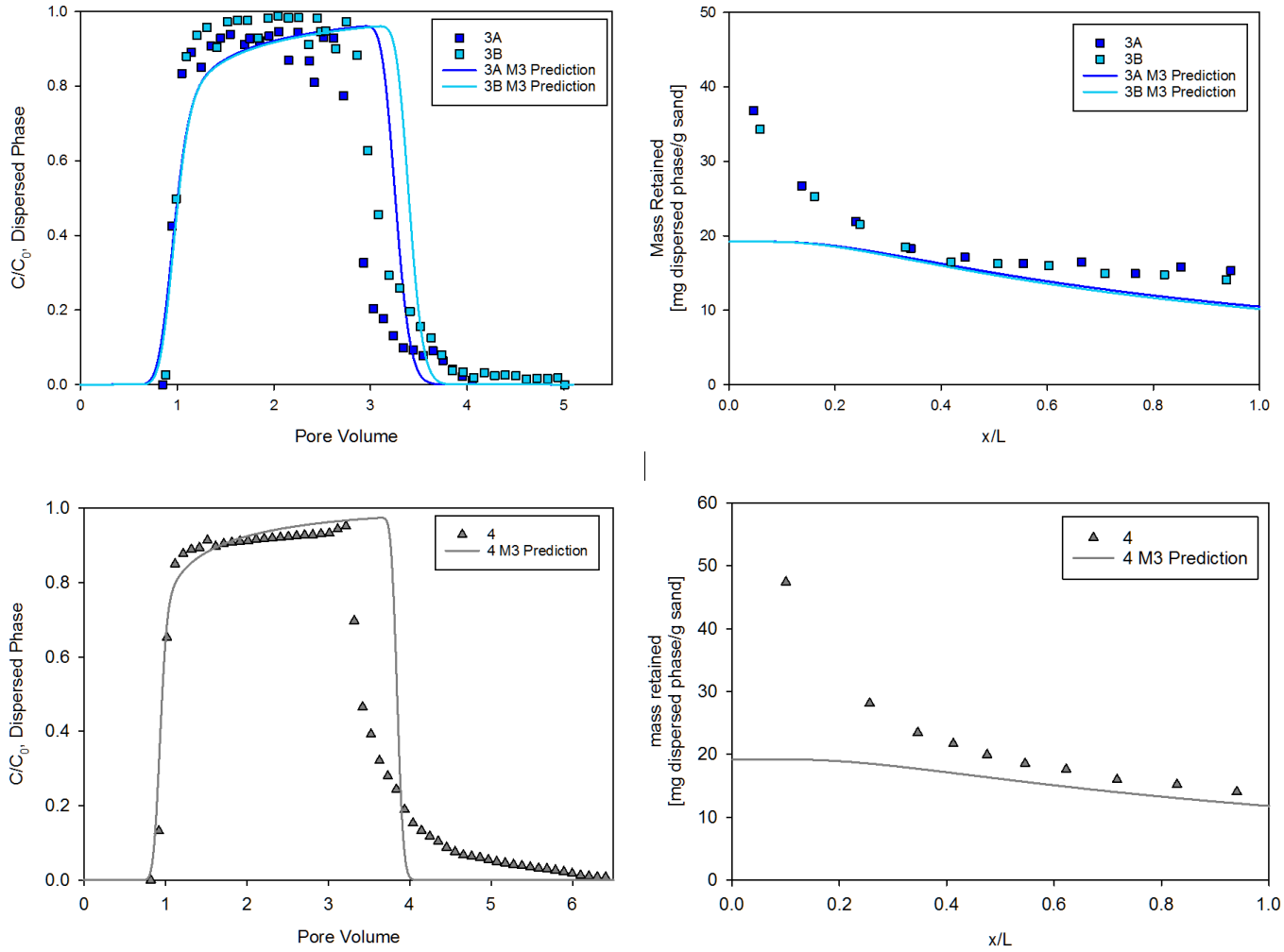

Figure 5.15: M-3 predictions for concentrated emulsion experiments 3 & 4.

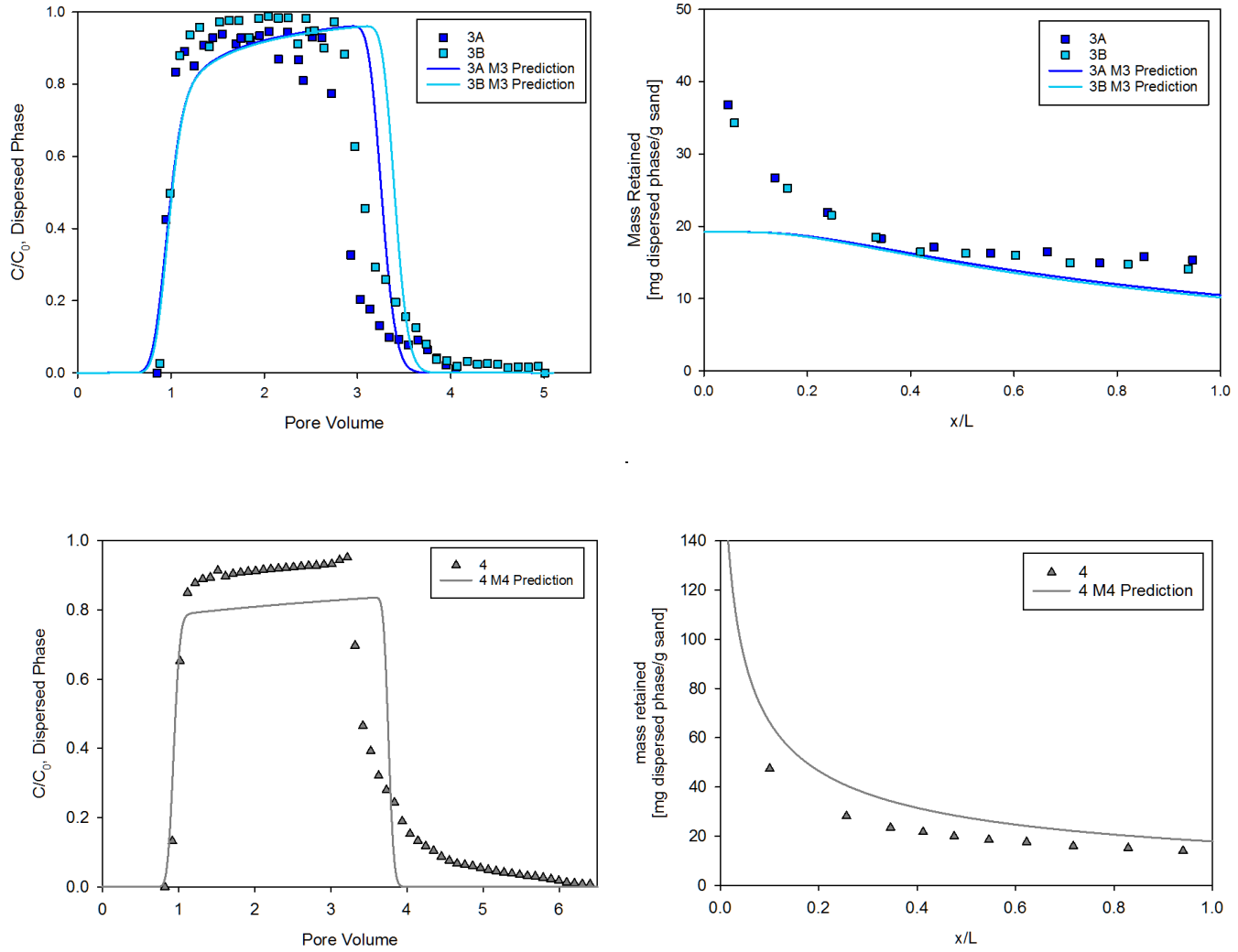

Figure 5.16: M-4 predictions for concentrated emulsion experiments 3 & 4.

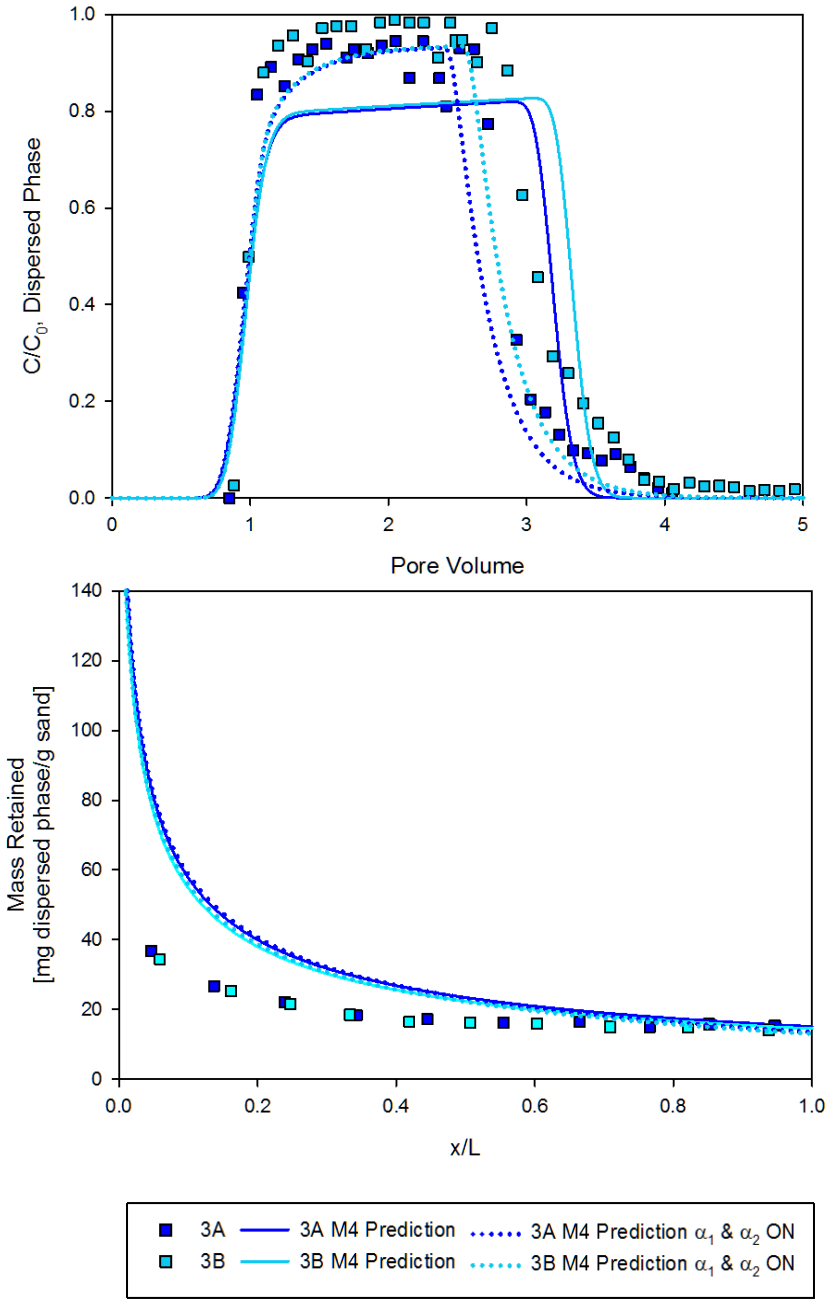

Figure 5.17: Emulsion transport and deposition predictions for experiment 3 with dispersive mixing corrections. (solid line) model prediction using dilute experiment fitted parameters; (dashed line) model predictions after dispersive mixing is corrected for influence of deposited mass with nonlinear model and viscous dispersive mixing

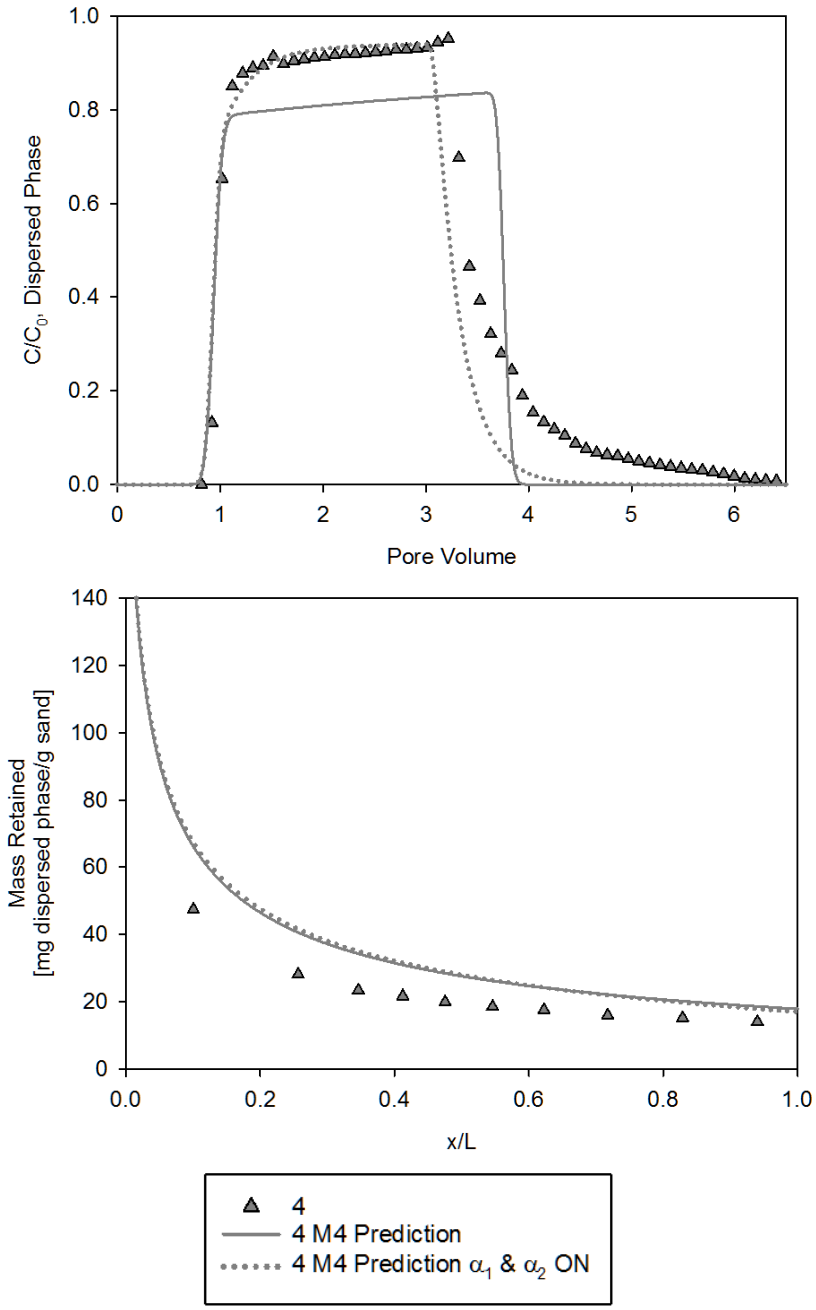

Figure 5.18: Emulsion transport and deposition predictions for experiment 4 with dispersive mixing corrections. (solid line) model prediction using dilute experiment fitted parameters; (dashed line) model predictions after dispersive mixing is corrected for influence of deposited mass with nonlinear model and viscous dispersive mixing.

Table 5.7: Statistical output for concentrated column model prediction with and without dispersive mixing corrections.

		Experiment								
		3A			3B			4		
Model	Simulation Basis	SSE_w	$AIC_{c,w}$	Model MB [%]	SSE_w	$AIC_{c,w}$	Model MB [%]	SSE_w	$AIC_{c,w}$	Model MB [%]
M-3	1	16.94	-7.48	101	9.86	-27.52	101	18.58	-36.88	101
	2	4.46	-31.81	83	5.33	-32.53	84	6.43	-71.44	88
M-4	1	18.25	-6.12	102	12.61	-22.09	102	12.26	-50.43	102
	2	13.34	-1.85	93	12.26	-22.70	94	8.39	-62.79	98
M-4B	1	12.47	-13.1	101	7.57	-33.4	101	13.37	-47.6	101
	2	3.90	-34.3	87	5.30	-41.3	88	5.62	-75.8	92

Simulation Basis: 1= Retention parameters fitted to dilute column experiments; 2= Retention parameters fitted to dilute column experiments plus saturation dependent dispersion (M_1=37.6; N_1=1.26) and viscous instabilities (E=1.7; H=2)
M-4B is M-4 where S_{max} is set to 50 mg·g-sand^{-1} while using the dilute fitted parameters
SSE_w= weighted sum of squared errors
$AIC_{c,w}$=sample size corrected Akaike information criteria using the weighted sum of the squared errors

Note: In some of the highly concentrated model simulations the inclusion of the additional dispersive mixing effects affected the model mass balance, presumably due to the highly non-linear behavior of the viscous instability term.

Droplet transport in the high concentration experiments (experiments 3 and 4) was predicted using the full model which includes retention parameters fit to low concentration columns plus saturation dependent dispersity and mixing due to the viscous instabilities (Figures 5.17 and 5.18). Inclusion of these additional effects improves model performance (See Table 5.7 for comparison of statistical outputs).

The fall of the breakthrough curve and subsequent tailing is better captured by including the terms to describe the mixing resulting from the viscous instabilities. The model prediction for experiment 3 somewhat under predicts the time of finger breakthrough (i.e., fall of the breakthrough curve), though it well predicts the tailing. Model prediction for experiment 4 are opposite - better description of finger breakthrough than the amount of tailing. One can improve model performance further through adjustment of the Koval parameters though this was not pursued here given that the aim was to provide predictive capability for emulsion transport at high concentration.

In both cases the model over predicts droplet retention with substantial differences between the model and experiment apparent near the inlet of the column. The predicted mass retained at the inlet corresponds to a water saturation of approximately 0.8. It is conceivable that extremely high retained fractions such as these would remobilize and thus not be observed in experiments. That is, the retained dispersed phase may act more like a mobile saturation. Following this line of reasoning, one could hypothesize an upper limit on retention that corresponds to immobile oil saturation. Unpublished column experiments

conducted within the Ramsburg Lab using procedures and media similar to those described herein suggest that the maximum entrapped saturation for SBO in Federal Fine sand is approximately 25% (i.e., 50 mg·g^{-1}). Interestingly no measured retained fraction exceeds this value. The hypothesis of a physical upper limit on the overall amount of retention was tested within the simulations by imposing an overall maximum retention of 50 mg·g^{-1} M-4. S_{max} represents the capacity of attachment sites which is only a fraction of the overall maximum retention (50 mg·g^{-1}). For the overall maximum, $S_{max\ tot}$ was executed within M-4 as described in Equations 5.22 and 5.23.

$$\frac{\rho_b}{n}\frac{\partial S}{\partial t} = s_{aq}\psi_{\max,tot}\left(k_r\psi_d + k_d\psi_b\right)C \qquad (5.22)$$

$$\psi_{\max,tot} = \left(1 - \frac{S_{tot}}{S_{\max,tot}}\right) \qquad (5.23)$$

Implementation of the $S_{max,total}$ term in M-4 increased the predictive capability of the model (Table 5.7) with visibly better descriptions at the top of the breakthrough curve and throughout the deposition profile (Figures 5.19 and 5.20).

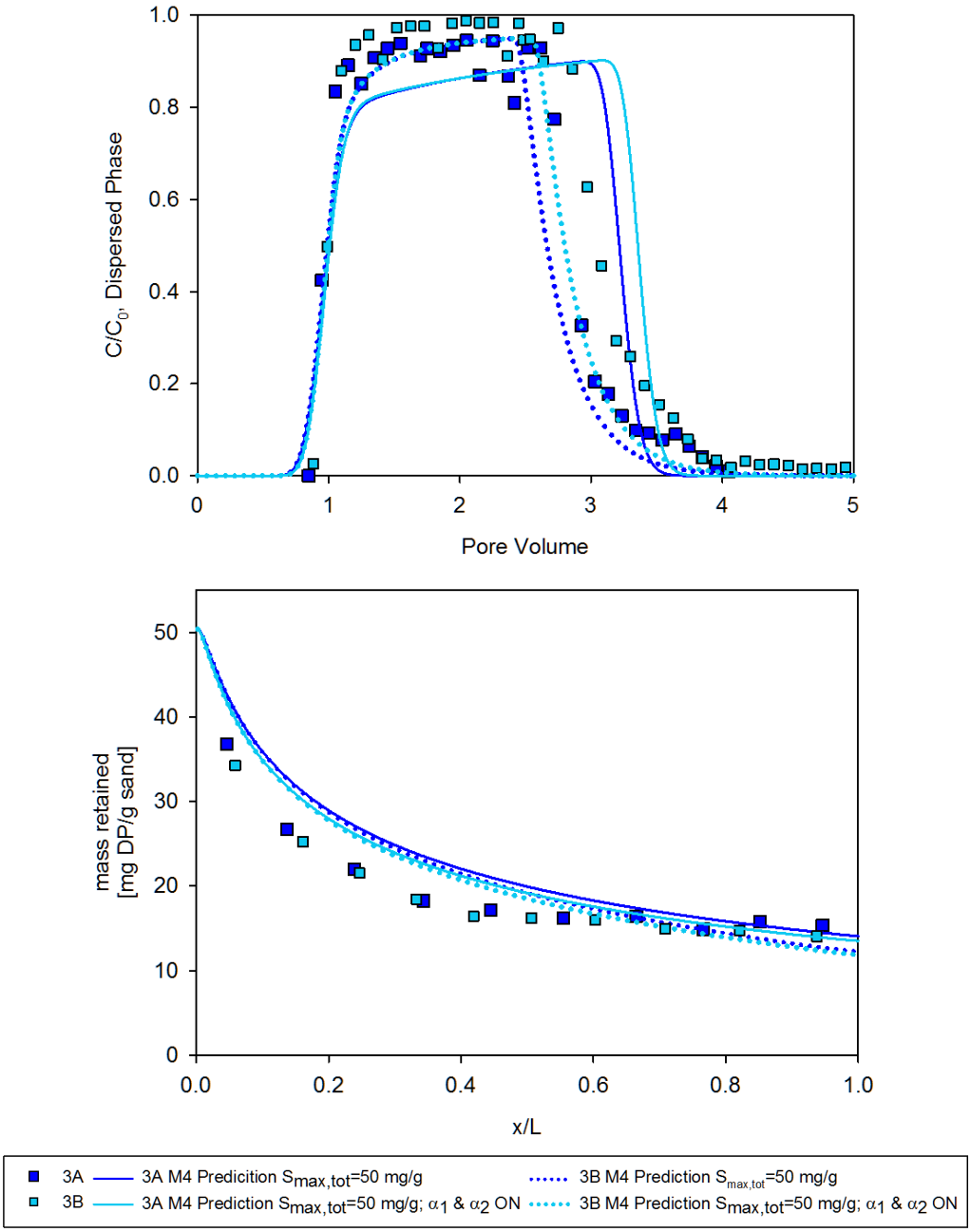

Figure 5.19: Emulsion transport and deposition predictions for experiment 3 with $S_{max,total}$ set to 50 mg·g^{-1} and dispersive mixing corrections.(solid line) model prediction using dilute experiment fitted parameters; (dashed line) model predictions after dispersive mixing is corrected for influence of deposited mass with nonlinear model and viscous dispersive mixing.

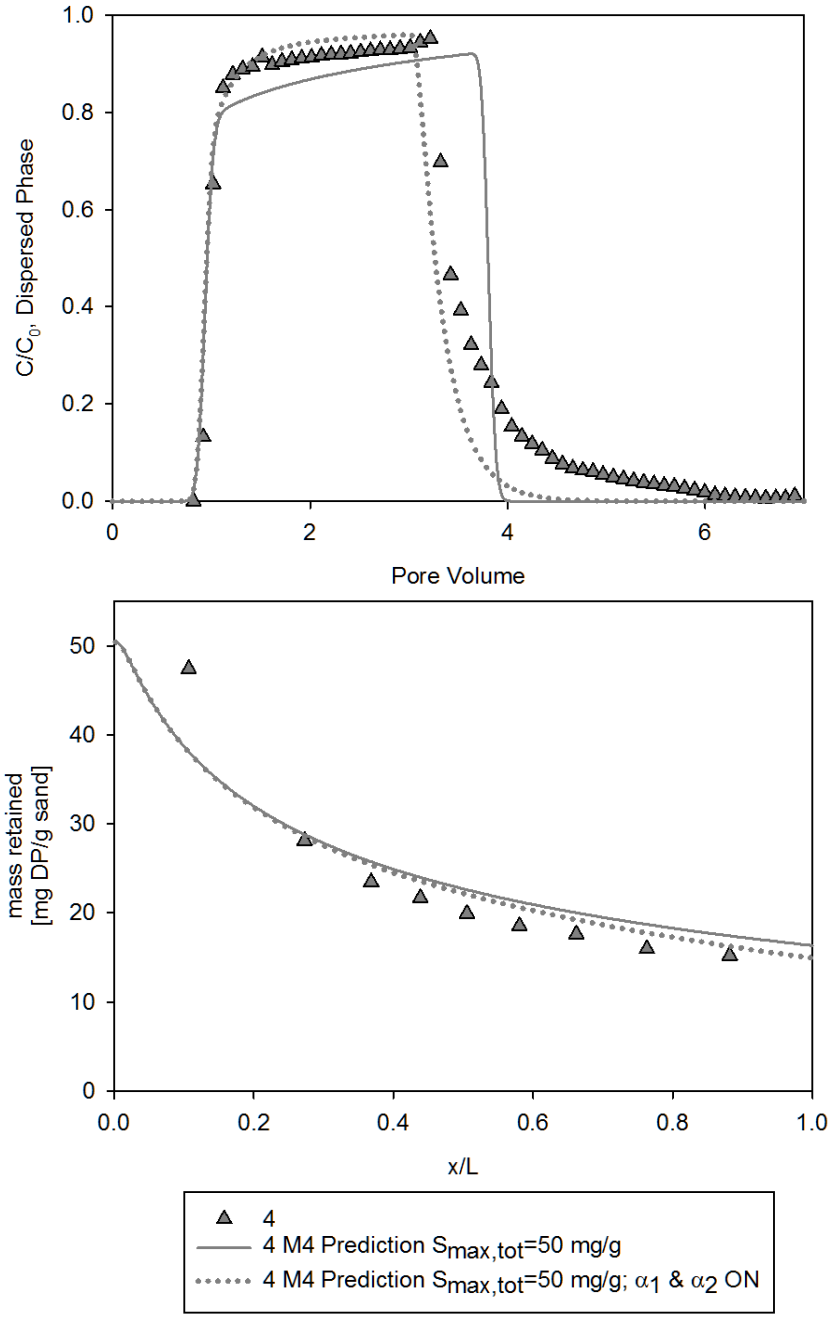

Figure 5.20: Emulsion transport and deposition predictions for experiment 4 with $S_{max,total}$ set to 50 mg·g^{-1} and dispersive mixing corrections. Model predictions are: parameters fit to dilute experiments (solid line); parameters fit to dilute experiments plus saturation dependent dispersion and influence of viscous instability (dashed line).

The near-inlet data have a strong influence on the fitted model parameters. This suggests that the spatial resolution employed when sampling the retention by excavating the column may influence the interpretation of the physical processes occurring during the transport of the emulsion. The model fits weighting routines were used in attempt to decrease this effect.

5.4.5 Emulsion deposition implications for field sites

In a practical sense the disagreement in retained concentrations near the column inlet is rather unimportant. It is substantially more important to predict deposition at distances from a well that exceed the 10 cm used in these laboratory experiments. When considering this, it is important to recognize that both experiments 3 and 4 have retention of approximately 15 $mg \cdot g^{-1}$ at the effluent end of the column. Experiment 4 has greater retention over the first 7 cm due to the longer pulse of an emulsion having greater dispersed phase content, but further from the inlet the retention is more uniform. Model simulations were used to explore the effects of input emulsion concentration, pulse duration, and distance from the injection point (Shown in Figures 5.21-5.23).

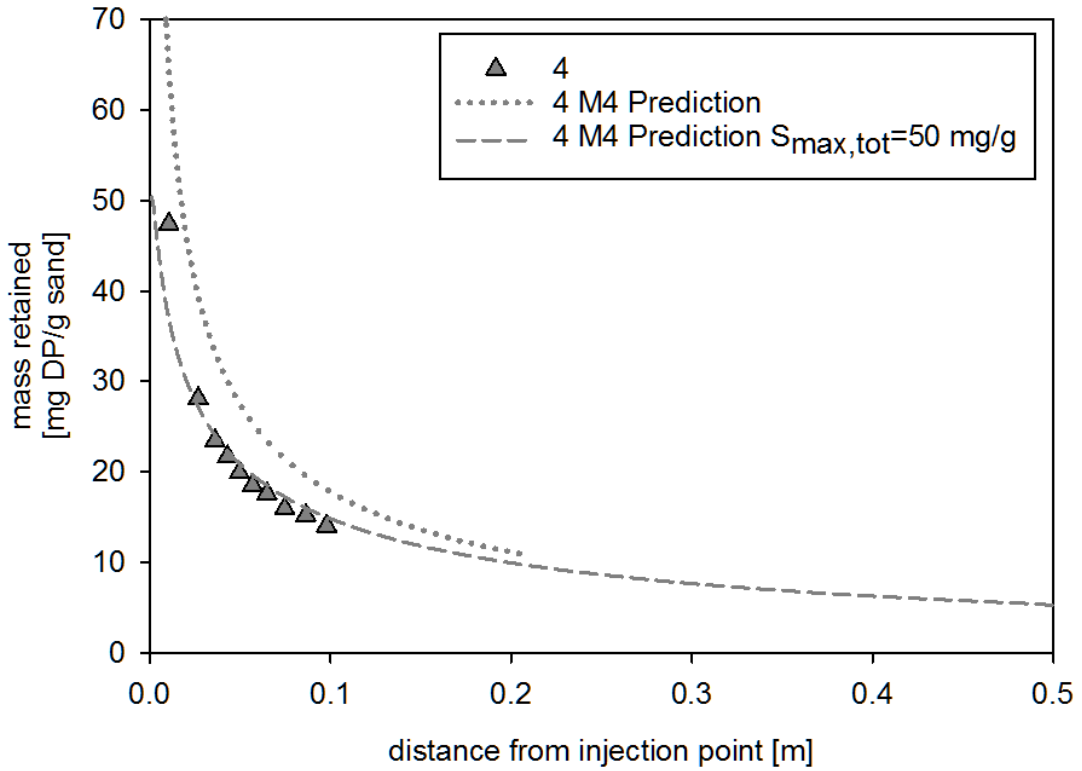

Figure 5.21: Prediction of dispersed phase concentrations at greater distances away from injection point.

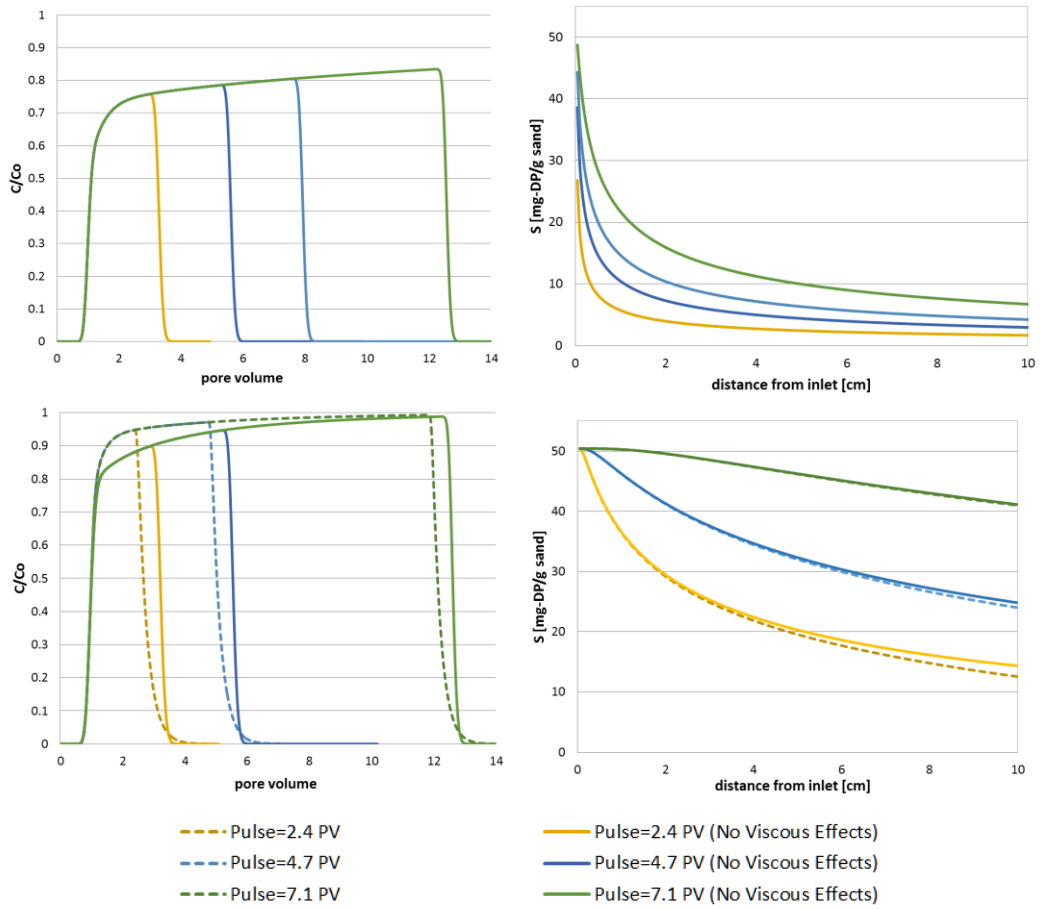

Figure 5.22: Influence of pulse duration and input concentration on emulsion transport and retention. Simulations shown are using model M-4B for a low concentration emulsion (C_0=2.3%) (top row); and a high concentration emulsion (C_0=22.7%) (bottow row). The effect of including the dispersive mixing correction is shown with the dashed line.

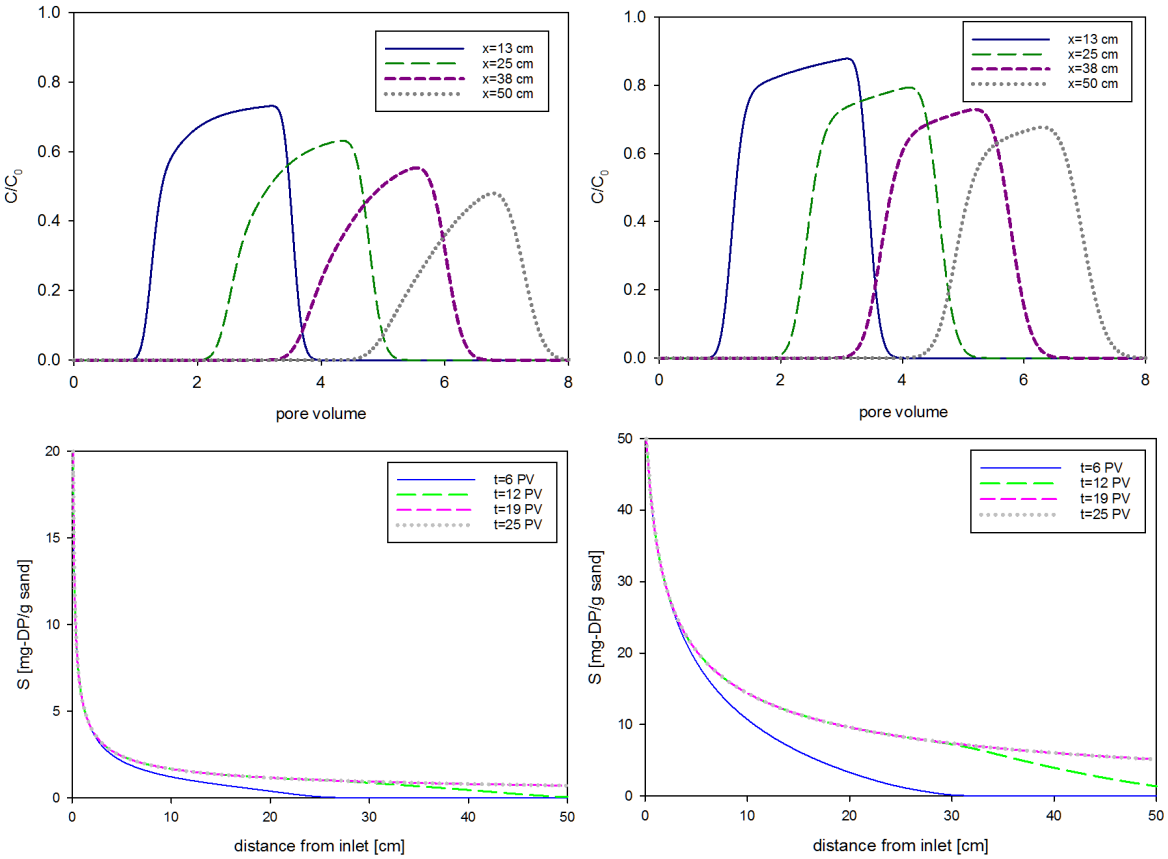

Figure 5.23: (top) Breakthrough curves simulations at various x-distances for a 7 PV pulse of a low concentration emulsion (C_0=2.3%) (left) and a high concentration emulsion (C_0=22.7%) (right). (bottom) The corresponding time evolution of droplet retention ove the course of injection is shown for low and high concentration emulsions.

Modeling simulations employing a longer pulse (Figure 5.22) provides insight into design considerations for using emulsions for remediation. The ability to understand, predict and subsequently control the amount of mass deposited is a foundational piece of emulsion remedial design. As pulse length was increased the mass deposited along the column continued to increase until maximum retention was reached (i.e., $S_{max,total}$ =50 mg·g^{-1}) . This finding suggests that the total injected mass (i.e., pulse length) and concentration are the key points controlling mass emplacement. Since amendments are held within the emulsion (or the oil droplets themselves) knowledge of total retained mass enables calculation of the potential extent of treatment. Additionally, the role of input concentration is also highlighted in Figure 5.22. At low concentration, the majority of mass becomes retained near the column inlet (i.e., hyper-exponential retention); however, with higher input concentration the retention profiles become shallower as solid phase concentrations reach the maximum as mass gets more distributed away from the injection point.

During these simulations many times numerical difficulties were encountered related to highly non-linear functionality of D_h in time and space in the longer simulations. To address the issue, the step size was varied in attempt to maintain mass balance. As noted in Table 5.3, model mass balance ranged between 83 and 102% when including the additional effects at high concentrations. Thus it is recommended that care be taken when using these models to employ the dispersivity correction.

5.5 CONCLUSIONS

The experimental results show that oil-in-water emulsions (even at 20% oil content) are well transported through a medium sand. The existing particle and emulsion models can describe low concentration behavior however are unable to describe transport and retention behavior of concentrated oil-in-water emulsions. Two additional mechanisms are hypothesized to be responsible for altering transport behavior with increasing input concentration- changing water saturation due to mass deposition and viscous instabilities due to the viscous nature of the concentrated emulsions. These additional mechanisms of decreasing water saturation and viscous instabilities can be expressed as additional dispersive mixing processes and can be incorporated into particle transport model formulations to describe emulsion transport at high concentrations. The resulting models can be used to estimate the required pulse length and/or input concentration needed to obtain the mass retention needed during remedial design.

Chapter 6: Alkalinity release from particle suspensions and particle-containing oil-in-water emulsions

6.1 ABSTRACT

A conceptual model for the oil-in-water emulsions was formed and validated. Preliminary experiments indicated the particles were successfully held in the oil-in-water emulsions and have the ability to release alkalinity across the oil-water interface of the emulsion droplets. Alkalinity release from the encapsulated particles was found to be slower than mineral dissolution rates associated with the bare particles. To better understand the likely mechanism(s) of alkalinity release extent and rate from particle suspensions and particle-containing emulsions a series of batch experiments and mathematical modeling was completed. Ultimately, this task aimed to model alkalinity extent and release to develop insights into avenues for controlling release. Specifically, the following hypotheses were addressed: (1) alkalinity release from particle suspensions follows a mineral dissolution mechanism; (2) encapsulating particles in oil-in-water emulsions adds resistance to mass transfer and thus cannot be successfully described with mineral dissolution models; and (3) release from emulsions can be described by incorporating a linear driving force expression to account for the resistance of mass transfer resistance across the oil-water interface. Work in this

chapter resulted in mathematical models for alkalinity release from particle suspensions and particle-containing emulsions.

6.2 INTRODUCTION

The overall alkalinity release was expressed by the following chemical reactions for $CaCO_3$ and MgO particles, respectively, where $CaCO_3$(s) releases alkalinity in the form of CO_3^{2-} and MgO(s) in the form of OH^-:

$$CaCO_3(s) \rightarrow Ca^{2+} + CO_3^{2-} \qquad (6.1)$$

$$Mg(OH)_2 \rightarrow Mg^{2+} + 2OH^- \qquad (6.2)$$

Dissolution of minerals was modeled using empirical rate laws. Some expressions presented in literature were developed to account for the thermodynamic control on the rate. Thermodynamic control is often implemented through a term quantifying the saturation index (SI) as Ω.

$$\Omega = \frac{IAP}{K_{sp}} \qquad (6.3)$$

Where: *IAP* is the ion activity product; and K_{sp} is the solubility product. Both values are system specific. The SI compares the distance of the current solution from equilibrium by determining the ratio of the non-equilibrium state (calculated as the ion activity product, *IAP*) to the equilibrium conditions, K_{sp}. It was hypothesized that such modification of rate expressions become critical when

considering release in systems approaching saturation as well as in systems under non-sink conditions.

The linear driving force (LDF) model approach was used to model mass transfer across an interface (e.g., oil-water interface). The general LDF is expressed as:

$$\frac{dC}{dt} = kA_s(C^* - C(t)) \quad (6.4)$$

Where: C is the concentration of the species of interest; C^* is the equilibrium concentration [M]; k is the mass transfer coefficient [$L \cdot T^{-1}$]; and A_s specific surface area over which mass is transferred [L^{-1}].

6.3 Materials and Methods

6.3.1 Experimental Methods

A first set of preliminary batch experiments were completed to aid in the development of a conceptual model for particle-containing emulsions. These batch experiments quantified the metal content in the oil and aqueous phases of the emulsion with increasing contact time. More precisely, oil and particle dispersions of 100 nm MgO particles in SBO were prepared (approx. concentrations of 0.1, 0.5, and 1.0 mg-Mg·g-SBO^{-1}) via sonication for one minute. Oil-particle dispersions were then contacted with MilliQ water in acid-washed 35-mL glass vials with Teflon-sealed caps at an oil to aqueous ratio of 0.25 (v/v), along with appropriate blanks and controls. Vials were placed on

shaker trays at 25 °C and sampled after an equilibration time of 8 hours, 72 hours, and 14 days, respectively. Each set of vials was allowed to stand upright for up to one hour before sampling in order to allow the oil and water phases to separate as much as possible while minimizing the potential for particles to fall out of suspension. After phase separation, the oil and aqueous phases were sampled, respectively, and done with care as to ensure oil samples contain no water and aqueous samples contain no oil. This conservative sampling method left a small amount of the total mass unaccounted for as an oil-water mixture. In order to: (1) experimentally close the mass balance; and (2) provide a rough estimate of mass that could potentially be considered to exist at the oil-water interface, the remaining oil-water mixture was also sampled. Oil-phase samples were extracted from the top of each vial; water phase samples were then extracted from the bottom of each vial; and the remaining oil-water mixture was removed. Aqueous samples were acidified with concentrated nitric acid. The oil phase as well as the remaining oil-water mixture (i.e., considered to be the interface between the two phases) in each vial was then placed in a 105 °C oven until all visible water has evaporated and then sample were heated further at 550 °C for 2 hours. The ash remaining in each tube was digested with 5 mL concentrated nitric acid, placed on a shaker overnight, and then diluted with MilliQ to approximately 25% nitric acid for analysis by inductively-coupled plasma-optical emission spectroscopy (ICP-OES) (7300 DV, Perkin Elmer). Acidified samples were introduced via a cross-flow nebulizer at 0.5 $mL \cdot min^{-1}$. Detection was completed in axial mode with Mg and Ca quantified at wavelengths of 279.09 and 317.93 nm, respectively.

A different set of batch experiments were completed to evaluate the alkalinity release extent and rate. This type of batch experiments 500 mL batch reactors with approximately 350 mL of emulsion or an aqueous suspension of nanoparticles ($CaCO_3$ and MgO particles) were used. The glass reactor was fitted with a cap through which the pH probe and purge gas line were passed. The headspace of the reactor was continuously purged with nitrogen gas (N_2) to reduce the possibility of CO_2 uptake from the surroundings. Periodic additions of HCl (1 or 5 N) were used to reduce pH and initiate periods of release for kinetic rate experiments. The pH response was logged using a S40 SevenMulti pH meter (Mettler Toledo). These additions continued until the release capacity of the emulsion or suspension was exhausted (i.e., titrated to a final pH of 4.2). Droplet size distributions were characterized using light microscopy (Ziess Axiovert S100) coupled with MetaMorph (Molecular Devices) image analysis, as well as via dynamic light scattering (Malvern Zetasizer NanoZS). The buffering capacity was also determined by titrating particle-containing emulsions with HCl to exhaustion, allowing for calculation of the total buffering capacity based on amount of acid added. It was assumed that the alkalinity-releasing particles supply the buffering capacity and thus the utilization percentage of particle mass was used as a measured of release extent from emulsions.

6.3.2 Modeling Approach

Modeling alkalinity release from particle and emulsions was assessed using mineral dissolution and linear driving force models. The overall developed

release model as designed to have the ability to describe release via a: (1) LDF mechanism, (2) MD mechanism, or (3) combination of both LDF and MD mechanisms. Approaching release modeling in this manner allowed for the flexibility to test a variety of hypotheses related to the release mechanisms for both particle suspension and from emulsions. Additionally, the emulsion conceptual model work suggests that although alkalinity-releasing particles are mainly held within the oil phase, there is potential that particles could (a) reside at the oil-water interface, or (2) exist at free particles in the aqueous solution. The modeling approach allowed for further investigation and development of the emulsion conceptual model. See Appendix A.II for modeling details.

Alkalinity release from a particle suspension was conceptualized as a dissolution process occurring from the surface of all particles simultaneously, thus changing the interfacial area for surface transfer over the course of dissolution. The interfacial area was directly related to particle size, number of particles, and mass released by using a diminishing sphere approach to relate the particle mass to the specific surface area over the course of release.

$$A_s(t) = N_{particle} 6^{4/3} \pi^{1/3} \left(\frac{M_{particle}(t)}{\rho_{particle}}\right)^{2/3} \quad (6.5)$$

Where: $N_{particle}$ is the number of particles in solution [-], $M_{particle}(t)$ is the mass of particle at time t [M], $\rho_{particle}$ is the density of a particle [$M \cdot L^{-3}$].

Release from suspensions of MgO particles was explored via modifying empirical rate laws developed to describe mineral dissolution (Fedoročková and Raschman, 2008) to account for the thermodynamic control on the rate (Pokrovsky and Schott, 2004). The MgO system was selected for the main investigation due to the less complex nature of the magnesium system as compared to calcium carbonate.

$$\frac{d(MgO)_s}{dt} = -k\{H^+\}^{0.397}\left(1-\Omega^2\right)[=]\frac{M}{L^2T} \qquad (6.6)$$

$$\Omega = \frac{\{Mg^{2+}\}\{OH^-\}^2}{K_{sp}} \qquad (6.7)$$

Where: K_{sp} is defined in terms of $MgO_{(s)}+H_2O \rightarrow Mg^{2+} +2OH^-$, and employed here as 5.012×10^{-11}. Note that the rate law is based upon $MgO_{(s)}+2H^+ \rightarrow Mg^{2+} +H_2O$, which is the same reaction but the way the reaction is written matters when considering the reported value of K_{sp}. That is to say, the K_{sp} for the first reaction would be that of the second times K_w^2. k is the rate coefficient, here taken to be 7.97×10^{-5} mol·m^{-2}·s^{-1} as reported in Fedoročková and Raschman (2008). The model was therefore fully parameterized using information independent from the work presented here.

For calcite dissolution, the following mineral dissolution model was utilized (Plummer, et al., 1978) with the rate coefficient defined as:

$$r_{calcite} = k_1\{H^+\} + k_2\{CO_2\} + k_3\{H_2O\} \quad (6.8)$$

Where: $r_{calcite}$ is the forward rate of calcite dissolution [mols·m^{-2}·s^{-1}]; and k_1, k_2 and k_3 are rates as a function of temperature, with the overall dissolution rate expressed as Equation 6.9 in mols·s^{-1}:

$$\frac{d(CaCO_3)_s}{dt} = SSA \cdot r_{calcite}[1-(\frac{\{Ca^{2+}\}\{CO_3^{2-}\}}{K_{SP_{calcite}}})^{2/3}] \qquad (6.9)$$

Where: *SSA* is the specific surface area [m^2·L^{-1}]; $r_{calcite}$ is the forward rate of calcite dissolution [mols·m^{-2}s^{-1}]; giving the overall calcite dissolution in terms of moles per sec.

Encapsulation of particles within emulsion droplets was hypothesized to follow a linear driving force model. The specific linear driving force expressions used in the alkalinity release models from MgO and $CaCO_3$ particles are as follows:

$$\frac{dC_{Mg^{2+}}}{dt} = kA_s(C^*_{Mg^{2+}} - C_{Mg^{2+}}) \qquad (6.10)$$

$$\frac{dC_{Ca^{2+}}}{dt} = kA_s(C^*_{Ca^{2+}} - C_{Ca^{2+}}) \qquad (6.11)$$

Where: $C_{Mg}{}^{2+}$, $C_{Ca}{}^{2+}$ are the aqueous concentrations of Mg^{2+} and Ca^{2+} [M], respectively; k is the mass transfer coefficient [L·T^{-1}]; A_s specific surface [L^1]; $C^*_{Mg}{}^{2+}$, $C^*_{Ca}{}^{2+}$ are the equilibrium aqueous phase concentrations [M] calculated by solving for the equilibrium speciation at each time step as solution chemistry changed due to alkalinity release and acid input.

When fitting the LDF to experimental data a lumped mass transfer coefficient (i.e., $k_L = kA_s$) was employed. Using a lumped mass transfer coefficient here is acceptable since the size of the oil droplets were determine experimentally to remain unchanged through the alkalinity release process. This finding permitted the assumption that the interfacial area of the emulsion droplets does not change during the release period. With this assumption the lumped mass transfer coefficient may be taken as a constant during release. When considering alkalinity release from particles encapsulated in oil droplets (i.e., from emulsions) release was conceptualized as following a thin-film model with first order release kinetics. Both the concentration of particles within the oil droplets as well as the bulk aqueous solution were assumed to be well mixed (i.e., there are no concentration gradients within each phase). The assumption about mixing within the droplets has been shown to be reasonable in other contexts such as a nonaqueous phase liquid entrapped within a porous medium. The role of diffusion within the nonaqueous phase was shown to have negligable influence on the rate of solute partitioning between the aqueous and organic phases (Ervin et al., 2011). In the Ervin et al. (2011) study the droplets (or entrapped ganglia) of nonaqueos phase were >250 μm. Emulsion droplets have orders of magnitude shorter diffusion lengths (average size of emulsion droplet is ~2 μm). Thus, it was assumed that diffusion within the oil was not the rate-limiting step in the release process but rather the resistance was occurring on the aqueous side of the oil-aqueous interface.

Equilibrium solution chemistry influences the release rates as this controls the thermodynamic limit on the kinetics either in the linear driving force or in the omega term included in the MD model. Because of the thermodynamic control on release kinetics, accurate description of the aqueous species (both at equilibrium and non-equilibrium conditions) is critical for successfully evaluation of release behavior. Since some of the release models required parameters to be fit to experimental data, a complete and accurate description of aqueous chemistry became exceedingly important. Two chemical models were used: (1) simple equilibrium chemistry (SEC) model; and (2) a more complete chemical equilibrium model which employs an extensive database of possible chemical species when determine aqueous speciation (PHREEQC).

A simple equilibrium chemistry model was developed in MATLAB to include the major aqueous species present in MgO and $CaCO_3$ particle systems. The carbonate system was included for both types of particle systems with the initial total carbonate ($[C_{T,CO3}]$) calculated assuming that the initial water was equilibrated with the atmosphere. The following aqueous species were included in the analysis: $[H^+]$ $[OH^-]$ $[H_2CO_3^*]$ $[HCO_3^-]$ $[CO_3^{2-}]$ $[Na^+]$ $[Cl^-]$ $[Ca^{2+}]$ and $[Mg^{2+}]$. The equilibrium metal ion concentration (i.e., $[C^*_{Ca2+}]$ and $[C^*_{Mg2+}]$) was determined by solving the following system of equations (i.e., charge balance (Equation 6.12), carbonate speciation (Equation 6.13 and 6.14) (Benjamin, 2002) , total carbonate (Equation 6.15), water speciation (Equation 6.16), and solubility (Equation 6.15-6.17):

$$2\{H^+\}+\{Na^+\}+2\{Ca^{2+}/Mg^{2+}\}=\{OH^-\}+\{Cl^-\}+\{HCO_3^-\}+2\{CO_3^{2-}\} \quad (6.12)$$

$$\frac{\{HCO_3^-\}\{H^+\}}{\{H_2CO_3^*\}}=K_{a1}=10^{-6.35} \quad (6.13)$$

$$\frac{\{CO_3^{2-}\}\{H^+\}}{\{HCO_3^-\}}=K_{a2}=10^{-10.33} \quad (6.14)$$

$$C_T=[H_2CO_3^*]+[HCO_3^-]+[CO_3^{2-}] \quad (6.15)$$

$$\{OH^-\}\{H^+\}=K_w \quad (6.16)$$

$$\{Ca^{2+}\}\{CO_3^{2-}\}=K_{sp,CaCO_3} \quad (6.15)$$

The equilibrium Mg^{2+} concentration ($\{Mg^{2+}\}^*$) was determined by using the solubility product equation for $Mg(OH)_2(s)$ as follows:

$$Mg(OH)_2(s)+H_2O \leftrightarrow Mg^{2+}+2OH^- \quad (6.16)$$

$$\{Mg^{2+}\}\{OH^-\}^2=K_{sp,Mg(OH)_2} \quad (6.17)$$

The above chemical equations are written in terms of activities with the activity coefficients for each of the aqueous species are calculated using the extended Debye-Huckel equation (valid for ionic strengths less than 0.1 M) and the acidity constants are updated in the program for temperature.

A similar process of solving a system of equations was used when considering more complex aqueous chemistry, albeit with more chemical species

included in the analysis. The chemical database "minteq.v4" that accompanies PHREEQC was used for equilibrium calculations.

When considering $Mg(OH)_2$ (s) dissolution all the following aqueous species were included in PHREEQC: Mg^{2+}; $Mg(OH)^{+}$; $MgCO_3$; $MgHCO_3^{+}$; and $MgCl^{-}$. The distribution of these magnesium species between pH 7 and 10.5 is shown in Figure 6.1. The range of pH values investigated was based on experimental measured pH ranges for MgO particle-containing emulsions. This emulsion system was found to have an equilibrium pH value of approximately 10.5 and in the absence of other solutes, the relative amount of each magnesium species is: 91.4% Mg^{2+}; 8.08% $Mg(OH)^{+}$; 0.48% $MgCO_3$; <0.01% $MgHCO_3^{+}$; and <0.01% $MgCl^{-}$. PHREEQC better represented the approximately 8.5% of the total magnesium mass near equilibrium which can be important in determining the thermodynamic limit on the release, whereas SEC considered all aqueous magnesium mass to be Mg^{2+}. Away from equilibrium (>1 pH unit) the simplification of the SEC does not have an appreciable influence on the accuracy of the Mg^{2+} concentration.

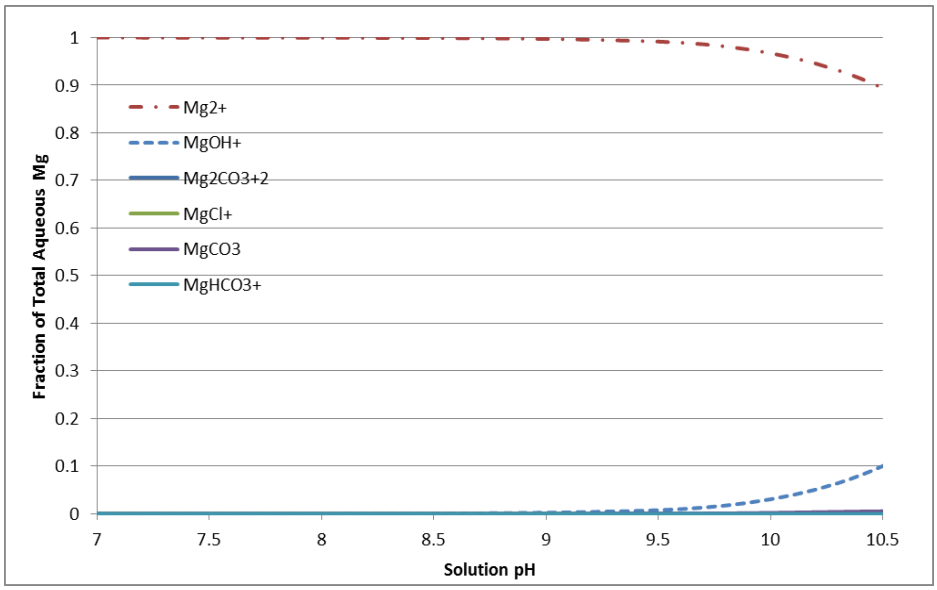

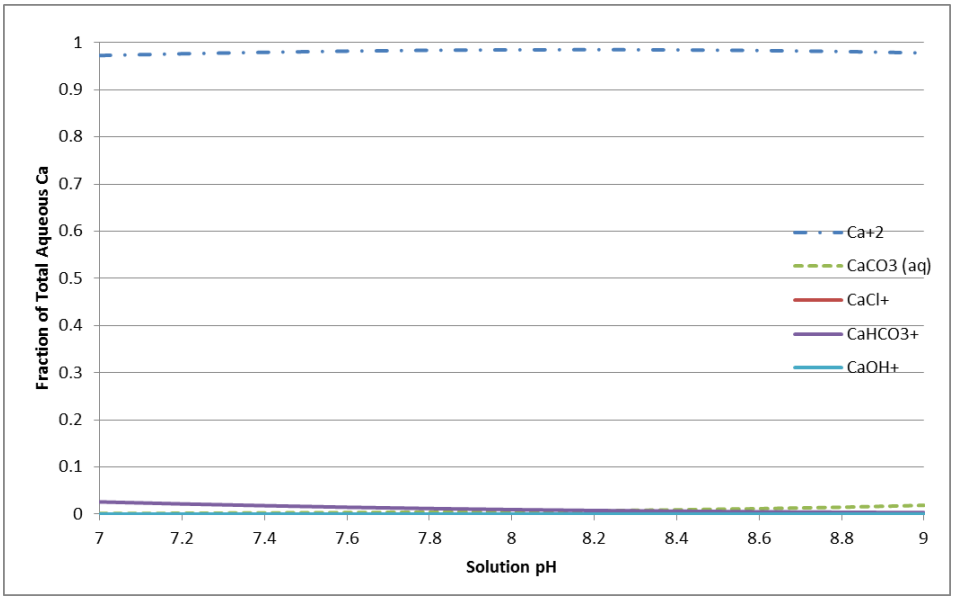

Figure 6.1: Equilibrium fractions of aqueous magnesium (top) and calcium (bottom) species at varying pH.

Shown in Figure 6.1 is the aqueous speciation of calcium between pH 7 and 9. The range of pH values investigated was based on experimental values of pH for particles in emulsion. The equilibrium value of $CaCO_3$-containing emulsions was measured to be near 8.9. At a pH value of 8.9 (established in the presence of calcite but absence of other solutes) the soluble calcium is distributed as: 97.8% Ca^{2+}; 1.9% $CaCO_3(aq)$; 0.3% $CaOH^+$; and >0.01% $CaHCO_3^+$ and $CaCl^+$. Unlike Mg, however, the accuracy of the SEC for calcium speciation was only limited to about 97% for the range of pH considered (Figure 6.1).

6.4 Results and Discussion

6.4.1 Emulsion Conceptual Model

Results from the preliminary experiments used to assess oil-encapsulation of the particles are shown in Figure 6.2. The experimental results indicate that (for a mass loading of 0.1% MgO (wt.%)) the fractionation of total magnesium mass was: 0.81 ± 0.08 (standard deviation) in the oil; 0.06 ± 0.01 in the aqueous phase; and 0.13± 0.02 of mass possibly associated with the oil-water interface, after an extended equilibration period with an aqueous phase. These experiments are difficult to conduct as gravity eventually separates the particles, aqueous phase, and the oil (i.e., $\rho_{particle} >> \rho_{water} > \rho_{oil}$) (i.e., promoting particle settling out of the oil phase). For this reason the interfacial fraction is essentially an artifact of the mixing process employed for this test. Thus, it should not be considered to be representative of the interface in the emulsions stabilized with Gum Arabic. The

experimental method does suggest, however, particle encapsulation- as more than 80% of the total magnesium mass is held in the oil. Additionally, the total concentrations of Mg associated with the aqueous phase range between 6 and 15 mg/L, with greater mass loading and longer equilibration time producing higher concentrations. The aqueous solubility of Mg in these systems was estimated using PHREEQC (Parkhurst and Appelo, 2013) to be 12.7 mg/L assuming the particle solid is brucite (i.e., $Mg(OH)_2$). Aqueous total magnesium concentrations below this solubility limit suggest that the aqueous phase likely does not contain solid particles. Still, results indicated that aqueous magnesium concentrations are near that of the calculated aqueous solubility for brucite. Additionally, the slow increase of aqueous magnesium concentrations with increasing contact time supports the hypothesis that a slow-release mechanism governs rates- presumed to be due to the resistance of mass transfer across the oil-water interface. Overall the results demonstrated that for all particle loadings, including loadings of 1 mg/g (and likely higher), most of the total magnesium mass is present in the oil phase even after long contact time with an aqueous phase.

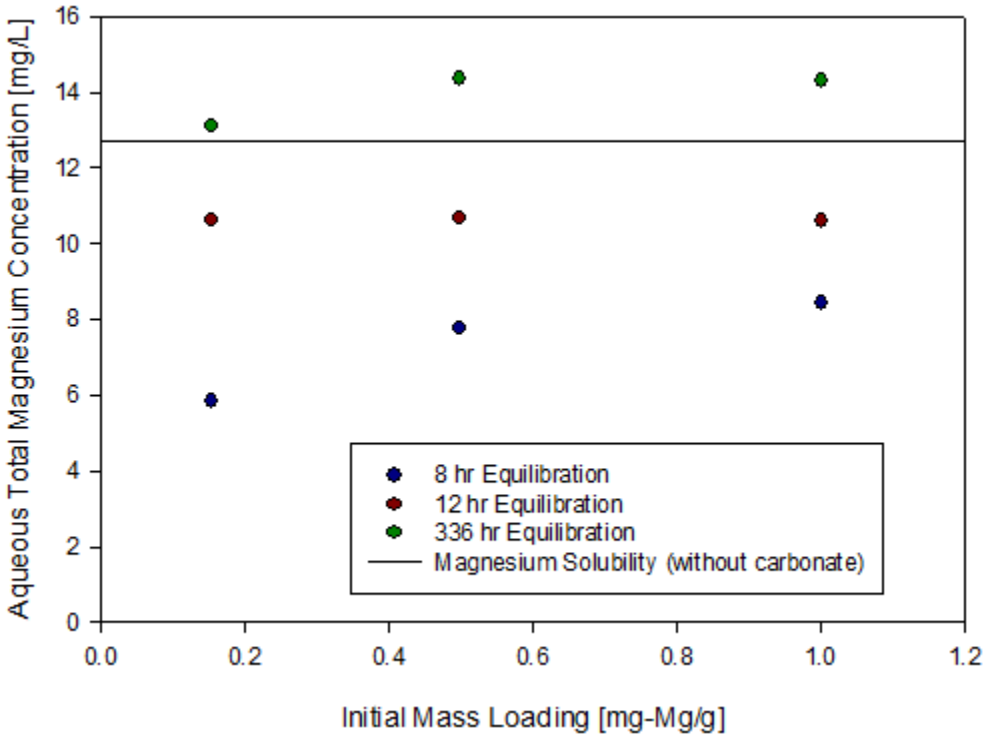

Figure 6.2: Mg total associated with the aqueous phase.

6.4.2 BUFFERING CAPACITY

The total buffering capacity of emulsions containing $CaCO_3$ and MgO particles held was determined at various input particle concentrations. Buffering capacity experimental results are shown in Figure 6.3 and Table 6.1. Emulsions containing MgO particles were found to have approximately 2.8 times the buffering capacity of the emulsions containing $CaCO_3$ particles (per particle mass basis)**.** Particle utilization rates were found to be between 70 and 95% depending on particle type.

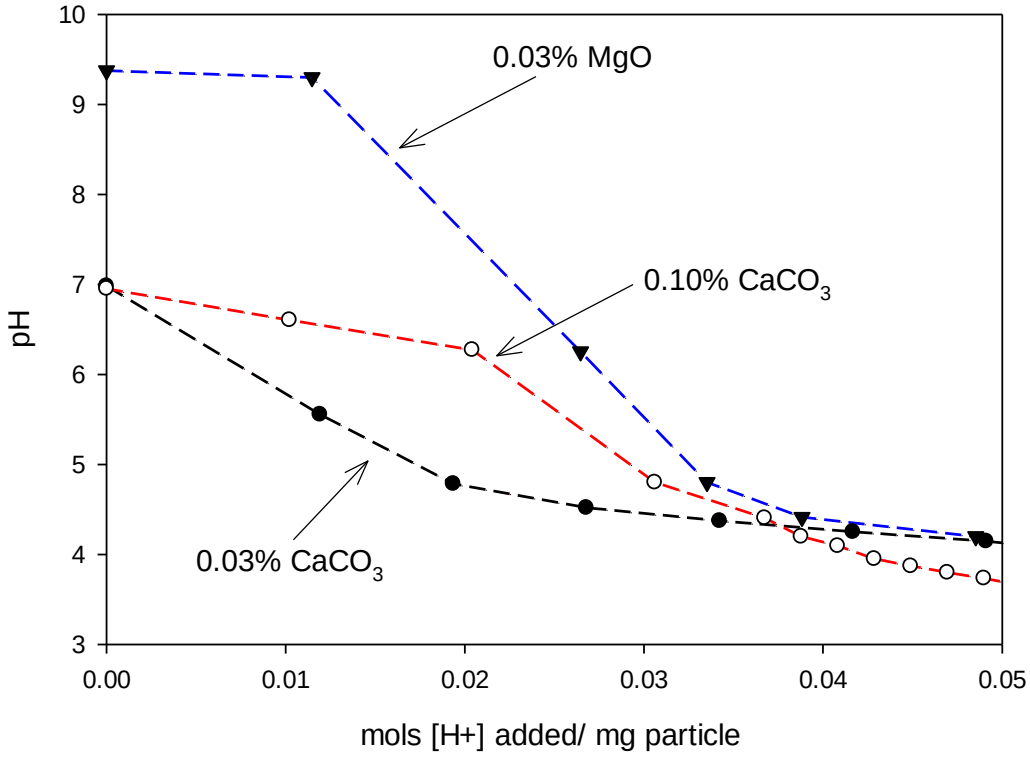

Figure 6.3: Example buffering capacity curves for $CaCO_3$ and MgO particle emulsions.

Table 6.1: Buffering capacity of emulsions containing $CaCO_3$ and MgO particles

Particle Mass Loading	Buffering Capacity [Alk meq/g-particle]		Alkalinity Utilization
[Particle wt./total emulsion]	Theoretical	Measured	[-]
0.03% $CaCO_3$	20.0	14.4	0.72
0.04% MgO	49.6	40.5	0.82
0.03% MgO		44.7	0.90
0.2% MgO		45.7	0.92
0.4% MgO		47.1	0.95

6.4.3 ALKALINITY RELEASE

To probe alkalinity release rates from $CaCO_3$ and MgO particle suspensions and particle-containing emulsions several batch experiments were completed using the batch system setup previously described. Representative results from kinetic release experiments from particle suspensions and particle containing emulsions are shown in Figures 6.4-6.6. Release from MgO particle suspensions are shown in Figure 6.4, and in Figure 6.5 for MgO particles contained in an emulsion. Additional experiments are shown for release from a $CaCO_3$ emulsion in Figure 6.6. Comparison of the results from these batch experiments illustrates the relative rates of alkalinity release. All experimental system shown in Figure 6.4 - 6.5 are approaching equilibrium pH; $CaCO_3$ systems are all approaching pH 8.5 and MgO systems approaching 10.4. Early time (i.e., when minimal acid has been added) responses of a suspension of nanoparticles and two emulsions, each encapsulating different amounts of the alkalinity release particles, are shown in Figures 6.7 and 6.8. Comparison of the results obtained with 0.03% wt. suspension of particles with those obtained using the same mass loading in the emulsion (0.03% wt. $CaCO_3$ emulsion) suggests that relatively rapid rate of alkalinity release from the nanoparticle suspensions can be purposefully reduced by encapsulating the particles within the oil droplets of the emulsion.

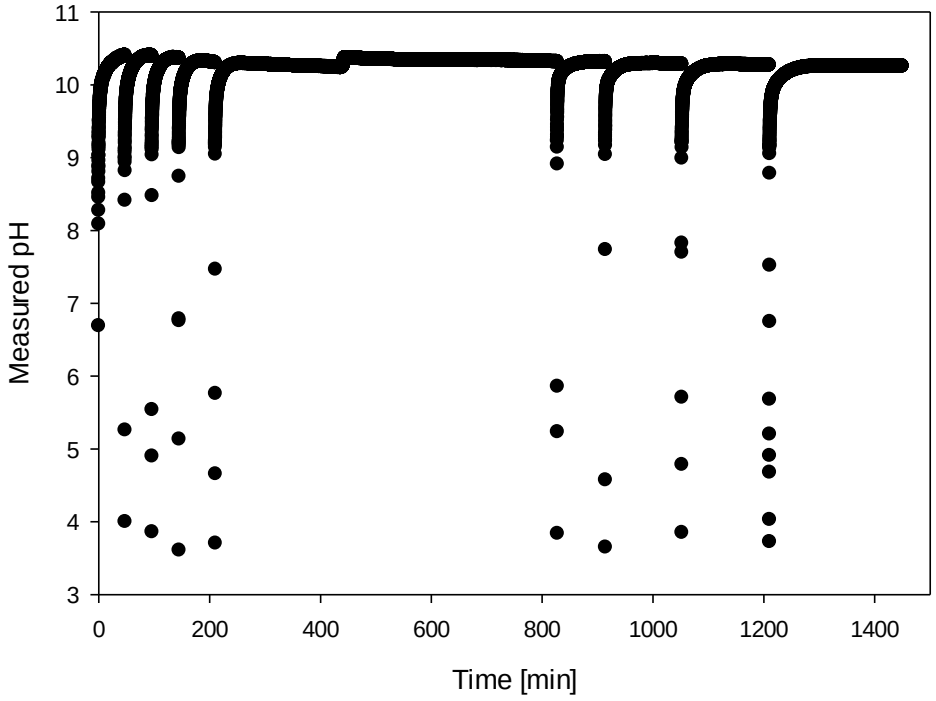

Figure 6.4: Illustrative data from a batch alkalinity experiment conducted with a 0.04% MgO particle suspension.

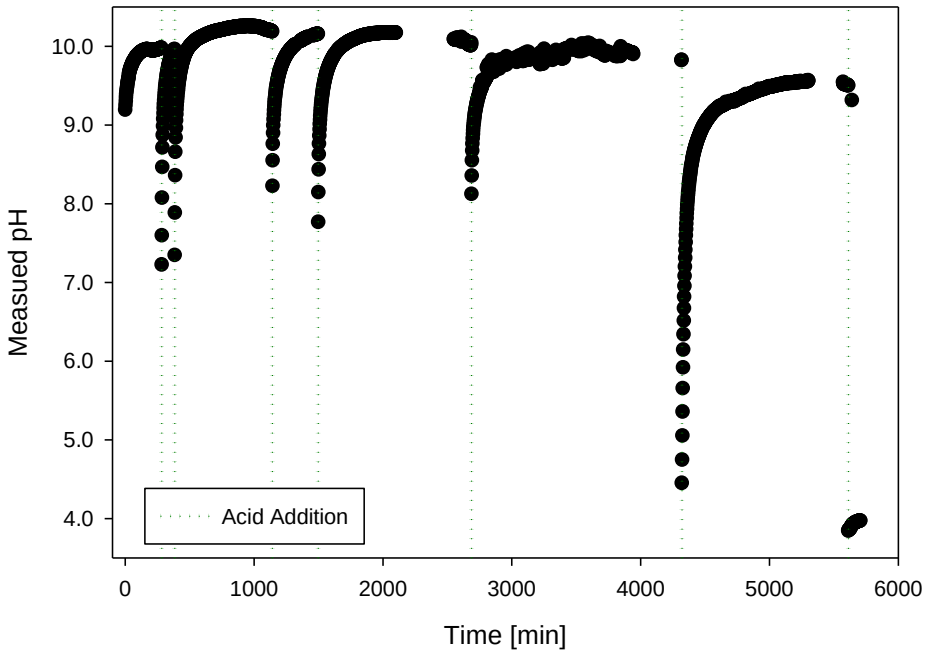

Figure 6.5: Illustrative data from a batch alkalinity release experiment conducted with an emulsion containing 0.04% MgO particles.

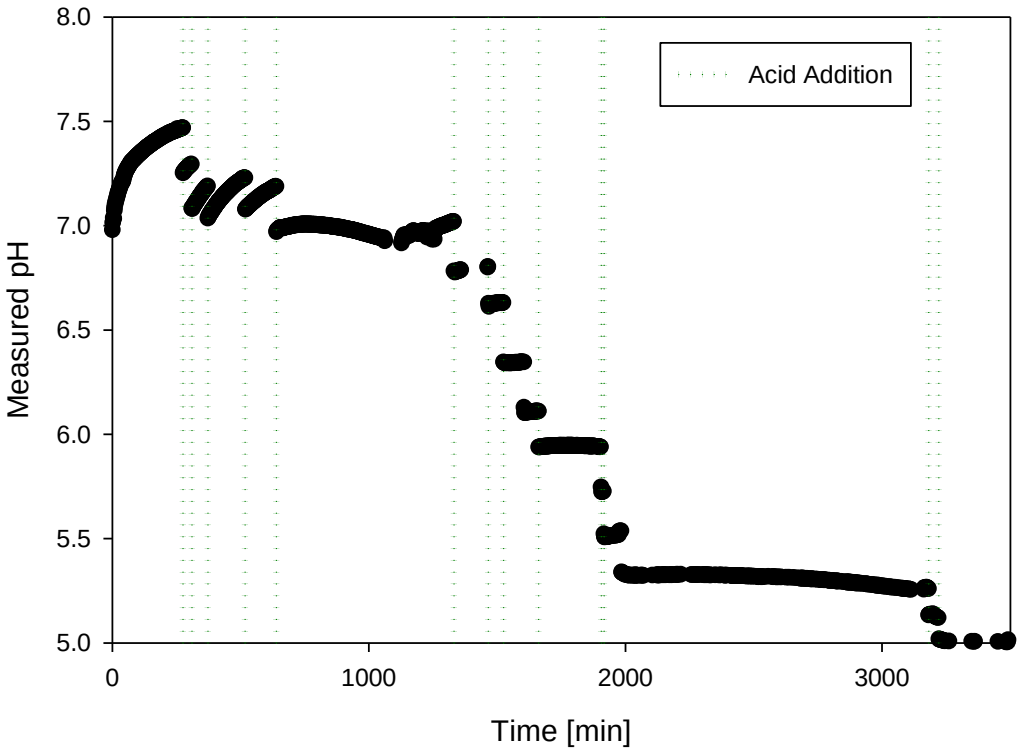

Figure 6.6: Illustrative data from a batch alkalinity release experiment conducted with an emulsion containing 0.02% $CaCO_3$ particle.

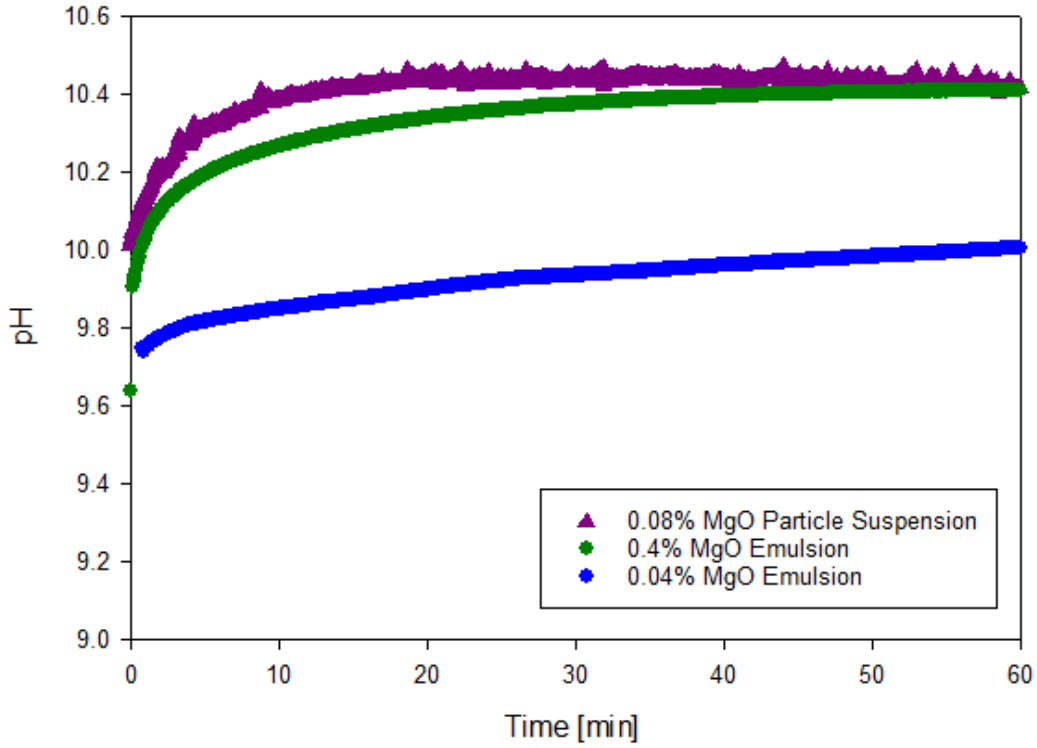

Figure 6.7: Representative pH rebound curves after HCl acid addition from MgO particle suspensions and emulsions with varying mass loadings.

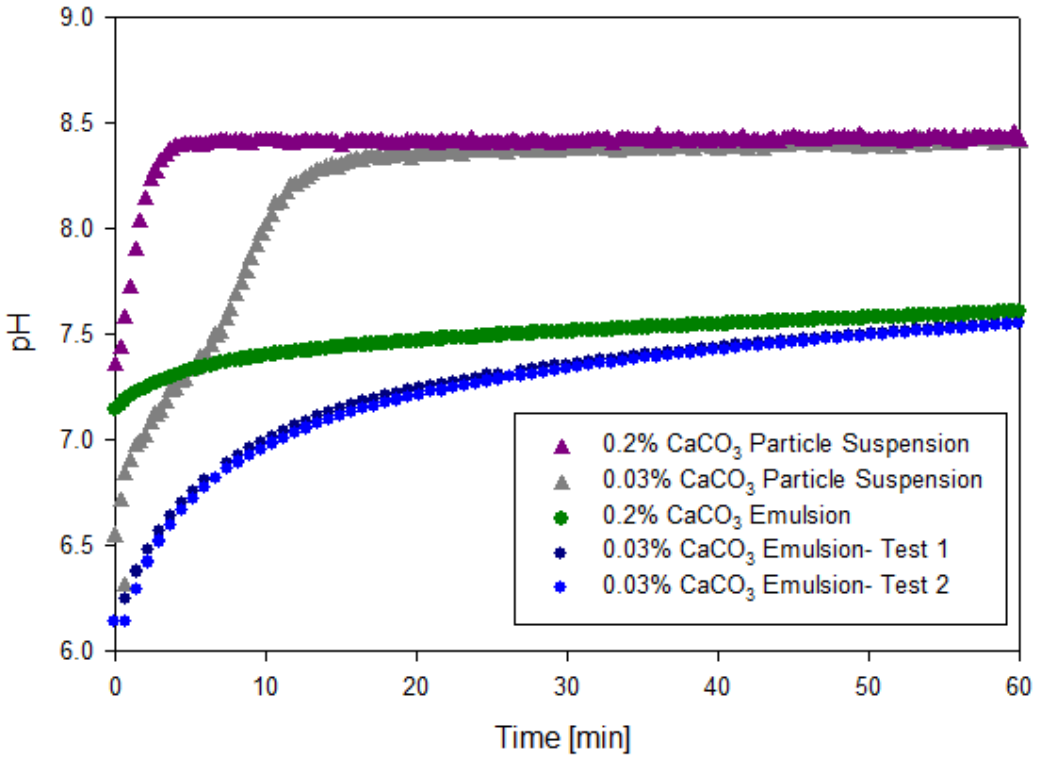

Figure 6.8: Representative pH rebound curves after HCl acid addition from $CaCO_3$ particle suspensions and emulsions with varying mass loadings.

The control being offered by the emulsion was attributed to the additional mass transfer step imposed by the oil phase. Moreover, the rate of release seemed to be further controlled through the mass loading of the particles within the oil droplets (compare curves of 0.03 and 0.2% mass loadings in the emulsion). Additionally, experimental results suggested that particle mass loading in emulsion systems may play a role in the release kinetics, where increasing mass loading increases in the kinetic release rate.

Upon completion of this first set of batch experiments, the focus was placed on MgO particles and thus most of the subsequent work relates to MgO release behavior. MgO was selected over $CaCO_3$ because MgO particles are able to supply nearly twice the alkalinity as $CaCO_3$ particles (per mass basis) and the utilization rate was also superior (Table 6.1). Thus from a practical sense, MgO particles are likely better suited to provide long term alkalinity than $CaCO_3$ (at least in terms of extent). Additionally, magnesium is less ubiquitous than calcium in environmental systems (in both groundwater and sands) and from an experimental methods sense, using magnesium allows for better quantification of total Mg which becomes increasing important when assessing transport and retention of particles in porous media (Chapter 7).

The MD model provided a good predictive capability for the MgO experiments capturing the release kinetics from particle suspension (illustrative data and prediction shown in Figure 6.9). Also shown in Figure 6.10 are the time variable properties within the model. These include Mg speciation within the

aqueous phase, value of the omega term, activity coefficients for mono (gamma1) and divalent (gamma2) ions, ionic strength (*I*), average particle radius, and total surface area (*TSA*).

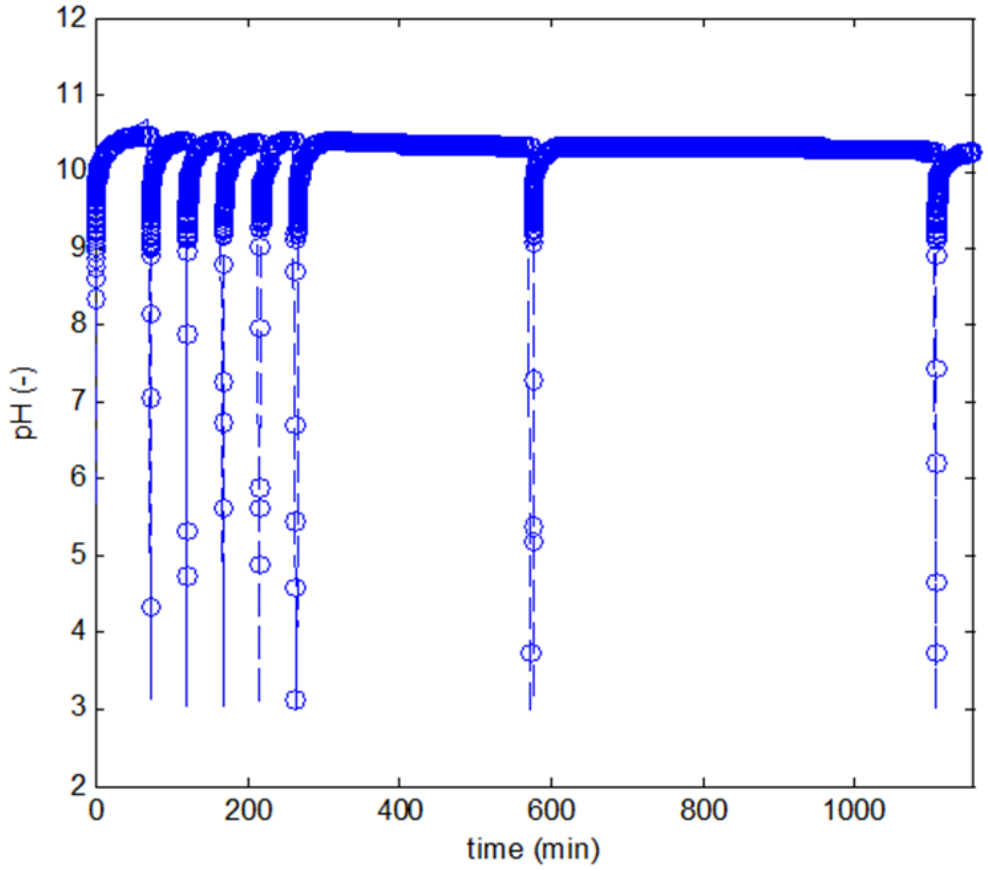

Figure 6.9: Alkalinity release data (open circles) from a suspension of MgO nanoparticles and corresponding rate law mineral dissolution model with complex chemistry considered (line).

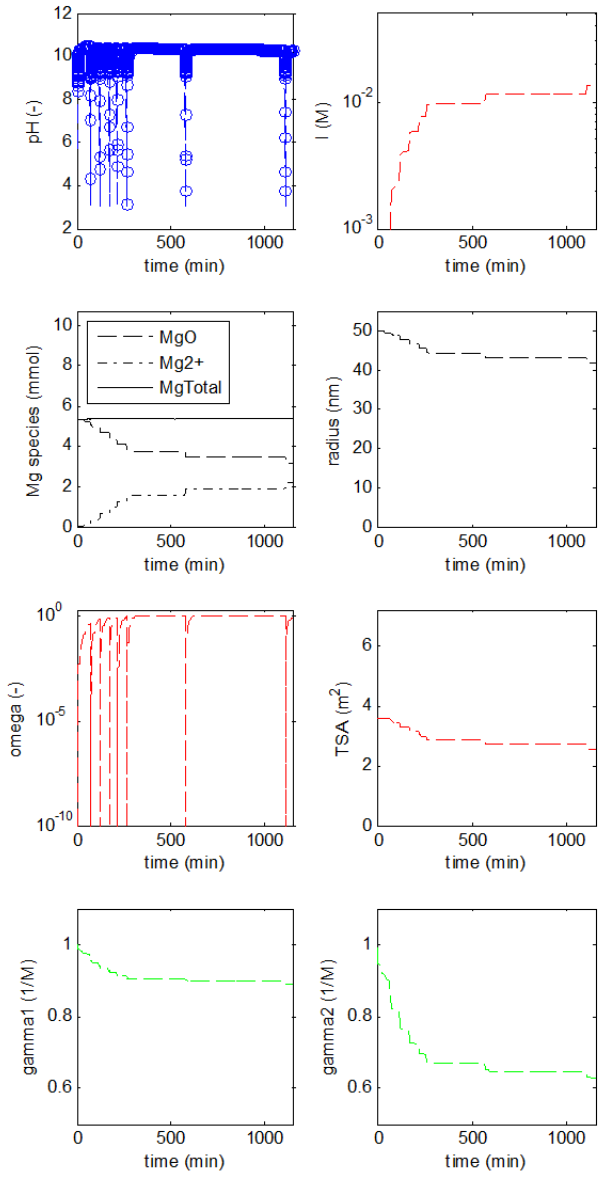

Figure 6.10: Time variable properties found within the release model: temporal pH, ionic strength (I), Mg speciation, average particle radius, omega term, total particle surface area (TSA), and activity coefficients of mono (gamma1) and divalent (gamma 2).

The linear driving force model was able to successfully capture the release kinetics from particles encapsulated in emulsion droplets for both particle types, with preliminary model investigations indicating that the lumped mass transfer coefficients for emulsions containing MgO particles tended to be larger than those produced using emulsions containing the same mass of $CaCO_3$ particles.

Alkalinity release from MgO emulsions with various particle loadings showed an increase in the fitted lumped mass transfer coefficient with increased mass loading (Table 6.2). For example, K_L went from $1.2x10^{-4}$ to $2.2x10^{-3}$ min^{-1} as the mass loading was increased was 0.04 to 0.4% (wt./wt.) (i.e., the release rate increased 18x for a 10x increase in particle mass loading). To ensure that the lumped mass transfer coefficient was successfully capturing the release kinetics (i.e., the pH rebound portion of the curve) the K_{sp} was allowed to vary slightly from $5.011x10^{-11}$ in each k_L fit, to deemphasize the influence of small variations in the description of extended equilibrium pH (i.e., at late times). Results suggest that particle loading offers another point of control for tailoring the rate of alkalinity release to meet site-specific needs, though it may come at the expense of the duration of treatment. Assessments of the capacity of the emulsion based delivery systems suggest that approximately 80% of the particle mass is available for immediate release from the oil in water emulsion (Table 6.1).

Table 6.2: Alkalinity release kinetics for MgO particle-containing emulsions.

Experiment	k_L **[min^{-1}]**	K_{sp}
0.04% MgO Emulsion	1.2×10^{-4}	2.8×10^{-11}
0.1% MgO Emulsion	2.6×10^{-4}	2.0×10^{-11}
0.2% MgO Emulsion	1.8×10^{-3}	1.6×10^{-11}
0.4% MgO Emulsion	1.0×10^{-3}	2.8×10^{-11}

Results of using the combination of MD and LDF are shown in Figure 6.11 for a 0.1% wt. MgO content emulsion. Here the fraction of the bare particles was varied and the mass transfer coefficient fit. Results generally suggest that mineral dissolution mechanisms are not applicable to describe alkalinity release from these emulsions. The best fit results were obtained when the fraction of bare particles was zero (i.e., $f_{,fast}$ 0) - indicating that all particles were successfully encapsulated. This finding was echoed by the 0.4% MgO emulsion modeling results (at early time), where $f_{,fast} = 2x10^{-7}$ and $k_L=1.7x10^{-5}$ min^{-1}. For successful comparison of release kinetics, all subsequent kinetic release models assumed all particles were successfully encapsulated (i.e., $f_{,fast}=0$). The preliminary emulsion conceptual model results (Figure 3.1) support the MD-LDF model finding that free particle mass is not a function of mass loading (over the range of experimental concentrations testes).

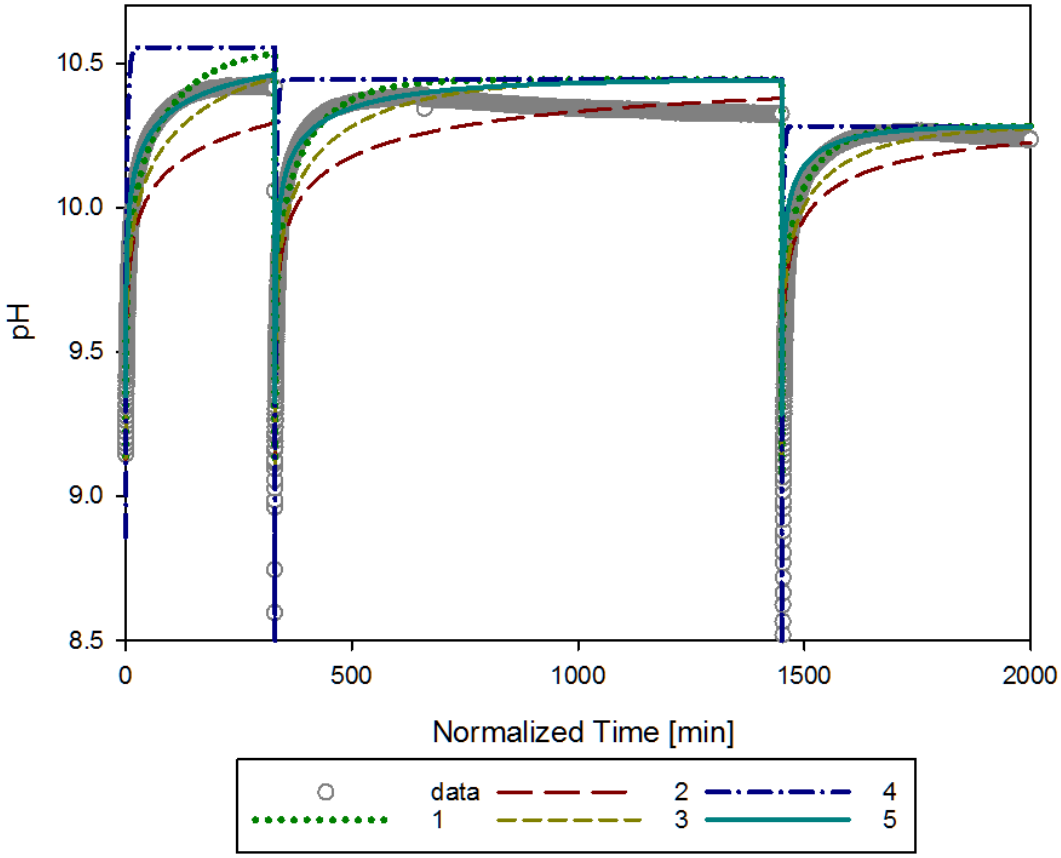

Figure 6.11: 0.1% MgO emulsion model fits where k_L was fit to a prescribed $f_{,fast}$ (1-dashed line) k_L=6.1x10^{-5} min^{-1} and $f_{,fast}$=0.05; (2-medium dashed line) k_L =6.0x10^{-5} min^{-1} and $f_{,fast}$ =0.00025; (3-short dashed line) k_L =6.0x10^{-5} min^{-1} and $f_{,fast}$=0.025; (4-dot and dashed line) k_L =6.0x10^{-6} min^{-1} and $f_{,fast}$ =0.99; and (5-solid line) k_L =2.7x10^{-4} min^{-1} and $f_{,fast}$ =0. All models were run with k_{diss}=1.2x10^{-3} min^{-1} and K_{sp}=5.01x10^{-11}.

Additionally, a theoretical comparison of the rates of alkalinity release using the LDF and rate law dissolution models (MD) for MgO was compared over a range of pH values to understand the influence of chemical equilibrium (i.e., particle solubility) on alkalinity release rates (Figure 6.12). This plot highlights one benefit of particle encapsulation- that alkalinity release rate is not a strong function of pH (expect at pH values nearing equilibrium (i.e., pH>9)).

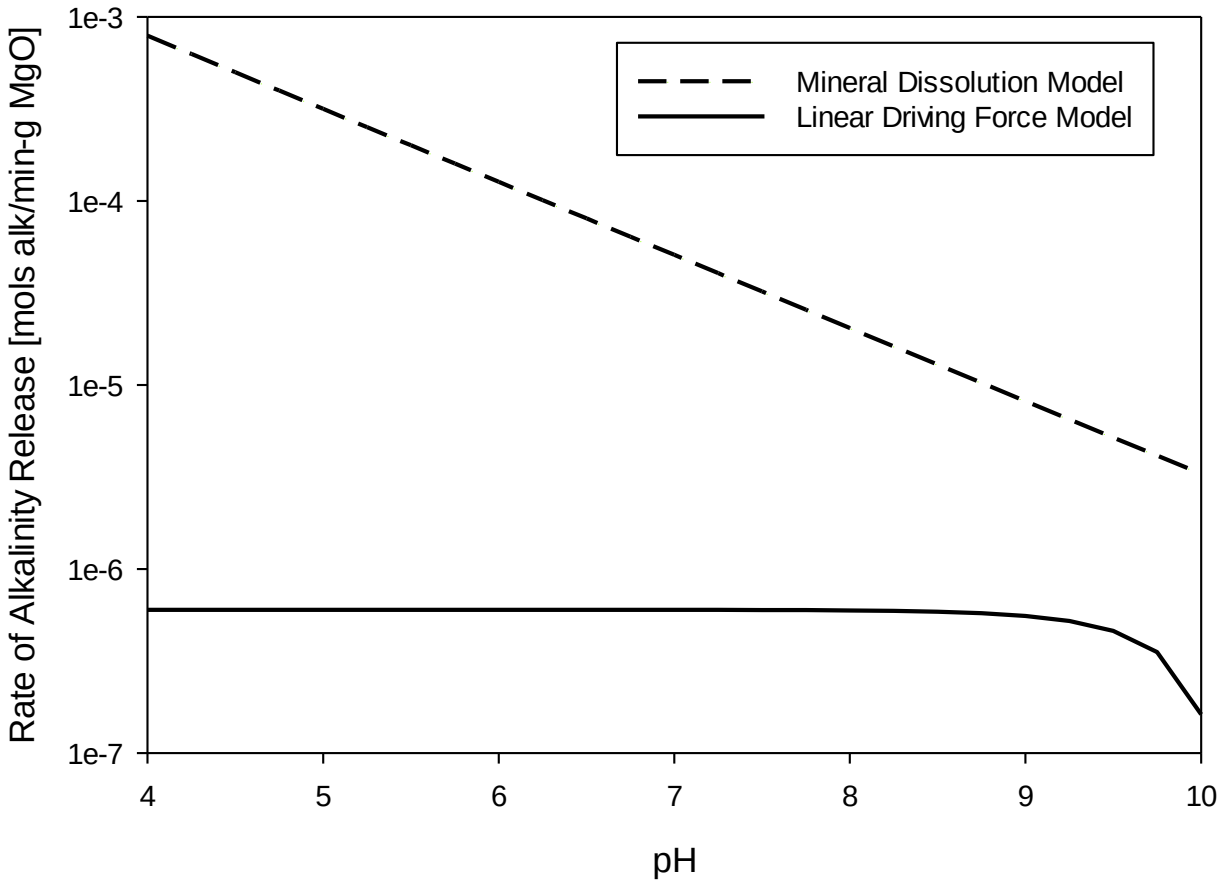

Figure 6.12: Comparison of the MD and LDF models as applied to particle dissolution. Note: release rates are shown on a log scale.

6.5 CONCLUSIONS

Preliminary batch experiments enhanced the conceptual understanding of where particles are held within the oil-in-water emulsions. These results demonstrated that particles placed in the oil phase remain there. The slow increase of aqueous magnesium concentrations with increasing contact time supported the hypothesis that a slow-release mechanism governs release rates. The attenuation of the alkalinity release (as compared to the mineral dissolution rates) is attributed to a resistance of mass transfer across the oil-water interface. Experimental results also indicated that a large fraction of the particles are encapsulated all particle loadings. Even at mass loadings of 1 mg·g-1 (and likely higher), most of the total magnesium mass was present in the oil even after an extended contact time with an aqueous phase.

Alkalinity release experiments confirmed the central, yet fundamental, concept that encapsulated alkalinity-releasing particles are still able to release alkalinity to the aqueous environment as evidenced by the particle utilization rates of 70 and 95% depending on particle type. Magnesium oxide particles seem to be more accessible for release than $CaCO_3$ particles when encapsulated in oil-in-water emulsions. Additionally, emulsion buffering capacity investigations showed that emulsions containing MgO particles have 2.8 times the buffering capacity of the emulsions containing $CaCO_3$ particles (per particle mass basis).

Release experiments, and subsequent modeling, indicated that rates are slower when particles are encapsulated in oil-in-water emulsions as compared to bare particles. The slower release rates from particles encapsulated within the oil was well described with the linear driving force model; whereas particle dissolution kinetics were more rapid and better described using existing empirical mineral dissolution models. This finding supported the hypothesis that emulsions provide resistance to mass transfer via the oil-water interface. Increased particle mass loading in emulsions was found to result in increased alkalinity release rates seen through visual inspection of release curves (Figures 6.7 and 6.8) and supported with model fitting results of k_L (Figure 6.11). Thus, particle mass loading may be a potential point of control on release kinetics from emulsions.

Chapter 7: Subsurface pH Control

7.1 ABSTRACT

Aqueous injections are commonly employed in field applications in conjunction with remedial activities for pH control. However, in-situ pH control via aqueous solutes is often cited as only providing a limited duration of treatment. The ability of aqueous solutions (both buffered and un-buffered) to control pH was assessed in 1-d column experiments. Such experiments were used as a benchmark for which pH treatment via emulsions could be evaluated. Focus was placed on assessing the effectiveness of oil-in-water emulsions for delivery of alkalinity releasing particles and the subsequent sustention of pH as alkalinity was released from retention droplets. Here, particle containing emulsions were injected into 1-d column and both emulsion droplet and total particle transport and retention measured through a medium sand (Federal Fine Ottawa sand) were measured. Installation of flow through pH probes also allowed for interrogation of pH treatment over the course of emulsion injection and subsequent flushing. The developed mathematical model was able to provide reasonable agreement to the experimental effluent pH data through fitting of a mass transfer coefficient. The fitted k were compared to those obtained values determined in batch experiments (Chapter 6) as well as to standard mass transfer coefficients correlations.

7.2 INTRODUCTION

Many remedial interventions require subsurface pH to be modified artificially. Typically, artificial pH control is completed via aqueous phase additions of alkaline solutions (e.g., sodium bicarbonate ($NaHCO_3$), sodium or calcium carbonate ($NaCO_3$ or $CaCO_3$), sodium hydroxide (NaOH), etc.), buffered aqueous solutions (e.g., phosphate buffers). However, there are many limitations to using aqueous phase additions. A major limitation relates to aqueous delivery being governed by ambient groundwater flow and thus preventing long-term control. Alternatively, encapsulation of remedial amendments with oil-in-water emulsions may provide extended treatment as active ingredients slowly release from the emulsions to the aqueous environment.

Emulsions are widely utilized in the food, medical and pharmaceutical industries to encapsulate, deliver, and release active ingredients. Environmental remediation technologies have also employed emulsions, most importantly here, as an amendment itself to promote remedial events such as contaminant biodegradation (e.g., Borden, 2007) and as a delivery vehicle to provide active ingredients to the subsurface (e.g., Berge & Ramsburg, 2009; Shen, et al., 2011; Ramsburg, et al., 2003). Oil-in-water emulsions containing food grade biodegradable oil and a stabilizing agent have been created to improve delivery of amendments (e.g., ZVI) to subsurface (e.g., Berge & Ramsburg, 2009; Quinn, et al., 2005).

To assess the ability of emulsion to provide long-term subsurface pH treatment, 1-d column experiments were conducted to support development of an overall mathematical model for pH control via particle-containing oil-in-water emulsions. Knowledge gained from previous chapters (i.e., emulsion transport, retention and alkalinity release mechanisms) was called upon when developing a model for pH treatment after emulsion injection. Deposited alkalinity releasing particles was evaluated on their ability to provide desired subsurface pH levels by extended controlled release of alkalinity. The effluent pH in these column experiments was modeled using solute transport equations employing expressions for the rate of release. It was hypothesized that the alkalinity release mechanisms described and quantified in Chapter 6 can be used to predict the release rates found in a 1-d column flow-through system. Successful modeling of alkalinity release can be used to identify the main control points of release rate and extent in order to better fulfill specific alkalinity requirements for subsurface pH control.

7.3 MATERIALS AND METHODS

7.3.1 EXPERIENTIAL METHODS

1-d column experiments were used to assess the pH control using injections of various aqueous solutes, both buffered and un-buffered, solutions. Briefly, Kontes borosilicate glass columns (4.9 cm i.d. x 13 cm) were dry packed with different size fractions of a representative medium-grain sandy medium Ottawa sands (Federal Fine Ottawa quartz sand from U.S. Silica) in one centimeter lifts and topped with a flow adapter to a packed height of approximately 10 cm. After dry packing, columns were flushed with CO_2 (top-down flow direction) for approximately 20 minutes. After CO_2 flushing, the column was preconditioned with a 10 mM NaCl electrolyte solution adjusted down to either a pH of 4 or 5 with hydrochloric acid (HCl). The column apparatus was equipped with two flow-thru micro pH probes (Microelectrodes, Inc.) connected through a Campbell Scientific data logger (CR1000 model) to monitor the influent and effluent pH in five-second intervals (Figure 7.1).

Both the effluent pH response to non-buffered aqueous solutions adjusted to specific pH value (4-10) and buffered aqueous solutions (phosphate buffer) were assessed using the experimental setup described above.

The use of particle suspensions for pH control was attempted in column experiments following a similar experimental procedure as columns where a suspension of bare particles was injected into the column via a peristaltic pump.

However, the bare particle suspensions were unable to be successfully injected into the column. The difficulties encountered when injecting bare particles highlights the need for particle modification (i.e., particle encapsulation).

The transport and deposition from $CaCO_3$ and MgO containing emulsions was investigated using 1-d column experiments. Due to the increased kinetic stability of the oil-in-water emulsions, injection of emulsions was into the sands columns was successful. Emulsions contained 0.02% wt. $CaCO_3$ and MgO, respectively, 20% soybean oil and was stabilized with 3.5% wt. Gum Arabic unless stated otherwise. For each experiment two columns were conducted in parallel - one as a control on droplet deposition, the other to assess alkalinity release (alkalinity release will be detailed in Chapter 6). It should be noted that column experiments were setup as to evaluate not only emulsion transport and deposition but also subsequent alkalinity release from retained droplets in a single experiment. The deposition control column was terminated after the emulsion (or particle) pulse was complete and flushed yielding a total of 5 pore volumes. The column was then sectioned and analyzed to develop the deposition profile. Total metal ion concentration (i.e., Mg or Ca depending on particle type used) were measured in the aqueous samples using ICP-OES after acidification of the samples. A retention profile of total metal concentrations is measured via ICP-OES.

Column experiments were also used to assess alkalinity release (i.e., via flow-thru micro pH probes connected to a data logger to monitor the influent and

effluent pH in five-second intervals (Figure 7.1) continued operating through the end of the release process, and then were also sectioned and analyzed at the completion of the release experiment. This protocol allowed for interrogation of the deposited fraction between the start and conclusion of the alkalinity release process.

Zeta potential measurements were determined using a Zetasizer Nano Z (Malvern) by measuring the electrophoretic mobility and converting to zeta potential via Henrys or Smoluchowski equation. The zeta potentials for particle-containing emulsions were only able to be measured at the equilibrium pH due to alkalinity release from emulsions. The inability to measure zeta potential at other pH values limited the understanding of how zeta potential and surface charge change over the large changes in pH seen in the batch and column experiments.

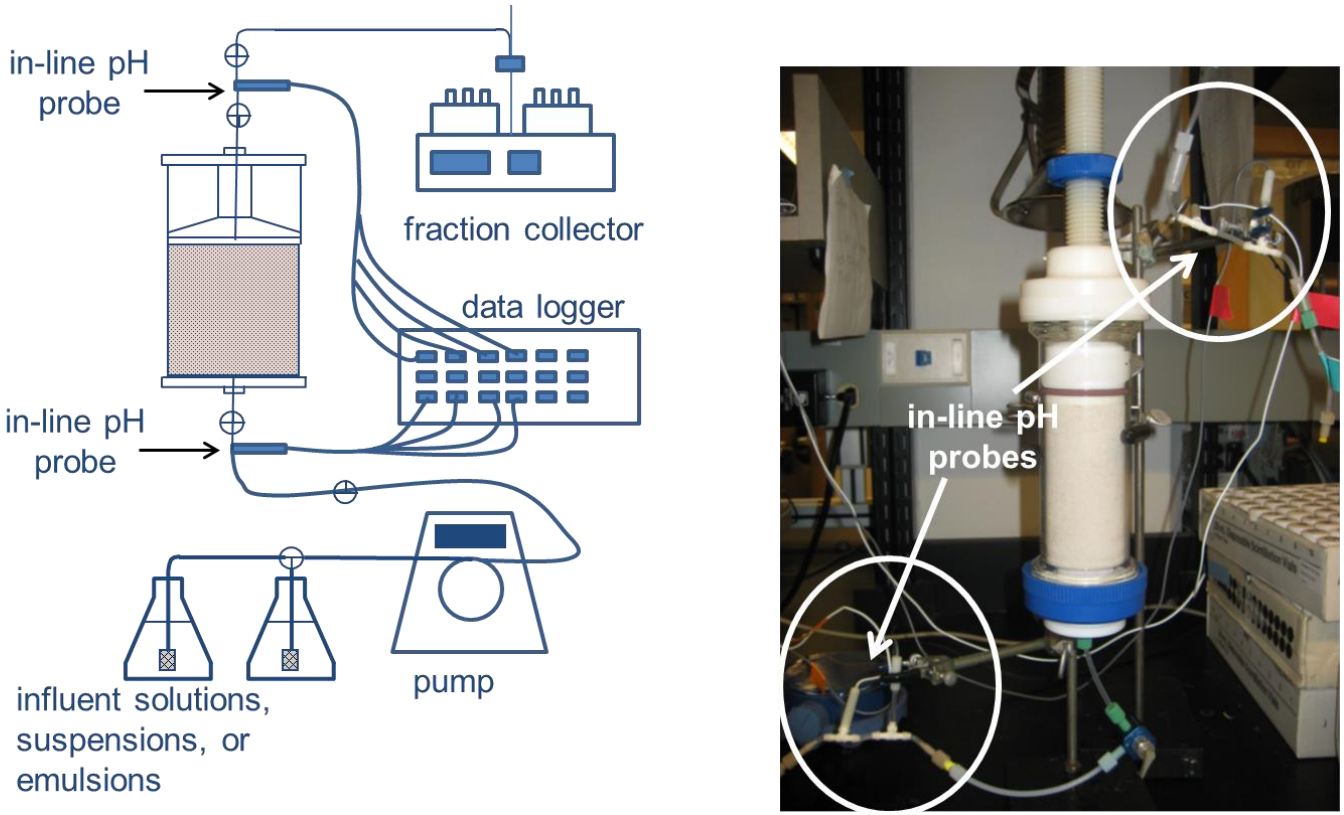

Figure 7.1: Schematic of column setup with flow-thru micro pH probes (left); image of column setup (right).

7.3.2 Modeling Approach

Modeling effluent pH after injection of oil-in-water emulsions was completed using an ADR expression where the alkalinity release from the entrapped emulsion, was added through a reaction term.

$$\frac{\partial(nS_wC)}{\partial t} = \frac{\partial}{\partial x}(nS_w\alpha v_x\frac{\partial C}{\partial x}) - \frac{\partial C}{\partial z}(nS_wv_xC) + nS_w \cdot k \cdot SSA(C^* - C) \quad (7.1)$$

The following assumptions were made about the porosity, water saturation and dispersivity of this system:

$$n \neq f(x,t);\ S_w = f(x) \neq f(t);\ \alpha = f(x) \neq f(t) \quad (7.2)$$

$$nS_w\frac{\partial C}{\partial t} = n\frac{\partial}{\partial x}\alpha \cdot v_xS_w\frac{\partial C}{\partial x} - \frac{\partial}{\partial x}nS_wv_xC + nS_w \cdot k \cdot SSA(C^* - C) \quad (7.3)$$

Expression 7.3 can be re-written in terms of Darcy flux, $q = nS_wv_x$ as shown in Equation 7.4.

$$nS_w\frac{\partial C}{\partial t} = \alpha \cdot q\frac{\partial^2 C}{\partial x^2} + (\alpha\frac{\partial q}{\partial x} + q\frac{\partial \alpha}{\partial x})\frac{\partial C}{\partial x} - C\frac{\partial q}{\partial x} - q\frac{\partial C}{\partial x} + nS_w \cdot k \cdot SSA(C^* - C) \quad (7.4)$$

From the phase mass balance $\frac{\partial q}{\partial x} = 0$, and assuming that the product of $\frac{\partial \alpha}{\partial x}\frac{\partial C}{\partial x}$ is negligible, and dividing by nS_w, Equation 7.4 can be reduced to the more common 1-D formulation of the ADR with a source term (Equation 7.5).

$$\frac{\partial C}{\partial t} = \alpha \cdot v_x\frac{\partial^2 C}{\partial x^2} - v_x\frac{\partial C}{\partial x} + k \cdot SSA(C^* - C) \quad (7.5)$$

This expression was approximated with a finite difference model (implicit in space, forward in time) to simulate the pH from alkalinity release in 1-d column experiments. The following boundary conditions were used to mimic a solute pulse injection: a Dirichlet (i.e., specified concentration) was used at the inlet (i.e., x=0, t=0, C=C_0; x=0, t<t_{pulse}, C=C_0; and x=0, t<t_{pulse}, C=0). A Neumann (i.e., $\frac{\partial^2 C}{\partial x^2} = 0$) was used at the outlet of the column. Alkalinity release was modeled for with the intrinsic mass transfer coefficient, k, as a fitted parameter. The mass transfer coefficient was modulated by the specific surface area available for mass transfer.

$$k_L(x) = k \cdot SSA(x) \qquad (7.6)$$

and,

$$SSA = \frac{SA_{drop} N_{drop}}{V_{total}} = \frac{SA_{drop}}{V_{total}} \frac{V_{DP}}{V_{drop}} = \frac{6 V_{f,DP}}{d_{drop}} \qquad (7.7)$$

Where: SSA is the specific surface area of droplets [cm^{-1}]; $V_{f,DP}$ is the volume fraction of dispersed phase retained [mL DP·mL-total volume^{-1}]; V_{drop}, SA_{drop}, and d_{drop} are the volume of a droplet [cm^3], surface area [cm^2] and diameter of a droplet [cm], respectively. V_{DP} and V_{total} are the total volume of the dispersed phase and system, respectively [mL:]. N_{drop} is the number of oil droplets [-]. The fractional mass remaining is defined as:

$$E(x,t) = \frac{M_{part}(x,t)}{M_{0,part}(x)} \qquad (7.8)$$

Thus the overall release expression goes to zero (i.e., $k_L(x)=0$) when there is no particle mass remaining (i.e., $Mg(OH)_2(x,t)=0$).

The alkalinity release mechanism was assumed to follow a linear driving force model (i.e., release from encapsulated particle in emulsion droplets). It was presumed that the metal ion will govern release. When considering release from MgO particles-containing emulsions, the governing species was the Mg^{2+} ion for release. The release was then expressed as:

$$(\frac{\partial Mg^{2+}}{\partial t})_{rxn} = k_{rel}(Mg^{2+*} - Mg^{2+}) \qquad (7.9)$$

Particle mass and ion release are directly related by Equation 7.10 in $[\frac{dmol}{dt}]$.

$$-\frac{dMg(OH)_2(s)}{dt} = \frac{dMg^{2+}}{dt} \quad (7.10)$$

Initial alkalinity particle mass available for alkalinity release was estimated from emulsion droplet retention. Spatial emulsion retention was modeled using hyper-exponential of the known experimental retention profile (see Equation 5.2 and related discussion).

When considering mass transfer across an interface with a linear driving force model, knowledge of the mass transfer coefficient, *k*, or the lumped mass

transfer coefficient, k_L, is required. Recall that these coefficients are related through the specific interfacial area as: $k_L=k\cdot A_s$. However, the specific interfacial area is often a difficult value to measure or estimate especially in porous media when only a portion of the NAPL interface may be in contact with the flowing aqueous phase, with the remaining surface area in contact with soil grains. In porous media, correlations employing the Sherwood number have been empirically related to Reynold's number (*Re*), NAPL saturation (S_N) and properties of the porous media (e.g., d_{50} and U_i)., (e.g., Miller et al., 1990; Powers et al., 1992, 1994a).

Three Sherwood dissolution models were explored- two developed for dissolution from NAPL droplets in porous media (Powers et al., 1992 with Equation 7.11 and Nambi & Powers (2003) in Equation 7.12) and one for dissolution from solid spheres in a packed bed reactor (Wilson and Geankoplis (1996). NAPL dissolution models were calculated with a modified Sherwood number is defined as either:

$$Sh' = 57.7 \cdot \mathrm{Re}'^{0.61} d_{50}{}^{0.64} Ui^{0.41} \quad (7.11)$$

$$Sh' = 37.2 \cdot S_N{}^{1.24} \mathrm{Re}'^{0.61} \quad (7.12)$$

Where: S_N is the NAPL saturation [-] and Reynolds number in these correlations is calculated as:

$$\mathrm{Re}' = \frac{\rho \cdot q \cdot d_{50}}{\mu} \quad (7.13)$$

The lumped mass transfer coefficient can then be calculated from *Sh'* by Equation 7.15.

$$k_L = Sh' \cdot \left(\frac{D_{ab}}{d_{50}^{\,2}}\right) \qquad (7.14)$$

Where: ρ and μ are the density and viscosity of the aqueous fluid, respectively; D_{ab} is the diffusion coefficient of the dissolved solute in the aqueous fluid.

For dissolution from solid spheres in a packed bed, Wilson and Geankoplis (1996) give the mass transfer coefficient as:

$$k_L = 1.09\left(\frac{d_{50} \cdot q}{D_{ab}}\right)^{-2/3} \cdot \frac{q}{n} \qquad (7.15)$$

7.4 Results and Discussion

7.4.1 Aqueous Injections

Column experiments were completed to evaluate pH treatment with aqueous additions (buffered and un-buffered). An example response from a control columns conducted using Ottawa Federal Fine sand is shown in Figure 7.2. In this column experiment MilliQ water was adjusted to pH 4 using HCl and to pH 6 using NaOH in a background solution of 10 mM NaCl. Similar behavior was seen when influent water was buffered using a phosphate buffer to a pH of approximately 4 and 8 and non-buffered at pH 7 (Figure 7.3). Results suggest ion exchange with the sand surface can influence pH adjustment. If no interaction with the sand grains occurred then effluent pH should directly mimic influent

solution pH, albeit offset by 1 PV. Thus, these experimental results indicate some interaction between solutes and the sand. Most likely H^+ ions are directly interacting given the effect on pH; however, other aqueous species linked to pH may also exchange with the sand. Although some exchange was observed it was assumed that the solid had only modest capacity for such exchange was therefore neglected when simulating the release from emplaced emulsion droplets.

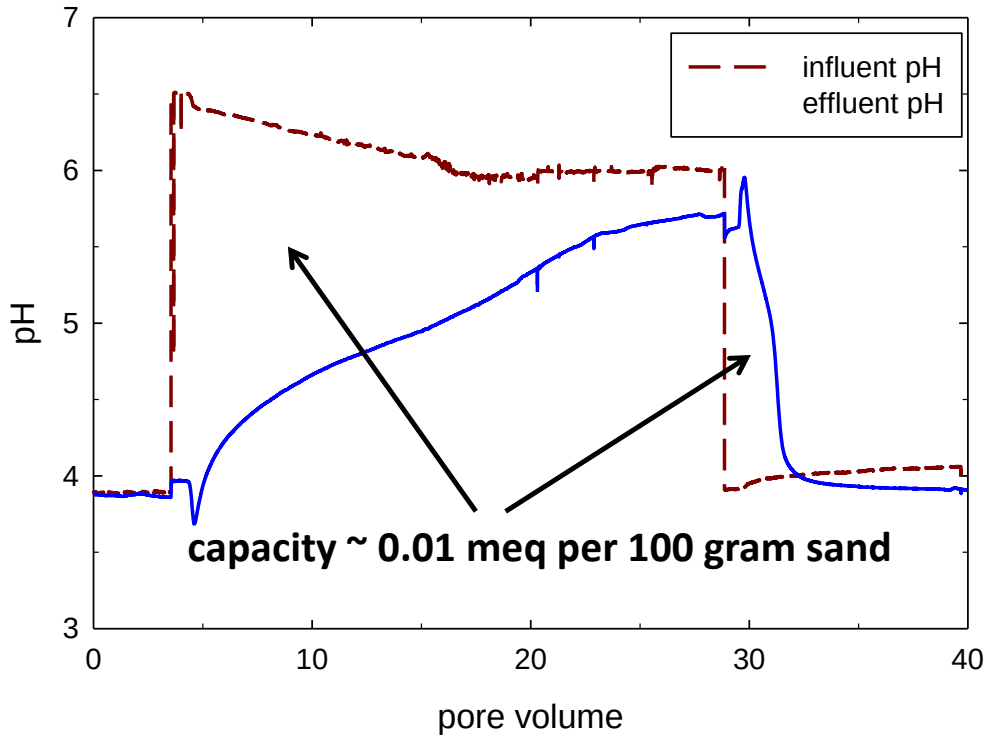

Figure 7.2: pH adjustment using aqueous solutions in Ottawa Federal Fine sand. 10 mM NaCl solution was adjusted down to pH 4 using HCl and back up to pH 6 using NaOH. The background electrolyte was added to keep ionic strength constant between the pH adjusted solutions. Column Parameters: n=0.37; Q=1 mL·min^{-1}; PV=67 mL; α= 0.04 cm.

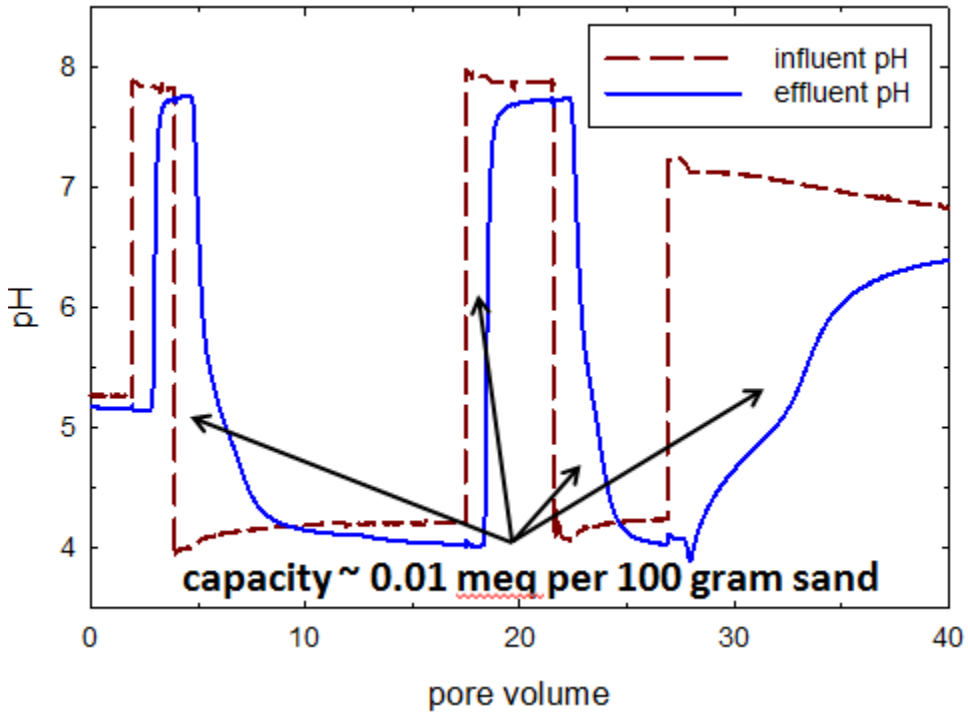

Figure 7.3: pH control using aqueous additions of both buffered and unbuffered solutions on 20-30 Ottawa sand. A phosphate buffer was used to buffer solution to a pH of 4 and 8, followed by an unbuffered solution adjusted to pH 7 with NaOH. Column Parameters were: n=0.36; Q=1 mL·min^{-1}; PV=64 mL.

7.4.3 TRANSPORT AND RETENTION OF EMULSIONS CONTAINING PARTICLES

Shown in Figure 7.4 are the emulsion breakthrough curves when a 0.02% $CaCO_3$ (experiment 3) and a 0.02% MgO emulsion (experiment 8) were injected into Federal Fine Ottawa sand, respectively. Breakthrough curves suggest that the emulsions (even when containing particles) are well transported in sandy porous media. The deposition profiles for these columns were quantified for retention of the dispersed phase of the emulsion (Figures 7.4 – 7.7). Recall that in the case of the deposition control, the column was terminated after the emulsion delivery phase. For the alkalinity release experiment, flow continued for an additional 50 pore volumes. It is interesting to note similarity and reproducibility of the deposition profiles (and the breakthrough curves). The similarity of the deposition profiles suggests droplet attachment to the sand grains is not strongly influenced by the longer duration flushing and release of the encapsulated nanoparticles. This suggests that once delivered the emulsion is relatively stationary within the treatment zone - an important aspect of targeted delivery. However, it should be noted that droplet retention of the MgO emulsion (~11%) was lower than that observed for the $CaCO_3$ emulsion columns (~30%).

Table 7.1: Column parameters for experiments conducted with emulsions containing particles.

experiment	porous media	porosity	bulk density	packed length	pore volume	measured flow rate	initial dispersivity	dispersed phase content	measured viscosity	modeled viscosity[c]	mobility ratio	emulsion introduced	recovered in effluent	retained in column	mass balance
		n	ρ_b	L	PV	Q	α_0	C_0	μ	μ_e	M				MB
		[-]	[g·cm^{-3}]	[cm]	[mL]	[mL·min^{-1}]	[cm]	[% wt.]	[mPa·s]	[mPa·s]	**[-]**	[PV]	[g]	[g]	[%]
3A*	FF	0.38	1.64	10.4	71.9	1.03	0.084	22.7 (±0.4)	7.9[b]	7.5	7.9	2.4	28.3	5.91	98
3B*	FF	0.37	1.68	10.2	67.8	1.03	0.072					2.5	30.5	5.73	100
8A**	FF	0.37	1.66	10.3	69.5	1.00	0.033	23.5 (±0.1)	n.m.[a]	8.2	8.6	2.1	28.1	2.54	96
8B**	FF	0.38	1.65	10.3	70.7	1.02	0.036					2.1	28.4	2.15	98

* 0.02% $CaCO_3$ alkalinity-releasing particles present in emulsion
** 0.02% MgO alkalinity-releasing particles present in emulsion
[a] not measured due to insufficient sample volume
[b] single measurement
[c] emulsion viscosity modeled using expression presented in Chapter 3 based on Sibree (1930) and Broughton and Squires (1937)
μ_d is the displacing fluid viscosity. These experiments used water as the displacing fluid; μ_d =0.954 mPa·s (i.e., the viscosity of water at 22°C)
± indicates standard deviation

Additionally, the transport and deposition of total metal (i.e., calcium for the $CaCO_3$ and total magnesium for MgO emulsions) was also assessed. The total metal behavior was used as a proxy for alkalinity release. Total calcium and magnesium concentrations were measured using ICP-OES after acidification of the samples. The breakthrough curve for total calcium and magnesium, respectively, are shown in Figure 7.5 and Figure 7.7. In both set of experiments, the particle metal transport behavior was found to be similar to the breakthrough curve for the dispersed phase of the emulsion, suggesting that the alkalinity particles are held and transported with the emulsion. However, slight tailing in both the total calcium and magnesium was observed between pore volumes 3 and 5. Tailing could be due to retardation of the proxy metal ions resulting from interactions with the sand grains.

Because of the nearly ubiquitous presence of calcium in the system and the many possible interactions Ca^{2+} can undergo, the calcium retention data had significant variability. This can be seen with both in the total calcium deposition profiles (Figure 7.5). The deposition profile for total calcium suggest that levels are very near the background concentration of total calcium on the sand (reported above, $(6.5\pm0.7)\times10^{-3}$ mg/g). It should be noted that the acid digestion method used to quantify total calcium measures all calcium present in the system regardless of origin and thus the calcium concentrations may not be an accurate proxy for carbonate.

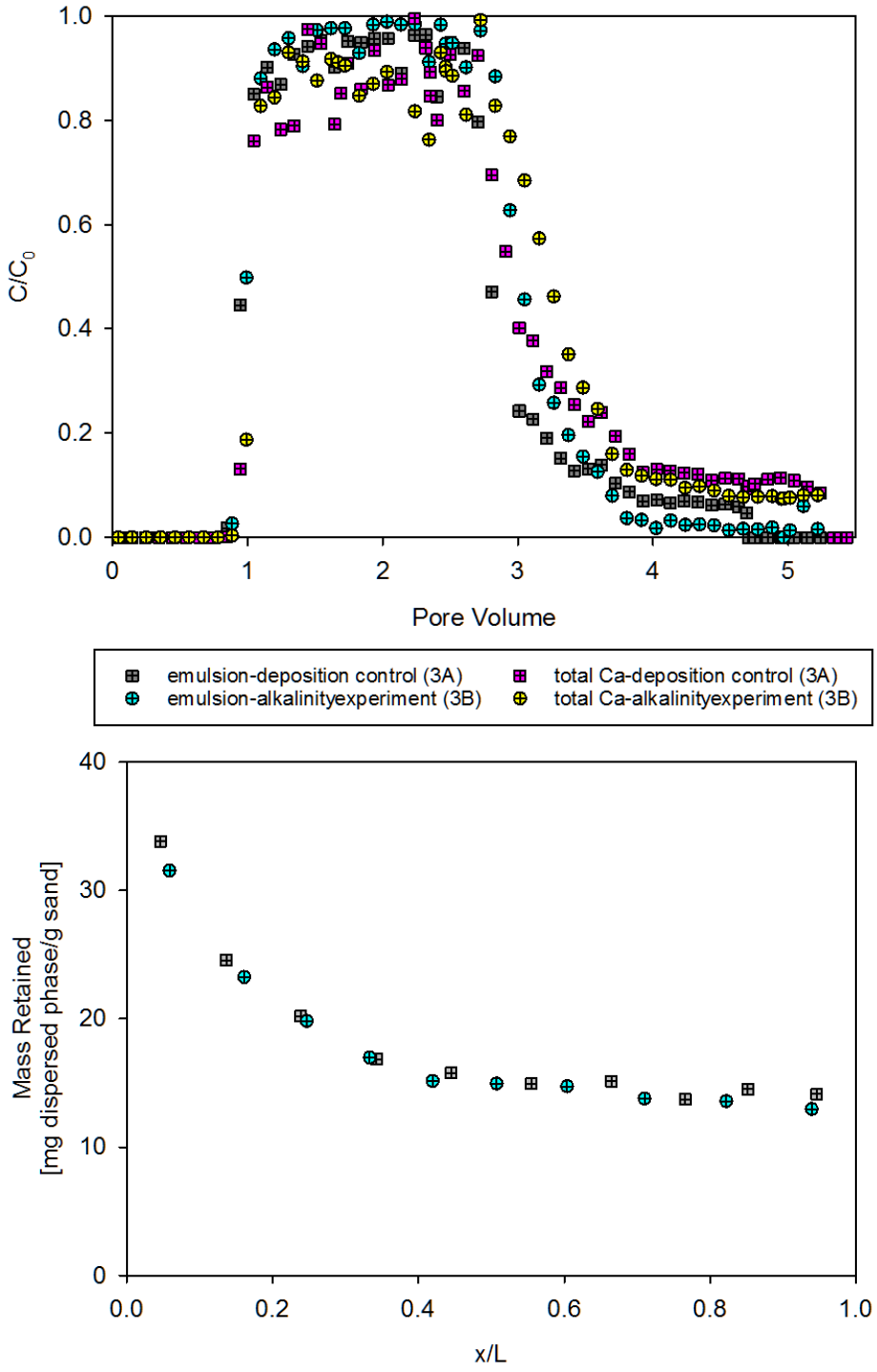

Figure 7.4: (top) Emulsion and total calcium breakthrough curves and (bottom) deposition profiles for $CaCO_3$ containing emulsion deposition control column (3A) and alkalinity release column (3B).

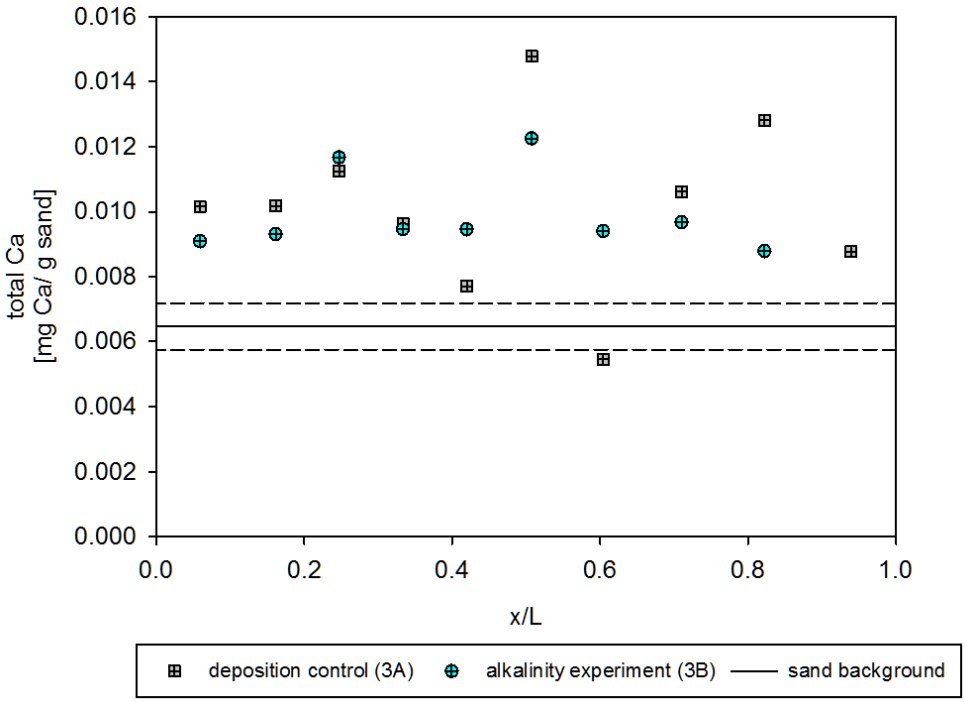

Figure 7.5: Total calcium deposition profiles for the $CaCO_3$ containing emulsion deposition control column (3A); and alkalinity release experiment (3B). The solid line indicates the background concentration of the Ottawa sand and dashed lines show the standard deviation.

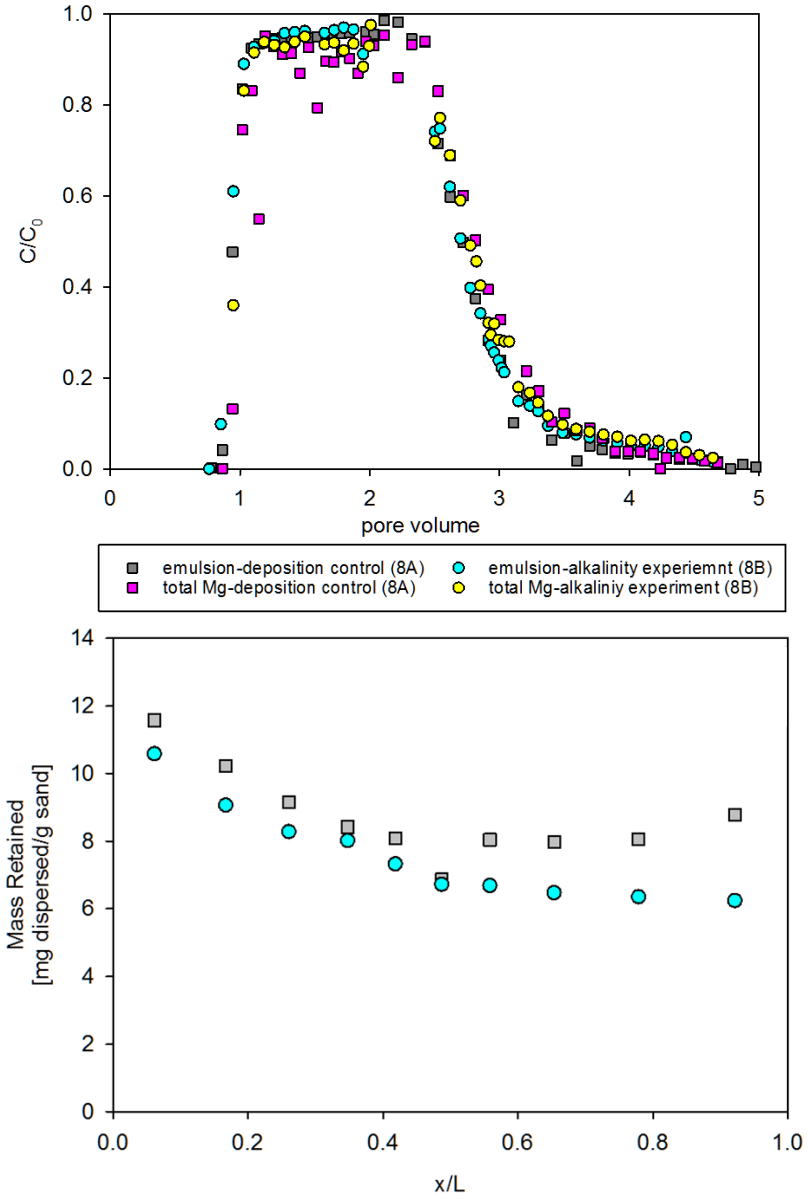

Figure 7.6: (top) Emulsion and total magnesium breakthrough curves and (bottom) deposition profiles for MgO containing emulsion deposition control column (8A) and alkalinity release column (8B).

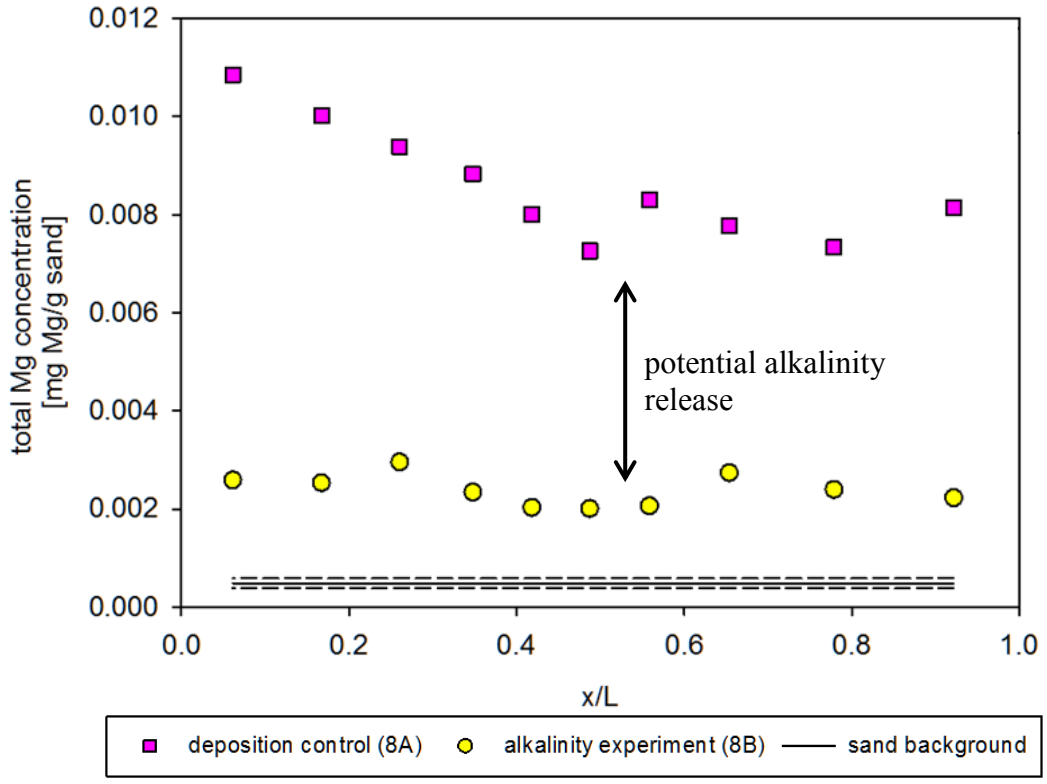

Figure 7.7: Total magnesium deposition profiles for the MgO containing emulsion deposition control column (8A); and alkalinity release experiment (8B). The solid line indicates the background concentration of the Ottawa sand and dashed lines show the standard deviation.

Similar transport is noted between the emulsion and the total magnesium in this column experiment supporting the assumption that the magnesium particles are held within the emulsion droplets and transport with the emulsion during injection and initial flushing. Given that emulsion retention was not greatly affected by long term flushing (as seen in Figure 7.4 and Figure 7.6) but that there was a marked decrease in magnesium deposition after alkalinity release indicates that once the emulsion droplets are retained in the sand they are no longer able to be transported but that that magnesium particles themselves are able to release alkalinity from the retained droplets (Figure 7.7). This behavior was harder to distinguish in the $CaCO_3$ emulsion columns due to the difficulties and inaccuracies of measuring total calcium as opposed to total magnesium.

7.4.4 pH CONTROL USING OIL-IN-WATER EMULSIONS

The sustained release of alkalinity from the retained droplets containing $CaCO_3$ and MgO particles respectively is shown in Figure 7.8. The pH was maintained above 6 for greater than 25 pore volumes after the delivery of the $CaCO_3$ emulsion (note that the influent to the column was at pH 5). While the pH in these experiments overshoots the optimal range for bioremediation, it should be noted that the influent water lacks appreciable buffering capacity. Thus it may be reasonable assume that groundwater will mitigate the pH overshoot. Future work should explore the role of groundwater composition, specifically the natural buffering capacity, on the pH release from the emplaced emulsion.

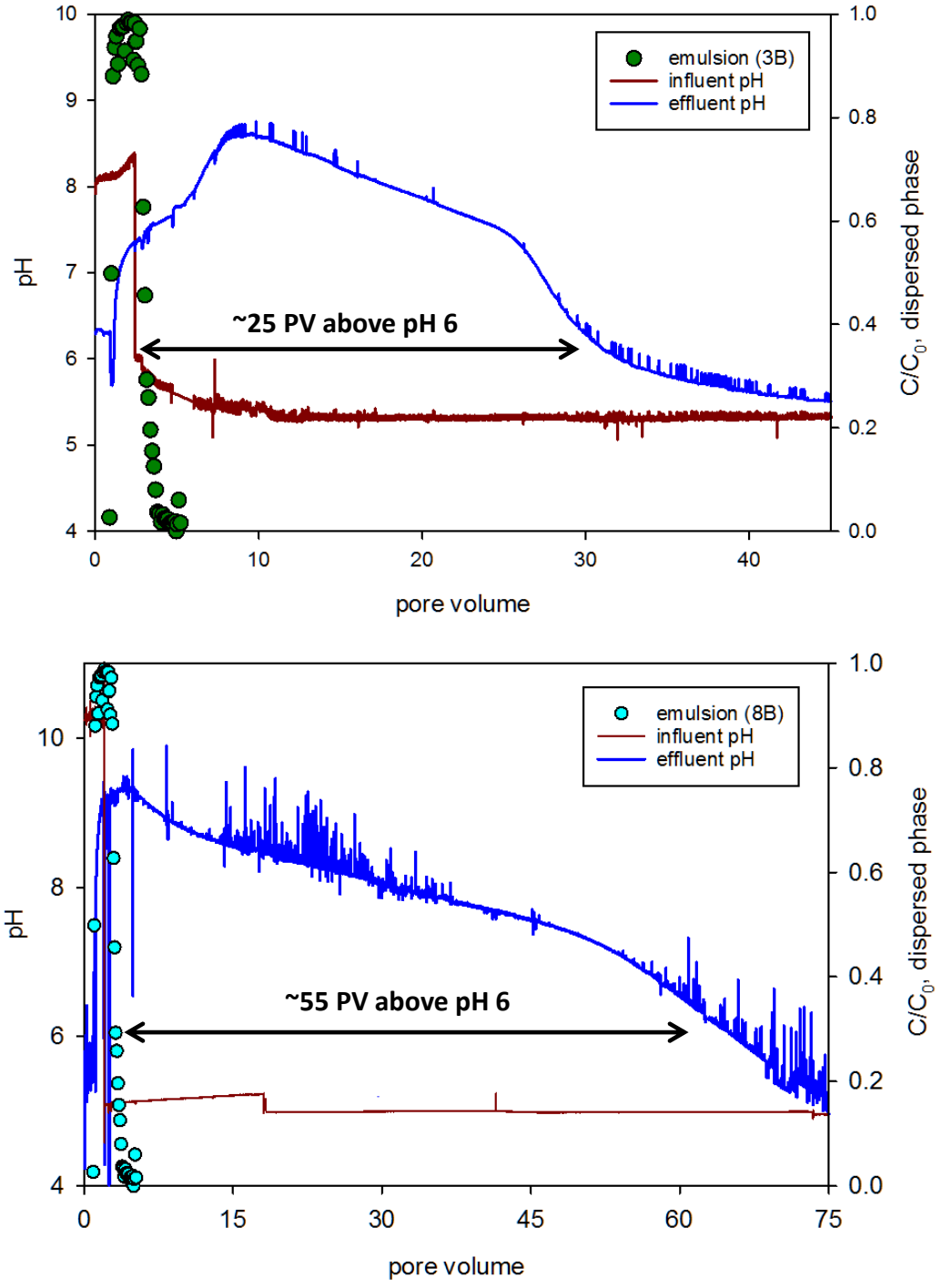

Figure 7.8: Sustained alkalinity release from a 0.02% (wt.) (top) $CaCO_3$ emulsion (3B), and (bottom) MgO emulsion (8B).

It should be noted that on a mass basis MgO particles are able to supply two times the alkalinity than $CaCO_3$ particles due to differences in the molecular weight of the minerals. Given the low particle loading (0.02% wt.), greater particle loadings are anticipated to offer increased durations of treatment, though there may be a trade off in that higher loadings produce faster rates of release.

Modeling pH treatment was completed for MgO release based on the linear driving force model formulation developed in the previous chapters. The model simultaneously fit the mass transfer coefficient, k, and K_{sp} to the experimental data. The best model fit gave k=8.1x10^{-7} cm·min^{-1} and K_{sp}= 3.2x10^{-11} and provided a good description of the experimental data over the course of alkalinity release (>75 PV, Figure 7.9).

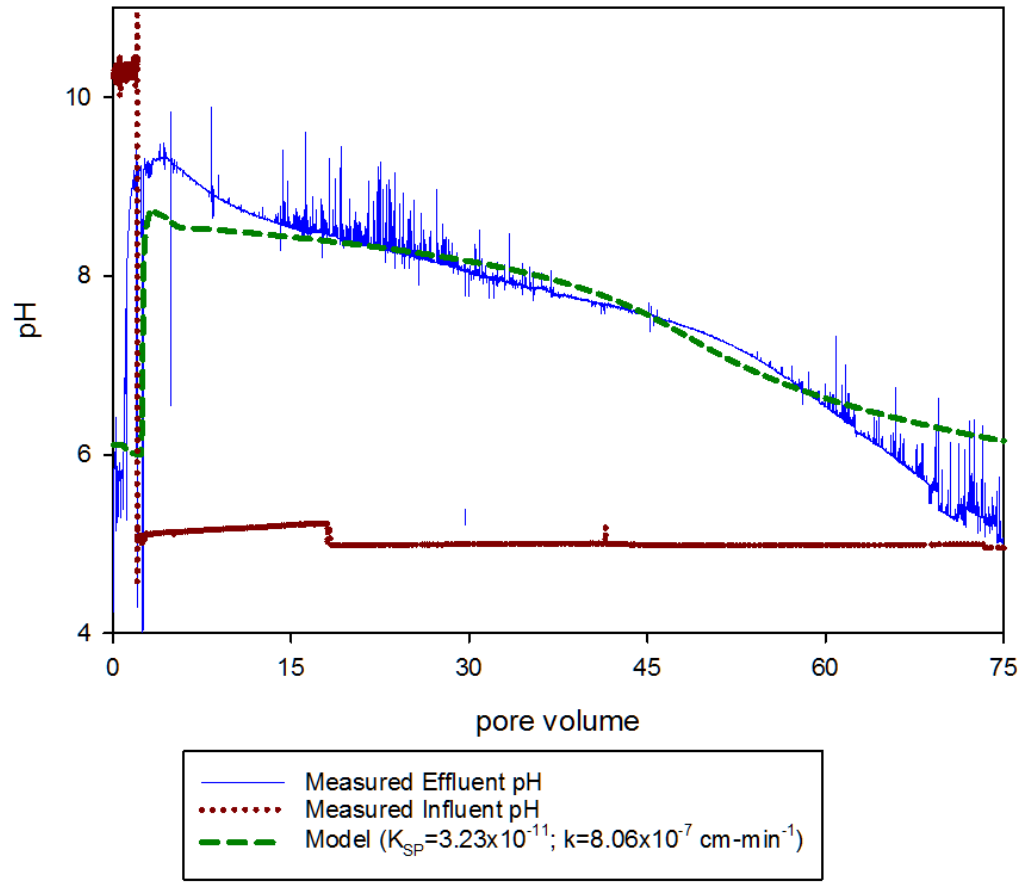

Figure 7.9: Experimental and corresponding model for effluent pH due to alkalinity release from 0.02% MgO (8B) emulsion. Fitted parameters: K_{sp}= 3.2x10^{-11}; k=8.1x10^{-7} cm·min^{-1}. Model mass balance=98% ($Ca_{,tot}$, $Na_{,tot}$, $Mg_{,tot}$).

The pH model is highly sensitive to both the K_{sp} and k values as evidenced through Figure 7.10. An order of magnitude variation in either parameter will change the pH (over the first 30 PVs) dramatically. Varying k from 8.06×10^{-8} $cm \cdot min^{-1}$ up two orders of magnitude to 8.06×10^{-6} $cm \cdot min^{-1}$ the pH increases from 5 to 10; and similarity increasing K_{sp} from 5.0×10^{-12} to 3.2×10^{-10} changes early time pH from 5.5 to 9.5. There are very few reports of K_{sp} for MgO and $Mg(OH)_2$ in the literature, and the data that do exist vary considerably (5.61×10^{-12} Olmsted & Williams, 2007; 1.8×10^{-11} Sillen, et al., 1964; 5.012×10^{-11} Pokrovsky and Schott, 2004). Still, the K_{sp} value fit to the column experiment not only fell within the range of literature values, but also is in good agreement with the fitted solubility product values from the batch experiment modeling (i.e., K_{sp} fitted in batch experiments ranged from $1.6\text{-}2.8 \times 10^{-11}$). In the batch experiments, the system was allowed to come back to the equilibrium after each acid addition-thus providing richer information from which to base the estimate of K_{sp} than that obtained in the column experiments. Thus, while it is reasonable to assume there are multiple combinations of K_{sp} and k that will produce similar fits of the column data, the fit reported herein provides values of K_{sp} that are well aligned with independent experiments.

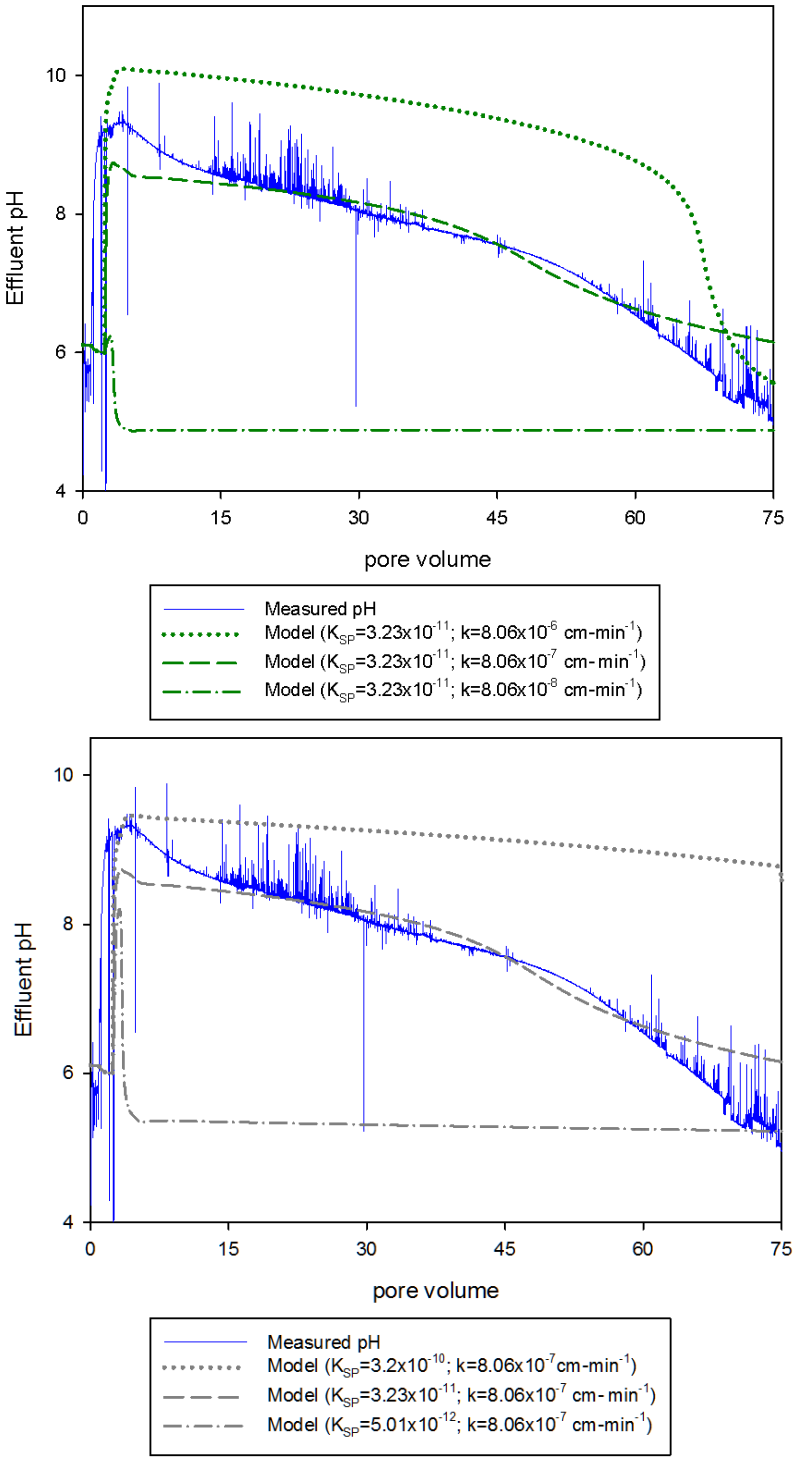

Figure 7.10: Sensitivity analysis for MgO release model. Model simulations show the (top) influence of release rate, *k*, and (bottom) K_{sp} on pH treatment.

The intrinsic mass transfer coefficient fit to the column experiment release data was also comparable to the *k* values for release in the batch experiments (see Table 7.2). The Sherwood number correlations obtained for entrapped, pure component NAPLs provided estimates of *k* that are nearly two orders of magnitude higher (see Table 7.2). This is interesting as these correlations have been shown to also be good descriptions of solute absorption and release by NAPL (e.g., Ramsburg et al. 2011 and Ervin et al. 2011), much in a similar manner to the conceptual model of release presented in Chapter 6. A key difference between these correlations and experiments conducted here, however, is the distribution of the retained oil droplets - retained on the solid phase as opposed to entrapped ganglia. In addition to these liquid phase mass transfer correlations, Table 7.2 also notes Wilson and Geankoplis (1966), developed for the dissolution of solids in porous media, dramatically over estimates the mass transfer coefficient. The much slower mass transfer coefficient found using the emulsion suggests that the emulsion encapsulation was successful in controlling the rate of amendment release. In addition to the differences in oil distribution between the fitted coefficient and that obtained from the liquid phase correlations, it is possible that the gum Arabic wrapping used to promote emulsion stabilization is partially responsible for this control. Future studies could explore this possibility by altering the stabilization agent or concentration of gum Arabic employed.

Table 7.2: Comparison of mass transfer coefficients

	mass transfer coefficient, *k* [cm·min^{-1}]
Experimental Fits	
batch experiments [a]	0.1-2.5 x 10^{-7}
column experiment (8B)	8.1 x 10^{-7}
Sherwood Correlations	
Powers et al. (1992) [b]	5.6-6.3 x 10^{-5}
Nambi & Powers (1994) [b,c]	4.9-8.7 x 10^{-5}
Wilson & Geankoplis (1966)[b]	2.6-2.9 x 10^{-4}

[a] fitted rate coefficients were found to vary based on particle concentration in the batch systems. The range shown here is for 0.04% and 0.4% MgO emulsions.
[b] the lumped mass transfer coefficient (k_L) predicted from correlation was used to determine the intrinsic mass transfer (k) coefficient using the specific surface area calculated over the length of the column.
[c] correlation uses NAPL saturation. The range of k given is for the high and low saturation values (i.e., saturation at the column inlet and outlet, respectively).

7.5 CONCLUSIONS

Experimental investigations showed that pH treatment via either buffered or un-buffered aqueous solutions was only able to provide treatment during injection (i.e., active treatment). The minerals associated with the porous medium have little capacity to release alkalinity and influence pH. Adjustment of pH in soils containing even small capacities to release H^+ (0.01 meq per 100 g sand) can provide difficulty for aqueous solutions (e.g., solutions of NaOH). Aqueous additions provide little to no capability to sustain pH adjustment after delivery (i.e., in the absence of continual addition).

When considering oil-in-water emulsions, experimental results confirm that particles are held within the emulsion droplets- verified through measurement of the total metal transport and retention. These results indicate that emulsion droplet transport and retention can be used to describe alkalinity particle behavior (Chapter 5). Additionally, droplet retention was not affected by long-term flushing, decreasing the required model complexity that would be need if droplet remobilization occurred.

Alkalinity particles encapsulated within emulsion droplets are able to release to the aqueous environment as evidenced through comparison between the total metal concentrations before and after extended flushing with pH 4 solution. Even at low mass loadings (0.02%) particle-containing oil-in-water emulsions were

able to provide long term treatment sustaining pH above 6 for between 25 PV ($CaCO_3$) and 55 PV (MgO).

Extended pH treatment from an emulsion injection was able to be successfully described with the developed mathematical model for both MgO and $CaCO_3$ particles ($CaCO_3$ preliminary modeling results shown in Appendix IV) by employing a linear driving force release model. The mass transfer coefficient fit to the flow through column system was (k= 8.1x10^{-7} cm·min^{-1}) comparable to those determined through the batch experiments (k= 0.1-2.5 x 10^{-7} cm·min^{-1}). Mass transfer rates were at 2-3 orders of magnitude slower than predicted from dissolution correlations; however, the droplet encapsulation may explain the lower rates.

Although good agreement was achieved with the model, sensitivity analysis reveals an interdependence between the K_{sp} and k values. Thus care should be taken when employing the model described herein. More specifically, it is recommended that any additional modeling efforts use the K_{sp} value obtained from the batch experiments as an independently derived model parameter. Alternatively, improved knowledge of the solubility product value would greatly improve confidence of the fitted mass transfer coefficients and in the overall predictive capabilities of the model.

Chapter 8: Conclusions and Recommendations

8.1 CONCLUSIONS AND RECOMMENDATIONS

The work described here further illustrates how oil-in-water emulsions can be used for encapsulate active ingredients used in subsurface remediation. In this respect, the work builds on previous efforts aimed at supplying solutes (e.g., Ramsburg et al., 2003) and reactive iron particles (Berge et al. 2008; Long et al. 2011). Unlike these previous studies, this research focused on controlling the delivery and release of alkalinity - an important amendment for numerous treatment technologies.

Alkalinity-releasing particles were successfully encapsulated with oil-in-water emulsions using gum Arabic as a stabilizer. Droplet imaging and emulsion stability (as well as subsequent batch and column) results suggest alkalinity-releasing particles are held within the soybean oil droplets of the emulsion. Furthermore, results indicate this mode of encapsulation may be able to support a range of particle mass loadings that can likely exceed greater than 1 mg particle per g oil. Developed emulsions have desirable injection properties- kinetic stability for greater than 20 hours, density is near that of water, and a manageable viscosity for subsurface injection.

The amount of emulsion retention was linked to the dispersed phase content and emulsion injection duration. Mixing during the transport of concentrated emulsions was enhanced by a viscous instability produced when pulses of emulsion were followed by un-amended chase water, as is common in application. This additional mixing occurs on the back-end of the pulse and was well described through the inclusion of an additional dispersive mixing term that employed an established empirical model for viscous instabilities. In addition, retention of the emulsions was found to substantially increase dispersive mixing. This effect was made apparent in the emulsion systems where significant mass was retained over a relatively short time frame (i.e., approximately 5 PVs).

However, the influence of decreasing water saturation (in space and time) on dispersivity was also found to be a more universal concept for any partially saturated system. Investigations using literature data indicate that even low to moderate saturations of non-wetting phase can greatly influence dispersivity in partially saturated media (i.e., for both NAPL-water and air-water system). Water saturation was found to be the best overall predictor of dispersivity. Additionally, values of dispersivity obtained under saturated conditions were found to scale for an improved estimate of mixing under partially saturated conditions. This concept (and developed correlation) may have utility for systems with transient water saturation (e.g., infiltration and irrigation events, chemical or biological reactions occurring within porous media, NAPL source depletion and delivery of foams and emulsions used in site remediation). These findings have appreciable significance

for many applications where the influence of saturation on solute transport behavior is often neglected. All developed predictive models were formulated for easy incorporation into flow and transport simulations.

At higher concentration, modeling simulations indicated the possibility of a maximum retention value within the Federal Fine sand. This maximum retention was estimated to be approximately 50 mg-DP/g-sand based on results from column experiments aimed at ascertaining the maximum entrapped saturation of soybean oil (results from a different study conducted in the Ramsburg laboratory). While this maximum value makes sense conceptually with the results presented herein, more research is needed to clarify and quantify the role of any maximum retention. This could be accomplished using column experiments of longer pulse duration.

While this work included experiments aimed at ascertaining how properties of the porous medium influence droplet retention, additional research is certainly warranted. All media examined herein were homogenous sand packs absent of the textural and mineral interfaces more typically encountered in application. Emulsion transport and retention in media that is even mildly physically and chemical heterogeneous has received very limited attention to date-with only a few studies looking at materials other than sands (e.g., Coulibaly and Borden, 2004; Coulibaly et al., 2006). Although the experiments completed here are limited to sands, an important contribution of the work is the modeling approach that provides a framework in which to explore more complex media.

Rates of alkalinity release from encapsulated particles during column experiments were similar to those found in the batch systems. Although good agreement was achieved with the model, sensitivity analysis reveals an interdependence between the K_{sp} and k values. Thus care should be taken when employing the model and future research should aim to better constrain the model. It is noted, however, that the similarity between the batch and column fitted values of K_{sp} suggests that independently determined parameters may provide a reasonable path forward in the absence of more reliable measurements of K_{sp} (which is very difficult for MgO and $Mg(OH)_2$). Improved knowledge of the solubility product value would greatly improve confidence of the fitted mass transfer coefficients and in the overall predictive capabilities of the model.

Overall, the release results highlight the ability of emulsions to provide reasonable alkalinity release rates (i.e., orders of magnitude reduction over bare particles)- a good thing in practice as the fast mineral dissolution kinetics can otherwise result in sharp changes in pH. Importantly, rate coefficients for the release of alkalinity from the emulsion were found to be multiple orders of magnitude slower than would otherwise be predicted from mass transfer correlations developed for solids and liquids (Powers et al. 1992; Nambi & Powers, 2003; Wilson and Geankoplis, 1966). These rates of release were found to produce extended periods of treatment (e.g., >50 PV) of pH ~ 5 water entering the columns after emulsion delivery. While not explicitly shown here, it is envisioned that the duration of treatment can be extended by increasing the mass

of particles encapsulated. Column experiments described herein employed mass loadings of 0.02%, however, emulsions created for the batch evaluations included particle contents up to 0.4% without alteration of the emulsion characteristics. Note that the column experiments reported here used the lower mass loadings simply out of experimental convenience. Future efforts should aim to better understand the upper limit on particle loadings in terms of emulsion stability, transport and alkalinity release. Quantification of the maximum capacity of the oil droplets to hold particles would provide insight into remedial design by determining the upper limit of mass loading into droplets. In addition, future efforts should focus on extending this work to control the release of other amendments used in subsurface remediation (e.g., acid-releasing particles, nutrients, etc.).

8.2 Summary of Contributions

- Demonstrated that alkalinity-releasing particles encapsulated within soybean oil droplets remain accessible for dissolution and the emulsion encapsulation approach can be employed to control the rate of release. This is important because soybean oil is a common amendment in bioremediation where dechlorination processes may decrease pH. Thus providing both the oil and alkalinity together may serve to increase the effectiveness and rate of treatment.
- Identified key processes controlling the transport of concentrated emulsions in porous media to be the influence of decreasing water

saturation (due to droplet retention) and viscous instabilities on the dispersive mixing conditions. This becomes important because droplet concentration (i.e., oil content of the emulsion) may be the primary point of control on duration of treatment. Since there appears to be a tradeoff between particle mass loading and release rates, total particle mass (i.e., treatment capacity) may only be controlled by droplet concentration rather than mass loading in the oil droplets themselves.

- Predictors such as median grain size, uniformity index, porosity, and water saturation were found to provide meaningful predictions of dispersivity. Dispersivity in partially saturated media could be predicted using values obtained for the same medium but under fully water saturated conditions. The resulting simple dispersivity models may have utility for systems with transient water saturation and can be easily incorporated into existing transport models.
- Developed a mathematical model to describe the treatment of subsurface pH from retained emulsion droplets. Experiments showed improved subsurface pH control using oil-in-water emulsions over the commonly employed aqueous additions of both buffered and un-buffered solution.
- The developed mathematical models for emulsion transport and retention paired with the alkalinity release model can be used to develop strategies to “tune” alkalinity release to site specific requirements for pH control.

Chapter 9: References

Adamson, D. T., Lyon, D. Y. & Hughes, J. B., 2004. Flux and Product Distribution during Biological Treatment of Tetrachloroethene Dense Non-Aqueous-Phase Liquid. *Environmental Science & Technology,* 38(7), pp. 2021-2028.

Aelion, C. M. et al., 2009. Application of encapsulation (pH-sensitive polymer and phosphate buffer macrocapsules): a novel approach to remediation of acidic ground water. *Environmental Pollution* , 157(1), pp. 186-193.

Air Force Center for Engineering and the Environmental , 2007. *Protocol for In Situ Bioremediation if Chlorinated Solvents Using Edible Oil,* s.l.: s.n.

Akaike, H. (1974) A New Look at the Statistical Model Identification, *IEEE Transactions of Automatic Control*, 19 (6) 716-723, doi: 10.1109/TAC.1974.1100705

Alvarado, D. & Marsden, S., 1979. Flow of oil-in-water emulsions through tubes and porous media. *SPE J,* 19(6), pp. 369-377.

Andreeva, D. V., Gorin, D. A., Möhwald, H. & Sukhorukov, G. B., 2007. Novel type of self-assembled polyamide and polyimide nanoengineered shells--fabrication of microcontainers with shielding properties. *Langmuir,* pp. 9031-9036.

Anon., 2014. Oliveira, P.F.; Oliveira, T.M.; Spinelli, L.S.; Mansur, C.R.E. *Journal of Nanomaterials,* p. Article No. 723789.

Arcadis, 2002. *Technical Protocol for Using Carbohydrates to Enhance Reductive Dechlorination of Chlorinated Aliphatic Hydrocarbons,* s.l.: Report prepared for ESTCP (Contract #F41624-99-C-8032).

Arnold, W. A. & Roberts, A., 2000. Pathways of chlorinated ethylene and chlorinated acetylene reaction with Zn(O). *Environmental Science and Technology,* Volume 34, pp. 1794-1805.

Barr, D.W. (2001), Coefficient of permeability determined by measurable parameters, *Ground Water*, 39, 356-361, doi: 10.1111/j.1745-6584.2001.tb02318.x

Bear, J. (1961), Some Experiments in Dispersion, *J. Geophys. Res.*, 6 (8), 2455-2467, doi: 10.1029/JZ066i008p02455.

Bear, J. (1972), Dynamics of Fluids in Porous Media, American Elsevier Pub. Co., New York, USA.

Beazley, M. et al., 2007. Uranium Biomineralization as a Result of Bacterial Phosphatase Activity: Insights from Bacterial Isolates from a Contaminated Subsurface. *Environmental Science and Technology,* Volume 41, pp. 5701-5707.

Benjamin, M. M., 2002. *Water Chemsitry.* 1st ed. New York: McGraw-Hill Inc..

Berge, N. D. & Ramsburg, C. A., 2009. Oil-in-water emulsions for encapsulated delivery of reactive iron particles. *Environmental Science & Technology,* 43(13), pp. 5060-5066.

Bilia, A., Carelli, V., Di Colo, G. & Nannipieri, E., 1996. In vitro evaluation of a pH-sensitive hydrogel for control of GI drug delivery from silicone-based matrices. *International Journal of Pharmaceuticals,* pp. 83-92.

Blackwell, R.J. (1962) Laboratory Studies of Microscopic Dispersion Phenomena, *Soc. Petrol. Eng. J.*, 2, 1-8, doi: 10.2118/1483-G.

Bloom, P. R., 1999. Soil pH and pH Buffering. In: *Handbook of Soil Science.* s.l.:CRC Press, pp. 333-352.

Borden, R.C (2007), Effective distribution of emulsified edible oil for enhanced anaerobic bioremediation, *J. Contam. Hydrol.*, 94, 1-12, doi:10.1016/j.jconhyd.2007.06.001.

Borden, R. C. & Lee, M. D., 2002. *Method for remediation of aquifers.* United States of America , Patent No. 6,398,960.

Borden, R. C. & Lee, M. D., 2004. United States of America, Patent No. RE40,448 E.

Borden, R. C. & Lee, M. D., 2009. United States of America, Patent No. RE40734 E1.

Borden, R. C. & Rodriguez, X. B., 2006. Evaluation of Slow Release Substrates for Anaerobic Bioremediation. *Bioremediation Journal,* 10(1-2), pp. 59-69.

Borden, R., Lieberman, M. T. & Tillotson, J., 2008. *In situ ph adjustment for soil and groundwater remediation.* USA, Patent No. WO 2008137508 A1.

Borggaard, O., 1983. Effect of surface area and mineralogy of iron oxides on their surface charge and anion-adsorption properties. *Clays Clay Miner.* , Volume 31, pp. 230-232.

Bradford, S. a. et al., 2003. Modeling Colloid Attachment, Straining, and Exclusion in Saturated Porous Media. *Environmental Science & Technology,* Volume 37, pp. 2242-2250.

Bradford, S., Bettahar, M., Simunek, J. & van Genuchten, M. T., 2004. Straining and attachment of colloids in physically heterogeneous porous media. *Vadose Zone,* Volume 3, pp. 384-394.

Bradford, S. et al., 2003. Modeling Colloid Attachment, Straining, and Exclusion in Saturated Porous Media. *Environmental Science & Technology,* 37(10), pp. 2242-2250.

Bradford, S., Torkzaban, S., Kim, H. & Simunek, J., 2012. Modeling colloid and microorganism transport and release with transients in solution ionic strength. *Water Resources Research,* 48(9).

Brusseau, M.L., M. Narter, G. Schnaar, J. Marble (2009), Measurement and Estimation of Organic-Liquid/Water Interfacial Area for Several Natural Porous Media, *Environ. Sci. Technol*., 43(10), 3619-3625, doi:10.1021/ es8020827

Bunn, R., Magelky, R., Ryan, J. & Elimelech, M., 2002. Mobilization of natural colloids from an iron oxide-coated sand aquifer: Effect of pH and ionic strength. *Environmental Science and Technology,* 36(3), pp. 314-322.

Castelbaum, D., Olson, M. R., Sale, T. C. & Shackelford, C. D., 2011. Laboratory apparatus and procedures for preparing test specimens of slurry mixed soils. *Geotechnical Testing Journal,* 34(1), pp. 1-9.

Chen, J. L., Al-Abed, S. R., Ryan, J. a. & Li, Z., 2001. Effects of pH on dechlorination of trichloroethylene by zero-valent iron. *Journal of Hazardous Materials,* Volume 83, pp. 243-254.

Chuan, M., Shu, G. & Liu, J., 1996. Solubility of heavy metals in a contaminated soil: Effects of redox potential and pH. *Water, Air, and Soil Pollution,* Volume 90, pp. 543-556.

Clayton, M. H. & Borden, R. C., 2009. Numerical modeling of emulsified oil distribution in heterogeneous aquifers. *Ground water,* 47(2), pp. 246-258.

Cobos, S., Carvalho, M. S. & Alvarado, V., 2009. Flow of oil-water emulsions through a constricted capillary. *International Journal of Multiphase Flow*, 35(6), pp. 507-515.

Conca, J., and J. Wright (1992), Diffusion and Flow in Gravel, Soil, and Whole Rock, *Applied Hydrogeology*, 1, 5-24, doi: 10.1007/PL00010963

Costa, P. & Lobo, J. M. S., 2001. Modeling and comparison of dissolution profiles. *European Journal of Pharmaceutical Sciences* , pp. 123-133.

Cortis, A., and B. Berkowitz (2004), Anomalous Transport in "Classical" Soil and Sand Columns, *Soil Sci. Soc. Am. J.*, 68, 1539-1548, doi:10.2136/sssaj2004.1539

Coulibaly, K. M. & Borden, R., 2004. Impact of edible oil injection on the permeability of aquifer sands. *Journal of contaminant hydrology*, Volume 71, pp. 219-237.

Coulibaly, K. M., Long, C. M. & Borden, R. C., 2006. Transport of edible oil emulsions in clayey sands: One-dimensional column results and model development. *Journal of Hydrologic Engineering*, pp. 230-237.

Cowan, D., 2000. Innovative Abatement and Remediation of Perchlorate at McGregor, Texas Weapons Plant Site. *Soil Sediment & Groundwater*, Issue June/July, pp. 25-26.

Delgado, A. G. et al., 2012. Role of bicarbonate as a pH buffer and electron sink in microbial dechlorination of chloroethenes. *Microbial Cell Factories*, 11:128(1).

De Smedt, F., P.J. Wierenga (1979), A Generalized Solution for Solute Flow in Soils with Mobile and Immobile Water, *Water Resour. Res.*, 15(5), 1137-1141, doi: 10.1029/WR015i005p01137.

De Smedt, F., and P.J. Wierenga (1984), Solute Transfer Through Columns of Glass Beads, *Water Resour. Res.*, 20 (2), 225-232, doi: 10.1029/WR020i002p00225

De Smedt, F., F. Wauters, J. Sevilla (1986), Study of tracer movement through unsaturated sand, *Geoderma*, 38, 223-236, doi: 10.1016/0016-7061(86)90017-0

Devereux, O. F., 1974a. Emulsion Flow in Porous Solids I. A Flow Model. *The Chemical Engineering Journal*, Volume 7, pp. 121-128.

Devereux, O. F., 1974b. Emulsion Flow in Porous Solids II . Experiments with a Crude Oil-in-Water Emulsion in Porous Sandstone. *The Chemical Engineering Journal,* Volume 7, pp. 129-136.

Dunphy Guzman, K. A., Finnegan, M. P. & Banfield, J. F., 2006. Influence of Surface Potential on Aggregation and Transport of Titania Nanoparticles. *Environmental Science & Technology,* 40(24), pp. 7688-7693.

El Badawy, A. M. et al., 2010. Impact of environmental conditions (pH, ionic strength, and electrolyte type) on the surface charge and aggregation of silver nanoparticles suspensions. *Environmental Science and Technology*, 44(4), pp. 1260-1266.

Ervin, R. E., A. Boroumand, L.M. Abriola, C.A. Ramsburg (2011), Kinetic limitations on tracer partitioning in ganglia dominated source zones, *J. Contam. Hydrol.*,126, 195-207, doi:10.1016/j.jconhyd.2011.07.006.

Esahani, S., Muller, K., Chapra, S. & Ramsburg, C., 2014. *Transport and Rention of Emulsion Droplets in Sandy Porous Media.* San Francisco, CA. 15-19 December 2014, American Geophysical Union Fall Meeting, poster number H31C-0640.

Fattah, Q.N., and J.A. Hoopes (1985), Dispersion in Anisotropic, Homogeneous, Porous Media, *J. Hydraul. Eng.*, 111 (5), 810-827, doi: 10.1061/(ASCE)0733-9429(1985)111:5(810).

Flora, J. R., Baker, B. W. D., Zhu, H. & Aelion, C. M., 2008. Preparation of acidic and alkaline macrocapsules for pH control. *Chemosphere,* 70(6), pp. 1077-1084.

Foppen, J. W., van Herwerden, M. & Schijven, J., 2007. Transport of Escherichia coli in saturated porous media: dual mode deposition and intra-population heterogeneity. *Water Research,* Volume 41, pp. 1743-1753.

Fox, G. & Medina, V., 2005. Evaluating Factors Affecting the Permeability of Emulsions Used To Stabilize Radioactive Contamination from a Radiological Dispersal Device. *Environmental Science & Technology,* 39(10), pp. 3762-3769.

Freeze, R.A., and J.A. Cherry (1979), Groundwater, Prentice-Hall, Inc. Englewood Cliffs, New York, USA.

Fried, J.J., and M.A. Combarnous (1971), Dispersion in porous media, *In* Advances in Hydroscience , vol 7, 169-282 Academic Press, New York.

Friedlander, S. K., 1957. Mass and heat transfer to single spheres and cylinders at low Reynolds numbers. *AIChE Journal*, 3(1), pp. 43-48.

Fuller, M. E. et al., 2004. Enhancing the attenuation of explosives in surface soils at military facilities: combined sorption and biodegradation. *Environmental toxicology and chemistry / SETAC*, 23(2), pp. 313-324.

Furman, O. S., Teel, A. L. & Watts, R. J., 2010. Mechanism of base activation of persulfate. *Environmental Science and Technology,* Volume 44, pp. 6423-6428.

Gargiulo, G. et al., 2007. Bacteria transport and deposition under unsaturated. *Jounral of Contamimant Hydrology,* Volume 92, pp. 255-273.

Garner, K. L. & Keller, A. a., 2014. Emerging patterns for engineered nanomaterials in the environment: a review of fate and toxicity studies. *Journal of Nanoparticle Research*, 16(8), p. 2503.

Gelhar, L. W., C. Welty, K. Rehfeldt (1992), A Critical Review of Data on Field-Scale Dispersion in Aquifers, *Water Resour. Res.*, 28 (7), 1955-1974, doi: 10.1029/92WR00607.

Goldberg, E. & Scheringer, M., 2014. Critical assessment of models for transport of engineered nanoparticles in saturated porous media. *Environmental Science & Technology,* Volume 48, pp. 12732-12741.

Goltz, M. & Christ, J., 2012. Recirculation Systems. In: P. K. Kitanidis & P. L. McCarty, eds. *Devliery and Mixing in the Subsurface: Processess and Design Principles for In Situ Remediation.* New York: Springer Science, pp. 139-165.

Grant, G. P., and J.I. Gerhard (2007), Simulating the dissolution of a complex dense nonaqueous phase liquid source zone: 1. Model to predict interfacial area, *Water Resour. Res.*, 43, W12410, doi: 10.1029/2007WR006038

Grolimund, D., Elimelech, M. & Borkovec, M., 2001. Aggregation and deposition kinetics of mobile colloidal particles in natural porous media. *Colloids and Surfaces A: Physicochemical and Engineering Aspects,* Volume 191, pp. 179-188.

Grolimund, D. et al., 1998. Transport of in situ mobilized colloidal particles in packed soil columns. *Environmental Science and Technology,* 32(22), pp. 3562-3569.

Guillen, V. R., Romero, M. I., Carvalho, M. D. S. & Alvarado, V., 2012. Capillary-driven mobility control in macro emulsion flow in porous media. *International Journal of Multiphase Flow,* Volume 43, pp. 62-65.

Gupta, P., Vermani, K. & Garg, S., 2002. Hydrogels: from controlled release to pH-responsive drug delivery. *Drug Discovery Today*, pp. 569-579.

Gupta, P., Vermani, K. & Garg, S., 2002. Hydrogels: from controlled release to pH-responsive drug delivery. *Drug Discovery Today*, pp. 569-579.

Haga, D., Y. Niibori, T. Chida (1999), Hydrodynamic dispersion and mass transfer in unsaturated flow, *Water Resour. Res.*, 35 (4), 1065-1077.

Hajnos, M., 2011. Buffer Capacity of Soils. In: *Encyclopedia of Agrophysics.* s.l.:Springer Science+ Business Media, pp. 59-105.

Hammond, E. et al., 2005. Soybean Oil. In: F. Shahidi, ed. *Industrial Oil and Fat Products.* s.l.:John Wiley & Sons, Inc. , pp. 577-653.

Harkness, M. & Fisher, A., 2013. Use of emulsified vegetable oil to support bioremediation of TCE DNAPL in soil columns. *Journal of Contaminant Hydrology,* Volume 151, pp. 16-33.

Hassanizadeh, S. (1996), On the Transient Non-Fickian Dispersion Theory, *Transport in Porous Media*, 2, 107-124, doi: 10.1007/BF00145268.

Helling, C., Chesters, G. & Corey, R., 1964. Contribution of Organic Matter and Clay to Soil Cation-Exchange Capacity as Affected by the pH of the Saturating Solution. *Soil Sci. Soc. Am. J.*, Volume 28, pp. 517-520.

Henn, K. W. & Waddill, D. W., 2006. Utilization of nanoscale zero-valent iron for source remediation—A case study. *Remediation Journal,* 16(2), pp. 54-77.

Hiortdahl, K. M. & Borden, R. C., 2014. Enhanced reductive dechlorination of tetrachloroethene dense nonaqueous phase liquid with EVO and Mg(OH)2. *Environmental Science & Technology,* Volume 48, pp. 624-631.

Hofman, J. & Stein, H., 1991. Permeability reduction of porous media on transport of emulsions through them. *Colloids and Surfaces,* Volume 61, pp. 317-329.

Homsy, G., 1987. Viscous Fingering in Porous Media. *Ann. Rev. Fluid Mech. ,* Volume 19, pp. 271-311.

Huling, S. & Pivetz, B., 2006. *Engineering issue: In-situ chemical oxidation,* s.l.: United States Environmental Protection Agency.

Hunter, W. J., 2001. Use of vegetable oil in a pilot-scale denitrifying barrier. *Journal of Contaminant Hydrology,* 53(1-2), pp. 119-131.

Hunter, W. J., 2002. Bioremediation of chlorate or perchlorate contaminated water using permeable barriers containing vegetable oil. *Current microbiology,* Volume 45, pp. 287-292.

Hunter, W. J. & Shaner, D. L., 2009. Nitrogen limited biobarriers remove atrazine from contaminated water: laboratory studies. *Journal of Contaminant Hydrology,* Volume 103, pp. 29-37.

Hutin, A., Argillier, J. & Langevin, D., 2014. Mass Transfer between Crude Oil and Water. Part 1: Effect of Oil Components. *Energy & Fuels,* Volume 28, pp. 7331-7336.

Imhoff, P. T., Jaffé, P. R. & Pinder, G. F., 1994. An experimental study of complete dissolution of a nonaqueous phase liquid in saturated porous media. *Water Resources Research,* 30(2), pp. 307-320.

Jackson, R. E., Dwarakanath, V., Meinardus, H. W. & Young, C. M., 2003. Mobility control: How injected surfactants and biostimulants may be forced into low-permeability units. *Remediation Journal,* 13(3), pp. 59-66.

Jha, D. & Bose, P., 2005. Use of pyrite for pH control during hydrogenotrophic denitrification using metallic iron as the ultimate electron donor. *Chemosphere,* 7(1020-1031), p. 61.

Jimenez-Martinez, J., P.D. Anna, H. Tabuteau, R. Turuban, T.L. Borgne, Y. Méheust (2015), Pore-scale mechanism for the enhancement of mixing in unsaturated porous media and implications for chemical reactions, Geophys. Res. Lett., 42 (13), 5316-5324, doi: 10.1002/2015GL064513

Johnson, P. & Elimelech, M., 1995. Dynamics of colloid deposition in porous media: Blocking based on random sequential adsorption. *Langmuir,* Volume 11, pp. 801-812.

Jung, Y., Coulibaly, K. M. & Borden, R. C., 2006. Transport of edible oil emulsions in clayey sands: 3D sandbox results and model validation. *Journal of Hydrologic Engineering* , 11(3), pp. 238-244.

Kananizadeha, N., Chokejaroenrata, C., Li, Y. & Comfort, S., 2015. Modeling improved ISCO treatment of low permeable zones via viscosity modification: Assessment of system variables. *Journal of Contaminant Hydrology,* Volume 173, pp. 25-37.

Kasel, D. et al., 2013. Transport and retention of multi-walled carbon nanotubes in saturated porous media: effects of input concentration and grain size. *Water research,* Volume 47, pp. 933-944.

Kim, S., Kim, E., Kim, S. & Kim, W., 2005. Surface modification of silica nanoparticles by UV-induced graft polymerization of methyl methacrylate. *Journal of Colloid and Interface Science*, 292(1), pp. 93-98.

Klotz, D., H. Moser (1974), Hydrodynamic dispersion as aquifer characteristic: Model experiments with radioactive tracers, proceedings at *Isotope Techniques in Groundwater Hydrology*, Vol. II.

Kokal, S. L., Maini, B. B. & Woo, R., 1992. Flow of Emulsions in Porous Media. In: L. Schramm, ed. *Emulsions.* Washington DC: American Chemical Society, pp. 219-262.

Kokkinaki, A., O'Carroll, D., Werth, C. & Sleep, B., 2013. An evaluation of Sherwood-Gilland models for NAPL dissolution and their relationship to soil properties. *Journal of Contaminant Hydrology,* Volume 155, pp. 87-98.

Koval, E., 1963. A Method for Predicting the Performance of Unstable Miscible Displacement in Heterogeneous Media. *Society of Petroleum Engineers Journal*, pp. 145-154.

Kretzschmar, R., Borkovec, M., Grolimund, D. & Elimelech, M., 1999. Mobile subsurface colloids and their role in contaminant transport. *Advances in Agronomy,* Volume 66, pp. 121-194.

Krynicki, K., C. D. Green, D. W. Sawyer (1978), Pressure and temperature-dependence of self-diffusion in water, *Faraday Discuss. Chem. Soc*., 66, 199, doi: 10.1039/DC9786600199

Kwon, T. et al., 2005. The Solubilization Characteristics of DNAPLs by Oil-Based Emulsion. *Separation Science and Technology,* 40(1-3), pp. 685-698.

Lacroix, E., Brovelli, A., Barry, D. & Holliger, C., 2014. Use of silicate minerals for pH control during reductive dechlorination of chloroethenes in batch cultures

of different microbial consortia. *Applied and environmental microbiology*, 80(13), pp. 3858-3867.

Leach, O., 2011. *Understanding the role of metal solubility in controlled release of alkalinity using particle-containing oil-in-water emulsions,* Medford, MA: Honors Thesis Submitted to Tufts University, Department of Civil and Environmental Engineering.

Lee, Y.-C., Kwon, T.-S., Yang, J.-S. & Yang, J.-W., 2007. Remediation of groundwater contaminated with DNAPLs by biodegradable oil emulsion. *Journal of hazardous materials,* Volume 140, pp. 340-345.

Lee, Y.-C., Kwon, T.-S., Yang, J.-S. & Yang, J.-W., 2007. Remediation of groundwater contaminated with DNAPLs by biodegradable oil emulsion. *Journal of hazardous materials,* Volume 140, pp. 340-345.

Lee, J., D.B. Jaynes, R. Horton (2000), Evaluation of a Simple Method for Estimating Solute Transport Parameters: Laboratory Studies, *Soil. Sci. Soc. Am. J.*, 64, 492-498, doi: 10.2136/sssaj2000.642492x.

Lee, M.D., M.T. Lieberman, W.J. Beckwith, R.C. Borden, J.W. Everett, and L.G. Kennedy (2003), Pilots to enhance trichloroethene reductive dechlorination and ferrous sulfide abiotic transformation. In: V.S. Magar and M.E. Kelley (eds.), Proceedings of the Seventh International In Situ and On-Site Bioremediation Symposium, Orlando, FL. Battelle Press, Columbus, OH, June 2003.

Legatski, M. X., D.L. Katz (1967) Dispersion Coefficients for Gases Flowing in Consolidated Porous Media, *Soc. Petrol. Engrs J.*, 7, 43-50, doi: 10.2118/1594-PA

Lien, H. L. & Zhang, W. X., 2001. Nanoscale iron particles for complete reduction of chlorinated ethenes. *Colloids and Surfaces A: Physicochemical and Engineering Aspects,* Volume 191, pp. 97-105.

Lindow, N. L. & Borden, R. C., 2005. Anaerobic Bioremediation of Acid Mine Drainage using Emulsified Soybean Oil. *Mine Water and the Environment,* Volume 24, pp. 199-208.

Li, R. F. et al., 2010. Foam mobility control for surfactant enhanced oil recovery. *SPE Journal* , pp. 20-23.

Lide D.R., editor (1999), CRC Handbook of Chemistry and Physics (75th edn), Boca Raton FL, USA.

Liu, L., Baker, B., Flora, J. R. V. & Aelion, C. M., 2008. Kinetics of Acidic Macrocapsules in Controlling the pH of Groundwater. *Environmental Engineering Science,* 25(9), pp. 1345-1356.

Liu, Y. et al., 2005. TCE dechlorination rates, pathways, and efficiency of nanoscale iron particles with different properties. *Environmental Science and Technology,* 39(5), pp. 1338-1345.

Long, C.M., and R.C. Borden (2006), Enhanced reductive dechlorination in columns treated with edible oil emulsion, *J. Contam. Hydrol.*, 87, 54-72, doi: 10.1016/j.jconhyd.2006.04.010

Long, T., and C.A. Ramsburg (2011), Encapsulation of nZVI particles using a Gum Arabic stabilized oil-in-water emulsion, *J. Hazard. Mater.*, 189, 801-808, doi: 10.1016/j.jhazmat.2011.02.084

Lowry, G. V., Gregory, K. B., Apte, S. C. & Lead, J. R., 2012. Transformations of nanomaterials in the environment. *Environmental Science & Technology,* 46(13), pp. 6893-6899.

Luo, S. et al., 2014. Synthesis of nanoscale zero-valent iron immobilized in alginate microcapsules for removal of Pb(II) from aqueous solution. *Journal of Materials Chemistry A,* Volume 2, pp. 15463-15472.

Maciejewski, S. (1994), Numerical and experimental study of solute transport in unsaturated soils, *J. Contam. Hydrol.*, 14, 193-206; doi: 10.1016/0169-7722(93)90024-M

Maraqa, M.A., R.B. Wallace, T.C. Voice (1997), Effects of degree of water saturated on dispersivity and immobile water in sandy soil columns, *J. Contam. Hydrol.*, 25, 199-218, doi: 10.1016/S0169-7722(96)00032-0.

Martinez, R. J. et al., 2007. Aerobic uranium (VI) bioprecipitation by metal-resistant bacteria isolated from radionuclide- and metal-contaminated subsurface soils. *Environmental Microbiology,* 9(12), pp. 3122-3133.

MATLAB 2014a, The MathWorks, Inc., Natick, Massachusetts, United States.

McAuliffe, C., 1973. Oil in water emulsions and their flow properties in porous media. *J.Pet. Tech.,* pp. 727-733.

McBride, M. B., 1994. *Environmental Chemistry of Soils.* s.l.:Oxford University Press.

McCarty, P. L., Chu, M.-Y. & Kitanidis, P. K., 2007. Electron donor and pH relationships for biologically enhanced dissolution of chlorinated solvent DNAPL in groundwater. *European Journal of Soil Biology,* 43(5-6), pp. 276-282.

McCarty, P. L. & Criddle, C. S., 2012. Chemical and Biological Processes: The need for Mixing. In: *Delivery and Mixing in the Subsurface: Processes and Design Principles for In Situ Remediation.* s.l.:Springer Science & Business Media, pp. 7-49.

McClements, D. J., Decker, E. & Weiss, J., 2007. Emulsion-based delivery systems for lipophilic bioactive components. *Journal of Food Science,* 72(8), pp. 109-124.

Menzie, D.E., and S. Dutta (1988), Dispersivity as an oil reservoir rock characteristic, *U.S. Department of Energy Final Report*.

Meriç, S., Kaptan, D. & Olmez, T., 2004. Color and COD removal from wastewater containing Reactive Black 5 using Fenton's oxidation process.. *Chemosphere,* Volume 54, pp. 435-441.

Miller, C. T., Poirier-McNeil, M. M. & Mayer, A. S., 1990. Dissolution of Trapped Nonaqueous Phase Liquids: Mass Transfer Characteristics. *Water Resources Research* , pp. 2783-2796.

Millington, R. J., and J.P. Quirk (1961), Permeability of Porous Solids, *Trans. Faraday Soc*., 57, 1200-1207, doi: 10.1039/TF9615701200.

Montgomery, W. H., 2003. *Draft Treatability Study Report, Enhanced Bioremediation Via Vegetable Oil Emulsion Injection, Landfill 1 (LF-08). Prepared forWhiteman AFB and the Air Force Center for Environmental Excellence. April,* s.l.: s.n.

Moslemy, P., Neufeld, R. J. & Guiot, S. R., 2002. Biodegradation of gasoline by gellan gum-encapsulated bacterial cells. *Biotechnology and bioengineering,* 80(2), pp. 175-184.

Moslemy, P., Neufeld, R. J., Millette, D. & Guiot, S. R., 2003. Transport of gellan gum microbeads through sand: an experimental evaluation for encapsulated cell bioaugmentation. *Journal of Environmental Management,* 69(3), pp. 249-259.

Mulligan, C., Yong, R. & Gibbs, B., 2001. Remediation technologies for metal-contaminated soils and groundwater: an evaluation. *Engineering Geology*, Volume 60, pp. 193-207.

Muller, K.A., S. Ghazvinizadeh, S.C. Chapra, C.A. Ramsburg (2015), Transport and Retention of Concentrated Oil-in-Water Emulsions in Sandy Porous Media, presented at *American Geophysical Union Fall Meeting*, paper number H13P-04, San Francisco, CA. 14-18 December 2015.

Nambi, I. M. & Powers, S. E., 2003. Mass transfer correlations for nonaqueous phase liquid dissolution from regions with high initial saturations. *Water Resources Research,* 39(2).

Nash, J. E. and J. V. Sutcliffe (1970), River flow forecasting through conceptual models part I -A discussion of principles, J. Hydrol., 10 (3), 282-290*, doi: 10.1016/0022-1694(70)90255-6*

Nielsen, D.R., J.W., Biggar (1962), Miscible Displacement: III. Theoretical Considerations, *Soil Sci. Soc. Am. Proc*, 26, 216-221, doi:10.2136/sssaj1962.03615995002600030010x.

Niessner, J. & Hassanizadeh, S. M., 2009. Modeling Kinetic Interphase Mass Transfer for Two-Phase Flow in Porous Media Including Fluid–Fluid Interfacial Area. *Transport in Porous Media,* Volume 80, pp. 329-344.

Nishida, Y. et al., 2005. Surface modification of silica particles with polyimide by ultrasonic wave irradiation. *Advanced Powder Technology,* 16(6), pp. 639-648.

NPCS Board of Consultants & Engineers, 2009. Gum Arabic. In: *Handbook on Textile Auxiliaries, Dyes and Dye Intermediates Technology*. s.l.:NATIONAL INSTITUTE OF INDUSTRIAL RESEARCH, pp. 353-375.

Nützmann, G., S. Maciejewski, S., K. Joswig (2002), Estimation of water saturation dependence of dispersion in unsaturated porous media: experiments and modelling analysis, *Adv. Water Resour.*, 25, 565-576, doi: 10.1016/S0309-1708(02)00018-0.

O'Carroll, D. et al., 2013. Nanoscale zero valent iron and bimetallic particles for contaminated site remediation. *Advances in Water Resources,* Volume 51, pp. 104-122.

O'Carroll, D. et al., 2013. Nanoscale zero valent iron and bimetallic particles for contaminated site remediation. *Advances in Water Resources,* Volume 51, pp. 104-122.

Ogata A., and R.B Banks (1961), A solution of the differential equation of longitudinal dispersion in porous media, USGS, Professional Paper 411-A

Oliveira, P., Spinelli, L. & Mansur, C., 2012. The application of nanoemulsions with different orange oil concentrations to remediate crude oil-contaminated soil. *Journal of Nanoscience and Nanotechnology*, 12(5), pp. 4081-4087.

Olmsted, J. & Williams, G., 2007. *CRC Handbook of Chemistry and Physics*. 5th ed. s.l.:s.n.

Padilla, I.Y.; T.C. Yeh, M. Conklin (1999), The effect of water content on solute transport in unsaturated porous media, *Water Resour. Res.*, 35(11), WR900171, 3303-3313, doi:10.1029/1999WR900171.

Palmer, C. D. & Fish, W., 1992. *Ground Water Issue: Chemical Enhancements to Pump-and-Treat Remediation*, s.l.: United States Environmental Protection Agency .

Parkhurst, D.L., and Appelo, C.A.J. (2013), Description of input and examples for PHREEQC version 3--A computer program for speciation, batch- reaction, one-dimensional transport, and inverse geochemical calculations: U.S. Geological Survey Techniques and Methods, book 6, chap. A43, 497, http://pubs.usgs.gov/tm/06/a43

Parsons , 2002b. *Technology Application for Enhanced In-Situ Bioremediation of Chlorinated Aliphatic Hydrocarbons via Organic Substrate Addition for Site FF-*

87, Former Newark AFB, Ohio , s.l.: Prepared for the Air Force Center for Environmental Excellence, San Antonio, Texas. January.

Parsons , 2006b. *Final Project Completion Report, Demonstration Study for Enhanced In Situ Bioremediation of Chlorinated Solvents at Site LF05 (Former Tri-Services Landfill), Hickam Air Force Base, Oahu, Hawaii,* s.l.: Prepared for the Air Force Center for Environmental Excellence, Brooks City-Base, Texas. July.

Parsons, 2002a. *Final Phase II Field Feasibility Test for In Situ Bioremediation of Chlorinated Solvents Via Vegetable Oil Injection at Hanger K Area, Cape Canaveral Air Force Station, Florida,* s.l.: Prepared for the Air Force Center for Environmental Excellence, San Antonio, Texas. March.

Parsons, 2002c . *Final Field Feasibility Test for In-Situ Bioremediation of Chlorinated Solvents via Vegetable Oil Injection at Site N-6, Former Naval Support Activity Mid-South, Millington, Tennessee. July. Denver, Colorado,* s.l.: s.n.

Parsons, 2004b . *Final Project Completion Report for a Field Feasibility Test for In Situ Bioremediation of Chlorinated Solvents Via Vegetable Oil Injection at Site SS015, Travis Air Force Base, California,* s.l.: Prepared for the Air Force Center for Environmental Excellence, Brooks City-Base, Texas. July.

Parsons, 2004. *Principles and Practices of Enhanced Anaerobic Bioremediation of Chlorinated Solvents.,* s.l.: s.n.

Parsons, 2006a. *Final Project Completion Report for a Field Feasibility Test for In Situ Bioremediation of Chlorinated Solvents Via Vegetable Oil Injection at Site FTA-2 Tinker Air Force Base, Oklahoma,* s.l.: Prepared for the Air Force Center for Environmental Excellence, Brooks City-Base, Texas. May.

Parsons, 2007. *Final Project Completion Report for an Enhanced Bioremediation Field Feasibility Test at North Lobe of the AOC-2 TCE Plume, Naval Air Station Fort Worth Joint Reserve Base, Texas,* s.l.: Prepared for the Air Force Center for Engineering and the Environment, Brooks City-Base, Texas. June.

Patel, V. R. & Amiji, M. M., 1996. Preparation and characterization of freeze-dried chitosan-poly (ethylene oxide) hydrogels for site-specific antibiotic delivery in the stomach. *Pharmaceutical Research,* pp. 588-593.

Pennell, K.D., L.M. Abriola, W.J. Weber (1993), Surfactant-Enhanced Solubilization of Residual Dodecane in Soil Columns. 1. Experimental Investigation, *Environ. Sci. Technol*., 27 (12), 2332-2340, doi: 0013-938X/93/0927-2332.

Pennell, K.D., M. Jin, L.M. Abriola, G.A. Pope (1994), Surfactant enhanced remediation of soil columns contaminated by residual tetrachloroethylene, *J. Contam. Hydrol.*, 16, 35-53, doi: 10.1016/0169-7722(94)90071-X.

Pennell, K. D., Pope, G. A. & Abriola, L. M., 1996. Influence of Viscous and Buoyancy Forces on the Mobilization of Residual Tetrachloroethylene during Surfactant Flushing. *Environmental Science & Technology,* 30(4), pp. 1328-1335.

Perkins, T.K, and O.C. Johnson (1963), A Review of Diffusion and Dispersion in Porous Media, *Soc. Petrol. Eng. J.*, 3, 216-221, doi: 10.2118/480-PA.

Perlmutter, M. W. et al., 2000. *Innovative technology: In situ biotreatment of perchlorate-contaminated groundwater*.. Salt Lake, Air and Waste Management Association, 93rd Annual Conference and Exhibition.

Pfannkuch, H., 1984. Determination of the contaminant source strength from mass exchange processes at the petroleum-groundwater interface in shallow aquifer systems. *Peteroleum Hydrocarbons and Orangic Chemicals in Ground Water. National Water Well Assoication, Worthington, OH,* pp. 444-458.

Pfeiffer, P., Bielefeldt, A. R., Illangasekare, T. & Henry, B., 2005. Partitioning of dissolved chlorinated ethenes into vegetable oil. *Water Research,* 39(18), pp. 4521-4527.

Phenrat, T. et al., 2011. Polymer-modified Fe0 nanoparticles target entrapped NAPL in two dimensional porous media: effect of particle concentration, NAPL saturation, and injection strategy. *Environmental Science & Technology,* 45(14), pp. 6102-6109.

Phenrat, T. et al., 2008. Stabilization of aqueous nanoscale zerovalent iron dispersions by anionic polyelectrolytes: adsorbed anionic polyelectrolyte layer properties and their effect on aggregation and sedimentation. *Journal of Nanoparticle Research,* 10(5), pp. 795-814.

Phenrat, T. et al., 2007. Aggregation and Sedimentation of Aqueous Nanoscale Zerovalent Iron Dispersions. *Environmental Science & Technology,* 41(1), pp. 284-290.

Philips, J., Maes, N., Springael, D. & Smolders, E., 2013. Acidification due to microbial dechlorination near a trichloroethene DNAPL is overcome with pH buffer or formate as electron donor: experimental demonstration in diffusion-cells. *Journal of Contaminant Hydrology,* Volume 147, pp. 25-33.

Piegat, J. & Newman, W. A., 2008. *Maintaining Neutral pH in Deep Soils and Ground Water Utilizing Insoluble Colloidal Buffers.* Monterey, Sixth International Conference on Remediation of Chlorinated and Recalcitrant Compounds. Battelle Press.

Pinder, G. F. & Abriola, L. M., 1986. On the Simulation of Nonaqueous Phase Organic Compounds in the Subsurface. *Water Resources Research,* 22(9), pp. 109-119.

Plummer, L., Wigley, T. & Parkhurst, D., 1978. The kinetics of calcite dissolution in CO2-water systems at 5 degrees to 60 degrees C and 0.0 to 1.0 atm CO2. *American Journal of Science,* Volume 278, pp. 179-216.

Powers, S. E., Abriola, L. M., Dunkin, J. S. & Weber, W. J., 1994b. Phenomenological models for transient NAPL-water mass-transfer processes. *Journal of Contaminant Hydrology,* Volume 16, pp. 1-33.

Powers, S. E., Abriola, L. M. & Weber, W. J., 1992. An Experimental Investigation of Nonaqueous Phase Liquid Dissolution in Saturated Subsurface Systems ' Steady State Mass Transfer Rates. *Water Resources Research,* 28(10), pp. 1691-2705.

Powers, S. E., Abriola, L. M. & Weber, W. J., 1992. An Experimental Investigation of Nonaqueous Phase Liquid Dissolution in Saturated Subsurface Systems ' Steady State Mass Transfer Rates. *Water Resources Research,* 28(10), pp. 2691-2705.

Powers, S. E., Abriola, L. M. & Weber, W. J., 1994a. An Experimental Investigation of Nonaqueous Phase Liquid Dissolution in Saturated Subsurface Systems - Steady-State Mass-Transfer Rates. *Water Resources Research,* 30(2), pp. 321-332.

Quinn, J., Geiger, C. & Clausen, C., 2005. Field demonstration of DNAPL dehalogenation using emulsified zero-valent iron. *Environmental Science & Technology,* 39(5), pp. 1309-1318.

Quinn, J., Geiger, C. & Clausen, C., 2005. Field demonstration of DNAPL dehalogenation using emulsified zero-valent iron. *Environmental Science & Technology,* 39(5), pp. 1309-1318.

Ramsburg, C. A., Pennell, K. D., Kibbey, T. C. G. & Hayes, K. F., 2003. Use of a Surfactant-Stabilized Emulsion To Deliver 1-Butanol for Density-Modified Displacement of Trichloroethene. *Environmental Science & Technology*, 37(18), pp. 4246-4253.

Ramsburg, C.A., J.A. Christ, S. R. Douglas, A. Boroumand (2011), Analytical modeling of degradation product partitioning kinetics in source zones containing entrapped DNAPL, *Water Resour. Res.,* 47, W03507, doi: 10.1029/2010WR009958.

Ramsburg, C., Thornton, C. & Christ, J. (2010), Degradation product partitioning in source zones containing chlorinated ethene dense non-aqueous-phase liquid. *Environmental Science & Technology,* 44(23), pp. 9105-9111.

Raoff, A., and S.M. Hassanizadeh (2013), Saturation-dependent solute dispersivity in porous media: Pore-scale processes, *Water Resour. Res.*, 49, 1943-1951, doi: 10.1002/wrcr.20152.

Robinson, C. et al., 2009. pH control for enhanced reductive bioremediation of chlorinated solvent source zones. *The Science of the Total Environment,* 407(16), pp. 4560-4573.

Robinson, M., Pask, J. & Fuerstenau, D., 1964. Surface charge of alumina and magnesia in aqueous media. *Journal of the American Ceramic Society*, 47(10), pp. 516-520.

Rogers, B., B.E. Logan (2000), Bacterial Transport in NAPL-Contaminated Porous Media, *J. Environ. Eng*., 126 (7), 657-666, doi:10.1061/(ASCE)0733-9372(2000)126:7(657).

Roland, U., Holzer, F., Buchenhorst, D. & Kopinke, F. D., 2007. Results of field tests on radio-wave heating for soil remediation. *Environmental Science and Technology.*

Rose, W. & Bruce, W., 1949. Evaulation of capillary character in petroleum reservoir rock.. *Transactions of the Metallurgical Society of American Institue of Mining,* Volume 186, pp. 127-142.

Ross, C., Murdoch, L. C., Freedman, D. L. & Siegrist, R. L., 2005. Characteristics of Potassium Permanganate Encapsulated in Polymer. *Journal of Enironmental Engineering*, 131(8), pp. 1203-1211.

Rossi, M., P. Lehmann, N. Ursino, O. Ippisch, H. Flühler (2007), Solute mixing during imbibition and drainage in a macroscopically heterogeneous medium, *Water Resour. Res.*, 43(4), W04428, doi: 10.1029/2005WR004038

Rust, C. M., Aelion, C. & Flora, J. R., 2002. Laboratory sand column study of encapsulated buffer release for potential in situ pH control. *Journal of Contaminant Hydrology*, 54(1-2), pp. 81-98.

Rust, C. M., Aelion, C. M. & Flora, J. R. V., 2000. Control of pH during denitrification in subsurface sediment microcosms using encapsulated phosphate buffer. *Water Research*, 34(5), pp. 1447-1454.

Ryan, J. & Gschwend, P. M., 1994. Effects of Ionic Strength and Flow Rate on Colloid Release: Relating Kinetics to Intersurface Potential Energy. *Journal of colloid and interface science*, Volume 164, pp. 21-34.

Sabatini, D., Knox, R. & Harwell, J., 1996. *Surfactant-enhanced DNAPL remediation: surfactant selection, hydraulic efficiency, and economic factors*, s.l.: EPA. Environmental Research Brief.

Sahimi, M., B.D. Hughes, L.E. Scriven, H.T. Davis (1986), Dispersion in flow through porous media-I. One-phase flow, *Chem. Eng. Sci.*, 41(8), 2103-2122, doi:10.1016/0009-2509(86)87128-7.

Saleh, N. et al., 2008. Ionic Strength and Composition Affect the Mobility of Surface Modified Fe0 Nanoparticles in Water-Saturated Sand Columns. *Environental Science and Technology*, 42(9), pp. 3349-3355.

Saleh, N. et al., 2005. Adsorbed triblock copolymers deliver reactive iron nanoparticles to the oil/water interface. *Nano Letters*, 5(12), pp. 2489-2494.

Sato, T., H. Tanahashi, H. Loáiciga (2003), Solute dispersion in variably saturated sand, *Water Resour. Res.*, 39(6), 1-7, WR001649, doi: 10.1029/2002WR001649.

Scheidegger, A.E. (1960), The Physics of Flow Through Porous Media, University of Toronto Press, Toronto, Ontario.

Scheidegger, A.E. (1961), General Theory of Dispersion in Porous Media, *J. Geophys. Res.*, 66, 3273-3278, doi: 10.1029/JZ066i010p03273.

Schijven, J. F., Hassanizadeh, S. & de Bruin, R. H., 2002. Two-site kinetic modeling of bacteriophages transport through columns of saturated dune sand. *Journal of Contaminant Hydrology,* Volume 57, pp. 259-279.

Sedivy, R., Shafer, J. & Bilbrey, L., 1999. Design screening tools for passive funnel and gate systems. *Groundwater Monitoring & Remediation,* pp. 125-133.

Shen, X. et al., 2011. Foam, a promising vehicle to deliver nanoparticles for vadose zone remediation. *Journal of Hazardous Materials,* Volume 186, pp. 1773-1780.

Shiau, B.-J., Sabatini, D. A. & Harwell, J. H., 1994. Solubilization and Microemulisification of Chlorinated Solvents using diret food additive (edible) surfactants. *Groundwater*, 32(4), pp. 561-569.

Siegel, R. A., Falamarzian, M., Firestone, B. A. & Moxley, B. C., 1988. pH-Controlled Release from Hydrophobic/Polyelectrolyte Coppolymer Hydrogels. *Journal of Controlled Release,* pp. 179-182.

Sillen, L. G., Martell, A. E. & Bjerrum, J., 1964. *Stability constants of metal-ion complexes.* London: Chemical Society.

Silva, C. M. et al., 2006. Microencapsulation of hemoglobin in chitosan-coated alginate microspheres prepared by emulsification/internal gelation. *The AAPS journal,* 7(4).

Simunek, J., M. Th. Van Genuchten, M. Sejna, N. Toride, F.J. Leij (2005), Studio of Analytical Models for Solving the Convection-Dispersion Equation (STANMOD), version 2.07

Solutions-IES and Terra Systems, Inc. (TSI), 2004. *Enhanced In Situ Reductive Dechlorination of Trichloroethene Using Edible Oil Emulsion, Altus Air Force Base,* s.l.: Prepared for the Air Force Center for Environmental Excellence, Brooks City-Base, TX, September.

Solutions-IES and TSI, 2005. *Enhanced In Situ Reductive Dechlorination of Trichloroethene Using Edible Oil Emulsion, Edwards Air Force Base,* s.l.: Prepared for the Air Force Center for Environmental Excellence, Brooks City-Base, TX. February..

Song, H. & Carraway, E. R., 2005. Reduction of chlorinated ethanes by nanosized zero-valent iron: Kinetics, pathways, and effects of reaction conditions. *Environmental Science and Technology,* 39(16), pp. 6237-6245.

Soo, H. & Radke, C. J., 1984a. The flow mechanism of dilute, stable emulsions in porous media. *Industrial and Engineering Chemistry Fundamentals,* Volume 23, pp. 342-347.

Soo, H. & Radke, C. J., 1986. A Filtration Model For the Flow of Dilute, Stable Emulsions in Porous Media - I. Theory. *Chemical Engineering Journal,* 41(2), pp. 263-272.

Soo, H., Williams, M. & Radke, C., 1986. A filtration model for the flow of dilute, stable emulsions in porous media—II. Parameter evaluation and estimation. *Chemical Engineering Science,* 41(2), pp. 273-281.

Sorbie, K., Zhang, H. & Tsibuklis, N., 1995. Linear Viscous Fingering: New Experimental Results, Direct Simulation and the Evaluations of Averaged Models. *Chemical Engineering Science,* 50(4), pp. 601-616.

Steel, K. M., Alizadehhesari, K., Balucan, R. D. & Bašić, B., 2013. Conversion of CO2 into mineral carbonates using a regenerable buffer to control solution pH. *Fuel,* Volume 111, pp. 40-47.

Steffan, R., Schaefer, C. & Lippincott, D., 2010. *Bioaugmentation for Groundwater Remediation,* s.l.: s.n.

Steffan, R., Schaefer, C. & Lippincott, D., 2010. *Final Report: Bioaugmentation for Groundwater Remediation,* s.l.: s.n.

Strategic Environmental Research and Development Program, 2006. *Reaction and Transport Processes Controlling In Situ Chemical Oxidation of DNAPLs,* s.l.: s.n.

Stumm, W. & Morgan, J., 1996. *Aquatic Chemistry: Chemical Equilibria and Rates in Natural Waters.* 3rd ed. s.l.:John Wiley & Sons Inc..

Szynalski, K., 2003. *Ecophysiology and molecular identification of microbial populations involved in the reductive dechlorination of chloroethenes Ph.D. thesis 2898.* Ecole Polytechnique Fédérale de Lausanne, Lausanne, Switzerland: s.n.

Taghavy, A., A. Mittelman, Y. Wang, K.D. Pennell, L.M. Abriola (2013), Mathematical Modeling of the Transport and Dissolution of Citrate- Stabilized Silver Nanoparticles in Porous Media, *Environ. Sci. Technol*., 47, 8499-8507, doi: 10.1021/es400692r.

Taylor, T. P. (1999), Characterization and surfactant enhanced remediation of organic compounds in saturated porous media, Ph.D. dissertation, Dep. Of Civil and Environ. Eng., Georgia Institute of Technology, Atlanta, GA, USA.

Taylor, T.P., K.D. Pennell, L.M. Abriola, J.H. Dane (2001), Surfactant enhanced recovery of tetrachloroethylene from a porous medium containing low permeability lenses 1. Experimental studies, *J. Contam. Hydrol.*, 48, 325-350.

Taylor, T.P., K.M. Rathfelder, K.D. Pennell, L.M. Abriola (2004), Effects of ethanol addition on micellar solubilization and plume migration during surfactant enhanced recovery of tetrachloroethene, *J. Contam. Hydrol.*,69, 73-99, doi: 10.1016/S0169-7722(03)00151-7

Tchelepi, H. A., 1994. *Viscous fingering, gravity segregation and permeability heterogeneity in two-dimensional and three-dimensional flows*, s.l.: s.n.

The Interstate Technology & Regulatory Council, 2011. *Permeable Reactive Barrier: Technology Update,* s.l.: s.n.

Thomas, G. W. & Hargrove, W. L., 1984. The Chemistry of Soil Acidity. In: F. Adams, ed. *Soil Acidity and Liming.* s.l.:American Society of Agronomy, Crop Science Society of America, Soil Science Society of America, pp. 3-56.

Todd, M. & Longstaff, W., 1972. The Development, Testing, and Application Of a Numerical Simulator for Predicting Miscible Flood Performance. *Journal of Petroleum Technology,* 24(7), pp. 874-882.

Toride, N., M. Inoue, F. J. Leij (2003), Hydrodynamic Dispersion in an Unsaturated Dune Sand, *Soil Sci. Soc. Am. J.*, 67, 703-712, doi: 10.2136/sssaj2003.0703.

Toride, N., F. J. Leij, and M. T. van Genuchten (1995), The CXTFIT code for estimating transport parameters from laboratory or field tracer experiments, Version 2.1, U. S. Salinity Lab. Agric. Res. Serv. Rep. 137, pp. 119, U.S. Dep. of Agric., Riverside, Calif.

Trumm, D., June 23-26, 2009. *Selection of active and passive treatment systems for AMD - flow charts for New Zealand conditions.* Skelleftea, Sweden, 8th ICARD.

TSI and Soltuions-IES, 2004. *Installation Report: Technology Application of Low Cost Emplacement of Slowly-Soluble Organic Substrate for Enhanced In Situ Reductive Dechlorination of Halogenated Aliphatic Hydrocarbons, Arnold Air*

Force Base, s.l.: Prepared for the Air Force Center for Environmental Excellence, Brooks City-Base, TX. June.

TSI and Solutions-IES, 2003. *Interim Report: Technology Application of Low Cost Emplacement of Insoluble Organic Substrate for Enhanced In Situ Reductive Dechlorination of Halogenated Aliphatic Hydrocarbons, Dover Air Force Base,* s.l.: Prepared for the Air Force Center for Environmental Excellence, Brooks City-Base, TX. March.

Tufenkji, N. & Elimelech, M., 2004. Correlation Equation for Predicting Single-Collector Efficiency in Physicochemical Filtration in Saturated Porous Media. *Environmental Science and Technology,* 38(2), pp. 529-536.

Tufenkji, N. & Elimelech, M., 2004. Deviation from the classical colloid filtration theory in the presence of repulsive DLVO interactions. *Langmuir,* Volume 20, pp. 10818-10828.

Tufenkji, N. & Elimelech, M., 2005. Spatial distributions of Cryptosporidium oocysts in porous media: Evidence for dual mode deposition. *Environmental science & technology,* Volume 39, pp. 3600-3629.

United States Air Force (USAF), 2007. *Final Treatability Study for Enhanced Monitored Natural Attenuation at DP98, Elmendorf Air Force Base, Alaska,* s.l.: Prepared by Parsons for AFCEE and Elmendorf AFB, Alaska. April.

United States Environmental Protection Agency, 2006. *In Situ Treatment Technologies for Contaminated Soil,* s.l.: s.n.

Vainberg, S., Condee, C. W. & Steffan, R. J., 2009. Large-scale production of bacterial consortia for remediation of chlorinated solvent-contaminated groundwater. *Journal of Industrial Microbiology & Biotechnology,* 36(9), pp. 1189-1197.

van Genuchten, M. Th., and P. J. Wierenga (1976), Mass Transfer Studies in Sorbing Porous Media I. Analytical Solutions, *Soil Sci. Soc. Am. J.*, 40, 473-480.

van Genuchten, M.Th. (1980a), A closed-form equation for predicting the hydraulic conductivity of unsaturated soils, *Soil Sci. Soc. Am. J.*, 44(5), 892-898

van Genuchten, M. Th. (1980b), Determining transport parameters from solute displacement experiments, research report No. 118, U. S. Salinity Laboratory, USDA, ARS, Riverside, CA.

Vanderborght, J., and H. Vereecken (2007), Review of Dispersivities for Transport Modeling in Soils, *Vadose Zone J.*, 6, 29-52, doi:10.2136/vzj2006.0096.

Vainberg, S. et al., 2006. *Production and Application of Large-Scale Cultures for Bioaugmentation.* s.l., s.n.

Valocchi, A. J., 1985. Validity of the Local Equilibrium Assumption for Modeling Sorbing Solute Transport Through Homogeneous Soils. *Water Resources Research,* 21(6), pp. 808-820.

van Breemen, N., Driscoll, C. & Mulder, J., 1984. Acidic deposition and internal proton sources in acidification of soils and waters. *Nature,* 307(16), pp. 599-604.

Vanukuru, B., Flora, J. R. V., Petrou, M. F. & Marjorie Aelion, C., 1998. Control of pH during denitrification using an encapsulated phosphate buffer. *Water Research,* 32(9), pp. 2735-2745.

Venkatadri, R. & Peters, R. W., 1993. Chemical Oxidation Technologies: Ultraviolet Light/Hydrogen Peroxide, Fenton's Reagent, and Titanium Dioxide-Assisted Photocatalysis. *Hazardous Waste and Hazardous Materials,* 10(2), pp. 107-149.

Venkataraman, P. et al., 2013. Attachment of a Hydrophobically Modified Biopolymer at the Oil − Water Interface in the Treatment of Oil Spills. *ACS Appl. Mater. Interfaces,* Volume 5, pp. 3572-3580.

Wada, K., 1989. Allophane and imogolite. In: *Minerals in soil environments.* Wadison, WI: Soil Science Society of America, pp. 1051-1087.

Wang, Y. (2009), Transport and Retention of Fullerene-based Nanoparticles in Water-Saturated Porous Media, Ph.D. dissertation, Dep. Of Civil and Environ. Eng., Georgia Institute of Technology, Atlanta, GA, USA.

Watson, D. et al., 2013. In situ bioremediation of uranium with emulsified vegetable oil as the electron donor. *Environmental science & technology,* Volume 47, pp. 6440-6448.

Watts, R. J., Udell, M. D., Rauch, P. a. & Leung, S. W., 1990. Treatment of Pentachlorophenol-Contaminated Soils Using Fenton's Reagent. *Hazardous Waste and Hazardous Materials,* 7(4), pp. 335-345.

Weaver, A. R. et al., 2004. Mapping Soil pH Buffering Capacity of Selected Fields in the Coastal Plain. *Soil Science Society of America Journal,* Volume 68, pp. 662-668.

Wildenschild, D., and K.H. Jensen (1999), Laboratory investigations of effective flow behavior in unsaturated heterogeneous sands, *Water Resour. Res.*, 35(1), 17-27, doi: 10.1029/98WR01958.

Winsor, P., 1948. Hydrotropy, solubilization, and related emulsification processes I. *Transaction Faraday Society,* Volume 44, pp. 376-382.

Winsor, P., 1954. *Solvent Properoties of Amphiphilic Compounds.* London: Butterworths Scientific Publications.

Yao, K. M., Habibian, M. T. & O'Melia, C. R., 1971. Water and waste water filtration. Concepts and applications. *Environmental Science & Technology,* 5(11), pp. 1105-1112.

Yu, S., 2003. *Kinetics and modeling investigations of the anaerobic reductive dechlorination of chlorinated ethylenes using single and binary mixed cultures and silicon-based organic compounds as slow-release substrates. Ph.D. thesis.* s, Oregon State University, Corvallis: s.n.

Yule, D.F., and W.R. Gardner (1978), Longitudinal and Transverse Dispersion Coefficients in Unsaturated Plainfield Sand, *Water Resour. Res.*, 14(4), 582-588, doi: 10.1029/WR014i004p00582.

Zhang, J., Z. Zheng, L. Chen, Y. Sun (2014), Effect of residual oil saturation on hydrodynamic properties of porous media, *J. Hydrol.*, 515, 281-291, doi:10.1016/j.hydrol.2014.04.067.

Zhong, L., Oostrom, M., Wietsma, T. W. & Covert, M. A., 2008. Enhanced remedial amendment delivery through fluid viscosity modifications: experiments and numerical simulations. *Journal of Contaminant Hydrology,* Volume 101, pp. 29-41.

Zhong, L. et al., 2011. Enhanced remedial amendment delivery to subsurface using shear thinning fluid and aqueous foam. *Journal of Hazardous Materials*, 191(1-3), pp. 249-257.

APPENDIX I: EMULSION TRANSPORT MODEL

Particle transport model for variable saturation in time and space with dispersivity is a function of saturation (i.e., α is comprised of mechanical and viscous effects). The mass balance equation for droplet/particles was represented by the following generalized equation for the aqueous phase:

$$\frac{\partial(ns_wC)}{\partial t}+\rho_b\frac{\partial S}{\partial t}=\frac{\partial}{\partial z}(ns_wD_h\frac{\partial C}{\partial z})-\frac{\partial C}{\partial z}(ns_wv_xC) \qquad \text{(A.1)}$$

Dispersive mixing is typically defined by Equation A.2

$$D_h=\alpha\cdot v_x \qquad \text{(A.2)}$$

Here, dispersive mixing is defined as the product of mechanical and viscous mixing:

$$D_h=(\alpha_{mech}+\alpha_{visc})\cdot v_x \qquad \text{(A.3)}$$

$$v_x=\frac{q}{nS_w} \qquad \text{(A.4)}$$

Where, mechanical mixing is dependent on the saturation of the dispersed phase (s_{DP}):

$$\alpha_{mech}=\alpha_0+M_1\cdot {s_{DP}}^{N_1} \qquad \text{(A.5)}$$

And viscous mixing is defined as:

$$\alpha_{visc}=L\cdot b(H\cdot E-1)^c \qquad \text{(A.6)}$$

Where: *b* and *c* are derived from the updated Flowers and Hunt (2007) method—*b*=0.135; *c*=1.85

Starting with expression A.1, plug in expression A.2 and A.4.

$$\frac{\partial(ns_wC)}{\partial t}+\rho_b\frac{\partial S}{\partial t}=\frac{\partial}{\partial z}(ns_w\alpha\cdot\frac{q}{ns_w}\frac{\partial C}{\partial z})-\frac{\partial}{\partial z}(ns_w\frac{q}{nS_w}C) \qquad \text{(A.7)}$$

Applying the following assumptions to Expression A.7:

- n, ρ_b and q are constant in z and t
- C, S_w, S_{DP}, S, D_h, v_x,α vary in z and t

$$nC\frac{\partial s_w}{\partial t} + ns_w\frac{\partial C}{\partial t} + \rho_b\frac{\partial S}{\partial t} = q(\frac{\partial \alpha}{\partial z}\frac{\partial C}{\partial z} + \alpha\frac{\partial^2 C}{\partial z^2} - \frac{\partial C}{\partial z}) \qquad \text{(A.8)}$$

Solid phase exchange expression is dependent on model selected. No particle detachment is included in the following expressions although the additional term can be easily added to the following expressions.

$$\frac{\partial S}{\partial t} = \frac{\partial S_{att}}{\partial t} + \frac{\partial S_{str}}{\partial t} \qquad \text{(A.9)}$$

$$\psi_b = \left(1 - \frac{S}{S_{\max}}\right) \qquad \text{(A.10)}$$

$$\psi_d = \left(\frac{d_{50} + z}{d_{50}}\right)^{-\beta} \qquad \text{(A.11)}$$

M-1: $\frac{\partial S_{att}}{\partial t} = \frac{ns_w}{\rho_b}k_{att}\psi_b C$; $\frac{\partial S_{str}}{\partial t} = 0$

M-2: $\frac{\partial S_{att}}{\partial t} = 0$; $\frac{\partial S_{str}}{\partial t} = \frac{ns_w}{\rho_b}k_{str}\psi_d C$

M-3: $\frac{\partial S_{att}}{\partial t} = \frac{ns_w}{\rho_b}k_{att}k_{str}\psi_d\psi_b C$; $\frac{\partial S_{str}}{\partial t} = 0$

M-4: $\frac{\partial S_{att}}{\partial t} = \frac{ns_w}{\rho_b}k_{att}\psi_b C$; $\frac{\partial S_{str}}{\partial t} = \frac{ns_w}{\rho_b}k_{str}\psi_d C$

Saturation of water and dispersed phase must equal 1;

$$s_w + s_{DP} = 1 \qquad \text{(A.12)}$$

Thus,

$$\frac{\partial s_{DP}}{\partial t} = -\frac{\partial s_w}{\partial t} \qquad \text{(A.13)}$$

Solid phase concentration is related to water saturation by:

$$s_w = 1 - \frac{S \cdot \rho_b}{\rho_{DP} n} \qquad \text{(A.14)}$$

Thus,

$$\frac{\partial s_w}{\partial t} = -\frac{\rho_b}{n\rho_{DP}} \frac{\partial S}{\partial t} \qquad \text{(A.15)}$$

Plug in equation A.15 into Equation A.8, divide by *n*, and group terms

$$\frac{\rho_b}{n}(1 - \frac{C}{\rho_{DP}})\frac{\partial S}{\partial t} + s_w \frac{\partial C}{\partial t} = \frac{q}{n}(\frac{\partial \alpha}{\partial z}\frac{\partial C}{\partial z} + \alpha \frac{\partial^2 C}{\partial z^2} - \frac{\partial C}{\partial z}) \qquad \text{(A.16)}$$

Discretization schemes

i is tnode; *j* is xnode; *k* is iteration;

$$\frac{\partial^2 C}{\partial z^2} \cong \frac{C_{j+1}^{n+1,k+1} - 2C_j^{n+1,k+1} + C_{j-1}^{n+1,k+1}}{dz^2} \text{ (Implicit)} \qquad \text{(A.17)}$$

$$\frac{\partial C}{\partial z} \cong \frac{C_{j+1}^{n+1,k+1} - C_{j-1}^{n+1,k+1}}{2dz} \text{ (Implicit, Central Differences)} \qquad \text{(A.18)}$$

$$\frac{\partial C}{\partial t} \cong \frac{C_j^{n+1,k+1} - C_j^n}{dt} \text{ (Forward)} \qquad \text{(A.19)}$$

Discretization of α in space:

For first node: (*i*=1)

$$\left.\frac{\partial \alpha}{\partial z}\right|_j^{n+1,k} \cong \frac{\alpha_{j+1}^{n+1,k} - \alpha_j^{n+1,k}}{dz} \text{ (Forward difference)} \qquad \text{(A.20)}$$

For last node: (*i*=*m*)

$$\left.\frac{\partial \alpha}{\partial z}\right|_j^{n+1,k} \cong \frac{\alpha_j^{n+1,k} - \alpha_{j-1}^{n+1,k}}{dz} \text{ (Backwards difference)} \qquad \text{(A.21)}$$

For all other nodes:

$$\left.\frac{\partial \alpha}{\partial z}\right|_j^{n+1,k} \cong \frac{\alpha_{j+1}^{n+1,k} - \alpha_{j-1}^{n+1,k}}{2dz} \text{ (Central difference)} \qquad \text{(A.22)}$$

Discretize S in time and set equal to $\frac{\partial S}{\partial t}$ as expressed in M1-M4

For M1-M3, set unused mechanism terms to 1 (e.g., k_{str} , ψ_b =1 if M1), and use previous iteration values expect for C.

$$\frac{\partial S}{\partial t} \cong \frac{S_j^{n+1,k+1} - S_j^n}{dt} = (\frac{n}{\rho_b} k_{att} k_{str} \psi_d)(\psi_{b\,j}^{\;n+1,k})(s_{w\,j}^{\;n+1,k})(C_j^{n+1,k+1}) \qquad \text{(A.23)}$$

$$S_c\big|_j^{n+1,k} = (\frac{n}{\rho_b} k_{att} k_{str} \psi_d)(\psi_{b\,j}^{\;n+1,k})(s_{w\,j}^{\;n+1,k}) \qquad \text{(A.24)}$$

Solve for $S_j^{n+1,k+1}$:

$$S_j^{n+1,k+1} = S_j^n + (\frac{dt \cdot n}{\rho_b} k_{att} k_{str} \psi_b)(\psi_{b\,j}^{\;n+1,k})(s_{w\,j}^{\;n+1,k})(C_j^{n+1,k+1}) \qquad \text{(A.25)}$$

For Model M4:

$$\frac{\partial S}{\partial t} \cong \frac{S_j^{n+1,k+1} - S_j^n}{dt} = (\frac{n}{\rho_b})(k_{att} \psi_{b\,j}^{\;n+1,k} + k_{str} \psi_d)(s_{w\,j}^{\;n+1,k})(C_j^{n+1,k+1}) \qquad \text{(A.26)}$$

$$S_c\big|_j^{n+1,k} = (\frac{n}{\rho_b})(k_{att} \psi_{b\,j}^{\;n+1,k} + k_{str} \psi_d)(s_{w\,j}^{\;n+1,k}) \qquad \text{(A.27)}$$

Solve for $S_j^{n+1,k+1}$:

$$S_j^{n+1,k+1} = S_j^n + (\frac{dt \cdot n}{\rho_b})(k_{att} \psi_{b\,j}^{\;n+1,k} + k_{str} \psi_d)(s_{w\,j}^{\;n+1,k})(C_j^{n+1,k+1}) \qquad \text{(A.28)}$$

Discretization of C in space and time:

$$\frac{\rho_b}{n}(1 - \frac{C_j^{n+1,k}}{\rho_{DP}})(S_{c\,j}^{\;n+1,k} C_j^{n+1,k+1}) + (s_{w\,j}^{\;n+1,k})(\left.\frac{\partial C}{\partial t}\right|_j^{n+1,k+1}) = \ldots$$

$$\ldots \frac{q}{n}[(\frac{\partial \alpha}{\partial z}\Big|_j^{n+1,k})(\frac{\partial C}{\partial z}\Big|_j^{n+1,k+1}) + (\alpha_j^{n+1,k})(\frac{\partial^2 C}{\partial z^2}\Big|_j^{n+1,k+1}) - (\frac{\partial C}{\partial z}\Big|_j^{n+1,k+1})] \qquad \text{(A.29)}$$

Note: $C_{j-1}^{n+1,k+1}$ as A; $C_j^{n+1,k+1}$ as B; $C_{j+1}^{n+1,k+1}$ as C; and C_j^n as CC

Plug in:

$$\frac{\rho_b}{n}(1-\frac{C_j^{n+1,k}}{\rho_{DP}})(S_c B) + (s_{w\,j}^{n+1,k})(\frac{B-CC}{dt}) = \frac{q}{n}[(\frac{\partial \alpha}{\partial z}\Big|_j^{n+1,k})(\frac{C-A}{2dz}) + (\alpha_j^{n+1,k})(\frac{C-2B+A}{dz^2}) - (\frac{C-A}{2dz})] \qquad \text{(A.30)}$$

Solve for CC and solve A B and C terms:

$$\text{A: } -\frac{\Delta t \cdot q(2\alpha_j^{n+1,k} + \Delta z - \frac{\partial \alpha}{\partial z}\Big|_j^{n+1,k}\Delta z)}{2s_w\Big|_j^{n+1,k} n\Delta z^2} \qquad \text{(A.31)}$$

$$\text{B: } \frac{2q\alpha_j^{n+1,k}\rho_{DP}\Delta t - S_{c\,j}^{n+1,k} C_j^{n+1,k}\rho_b \Delta t \Delta z^2 + S_{c\,j}^{n+1,k}\rho_b\rho_{DP}\Delta t\Delta z^2}{s_{w\,j}^{n+1,k} n\Delta z^2 \rho_{DP}} + 1 \qquad \text{(A.32)}$$

$$\text{C: } -\frac{\Delta t \cdot q(2\alpha_j^{n+1,k} - \Delta z + \frac{\partial \alpha}{\partial z}\Big|_j^{n+1,k}\Delta z)}{2s_w\Big|_j^{n+1,k} n\Delta z^2} \qquad \text{(A.33)}$$

Solving overall expressions as:

$Aa + Bb + Cc = C_j^n$ (for all nodes expect first and last)

Boundary Conditions:

Inlet BC: 3rd type

$$v_x C_{j-1}^{n+1} = v_x C_j^{n+1} - D_h \frac{\partial C}{\partial z}\Big|_j^{n+1}$$

$$C_{j-1}^{n+1} = C_j^{n+1} - \alpha \frac{\partial C}{\partial z}\Big|_j^{n+1} \qquad \text{(A.34)}$$

Discretize using backwards difference:

$$C_{j-1}^{n+1} = C_j^{n+1} - \alpha(\frac{C_j^{n+1} - C_0{}^{n+1}}{\Delta z}) \qquad \text{(A.35)}$$

At inlet, first interior node: j=1;

$$A(C_j^{n+1} - \alpha(\frac{C_j^{n+1} - C_0{}^{n+1}}{\Delta z})) + Bb + Cc = C_j^{n+1}$$

$$(B - A(\frac{\alpha}{\Delta z} - 1)b + Cc = C_j^n - A(\frac{\alpha}{\Delta z})C_0^{n+1} \qquad \text{(A.36)}$$

Outlet: zero dispersive flux, $\frac{\partial C}{\partial z} = 0$ at $x=L$

$$\frac{\partial C}{\partial z} = \frac{c - b}{\Delta z} \qquad \text{(A.37)}$$

$$c = \frac{\partial C}{\partial z}\Delta z + b$$

$$Aa + Bb + C(\frac{\partial C}{\partial z}\Delta z + b) = C_j^n$$

$$Aa + Bb + Cb = C_j^n$$

$$Aa + (B + C)b = C_j^n \qquad \text{(A.38)}$$

APPENDIX II: ALKALINITY RELEASE MODEL FOR BATCH SYSTEMS

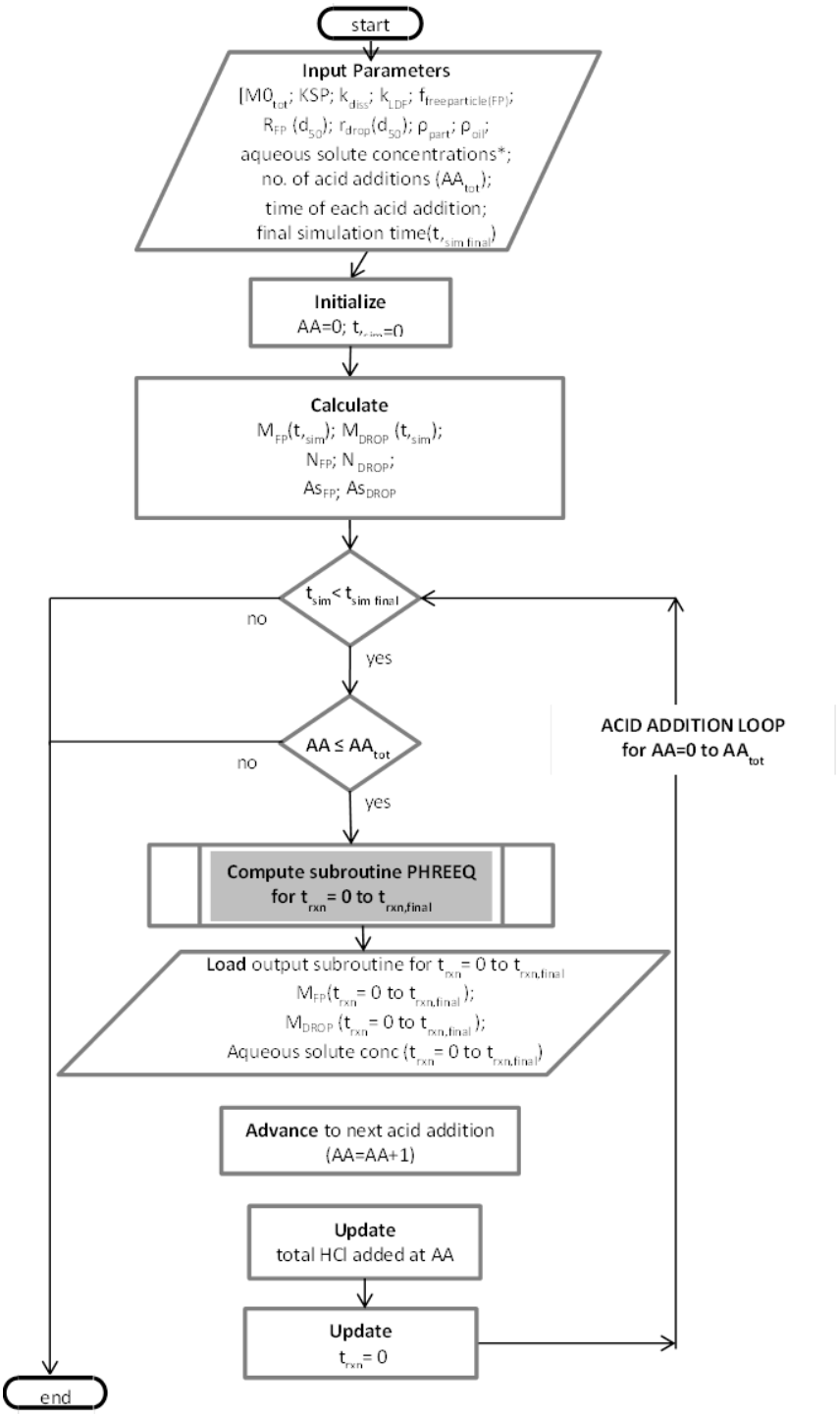

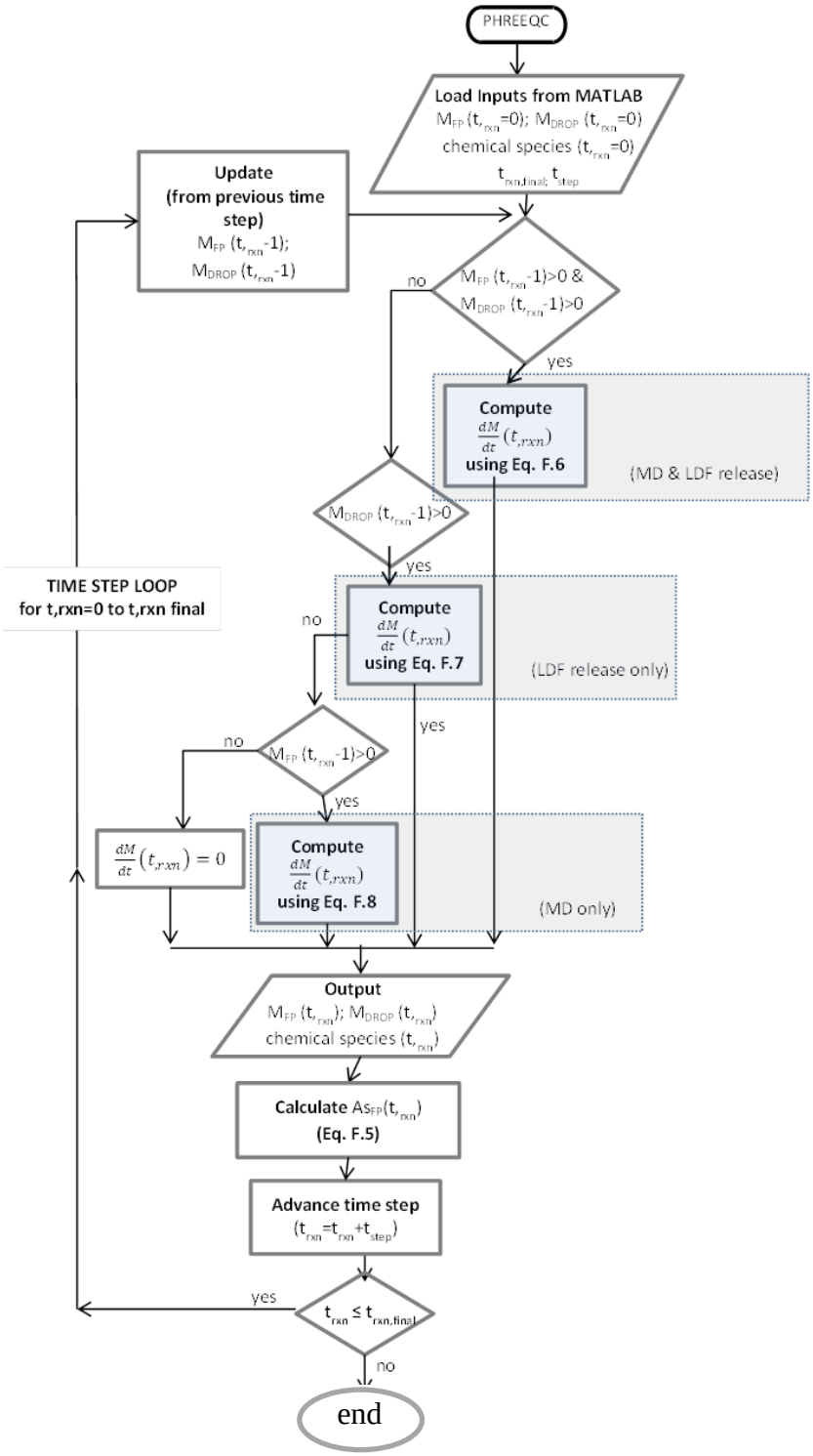

Figure A.I: Flow diagram for alkalinity release model. (top) diagram of overall model; (bottom) diagram of subroutine PHREEQC model.

Table AII.1: Alkalinity release model flow chart notes.

Note: *MilliQ water was assumed to be equilibrated with the atmosphere (i.e., C_T= 1.5e^{-5} M). Additional solutes can be added to the aqueous chemistry if applicable.

Symbols Referenced in Flow Chart

M_{FP}=Mass of free particles
f_{FP}= Fraction of total input particle mass present as free particles
$M_{0,tot}$ =Input particle mass
M_{drop}=Mass of particles encapsulated within droplets
f_{drop}= Fraction of total input particle mass encapsulated within droplets
r_{FP}= radius of free particles (d_{50})
r_{drop}= radius of droplets (d_{50})
N_{FP}=Total number of free particles
N_{drop}=Total number of droplets
k_{diss}= mineral dissolution rate constant
$A_{s,FP}$=Total surface area of free particles
$A_{s,drop}$=Total surface area of droplets
k_{LDF}=interphase mass transfer coefficient
$\{C^*\}$=equilibrium ion concentration (e.g., $\{Mg^{2+*}\}$ equilibrium magnesium ion concentration)
$\{C\}$= ion concentration

Equations Referenced in Flow Chart

Note: chemical equations F.7-F.9 have been shown release from magnesium particles to provide a more complete illustration of the interconnectedness of the release expressions through chemical species when both LDF and MD models are considered. Equations F.7-F.9 can be written to describe release from calcium carbonate particles.

$$M_{FP} = f_{FP} M_{0,tot} \quad \text{(F.1)}$$

$$M_{drop} = (1 - f_{FP}) M_{0,tot} \quad \text{(F.2)}$$

$$N_{FP} = \frac{\frac{M_{FP}}{\rho_{FP}}}{\frac{4}{3}\pi (r_{FP})^3} \quad \text{(F.3)}$$

$$N_{drop} = \frac{V_{DP,tot}}{\frac{4}{3}\pi (r_{drop})^3} \quad \text{(F.4)}$$

$$A_{s,FP}(t) = N_{FP} 6^{4/3} \pi^{1/3} \left(\frac{M_{FP}(t)}{\rho_{FP}}\right)^{2/3} = N_{FP} \cdot 4\pi (r_{FP}(t))^2 \quad \text{(F.5)}$$

$$A_{s,drop} = N_{drop} \cdot 4\pi (r_{drop})^2 \quad \text{(F.6)}$$

$$\frac{dC_{Mg^{2+}}}{dt} = [-k_{diss} A_{s,FP}(t)\{H^+\}^{0.397}(1-(\frac{\{Mg^{2+}\}\{OH^-\}^2}{K_{sp}})^2) + \ldots$$

$$\ldots k_{LDF} A_{s,drop}(\{Mg^{2+^*}\} - \{Mg^{2+}\}) \quad \text{(F.7)}$$

$$\frac{dC_{Mg^{2+}}}{dt} = [-k_{diss} A_{s,FP}(t)\{H^+\}^{0.397}(1-(\frac{\{Mg^{2+}\}\{OH^-\}^2}{K_{sp}})^2) \quad \text{(F.8)}$$

$$\frac{dC_{Mg^{2+}}}{dt} = k_{LDF} A_{s,drop}(\{Mg^{2+^*}\} - \{Mg^{2+}\}) \quad \text{(F.9)}$$

APPENDIX III: PH MODELING

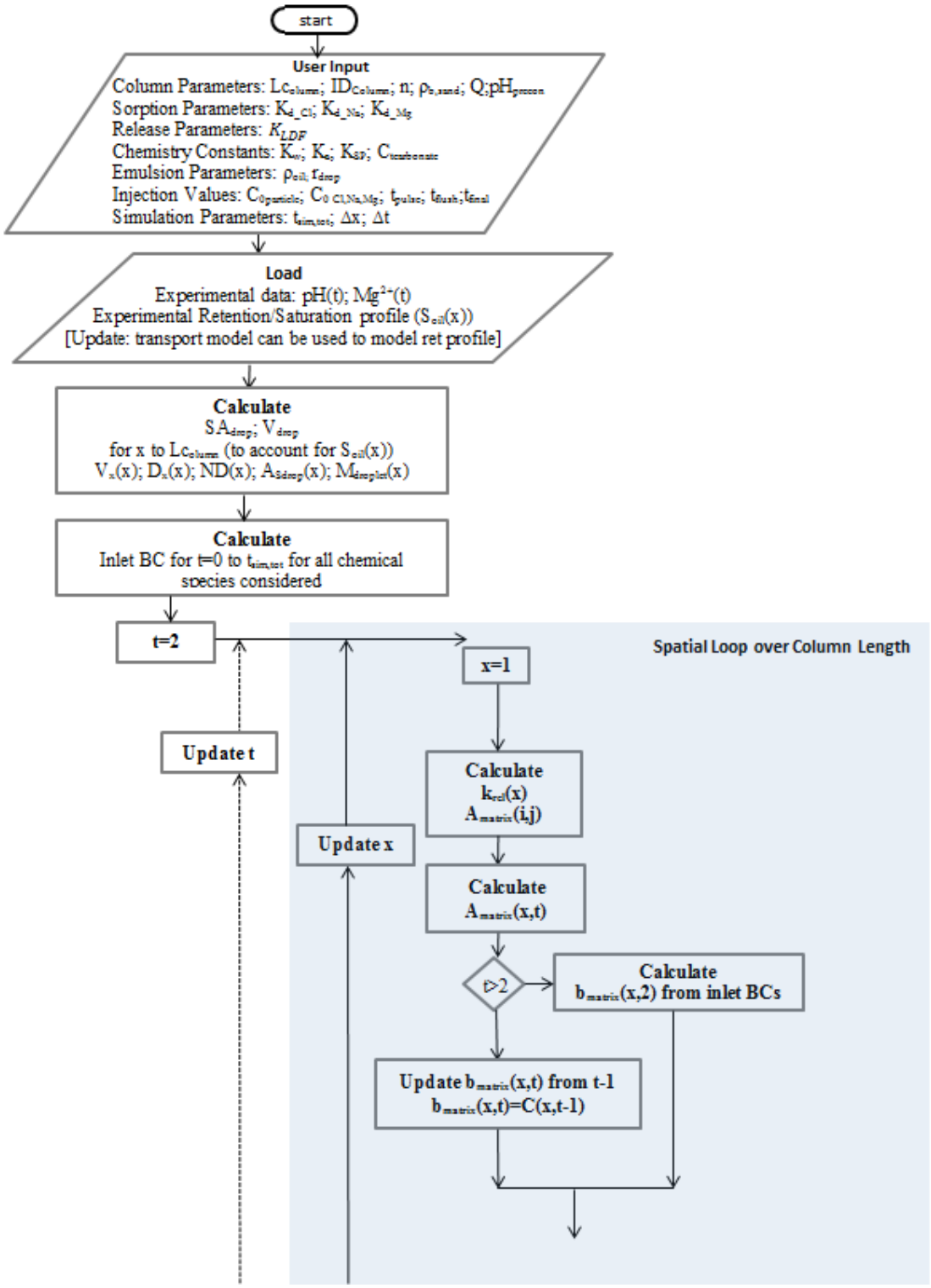

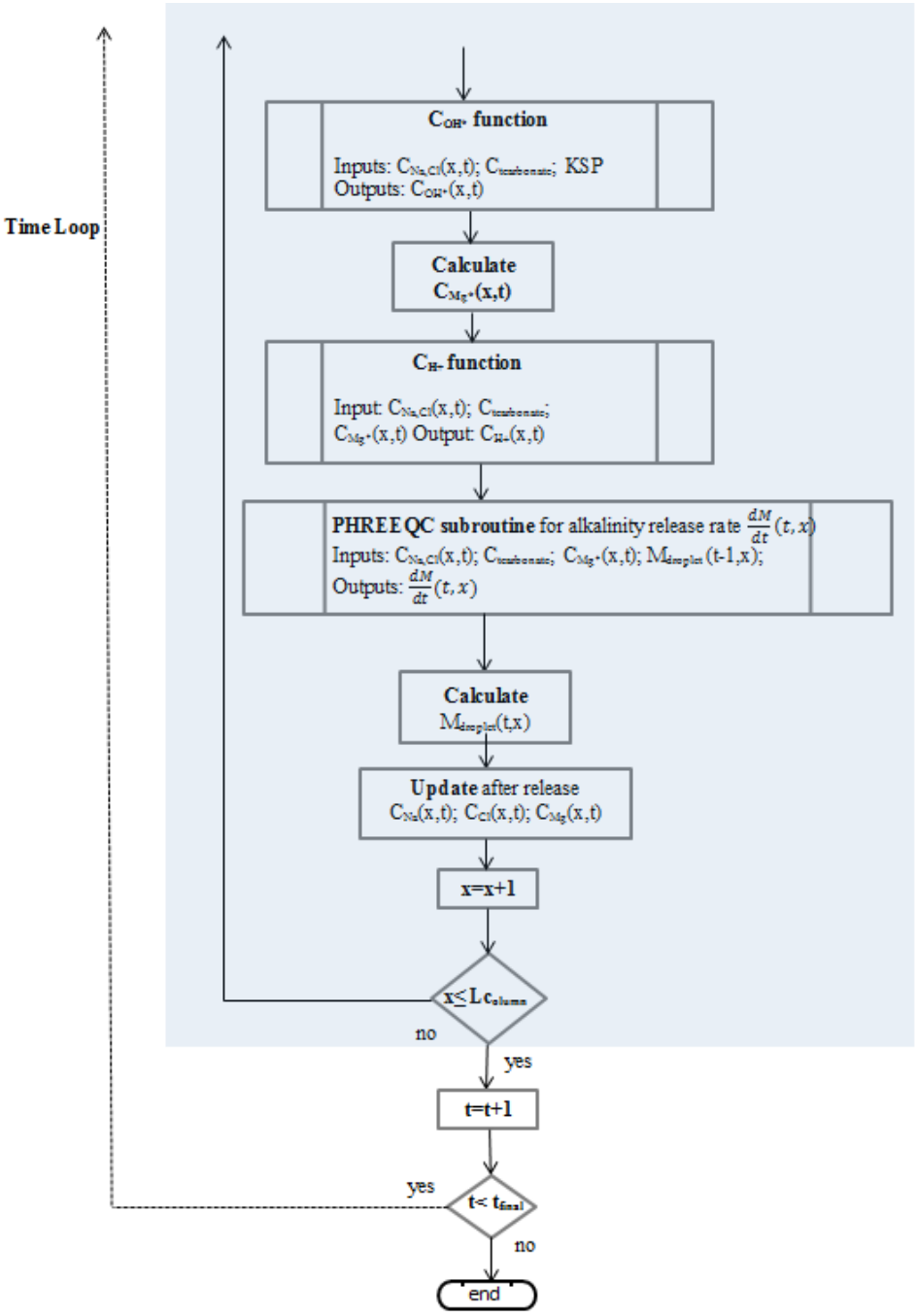

Figure AII.1: Modeling approach for alkalinity transport and release from oil-in-water emulsions in 1-d column systems.

Note:MilliQ water was assumed to be equilibrated with the atmosphere (i.e., C_T=1.5e-5 M). Additional solutes can be added to the aqueous chemistry if applicable.

Symbols:

L= length of soil column [cm]
ID= inner diameter of soil column [cm]
CA= cross sectional area of the column [cm^2]
n=porosity [-]
$\rho_{b,sand}$= bulk density of sand [$g \cdot mL^{-1}$]
Q_{inject}= flow rate of injection [$mL \cdot min^{-1}$]
Q_{flush}= flow rate of flush [$mL \cdot min^{-1}$]
$K_{d\_Cl,Na,Mg}$= linear partitioning/distribution coefficient [$L\text{-}aq \cdot kg^{-1} \cdot solid^{-1}$]
$K_{LFD=}$linear driving force mass transfer coefficient [$cm \cdot min^{-1}$]
K_w= water dissociation constant
K_a = Acid dissociation constant(s)
K_{sp}= Solubility product constant for particle of interest (e.g., $Mg(OH)_2$)
$C_{tcarbonate}$= Total carbonate concentration [M]
ρ_{oil}=density of oil [$g \cdot mL^{-1}$]
r_{drop}= radius of droplet [cm]
$C_{0particle}$=initial particle mass concentration in oil phase [g particle·g oil^{-1}]
$C_{0\ Cl,Na,Mg}$= initial concentration of solutes [M]
t_{pulse}=duration of pulse [min]
t_{flush}=duration of flush [min]
$t_{sim,tot}$=total length of simulation [min]
Δx=model distance step [cm]
Δt=model time step [min]
pH_{exp}= temporal experimental data for effluent pH [-]
Mg_{exp}^{2+}= temporal experimental data for effluent Mg^{2+} [M]
S_{DP}=experimental spatial distribution of dispersed phase saturation retained in porous media [-]
$v_x(x)$=pore water velocity [$cm \cdot min^{-1}$]
$\alpha(x)$= Dispersivity [cm]
$D_h(x)$= Dispersivity coefficient [$cm^2 \cdot min^{-1}$]
$ND(x)$= numerical dispersion[cm]
$M_{0,tot}$=Input particle mass [g]
M_{drop}= Mass of particles encapsulated within droplets [g]
r_{drop}= radius of droplets (d_{50})
N_{drop}= Total number of droplets [-]
$A_{s,drop}$= Total surface area of droplets [cm^3]
k_{LDF}= interphase mass transfer coefficient [min^{-1}]
$\{C^*\}$= equilibrium ion concentration (e.g., $\{Mg^{2+*}\}$= equilibrium magnesium ion concentration)
$\{C\}$= ion concentration

Additional Equations: (see model description for equations)

$$v_x = \frac{Q}{\frac{\pi(\frac{ID}{2})^2}{n}}$$

$$D_h = \alpha \cdot v_x$$

$$ND = D_h - 0.5{v_x}^2 \Delta t$$

$$N_{drop} = \frac{V_{DP,total}}{\frac{4}{3}\pi(r_{drop})^3}$$

$$A_{s,drop} = N_{drop} \cdot 4\pi(r_{drop})^2$$

$$M_{0,drop}(x) = C_{0,part} S_{DP}(x) \rho_{DP} \cdot CA \cdot n \cdot x$$

The ADR equation was discretized as:

$$\frac{\partial^2 C}{\partial x^2} = \frac{C_{i+1}^{l+1} - 2C_i^{l+1} + C_{i-1}^{l+1}}{\Delta x^2} \text{ [Implicit]} \quad \text{(A.39)}$$

$$\frac{\partial C}{\partial x} = \frac{C_{i+1}^{l+1} - C_{i-1}^{l+1}}{2\Delta x} \text{ [Implicit, central differences]} \quad \text{(A.40)}$$

$$\frac{\partial C}{\partial t} = \frac{C_i^{l+1} - C_i^{l}}{\Delta t} \quad \text{[Forward method]} \quad \text{(A.41)}$$

APPENDIX III: ADDITIONAL EMULSION TRANSPORT MODEL RESULTS

Table AIII.1 provides the statistical output for the dilute column model fits and for the subsequent predictions when: (*i*) influence of water saturation (α_1); (*ii*) influence of viscous instabilities (α_2); and (*iii*) both water saturation and viscous effects (α_1 & α_2) are added to the model.

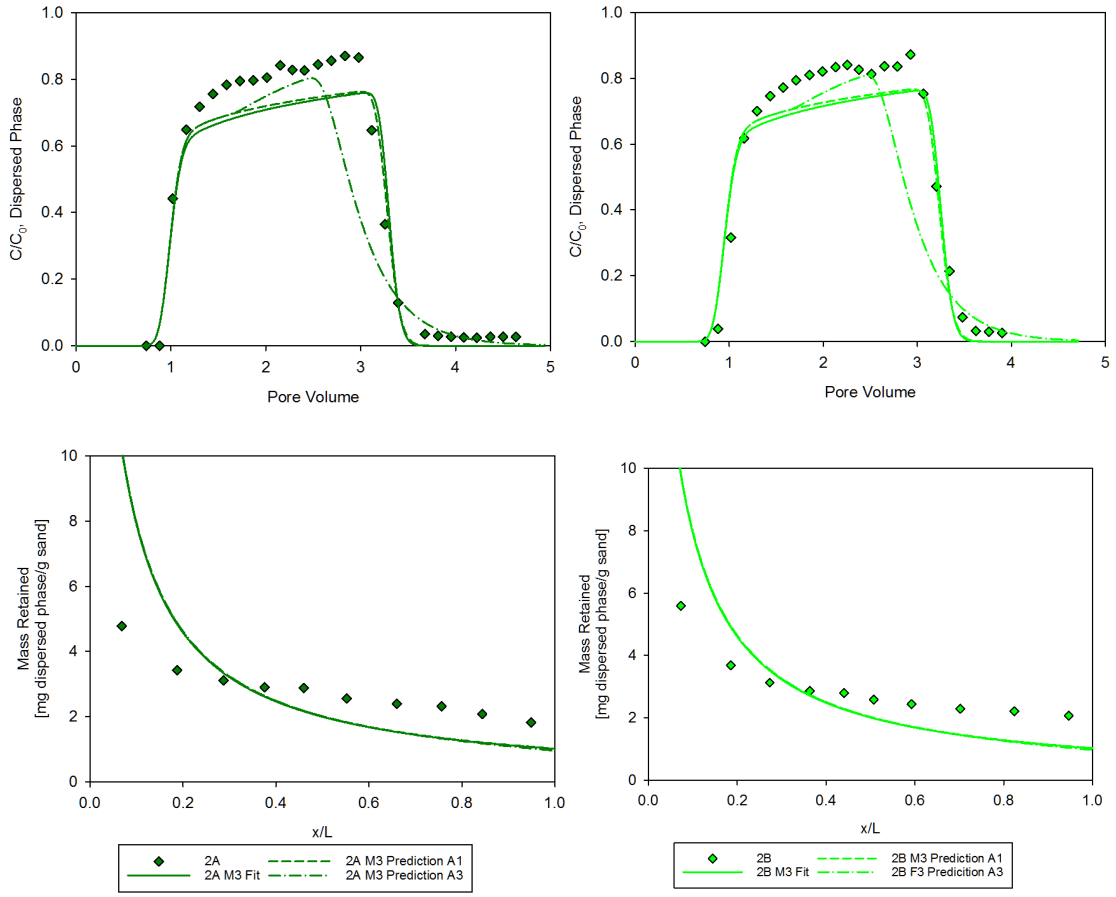

Figure AIII.2: Model 3 predictions for concentration emulsion columns (experiments 1 & 2).

Table AIII.1: Model 3 fits and subsequent predictions to experiments 1-2.

Model Output	**Experiment**	**Fit**	**α_1 ON**	**α_1 & α_2 ON**
$SSE_{,BTC}$	1A (AA)	0.26	0.23	0.34
$SSE_{,BTC\_w}$		1.75	1.53	2.27
$SSE_{,RP}$		0.00	0.00	0.00
$SSE_{,RP\_w}$		0.76	0.80	0.84
$SSE_{,total}$		0.26	0.23	0.34
$SSE_{,total\_w}$		2.50	2.33	3.11
AIC_c		-86.14	-88.58	-81.23
AIC_{c_w}		-44.05	-45.37	-39.97
$SSE_{,BTC}$	1B (BB)	0.19	0.16	0.52
$SSE_{,BTC\_w}$		1.27	1.04	3.49
$SSE_{,RP}$		0.00	0.00	0.00
$SSE_{,RP\_w}$		0.74	0.76	0.78
$SSE_{,total}$		0.19	0.16	0.52
$SSE_{,total\_w}$		2.01	1.80	4.27
AIC_c		-92.28	-95.92	-73.33
AIC_{c_w}		-48.16	-50.16	-34.07
$SSE_{,BTC}$	2A (A)	0.19	0.15	0.56
$SSE_{,BTC\_w}$		1.53	1.15	4.39
$SSE_{,RP}$		0.00	0.00	0.00
$SSE_{,RP\_w}$		4.60	4.67	4.73
$SSE_{,total}$		0.19	0.15	0.56
$SSE_{,total\_w}$		6.13	5.82	9.12
AIC_c		-77.88	-82.58	-60.43
AIC_{c_w}		-20.90	-21.75	-14.34
$SSE_{,BTC}$	2B (B)	0.16	0.14	0.64
$SSE_{,BTC\_w}$		1.17	1.00	4.67
$SSE_{,RP}$		0.00	0.00	0.00
$SSE_{,RP\_w}$		2.64	2.69	2.73
$SSE_{,total}$		0.16	0.14	0.64
$SSE_{,total\_w}$		3.81	3.69	7.40
AIC_c		-69.63	-72.01	-49.19
AIC_{c_w}		-22.93	-23.43	-13.13

Table AIII.1 provides the statistical output for the dilute column model fits and for the subsequent predictions when: (*i*) influence of water saturation (α_1); (*ii*) influence of viscous instabilities (α_2); and (*iii*) both water saturation and viscous effects (α_1 & α_2) are added to the model. The results indicate the influence of water saturation on emulsion transport regardless of input concentration increase the model fit to the experimental data as evidenced by the decreasing AIC_c value. The additional viscous instabilities dispersive effects; however, decrease the goodness of fit, suggesting that the functionality of viscous effects may be a function on concentration or that the developed functionality is a poor description at lower emulsion viscosity. However, it is hypothesized that the developed emulsion viscosity model (as a function of input dispersed phase concentration Equation 3.4) overestimates the viscosity of low concentration emulsions. If the emulsion viscosity model predicted higher viscosity, then the additional dispersive mixing added due to viscous instabilities would be much higher than actual mixing.

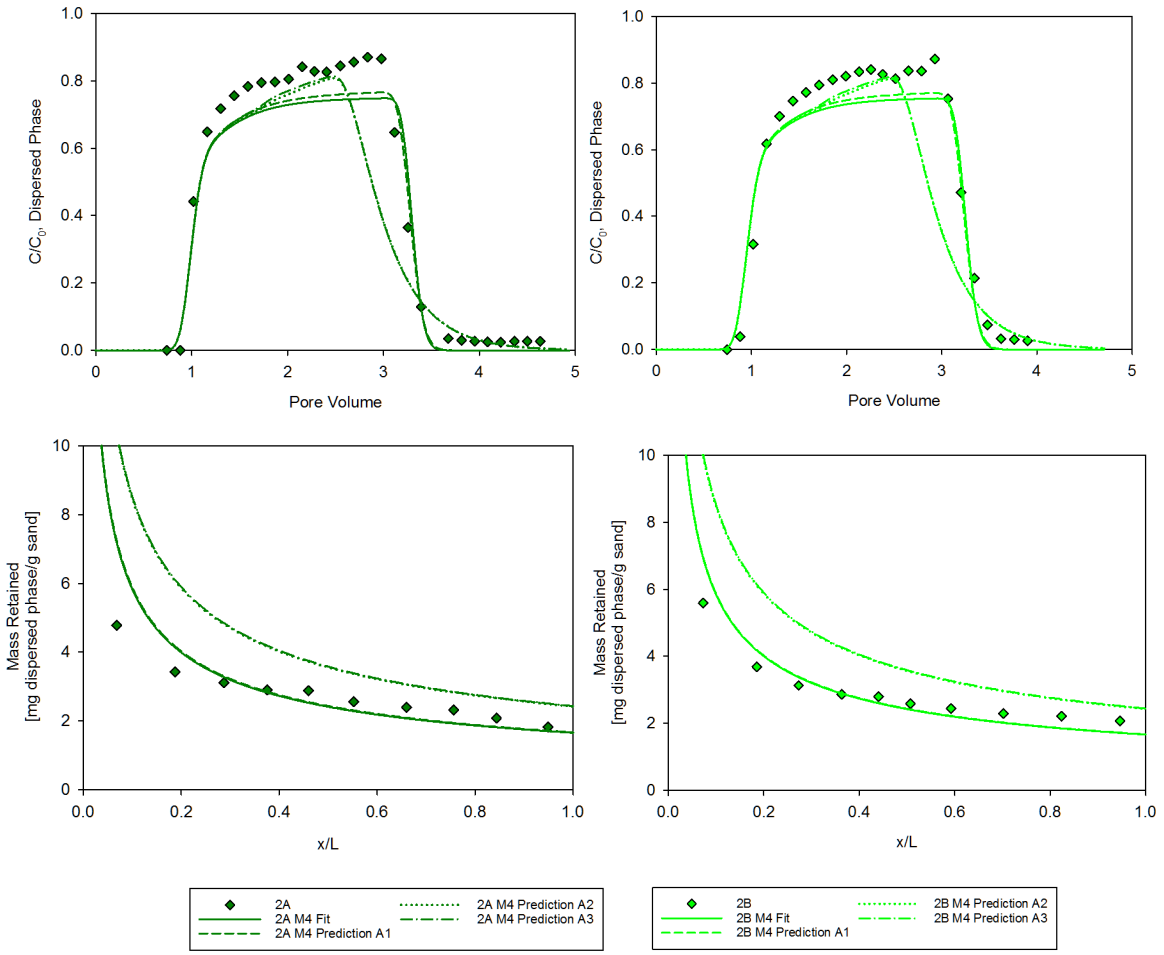

Figure AIII.3: Model 4 predictions for concentration emulsion columns (experiments 1 & 2).

Table AIII.2:Model 4 fits and subsequent predictions to experiments 1-2.

Model Output	Experiment	Fit	α_1 ON	α_2 ON	α_1 & α_2 ON
$SSE_{,BTC}$	1A (AA)	0.29	0.27	0.34	0.35
$SSE_{,BTC\_w}$		1.94	1.80	2.25	2.34
$SSE_{,RP}$		0.00	0.00	0.00	0.00
$SSE_{,RP\_w}$		0.31	0.30	0.30	0.30
$SSE_{,total}$		0.29	0.27	0.34	0.35
$SSE_{,total\_w}$		2.25	2.11	2.55	2.64
AIC_c		-84.23	-85.57	-81.41	-80.65
AIC_{c_w}		-46.07	**-47.27**	-43.70	-43.06
$MB_{,model}$		1.010	1.017	0.985	0.990
$SSE_{,BTC}$	1B (BB)	0.19	0.17	0.51	0.52
$SSE_{,BTC\_w}$		1.29	1.12	3.38	3.46
$SSE_{,RP}$		0.00	0.00	0.00	0.00
$SSE_{,RP\_w}$		0.76	0.73	0.72	0.70
$SSE_{,total}$		0.19	0.17	0.51	0.52
$SSE_{,total\_w}$		2.05	1.85	4.10	4.16
AIC_c		-91.87	-94.54	-73.91	-73.49
AIC_{c_w}		-47.78	-49.71	-34.83	-34.57
$MB_{,model}$		1.017	1.024	0.991	0.996
$SSE_{,BTC}$	2A (A)	0.16	0.13	0.55	0.54
$SSE_{,BTC\_w}$		1.29	0.99	4.30	4.26
$SSE_{,RP}$		0.00	0.00	0.00	0.00
$SSE_{,RP\_w}$		0.87	0.91	0.92	0.95
$SSE_{,total}$		0.16	0.13	0.55	0.54
$SSE_{,total\_w}$		2.17	1.89	5.22	5.21
AIC_c		-80.62	-85.08	-60.79	-60.92
AIC_{c_w}		-38.06	-40.29	-23.55	-23.57
$MB_{,model}$		1.009	1.016	0.962	0.967
$SSE_{,BTC}$	2B (B)	0.12	0.10	0.61	0.61
$SSE_{,BTC\_w}$		0.89	0.72	4.42	4.41
$SSE_{,RP}$		0.00	0.00	0.00	0.00
$SSE_{,RP\_w}$		0.28	0.30	0.31	0.32
$SSE_{,total}$		0.12	0.10	0.61	0.61
$SSE_{,total\_w}$		1.17	1.02	4.73	4.74
AIC_c		-73.69	-76.79	-49.99	-50.02
AIC_{c_w}		-40.35	-42.44	-19.73	-19.72
$MB_{,model}$		1.022	1.017	1.017	0.982

Table AIII.3: Model 4 predictions for concentration emulsion columns (experiments 3-4)

Model Output	Experiment	Prediction	α_1 ON	α_2 ON	α_1 & α_2 ON
$SSE_{,BTC}$	3A	1.11	0.65	0.46	0.48
$SSE_{,BTC\_w}$		9.43	5.58	3.89	4.12
$SSE_{,RP}$		0.00	0.00	0.00	0.00
$SSE_{,RP\_w}$		8.82	9.16	9.05	9.22
$SSE_{,total}$		1.11	0.66	0.46	0.49
$SSE_{,total\_w}$		18.25	14.74	12.94	13.34
AIC_c		-57.20	-66.74	-73.28	-72.26
AIC_{c_w}		-6.12	-10.02	-12.40	-11.85
$MB_{,model}$		1.021	1.026	0.932	0.934
$SSE_{,BTC}$	3B	0.98	0.58	0.84	0.88
$SSE_{,BTC\_w}$		6.46	3.80	5.48	5.79
$SSE_{,RP}$		0.00	0.00	0.00	0.00
$SSE_{,RP\_w}$		6.15	6.42	6.35	6.47
$SSE_{,total}$		0.99	0.58	0.84	0.88
$SSE_{,total\_w}$		12.61	10.22	11.83	12.26
AIC_c		-78.54	-90.26	-82.14	-80.95
AIC_{c_w}		-22.09	-26.73	-23.49	-22.70
$MB_{,model}$		1.017	1.022	0.935	0.936
$SSE_{,BTC}$	4	1.14	0.62	0.63	0.70
$SSE_{,BTC\_w}$		10.48	5.68	5.78	6.41
$SSE_{,RP}$		0.00	0.00	0.00	0.00
$SSE_{,RP\_w}$		1.77	1.96	1.91	1.97
$SSE_{,total}$		1.14	0.62	0.63	0.70
$SSE_{,total\_w}$		12.26	7.64	7.69	8.39
AIC_c		-127.68	-147.61	-147.04	-143.66
AIC_{c_w}		-50.43	-65.81	-65.60	-62.79
$MB_{,model}$		1.022	1.034	0.982	0.984

Table AIII.3 lists the statistical output for the concentrated emulsion columns (using the fitted parameters to the dilute columns) and for the subsequent predictions when: (*i*) influence of water saturation (α_1); (*ii*) influence of viscous instabilities (α_2); and (*iii*) both water saturation and viscous effects (α_1 & α_2) are added to the model. It should be noted that the model mass balance decreases as the additional dispersive mixing mechanisms are added due to the numerical methods of how the equations are solved. Thus, the results (in particular the statistical values in Table AIII.3) should be used with caution. The model and applications should be used in a more conceptual matter.

APPENDIX IV: ADDITIONAL EMULSION COLUMN EXPERIMENTS

Table AIV.1: Additional experiments- column parameters.

experiment	porous media	porosity	bulk density	packed length	pore volume	measured flow rate	initial dispersivity	dispersed phase content	measured viscosity	modeled viscosity[c]	mobility ratio	emulsion introduced	recovered in effluent	retained in column	mass balance
		n	ρ_b	L	PV	Q	α_0	C_0	μ	μ_e	M				MB
		[-]	[g·cm^{-3}]	[cm]	[mL]	[mL·min^{-1}]	[cm]	[% wt.]	[mPa·s]	[mPa·s]	**[-]**	[PV]	[g]	[g]	[%]
I.A *	FF	0.36	1.69	10.4	68.5	1.02	0.036	23.2 (±0.1)	7.3 (±0.1)	7.9	8.3	2.3	21.8	9.99	97
I.B *	FF	0.37	1.69	10.2	67.6	0.98	0.035					2.1	19.1	9.40	97

* 0.02% $CaCO_3$ alkalinity-releasing particles present in emulsion

[a] not measured due to insufficient sample volume

[b] single measurement

[c] emulsion viscosity modeled using expression presented in Chapter 3 based on Sibree (1930) and Broughton and Squires (1937)

μ_d is the displacing fluid viscosity. These experiments used water as the displacing fluid; μ_d =0.954 mPa·s (i.e., the viscosity of water at 22°C)

± indicates standard deviation

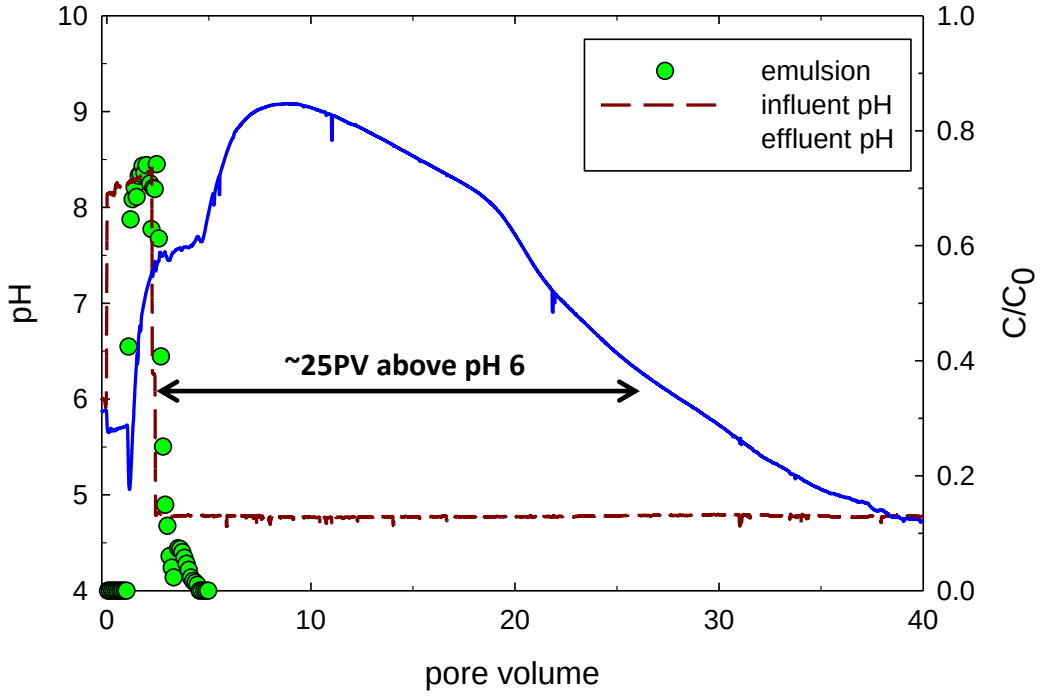

Figure AIV.1: Sustained alkalinity release (column I.B) from a 0.02% (wt.) $CaCO_3$ emulsion.

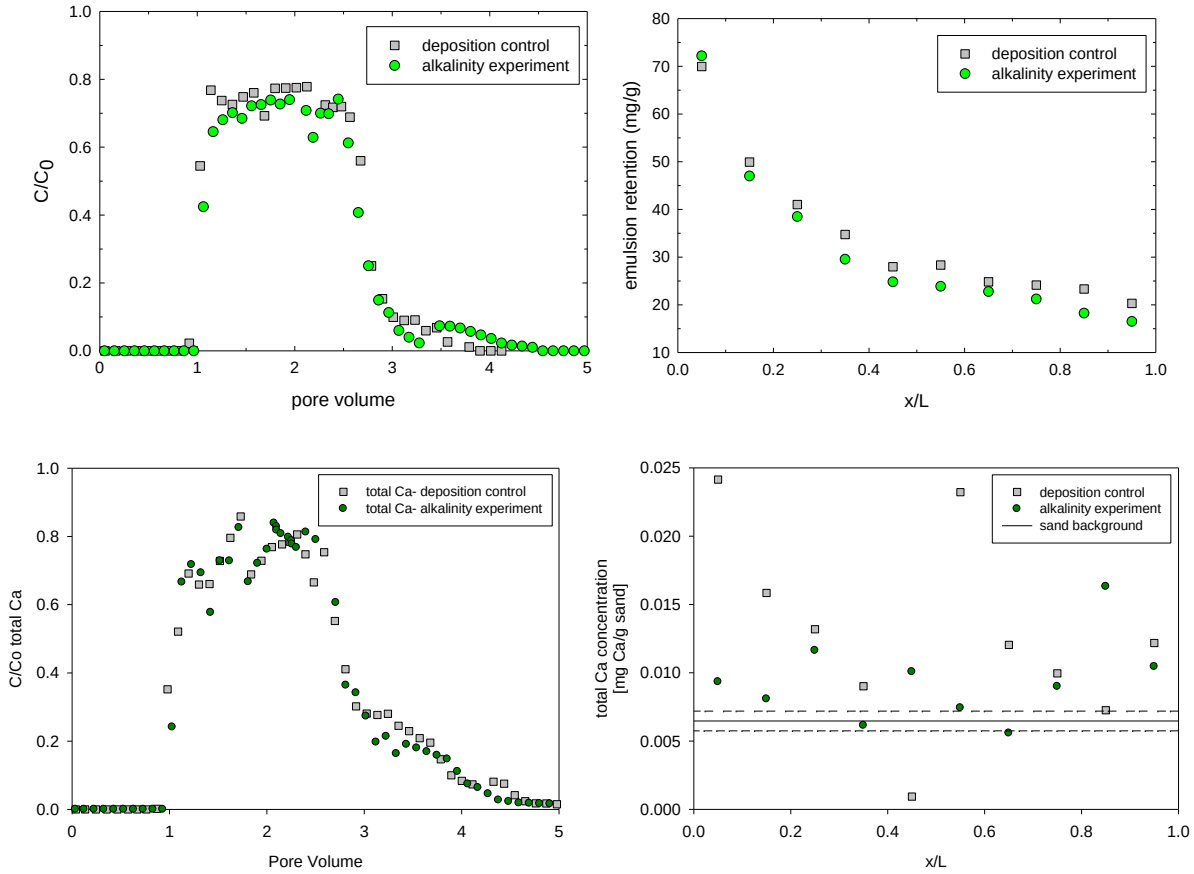

Figure AIV.2: (top) emulsion and (bottom) total calcium breakthrough curves and deposition profile in parallel column experiments conducted with the 0.02% $CaCO_3$ containing emulsion (experiment I.A & I.B). The solid line indicates the background concentration of the Ottawa sand and dashed lines show the standard deviation.

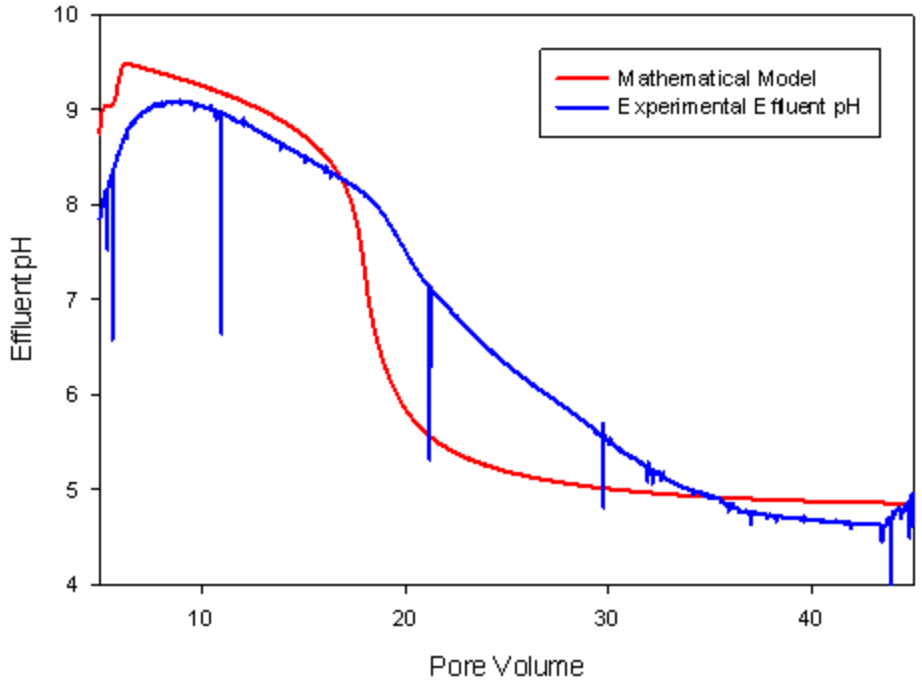

Figure AIV.3: Experimental and corresponding model for effluent pH due to alkalinity release from 0.02% $CaCO_3$ (Col I.B) emulsion.

VITA

Katherine Muller grew up outside of Portland, Oregon. Her introduction to engineering was from her grandfather, Don Scurlock, who was a mechanical engineer. Through the many projects the two completed together, his passion for engineering and problem solving was clear- and contagious.

In 2005, Katie was accepted to the school of engineering at Tufts University and graduated with a Bachelor of Science degree in Environmental Engineering in 2009. While an undergraduate student, Katie had the opportunity to work in the IMPES laboratory under the direction of Professor Andrew Ramsburg and as a senior, Katie completed her senior project under Professor John Durant related to air pollution in the Boston area. These research experiences, although very different, were instrumental in developing Katie's enthusiasm for the research process.

Due to the advice from Professor John Durant, directly upon graduating Katie decided to continue her engineering education at Tufts University with Professor Andrew Ramsburg. Although originally she had intended to get a Master's degree, the opportunity arose to continue studying. Katie completed her doctorate in July 2016 and will continue her research career as a post-doc at Oak Ridge National Laboratory.

Outside of work, Katie is an avid runner having completed several marathons, including the Boston Marathon in 2015.